

2016-08-16

# Carbon nanotubes micro-arrays: characterization and application in biosensing of free proteins and label-free capture of breast cancer cells

Farhad Khosravi

*Worcester Polytechnic Institute*

Follow this and additional works at: <https://digitalcommons.wpi.edu/etd-dissertations>

---

## Repository Citation

Khosravi, F. (2016). *Carbon nanotubes micro-arrays: characterization and application in biosensing of free proteins and label-free capture of breast cancer cells*. Retrieved from <https://digitalcommons.wpi.edu/etd-dissertations/347>

This dissertation is brought to you for free and open access by Digital WPI. It has been accepted for inclusion in Doctoral Dissertations (All Dissertations, All Years) by an authorized administrator of Digital WPI. For more information, please contact [wpi-etd@wpi.edu](mailto:wpi-etd@wpi.edu).

**CARBON NANOTUBES MICRO-ARRAYS:  
CHARACTERIZATION AND APPLICATION IN BIOSENSING OF FREE  
PROTEINS AND LABEL-FREE CAPTURE OF BREAST CANCER CELLS**

By

Farhad Khosravi

A Dissertation

Submitted to the Faculty of the

WORCESTER POLYTECHNIC INSTITUTE

In partial fulfillment of the requirements for the

Degree of Doctor of Philosophy

in

Mechanical Engineering

---

July 2016

APPROVED:

---

Professor Balaji Panchapakesan, Advisor

---

Professor Christopher R. Lambert, Committee Member

---

Professor Yuxiang Shawn Liu, Committee Member

---

Professor Pratap Mahesh Rao, Committee Member

---

Professor Shesh N. Rai, Committee Member

---

Professor Mark W. Richman, Graduate Committee Representative

ABSTRACT  
CARBON NANOTUBES MICRO-ARRAYS:  
CHARACTERIZATION AND APPLICATION IN BIOSENSING OF FREE  
PROTEINS AND LABEL-FREE CAPTURE OF BREAST CANCER CELLS

Farhad Khosravi

Worcester Polytechnic Institute 2016

Circulating tumor cells (CTCs) are cells released into the bloodstream from primary tumors and are suspected to be one of the main causes behind metastatic spreading of cancer. The ability to capture and analyze circulating tumor cells in clinical samples is of great interest in prevailing patient prognosis and clinical management of cancer.

Carbon nanotubes, individual rolled-up graphene sheets, have emerged as exciting materials for probing the biomolecular interactions. With diameter of about 1 nm, they can attach themselves to cell surface receptors through specific antibodies and hold a great potential for diagnostic cellular profiling. Carbon nanotubes can be either semiconducting or metallic, and the electronic properties of either type rivals the best known materials. Small size of nanotubes and the ability to functionalize their surface using 1-Pyrenebutanoic Acid, Succinimidyl Ester (PASE), enables a versatile probe for developing a platform for capture and analysis of cancer biomarkers and circulating tumor cells. Although nanotubes have previously been used to electrically detect a variety of molecules and proteins, here for the first time we demonstrate the label free capture of spiked breast cancer cells using ultra-thin carbon nanotube film micro-array devices in a drop of buffy coat and blood. A new statistical approach of using Dynamic

Time Warping (DTW) was used to classify the electrical signatures with 90% sensitivity and 90% specificity in blood. These results suggest such label free devices could potentially be useful for clinical capture and further analysis of circulating tumor cells.

This thesis will go in-depth the properties of carbon nanotubes, device fabrication and characterization methodologies, functionalization protocols, and experiments in buffy coats and in blood. Combination of nano and biological materials, functionalization protocols and advanced statistical classifiers can potentially enable clinical translation of such devices in the future.



## BIOGRAPHICAL SKETCH

Farhad Khosravi was born in Tehran, Iran. He immigrated to the United States of America in 2001. He was elected the senior class president in high school and received the principal's award on his last year of school for his academic achievements. He then attended University of Louisville for his undergraduate degree, where he worked as a math tutor, holding help sessions and assisting engineering students with their studies. He completed three engineering co-op programs at Brown Forman Corporation and MedVenture Technologies as a research & development and product engineer intern. As a member of the biomedical engineering society he led the web development of the national chapter and attended national society meetings and conferences. He received his Bachelor's degree in Bioengineering in 2011.

Farhad then began his graduate studies at University of Louisville, where his work on carbon nanotubes and cell capture with Professor Balaji Panchapakesan has been supported by NIH, R15CA156322. In 2012, Farhad completed his Master's degree with honors, majored in Bioengineering, and then elected to continue his graduate studies enrolling in University of Louisville's Mechanical Engineering Department's Ph.D. program. During this transition time, Farhad co-founded a start-up company, Integrated NanoSystems LLC, to further pursue his research interest in the field of nanotechnology and received a Phase Zero grant from Kentucky Science and Engineering Foundation. In 2014, Farhad transferred to Worcester Polytechnic Institute to continue his graduate studies under Professor Panchapakesan.

## ACKNOWLEDGMENTS

This thesis would not have been possible without the generous support I have received throughout the last four years in Louisville and Worcester. Many people have provided assistance and support for the research projects presented here, and many others have provided much-needed encouragement through the inevitable challenges of graduate school. Although mere words are inadequate to express my gratitude, it gives me great pleasure to have this small opportunity to thank everyone who contributed to this work, from my family to my friends and my colleagues.

Foremost, I would like to express my special appreciation and thanks to my advisor Professor Balaji Panchapakesan, you have been a tremendous mentor for me. I would like to thank you for your continuous support and enthusiasm encouraging my research and for allowing me to grow as a research scientist. Your advice on both research as well as on my career have been priceless. I would also like to thank my committee members, Professors Christopher R. Lambert, Yuxiang Shawn Liu, Pratap Mahesh Rao, and Shesh N. Rai for their support and encouragement.

It has been both a pleasure and an honor to have had the opportunity to complete my graduate studies at Worcester Polytechnic Institute. My experience here at this institute has truly been priceless and will leave a significant mark in my life.

## TABLE OF CONTENTS

<b>ABSTRACT</b>	i
<b>BIOGRAPHICAL SKETCH</b>	iii
<b>ACKNOWLEDGMENTS</b>	iv
<b>TABLE OF CONTENTS</b>	v
<b>LIST OF FIGURES</b>	x
<b>ABBREVIATIONS</b>	xxv
<b>1. INTRODUCTION</b>	1
1.1. CIRCULATING TUMOR CELLS (CTC)	1
1.2. PRINCIPLES OF ENRICHMENT FOR CTC	10
1.2.1. PHYSICAL PROPERTY BASED SEPARATION OF CTC	10
1.2.2. BIOLOGICAL PROPERTY BASED ISOLATION OF CTC	14
1.3. METHODS OF CTC ENRICHMENT AND DETECTION	18
1.3.1. IMMUNOMAGNETICS	18
1.3.2. MICROFLUIDICS	20
1.3.3. FILTRATION	23
1.3.4. NANOSUBSTRATE	25
1.3.5. IN VIVO	26
1.3.6. MICROCANTILEVER	27
1.3.7. COMMERCIALY AVAILABLE CTC DEVICES	29
<b>2. BACKGROUND</b>	38
2.1. CARBON NANOTUBES (CNT)	38
2.1.1. MOLECULAR BOND STRUCTURE	39
2.1.2. PRODUCTION OF CNT	41
2.1.3. CHIRALITY	42
2.1.4. ELECTRICAL PROPERTIES AND BAND STRUCTURE	43
2.1.5. MECHANICAL PROPERTIES	46
2.1.6. CHEMICAL AND BIOLOGICAL PROPERTIES	46
2.1.7. PROPERTIES BASED ON SMALL SIZE AND DIAMETER	47

2.2. CARBON NANOTUBE FIELD EFFECT TRANSISTORS (CNT-FET)	48
2.2.1. ELECTROLYTE-GATED CNT-FET	52
2.3. CARBON NANOTUBES (CNT) FOR SENSING AND BIOLOGICAL APPLICATIONS	56
2.3.1. CNT FOR GAS SENSING	57
2.3.2. CNT FOR BIOSENSING	60
2.3.3. CNT FOR OTHER BIOLOGICAL APPLICATION	66
2.3.4. DISCUSSION AND ANALYSIS	68
<b>3. CHARACTERIZATION AND METHODS</b>	71
3.1 CNT DEVICE DESIGN AND FABRICATION	72
3.1.1 VACUUM FILTRATION AND CNT-NETWORK FORMATION	73
3.1.2. CLEAN ROOM PROCESSING	77
3.1.3. CNT DEVICE GENERATION I, II, AND III	81
3.2. CNT ULTRA-THIN FILM	84
3.3. MEASUREMENT SETUP	87
3.4. DEVICE CHARACTERIZATION	90
3.4.1. CHARACTERIZATION OF CARBON NANOTUBES (CNT)	90
3.4.2. DEVICE AND THIN FILM CHARACTERIZATION	94
3.4.3. PERCOLATION THEORY VS. CNT FILM MASS	98
3.4.4. CNT DEVICE FET CHARACTERISTICS	105
<b>4. CNT DEVICE FUNCTIONALIZATION AND SENSOR CHARACTERISTICS</b>	109
4.1. CNT FUNCTIONALIZATION	109
4.1.1. GENERAL CNT FUNCTIONALIZATION PROTOCOL	112
4.2. GOLD NANOPARTICLES (NP) STUDIES	113
4.2.1. GOLD NPs FUNCTIONALIZATION METHOD	113
4.2.2. RESULTS	115
4.3. CNT DEVICE SENSOR CHARACTERISTICS	118
4.3.1. UNDERSTANDING SEMICONDUCTING CNT FOR CHEMICAL SENSING	120

4.3.2. $\text{Hg}^{2+}$ AND $\text{NH}_4^+$ ION EXPERIMENTATION METHODS	123
4.3.3. LANGMUIR ISOTHERM MODEL FOR BIOSENSORS	123
<b>5. CNT DEVICES FOR CAPTURE AND SENSING OF CANCER BIOMARKER PROTEINS</b>	129
5.1. INTRODUCTION	129
5.2. RESULTS	130
5.2.1. DETECTION OF BIOTIN ON CNT DEVICES	130
5.2.2. DETECTION OF FREE EpCAM ON CNT DEVICES	132
5.3. CONCLUSION AND ANALYSIS	132
5.4. EXPERIMENTAL	135
5.4.1. CNT DEVICE FABRICATION	135
5.4.2. CNT DEVICE FUNCTIONALIZATION	135
5.4.3. EXPERIMENTAL SET-UP	136
<b>6. ULTRASENSITIVE AND LABEL-FREE SENSING OF IL-6 BASED ON PASE FUNCTIONALIZED CARBON NANOTUBE MICRO-ARRAYS WITH RNA-APTAMERS AS MOLECULAR RECOGNITION ELEMENTS</b>	137
6.1. INTRODUCTION	137
6.1.1. APTAMERS	137
6.1.2. INTERLEUKIN-6 (IL-6)	138
6.2. RESULTS	141
6.3. DISCUSSION AND CONCLUSIONS	148
6.4. MATERIALS AND METHODS	150
6.4.1. DEVICE FABRICATION	150
6.4.2. DEVICE FUNCTIONALIZATION	150
6.4.3. TESTING	150
<b>7. NANOTUBE DEVICES FOR CAPTURE AND DIGITAL PROFILING OF CIRCULATING TUMOR CELLS</b>	152
7.1. INTRODUCTION	152
7.2. CELL CULTURE	153
7.2.1. IMMUNOFLUORESCENT STAINING AND CONFOCAL MICROSCOPY	155

7.2.2. CELL CULTURE PREPARATION FOR TESTING	160
7.3. RESULTS	160
7.3.1. NANOTUBE DEVICE ARRAY TESTING IN CELL CULTURES	161
7.4. KOHLRAUSCH-WILLIAMS-WATTS (KWW) FUNCTION MODEL	166
7.5. CONCLUSIONS	169
7.6. EXPERIMENT	170
7.6.1. CARBON NANOTUBE SENSOR FABRICATION	170
7.6.2. CNT FUNCTIONALIZATION	171
7.6.3. EXPERIMENTAL SET-UP	171
<b>8. LABEL-FREE CAPTURE OF BREAST CANCER CELLS SPIKED IN BUFFY COATS USING CARBON NANOTUBE ANTIBODY MICRO-ARRAYS</b>	172
8.1. INTRODUCTION	172
8.2. RESULTS	175
8.2.1. FABRICATION OF NANOTUBE SENSOR ARRAYS	177
8.2.2. ANTIBODY FUNCTIONALIZATION	179
8.2.3. TESTING IN BUFFY COATS AND DEVELOPMENT OF A STATISTICAL CLASSIFIER FOR LIQUID BIOPSY	180
8.2.4. CONSTRUCTION OF THE CLASSIFIER	183
8.2.5. TRAINING SET CLASSIFICATION	190
8.2.6. BLINDED TEST CLASSIFICATION	191
8.2.7. HEAT MAP	193
8.2.8. CELL CAPTURE WITH SINGLE CELL SENSITIVITY AND CONFOCAL MICROSCOPY	195
8.3. DISCUSSION AND OUTLOOK	198
8.4. METHODS	199
8.4.1. CNT-NETWORK FORMATION	199
8.4.2. CLEAN ROOM PROCESSING	200
8.4.3. RAMAN SPECTROSCOPY	200
8.4.4. DEVICE FUNCTIONALIZATION	200
8.4.5. CELL CULTURE AND PREPARATION	201

8.4.6. CONFOCAL MICROSCOPY	201
8.4.7. DEVICE TESTING	202
8.4.8. STATISTICAL CLASSIFIER	202
8.4.9. DYNAMIC TIME WARPING (DTW)	203
8.4.10. K-NEAREST NEIGHBORS CLASSIFIER	204
<b>9. LABEL-FREE CAPTURE OF BREAST CANCER CELLS SPIKED IN BLOOD USING CARBON NANOTUBE ANTIBODY MICRO-ARRAYS</b>	206
9.1. INTRODUCTION	206
9.2. MATERIAL AND METHODS	209
9.2.1. DEVICE DESIGN AND PRINCIPLE	209
9.2.2. DEVICE FUNCTIONALIZATION	211
9.2.3. BLOOD SAMPLE PREPARATION	214
9.2.4. CELL CULTURE AND PREPARATION	216
9.2.5. EXPERIMENTAL DESIGN AND TESTING	217
9.3. RESULTS	220
9.3.1. STATISTICAL ANALYSIS	224
9.3.2. OPTICAL MICROSCOPE IMAGE ANALYSIS	230
9.3.3. CONFOCAL IMAGE ANALYSIS	235
9.4. CONCLUSION AND FUTURE WORK	237
<b>10. CONCLUSIONS AND FUTURE DIRECTIONS</b>	241
10.1. CONCLUSIONS	241
10.2. SUMMARY	244
10.3. FUTURE DIRECTIONS	249
<b>REFERENCES</b>	252

## LIST OF FIGURES

<b>Figure 1.</b> Schematic showing the shedding of tumor cell into the blood stream and seeding new tumors through metastases. The cancer cells that enter the blood vessels and circulate with normal blood cells are considered circulating tumor cells (CTC) [28].	3
<b>Figure 2.</b> Kaplan Meier Analysis of overall survival for patients with metastatic breast cancer (a), metastatic colorectal cancer (b), and prostate cancer (c). Patients were divided into those with Favorable and Unfavorable CTC. The cutoff value between favorable and unfavorable CTC was $\geq 5$ CTC/7.5mL blood for breast and prostate cancer and $\geq 3$ CTC/7.5mL blood for prostate cancer [33, 57]. For example patient with 1 CTC/7.5 mL was labeled favorable.	7
<b>Figure 3.</b> Isolation and enrichment of CTCs from blood of cancer patients is based on the physical or biological properties of CTCs [18]. Physical property based separation include size (membrane filter devices [128, 129]), deformability (microfluidics system in a chip [81-99]), electric charge (dielectrophoresis [115, 116]), and density (Ficoll centrifugation [58]). Biological based property isolation is based on: the expression of cell surface markers, (i.e. epithelial cell adhesion molecule (EpCAM)) for positive selection and CD45 for negative selection; anti-body (i.e. anti-EpCAM) or anti-CD45 antibodies conjugated with magnetic beads, for enriching CTCs in a magnetic field [34, 65-72]; anti-EpCAM antibodies on microposts or columns of nanobeads [73-80]; anti-EpCAM antibodies conjugated to 3 $\mu\text{m}$ beads to increase the size of CTCs before filtration [141]; anti-EpCAM, anti-HER2/neu, anti-EGFR antibodies on different sizes of nanoparticles for capturing and detecting different CTCs [114].	11
<b>Figure 4.</b> Microvortex chip design and principle. (A and B) show channels and reservoir arrangement ( $W_C = 40 \mu\text{m}$ , $H = 80-85 \mu\text{m}$ , and $L_C = 4 \text{ mm}$ ). (C) Demonstrates the wall effect forces ( $F_{LW}$ ) and shear-gradient lift forces ( $F_{LS}$ ). (D) Shows the migration of cells to dynamic lateral equilibrium positions ( $X_{eq}$ ) and (E) trapping of CTC in reservoirs ( $W_R = 480 \mu\text{m}$ and $L_R = 720 \mu\text{m}$ ) [96].	13
<b>Figure 5.</b> Schematic diagram of a microfluidic device for cancer cell separation using multi-orifice flow fractionation and DEP. In the first separation region, the relatively larger MCF-7 cells and a few blood cells pass through the center channel and enter the DEP channel, after which most blood cells exit through outlet I. In the focusing region, all cells experience a positive DEP force and then align along both sides of the channel. Finally, the second separation region selectively isolates MCF-7 cells via DEP [115].	15
<b>Figure 6.</b> Schematic illustrating the CTC capture using antibody conjugated magnetic bead and fluorescence imaging [65].	19



- Figure 7.** CTC-chip for isolation of CTCs from whole blood using a microfluidic device. (a) The sample is continually mixed on a rocker, and pumped through the chip using a pneumatic-pressure-regulated pump. (b) The CTC-chip with microposts etched in silicon. (c) Whole blood flowing through the microfluidic device. (d) Scanning electron microscope image of a captured NCI-H1650 lung cancer cell spiked into blood (colored red). The inset shows a high magnification view of the cell [73]. ..... 22
- Figure 8.** 3D microfilter device for viable CTC enrichment from blood. (a) Shows the filtration process and forces on a trapped cell.  $F_L$ : force caused by fluidic pressure from top.  $F_S$ : supporting force from bottom membrane.  $F_T$ : tension stress force on plasma membrane. (b) Device design of a single hexagon-shaped microfilter patch [84]. ..... 24
- Figure 9.** NanoVelcro chip. Schematic overlooking the first, second, and third generation of the device. This device takes advantage of nanosubstrates and microfluidics to capture isolate and release CTCs for further analysis [201].... 26
- Figure 10.** Stainless steel seldinger guidewire functionalized with anti-EpCAM antibodies to capture CTC inside the patients vein, in vivo approach [18]. ..... 27
- Figure 11.** Schematic showing principle of microcantilever sensor operation. (a) Microcantilever coated with non-specific reference peptide, shows no response in form of a deflection to the presence of normal cells or CTCs. (b) Microcantilever functionalized with cancer targeting peptide demonstrates a strong response in form of a deflection as CTCs interact with the cantilever [140]. Position sensitive device (PSD). ..... 29
- Figure 12.** Graphene lattice and construction of a carbon nanotube (CNT) and their band structure (A) honey comb structure of graphene lattice sheet, a CNT can be constructed by rolling up a graphene sheet. The chiral vector  $C_h$  points from the origin to the point which is rolled up to the origin, here,  $C_h = 3a_1 + 2a_2$ , so this is known as an  $(n, m) = (3, 2)$  nanotube [228]. (B) shows an illustration of rolled up zigzag, arm-chair, and chiral single walled carbon nanotubes (SWNTs) [228]. (C) Rolling a graphene sheet into a nanotube quantizes the wave states perpendicular to the nanotube axis, resulting in 1-D slices through the 2-D band structure. Depending on the way the tube is rolled up, the results can be either a metallic or Semiconducting SWNT [240]. (D) The allowed electron states in a CNT are determined by the intersections between the allowed wavevectors and the graphene band structure, which, near the fermi energy,  $E_F$ , is well-approximated by a series of cones [240]. ..... 40
- Figure 13.** Schematic showing the basic hexagonal bonding structure on a graphene sheet. Carbon nuclei shown as filled circle,  $\pi$ -bonds are out-of-plane, and  $\sigma$ -bonds connect the carbon nuclei in-plane [239]. ..... 41

**Figure 14.** Schematic of a typical carbon nanotube field-effect transistor (CNT-FET). (A) side view of a back-gated CNT-FET. Metal electrodes are contacted on either end of the CNT, allowing one to apply a source-drain voltage bias  $V_{DS}$  across it and to measure its conductance as a function of the back gate voltage  $V_G$ . The CNT is insulated from the gate by a dielectric material, typically  $\text{SiO}_2$ . (B) Conduction of a semiconducting CNT as a function of gate voltage ( $V_G$ ). (C) Band diagram of CNT for different gate voltages (marked with red dots in the  $I_{DS}$  vs.  $V_G$  curve (B)) as a function of position along the nanotube axis. At  $V_G = -8$  V, the Fermi level is deeper in the valence band, therefore allowing for higher conduction. At  $V_G = 0$  V, the Fermi level typically lies below the valence band edge due to the work function of the metal contact, as a result CNT is conducting. At  $V_G = 12$  V, the Fermi level lies in the band gap, in this case turning the transistor off..... 50

**Figure 15.** Schematic of an electrolyte-gated CNT-FET. Similar to Figure 14, CNT is contacted by metal electrodes (Ni/Au) on each side, allowing one to take conductance measurements. The gate voltage  $V_G$  is applied by a wire (i.e. Ag/AgCl reference) that is in contact with the electrolyte solution (i.e. ionic buffer solution). The voltage applied affects the CNT via ions in the electrolyte solution. For example, if voltage is applied to make the wire positively charged, the negative ions will get attracted to form a double layer. SU-8 polymer layer acts as an insulator to separate the charges in the electrolyte solution from the contacts, therefore only directly gating the CNT..... 54

**Figure 16.** Chemical gating effects to the semiconducting SWNT by gaseous  $\text{NH}_2$  and  $\text{NO}_2$ . Each gas causes a large threshold voltage shift in the  $I_{DS}$  vs.  $V_G$  curve. The measurements with these gases were carried out successively after sample recovery [290]..... 58

**Figure 17.** CNT DNA sensor and sensing mechanism, (a) optical image of the central region of a single sensor chip with four SWNT devices (scale bar 200  $\mu\text{m}$ ). (b) Schematic illustration of a single device during electrical measurement. Complementary ssDNA oligos hybridize to thiolated ssDNA coimmobilized with mercaptohexonal (MCH) on the gold electrodes. Real-time monitoring of 15mer (c) and 30mer (d) DNA hybridization in PBS, pH 7.4, is shown. The conductance of a nanotube device functionalized with thiolated ssDNA exhibits selective response to the addition of complementary ssDNA showing decrease in conductance at the time of sample addition [314]. ..... 62

**Figure 18.** (A1) Schematic diagram of a CNT-FET for protein detection. Antibody is bound to the CNT and binding to the target electrostatically gates the transistor, causing a change in conductance of the CNT. (A2) The electrochemical signal, plotted as normalized conductance, is shown when different concentrations of prostate specific antigen (PSA) are introduced to the device (arrow). Concentrations as low as  $1\text{ngmL}^{-1}$  can be detected [316]. (B) Immunoassay

detection principle using CNTs to immobilize multiple labels and secondary antibodies for signal amplification. HRP catalyzes  $H_2O_2$  and generates electrons for amperometric based measurement. (B1) conventional single HRP labeled secondary antibody (B2) multiple HRP and secondary antibody on carbon nanotube for signal amplification [315]..... 63

**Figure 19.** (A) Top panel shows a schematic picture of two electrodes connecting a semiconducting SWNT with GOx enzymes immobilized on its surface. (A) Bottom panel shows real time electronic response of the glucose, the substrate of GOx. Milli-Q water sample was added to the liquid at 100 sec (red arrow), and at 200 sec 0.1 mM glucose in milli-Q water was added to the liquid (blue arrow). The conductance of the GOx-coated SWNT is observed to increase upon addition of glucose to the liquid. Inset (a) shows the same measurement on a second device where the conductance was a factor of 10 lower. Inset (b) displays the same measurement on a semiconducting SWNT without GOx. As expected, no conductance increase is observed here [270]. (B) Shows the cell detection by metal-cluster-decorated CNT biosensor. The normalized conductance plot here shows the change in signal during exposure to *A. anophagefferens*. The insert at top is an optical image of *A. anophagefferens*. The inset at the middle shows a schematic illustration of cells on the devices with metal-clusters [318]. ..... 65

**Figure 20.** Schematic of a basic structure of carbon nanotube (CNT) device after microfabrication process. CNT film bridging the two source and drain Ni/Au electrodes on top of a Si/SiO<sub>2</sub> substrate. Source/drain electrodes are covered and insulated with a photoresist polymer layer, SU-8. .... 72

**Figure 21.** CNT film fabrication process. (A) Vacuum filtration setup, (B) CNT stock solution before dilution, left side. CNT transferred onto nitrocellulose filter membrane (NCFM) after vacuum filtration (red circle), right side. CNT film diameter after filtration = 75 mm. (C) Shows the CNT film transferred onto 4" Si/SiO<sub>2</sub> wafer after acetone vapor bath step, red circle. SEM images (D and E) showing the structure of two different CNT films in the nano-scale on Si/SiO<sub>2</sub> wafer after the completion of CNT film fabrication process. (D) Shows a nematic and (E) Isotropic CNT film network. .... 76

**Figure 22.** Micro-array device micro-fabrication process. (a) 4" silicon wafer. (b) Dry-thermal oxidation. (c) CNT film transfer. (d) First photolithography step followed by patterning CNT film, Reactive-ion etching. (e) Second photolithography for patterning electrodes. (f) Sputtering Ni/Au and lift-off, in yellow. (g) SU-8 photoresist is spun on top of wafer, in green. (h) Third photolithography step is performed to open window through SU-8 layer and expose the CNT network. (i) Shows an optical microscope image of devices at the end of photolithography 1 (d), sputtering lift-off (f), and photolithography 3 (h) steps. .... 80

**Figure 23.** Generation I, II, and III of CNT devices, all are microfabricated on 4 inch silicon wafer. (A) 60 devices per wafer, CNT window on each device is 100X60  $\mu\text{m}$ . (B) 76 devices per wafer, CNT window on each device is 3000X3000  $\mu\text{m}$ . (C) 80 devices per wafer, three sensors per device for a total of 240 sensors. CNT window on each sensor is 20X20  $\mu\text{m}$ . ..... 83

**Figure 24.** SEM images of three different unique CNT film structure, (A) ultra-thin isotropic, (B) thin nematic, and (C) disordered isotropic. (A and B) are products of CNT suspended in aqueous surfactant solutions. CNT suspended in these solution produce an ultra-thin CNT films at very low concentration (A), i.e. 2  $\mu\text{g}$ . These films are ~10-50 nm thick and uniform. Increasing the concentration of CNT in aqueous surfactant solution results in a much different nematic CNT films. Nematic nucleation of CNT films occur as concentration increases, dark region of (B1). Resulting in locally aligned CNT on the film (B2 and B3). CNT films made from CNT suspended in organic solvents are very much different in micro and nano scale. Large mass of CNTs in these films are trapped in tangled ropes that can get as thick as 1  $\mu\text{m}$  or larger, (C2). As a result of this effect, much greater CNT mass is required to achieve a uniformly conductive film, i.e. 40  $\mu\text{g}$  vs. only 2  $\mu\text{g}$  for aqueous solution suspension. As a result, great fraction of these nanotubes are hidden and not exposed to the environment. .... 86

**Figure 25.** (A) Schematic demonstrates the electrical measurement setup. A DC bias voltage,  $V_{\text{DS}}$ , and gate voltage,  $V_{\text{G}}$ , was applied and the current  $I_{\text{DS}}$  passing through the drain was measured using the parameter analyzer while the LabVIEW program was used to control the parameters on the parameter analyzer and save the data to the computer. (B) Shows the humid chamber used to store devices with sample droplets during functionalization and testing to prevent the evaporation of the droplet. This was achieved by controlling the humidity inside the chamber using  $\text{H}_2\text{O}$  soaked cotton balls carefully placed on the outer edge of the chamber. (C) Showing the probe-station setup, including the vibration isolated base, optical microscope, and the three probes. This set-up specifically demonstrates the platform for liquid gated testing, devices with sample droplets, using a modified humid chamber allowing probe access to the device. .... 89

**Figure 26.** (A) Optical absorbance of Iso-semiconducting SWNT showing the S33 (~450-630 nm) and S22 (~900-1000 nm) transition peaks. (B) Transmittance of Iso-Semiconducting SWNT in aqueous surfactant solution. (C) Raman spectrum of Iso-Semiconducting SWNT film on silicon wafer showing a large G band, small D band and 2D band. The  $I_{\text{G}}/I_{\text{D}}$  ~30 was observed in these nanotubes.... 92

**Figure 27.** (A) SEM and (B and C) AFM images of ultra-thin SWNT network. .... 93

**Figure 28.** Electrical resistance of CNT devices fabricated from nematic films. (A) SEM image of the actual device fabricated from 10 and 40  $\mu\text{g}$  CNT films and

their corresponding high resolution images of the CNT network; (B) film resistance before and after annealing at 250 °C; (C) histogram suggesting high degree of control in device resistance over 14 devices..... 96

**Figure 29.** Electrical resistance of CNT devices fabricated from ultra-thin isotropic films. (A) SEM image of the actual device fabricated from 6, 4, 2, and 1  $\mu\text{g}$  CNT films and their corresponding high resolution images of the CNT network; (B) film resistance before and after annealing at 250 °C; (C) histogram suggesting high degree of control in device resistance over 58 devices..... 97

**Figure 30.** (A) Shows the measured CNT film resistance versus the source drain distance of generation 1, 2, and 3 CNT devices, for films of the same density. All three generations have unique constant separation distance, generation 1: 100  $\mu\text{m}$ , generation 2: 3000  $\mu\text{m}$ , and generation 3: 20  $\mu\text{m}$ . inner box shows a zoom in on generation 1 and 3. (B) Demonstrates the sheet conductance versus CNT film mass in  $\mu\text{g}$ , inner box shows the data in logarithmic form. .... 100

**Figure 31.** Electrical properties of CNT-FET devices (6  $\mu\text{g}$ ) under dry conditions with a p-type back-gate (A and C) and under phosphate buffer solution with Ag/AgCl reference electrode (B and D). A & B show the  $V_{\text{DS}}$  sweep and C & D present the  $V_{\text{G}}$  sweep characteristic of the CNT-FET devices. .... 104

**Figure 32.** Transistor properties versus film mass: (A) presents mobility and on-off ratio of a back-gated CNT device in one plot, we can see that mobility is reversely related to on-off ratio. (B) Presents the mobility range for 40  $\mu\text{g}$  film. (C) presents the on-off ratio for a top-liquid-gated CNT device, gate is applied by Ag/AgCl reference electrode through electrolyte solution (1X PBS). ..... 107

**Figure 33.** (A) 1-Pyrenebutanoic Acid, Succinimidyl Ester (PASE) reacting with the amine groups on a biomolecule (i.e. protein) to form an amine bond resulting in a PASE-biomolecule complex. (B) PASE irreversibly adsorbing onto the sidewall of SWNT via  $\pi$ -stacking. (C) Amine groups on a biomolecule reacting with the anchored succinimidyl ester to form amide bonds to immobilize PASE-biomolecule complex on CNT surface. .... 111

**Figure 34.** Functionalization of PASE. Demonstrating the successful functionalization of PASE molecule onto CNT side walls, by binding of amine polymer conjugated gold NPs to the side walls of PASE functionalized CNT. (A) Schematic showing the Schematic of the PASE functionalization protocol and binding of amine NPs onto CNT surface by PASE linker molecule. (B and C) SEM images of CNT devices after NPs functionalization. (B) SEM image of positive control, PASE functionalized CNT, amine conjugated NPs are clearly binding to the PASE functionalized CNTs. (C) SEM image of negative control, bare CNT, showing no significant interaction between amine conjugated NPs and the bare CNT surface. .... 114

**Figure 35.** Functionalization of streptavidin. Demonstrating the successful functionalization of streptavidin onto CNT by PASE molecule, by showing the specific binding of biotin conjugated gold NPs to the side walls of streptavidin functionalized CNT. (A) Schematic showing the interaction of biotin conjugated NPs with the functionalized CNT surface. (B) Schematic showing the bare CNT presenting no binding site for biotin conjugated NPs. (C and D) SEM images of CNT devices after NP functionalization. (C) SEM image of positive control (A), biotin conjugated NPs are clearly binding to the streptavidin functionalized CNTs. (D) SEM image of negative control (B) showing no significant interaction between biotin conjugated NPs and the bare CNT surface. .... 117

**Figure 36.** Functionalization of antibodies. (a) Schematic of the PASE functionalization protocol; (b) SEM image of positive control suggesting high degree of antibody functionalization; (c) SEM image of negative control suggesting no functionalization; (d) comparison of different functionalization protocols including PASE–antibody, streptavidin–biotin and amine-polymer-NP conjugation..... 119

**Figure 37.** Understanding semiconducting nanotube network. (a) Real time response of device to concentrations of  $NH_4^+$ , 300 nM to 1.3 mM, and  $Hg^{2+}$ , 30 pM to 13  $\mu$ M, ions; (b) voltage sweep before and after exposure to  $NH_4^+$  and  $Hg^{2+}$  ions; (c) concentration sensitivity of voltage sweep for  $NH_4^+$  and  $Hg^{2+}$  ions; (d) normalized signal conductance versus concentration of  $Hg^{2+}$  ions suggesting Langmuir adsorption isotherm. The inset shows the percentage sensitivity versus concentration for  $Hg^{2+}$ . Similar results were seen for  $NH_4^+$  ions suggesting same sensing mechanism. .... 122

**Figure 38.** Schematic diagram depicting the measurement and the bases for the theoretical model. Showing the CNT device as described in Chapter 3 with a liquid droplet on top containing the analytes [A]. CNT film is functionalized with the binding sites [B]. [AB] shows the binding of analyte to the binding site on CNT surface. .... 125

**Figure 39.** (A) Normalized live response of six CNT devices, three functionalized with streptavidin (positive control in green) and three not functionalized bare CNT devices (negative control in red). 5  $\mu$ L of biotin solution, 1ng/mL in 1X PBS, was added to each device at 60 seconds and the electrical current of the device was recorded for the remaining 240 seconds. The functionalized devices current increased after biotin introduction suggesting negatively charged biotin molecules interacting with CNT surface while, the bare devices show no significant change thereby no specific interaction. Schematics in the right hand side of the figure illustrated the device functionalization state and its interaction with biotin molecule. (B) Shows the V-sweep response for before and after biotin introduction to the device. Functionalized positive control device, in

green, shows a shift in the positive direction, correlating with the live current reading while negative control, ion red, shows no change. .... 131

**Figure 40.** (A) The schematic of a protein/CTC detection scheme. The entire device except the active nanotube layer is sealed off using SU8 polymer. (B) CNT device history from bare to functionalization process and introduction of EpCAM molecule is presented in one graph as a function of V-sweep. .... 133

**Figure 41.** (A) Showing the typical V-sweep for three groups of devices, from left to right, not functionalized, IgG functionalized, and anti-EpCAM functionalized. In each case, initial sweep before EpCAM protein introduction and after sweep post EpCAM (1 $\mu$ g/mL) introduction to the device is presented. Both not functionalized and IgG functionalized showed no change with the introduction of EpCAM but anti-EpCAM functionalized showed a shift. (B) CNT device history from bare to functionalization process and introduction of EpCAM molecule is presented in one graph as a function of V-sweep. (C) Presents concentration dependent device response, showing detection of molecular EpCAM up to 1 ng/mL. .... 134

**Figure 42.** Schematic showing, (A) the reaction of PASE onto aptamer, (B) PASE conjugated aptamer functionalized CNT structure and aptamer interaction with IL-6 protein on the surface of the CNT. (C) Schematic illustration of the blocking of CNT surface with tween-20 molecule. (D and E) AFM image showing a phase image, (D), and Z-Axis image, (E), of bare CNT, (a) and (b), functionalized CNT with IL-6 aptamer, (c) and (d), and IL-6 protein binding to aptamer/CNT structure, (e) and (f). Images were obtained using dry tapping mode (Nanosurf NaioAFM system). Scale bar = 100 nm. .... 140

**Figure 43.** Device characterization showing optical images of the sensor array platform, (A, B, C and D), Raman characterization (E) and SEM image (F) of the CNT film imbedded within the sensors. .... 143

**Figure 44.** Electrical properties of CNT-FET devices before PASE-aptamer functionalization in phosphate buffer solution (1X PBS, pH 7.4). .... 144

**Figure 45.** (A-C) Sensor response of the CNT-biosensor at source-drain bias of 0.1 V and at the gate bias of 0 V. (A) indicates the response after the introduction of 20nM BSA (red line), 1mM MgCL2 1X PBS (gray line), 1pg IL-6 target protein (blue line) to functionalized CNT-biosensor and (B) 1 pg IL-6 target protein to bare unfunctionalized CNT-biosensor (green line). (C) Shows response of tween-20 blocked CNT-biosensor to IL-6 protein (blue line), and BSA (red line). Arrow indicates the point of sample injection. (D-H) Before and after  $I_{DS}$ - $V_{GS}$  characterization of IL-6 aptamer functionalized CNT-biosensor with (D) 1 pg and 1 ng IL-6 protein injection, (E) blank 1mM MgCL2 1X PBS samples,

and (F) 20 nM BSA. (G and H) show $I_{DS}$ - $V_{GS}$ response of tween-20 blocked CNT-biosensor to BSA (G), and IL-6 protein (H).....	146
<b>Figure 46.</b> (A) Time dependence of normalized source-drain current of the CNT-biosensor at the source-drain bias of 0.1 V and at gate bias of 0 V after the introduction of IL-6 target protein at various concentrations onto the IL-6 aptamer functionalized CNT-biosensor. Arrows indicate the points of IL-6 target protein injection. (B) The Sensitivity of IL-6 aptamer CNT-biosensor as a function of IL-6 protein concentration (1pg to 10 ng /mL) .....	148
<b>Figure 47.</b> Illustration of a cell membrane [413]. The plasma membrane is composed of many proteins, receptors, and channels embedded in a fluid bilayer of phospholipids. ....	153
<b>Figure 48.</b> (A, B, and C) optical microscope image showing the cells cultured at ~80% confluency. Cells are detached at this point to be counted and prepared for testing. (D) Shows an optical microscope image of the detached SKBR-3 cells (right) on a hemocytometer counting device (left). ....	155
<b>Figure 49.</b> Confocal microscopy images of MCF-7, SKBR-3, and MCF-10A cell lines immunostained for EpCAM and DAPI. MCF-7 and SKBR-3 cells are positive for both EpCAM (in red or green) and DAPI (in blue) while MCF-10A cells are negative for EPCAM.....	157
<b>Figure 50.</b> Confocal microscopy images of SKBR-3, MCF-7, and MCF-10A. (A) Presents SKBR-3 and MCF-7 cells immunostained for DAPI, IgG, and cytokeratin. SKBR-3 and MCF-7 cells are positive for cytokeratin (in green), and DAPI (in blue) while negative for IgG. (B) SKBR-3 and MCF-10A cells immunostained for DAPI, EpCAM, and IgG. EpCAM is positive for SKBR-3 and negative for MCF-10A, both cell lines are negative for IgG. IgG shows to be a universal negative control across cell lines. ....	158
<b>Figure 51.</b> Confocal microscope image of the SKBR-3 and MCF-10 cells immunostained for DAPI and HER-2. SKBR-3 is positive for HER-2 and DAPI. MCF-10A in negative for HER-2 and positive for DAPI. First and third columns present culture of cells and second and forth raw demonstrate single cell staining. ....	159
<b>Figure 52.</b> (A) Showing the CNT device testing set up with source, drain, and reference electrodes in contact on the device during testing on microarray chip. (B) Optical microscope image of a sensor device with a spiked SKBR-3 cancer cell sample droplet, scale bar 100 $\mu$ m. (C) Confocal image of a SKBR-3 cancer cell on the device stained for EpCAM, in red, and DAPI, in blue.....	162
<b>Figure 53.</b> Testing in Cell Cultures: (a) Normalized device conductance of anti-EpCAM functionalized device with SKBR-3 cancer cells; (b) Normalized	



device conductance of anti-EpCAM functionalized device with MCF-7 cancer cells; (c) Normalized device conductance of anti-EpCAM functionalized device with MCF10 A normal cells; (d) Representative graph of normalized device conductance of anti-IgG functionalized device with SKBR-3, MCF-7 and MCF10-A cells.....	164
<b>Figure 54.</b> Principle of electrical signal response of CNT micro-array devices. (A) Specific and non-specific interactions. (B) Interaction exponent modeled for range of $\beta$ for both specific and non-specific signal. ....	168
<b>Figure 55.</b> Schematic of Sensing Mechanism: Cooperative binding of anti-EPCAM antibodies to their corresponding receptors in cells on top of nanotube biosensors creates “spikes” in electrical conductance. ....	175
<b>Figure 56.</b> Device Characterization: (a) Optical image of the wafer with 60 devices manufactured using photolithography, metal deposition and etching; (b) scanning electron micrograph of carbon nanotubes; (c) Raman spectrum of semiconducting carbon nanotubes showing a large G band, small D band and 2D band. The $I_G/I_D \sim 30$ was observed in these nanotubes; (d) Test set up showing 6 devices on a chip and compares it to a penny. The source, drain and reference electrodes are observed. ....	178
<b>Figure 57.</b> Representative graph of the testing protocol. First drop of 5-10 $\mu$ l PBS is added to the sensor followed by wait period of several hundred seconds, followed by second PBS drop followed by wait period of several hundred seconds followed by addition of spiked buffy or plain buffy coat. This ensures the sample is behaving the same way over a time period before addition of the actual sample.....	179
<b>Figure 58.</b> Plots of representative electrical signatures from samples used in construction of a k-nn DTW distance-based classifier for breast cancer surface marker profiling. (A) Two plain buffy coat samples. (B) Two spiked buffy coat samples.....	182
<b>Figure 59.</b> Merge of sensor arrays with statistical classifiers in training set: Normalized conductance versus time data from the arrays grouped into two categories. (a) Plain buffy coat; (b) buffy coat spiked with MCF-7 cells. ....	184
<b>Figure 60.</b> Merge of sensor arrays with statistical classifiers in blinded set: Normalized conductance versus time data from the arrays grouped into two categories. (a) Plain buffy coat; (b) buffy coat spiked with MCF-7 cells. ....	184
<b>Figure 61.</b> Two qualitatively similar spiked signals. The bottom left figure shows the alignment of their time indices. The bottom right figure demonstrates the small DTW distance (in gray) between the two DTW aligned signals. ....	187

- Figure 62.** Two qualitatively different signals from different groups. The bottom left figure shows the alignment of their time indices. The bottom right figure demonstrates the large DTW distance (in gray) between the two DTW aligned signals. .... 188
- Figure 63.** Cross-Validation Results. For each choice of  $k$ , 10,000 bootstrapped datasets were used to measure the misclassification rate..... 190
- Figure 64.** Heat map. Summary of the relationship between electrical signatures and the cellular-proteomic features namely overexpression of EpCAM in spiked buffy coats versus buffy coats. The statistical classifier naturally partitions the buffy versus spiked buffy coats suggests specific interactions are quite unique in their electrical signatures compared to non-specific interactions and establishes a relationship between electrical conductance data with proteomic features. . 192
- Figure 65.** Cell Capture using EpCAM functionalized Nanotube Devices based on Optical Microscopy: (a) Optical microscopy of spiked cells in buffy coats using nanotube devices; (b) Optical microscopy of plain buffy coats. .... 194
- Figure 66.** Cell Capture using Nanotube Devices using Confocal Microscope: Representative confocal images from 6 devices imaged (4 shown) of captured cells in spiked buffy coats ranging from 1-17 cells per 5  $\mu$ l sample. .... 196
- Figure 67.** Dynamic time warping (DTW) for time series alignment. (A) Two qualitatively similar series. Red is a phase shift of blue with a slight vertical lift. Gray dashed line shows the vertical difference [445]. (The same series after dynamic time warping alignment.) ..... 204
- Figure 68.** (A) Optical image of the wafer with 76 devices manufactured using photolithography, metal deposition and etching; bottom right panel shows an optical image of a single CNT device and top right panel shows a SEM image of the CNT network bridging the source-drain electrodes.(B) Test set up showing 6 devices on a chip. The source, drain and reference electrodes are observed with a spiked blood and 1X PBS sample droplets on the devices. (C) Optical microscope image of a device with a 1X PBS ample droplet on top. Here one can see, from bottom to top, the gold electrode, SU-8 photoresist polymer layer covering the electrode and the edge of the CNT film, and the CNT ultra-thin film. Similarly (D) shows an optical microscope image of similar device after cancer cell spiked blood droplet injection..... 210
- Figure 69.** (A and B) Optical microscopic images of blood sample droplets on top of the device. (A) Three examples of spiked cancer cell blood samples. Spiked cancer cells are observed in the blood and marked with an arrow, one can clearly observe the cancer cells buried under the RBCs and on top of the substrate, CNT film. High concentration of RBCs is apparent on top of the

marked cancer cells in “Zone 1”. (B) Plain blood sample. There are no cancer cells or WBCs observed in plain blood samples when the microscope is focused in “Zone 1” plane. On the other hand when image is focused in the plane of “Zone 2” WBCs are apparent in the image (right panel), floating above the RBCs. (C) Illustration of blood sample observations under the microscope, showing the arrangement of RBCs, WBCs, and spiked cancer cells and the classification of “Zone 1” and “Zone 2” accordingly. .... 212

**Figure 70.** (A and B) Additional optical microscopic images of blood sample droplets on top of the device. (A) SKBR-3 spiked blood sample. SKBR-3 spiked cancer cells are observed in the blood at 20X magnification focused in “Zone 1”. 15 out of the 20 images analyzed to generate the data presented in Table 13 are shown here. (B) Plain blood sample. There are no cancer cells or WBCs observed in plain blood samples when the microscope is focused in “Zone 1” plane. On the other hand when image is focused in the plane of “Zone 2” WBCs are apparent in the image (right panel), floating above the RBCs. Scale bars on the first row correlate to all images in each column. .... 213

**Figure 71.** Capillary blood sampling using a lancing device. (A) Prepare the skin by applying sterile alcohol prep pads to the entry site and allow to air dry. (B) Load the lancing device with an ultra-thin lancet and prepare for puncture. (C) Puncture the skin with one quick, continuous and deliberate stroke. (D) Achieve a good flow of blood and wait for a ~100  $\mu$ L blood droplet to collect. (E) Collected exactly 50  $\mu$ L of the blood droplet using a micropipette, and then apply firm pressure to the site to stop bleeding. (F) Transfer the collected blood using a micropipette to a storage vial for further preparation. Prep pads, lancets, and lancing device were purchased from CVS pharmacy. .... 215

**Figure 72.** Schematic illustrating the (A) three CNT device functionalization variations, IgG, HER-2, and EpCAM antibody, functionalized to the surface of the CNT via PASE linker molecule, with tween-20 molecule covering the unfunctionalized CNT surface and (B) showing four sample types, plain blood, spiked SKBR-3 , MCF-7, and MCF-10A blood samples. .... 218

**Figure 73.** Signal type classification. Zone 1 represents devices that generated an increase in their signal after addition of sample droplet (>2%), blue line. Zone 2 represents devices that generated no significant change in their signal after addition of sample droplet (2%), black line. Zone 3 represents devices that generated decrease in their signal after addition of sample droplet (>2%), red line..... 220

**Figure 74.** Merger of device array data for 1000 cells/5  $\mu$ L variation. Each panel correlates with one combination of sample type and device type with respect to design of experiment presented in Table 10, 10 replicates each. Each row correlates to one type of device functionalization, HER-2, EpCAM, and IgG.

Plain blood samples are shown in red, MCF-10A in green, MCF-7 in orange and yellow, and SKBR-3 in blue and purple. The control buffer signal is shown in black marks in each panel as point of reference. If majority of signals in one panel were above or below the reference buffer control signal, they were plotted in marks, the rest of the data points that are not showing the same trend are plotted as dots. Arrow indicated the time of sample injection..... 221

**Figure 75.** Merger of device array data for 100 cells/5  $\mu$ L variation. Each panel correlates with one combination of sample and device type with respect to design of experiment presented in Table 10, 10 replicates each. Each row correlates to one type of device functionalization, HER-2, EpCAM, and IgG. Plain blood samples are shown in red, MCF-10A in green, MCF-7 in orange and yellow, and SKBR-3 in blue and purple. The control buffer signal is shown in black marks in each panel for point of reference. If majority of signals in one panel were above or below the reference buffer control signal, they were plotted in marks, the rest of the data points that are not showing the same trend are plotted as dots. Arrow indicated the time of sample injection. Plain blood panels are replicates from Figure 74, as there are no spiked cell concentration variations within these samples. .... 222

**Figure 76.** (A) Cross-validation estimated AUC for discriminating a high concentration of SKBR-3 cells given HER-2 antibody. (B) Cross-validation estimated AUC for discriminating a low concentration of SKBR-3 cells given HER-2 antibody. (C) Cross-validation estimated AUC for discriminating antibodies, anti-HER-2 and anti-IgG functionalized devices, given a high concentration SKBR-3 cells. .... 227

**Figure 77.** (A and D) Show optical microscope image of devices with spiked sample droplet on top. (B and E) Show binary conversion of the optical microscope images, highlighting the spiked cells in black and separating them from the background. (F and I) ImageJ analyses of binary images, based on diameter and shape, showing cell count map of each original optical image. (G-I) demonstrate surface area comparison of the square shaped device vs. circular droplet covering the device. CNT device is only covered by ~62% of the total droplet area..... 231

**Figure 78.** Histogram of number of cells counted per device based on 5X (A) and 20 X (B) magnifications optical microscope images. (C) Presents the histogram of diameter of all cells counted. .... 233

**Figure 79.** Cell differentiation using confocal microscopy: SKBR3 cells captured on chips from 3 devices showing positive staining for DAPI, cytokeratin (CK-19) and negative for CD45 and two images of leukocytes captured showing positive for DAPI and CD45 while negative for cytokeratin. (A) series of optical images;

(B) DAPI nuclear stain; (C) CK19 stain for cancer cell and (D) CD45 for leukocytes and (E) merged image of nuclear and cytoplasmic stains. .... 236

## LIST OF TABLES

<b>Table 1.</b> Summary of CTC isolation/detection technologies .....	8
<b>Table 2.</b> Commercially available technologies for CTC enrichment.....	31
<b>Table 3.</b> Spin-Coater setting for SC1813 photoresist.....	78
<b>Table 4.</b> Spin-Coater setting for SU8-2005 photoresist. ....	79
<b>Table 5.</b> Average film resistance summary .....	98
<b>Table 6.</b> Statistical comparison between specific and control signals in cell cultures.	165
<b>Table 7.</b> Training classification of biosensor signals based on dynamic time warping. .....	193
<b>Table 8.</b> Blinded set classification of biosensor signals based on dynamic time warping. .....	193
<b>Table 9.</b> Captured cells on each device for both case and controls using optical microscope. ....	197
<b>Table 10.</b> Design of experiments.....	217
<b>Table 11.</b> Signal classification results. ....	224
<b>Table 12.</b> CV-estimated confusion matrix for high concentration SKBR-3 cells.....	227
<b>Table 13.</b> Cell count data per device based on 20X images.....	234
<b>Table 14.</b> Cell count data per device based on 5X images.....	234
<b>Table 15.</b> CNT micro-arrays for detection and capture of proteins and cells. ....	241

## ABBREVIATIONS

CTC	circulating tumor cells
DTC	disseminated tumor cells
CNT	carbon nanotubes
SWNT	single wall carbon nanotubes
FET	field effect transistor
Ag/AgCl	silver/silver chloride
RBC	red blood cell
WBC	white blood cell
FISH	fluorescence in situ hybridization
PCR	polymerase chain reaction
depFFF	dielectrophoresis field flow fractionation
DEP	dielectrophoresis
EpCAM	epithelial cell adhesion molecule
PSMA	prostate specific membrane antigen
HER-2	human epidermal growth factor receptor 2
CK	cytokeratin
PDMS	polydimethylsiloxane
GNP	graphene nanoplates
EDTA	ethylene diamine tetra acetic acid
PASE	pyrenebutanoic acid, succinimidyl ester
MWNT	multi-walled carbon nanotubes
SWNT	single-walled nanotubes
CVD	chemical vapor deposition
PBS	phosphate-buffered saline
SDS	sodium dodecyl sulfate
PASE	1-pyrenebutanoic acid, succinimidyl ester
EMT	epithelial mesenchymal transition

## CHAPTER 1 INTRODUCTION

Cancer is one of the leading causes of death worldwide. In 2012 about 14.1 million new cancer cases and 8.2 million deaths occurred worldwide which is expected to increase to 13 million in 2030 [1, 2]. In the United States cancer is the second leading cause of death currently, after heart disease. In 2016, the National Institute of Health (NIH) projected that there will be 1,685,210 new cancer cases and 595,690 cancer deaths in United States [3]. However, the World health Organization claims at least 30% of these deaths can be prevented if patients are diagnosed and treated before cancer metastases. The progression of cancer from a localized to metastatic disease is fundamental to the advancement of this illness and is believed to cause 90% of all cancer related deaths [4-8]. Therefore understanding the state of metastases disease and its root cause could have a positive impact on patient management and survival in the clinic.

### 1.1. CIRCULATING TUMOR CELLS (CTC)

In 1869, Thomas Ashworth an Australian physician for the first time reported that cells in the blood stream of a man with metastatic cancer were similar to those in tumor tissue [9, 10]. He postulated that “cells identical with those of the cancer itself being seen in the blood may tend to throw some light upon the mode of origin of multiple tumors existing in the same person”. Ashworth observed under an optical microscope a tumor like cells at the internal saphena vein of cancer patient’s leg. Based on his observations, he concluded that certainly these tumor cells must have come from



an existing cancer structure and they must have passed through the greater part of the circulatory systems. He then suggested that this phenomenon can shed light upon the mode of origin of multiple tumors existing in the same person, metastases cancer [10].

The malignant cells shedding from solid tumors, both primary and metastatic lesions, were later referred to as circulating tumor cells (CTC). CTCs play a key factor in hematogenous dissemination spreading cancer to distant sites and in seeding new tumors and cancer metastases, Figure 1 [11, 12]. Tumor cells shed into the blood in discontinuous fashion and are eliminated for the most part from circulation. Even though most CTCs will never colonize any organs but the few cells that manage to establish conditions for growth at distant sites can develop into tumors through the seeding process resulting in poor prognosis for patients [13-16]. In the case for carcinomas, which are solid tumors derived from epithelial tissues and consist of 80% of all cancer cases diagnosed, prognosis of patients is mainly determined by the blood borne dissemination of tumor cells from the primary site to distant organs such as bone marrow, lungs, liver, or brain [8]. The subsequent outgrowth of these cells in their new microenvironment is the primary factor for metastases. After disseminating and establishing micrometastases state, these tumor cells can remain in dormant state for many years, even after complete resection of the primary tumor, before they give rise to overt metastases [17, 18]. Therefore understanding CTCs may be the first step to blocking metastases. Since the 1950s, numbers of studies have demonstrated the presence of CTC in blood and the possibility of prognostic value of CTC in breast cancer patients [19-27]. Furthermore in 1990s scientist started to express a

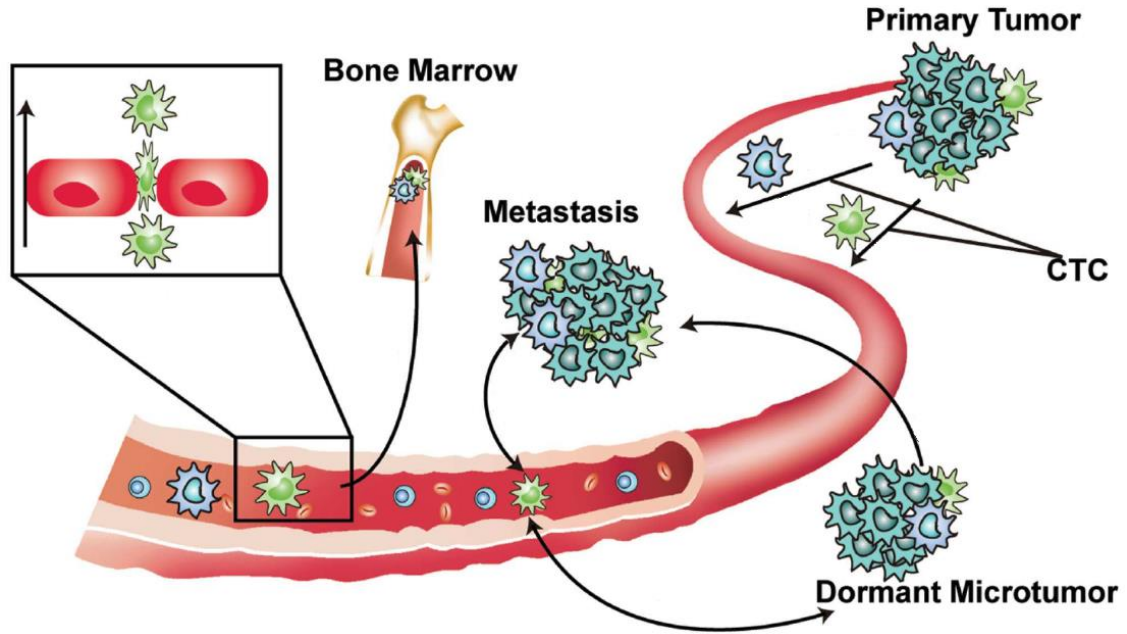


**Figure 1.** Schematic showing the shedding of tumor cell into the blood stream and seeding new tumors through metastases. The cancer cells that enter the blood vessels and circulate with normal blood cells are considered circulating tumor cells (CTC) [28].

understanding of the utility of CTC for diagnosis, studies by Shpall *et al.* [29, 30], Brugger *et al.* [31] and other researchers showed the presence of primary tumor cells lodged in the bone marrow before metastases became evident [32]. This trend has continued, a number of more recent studies have presented that CTCs may be used as a marker in cancer patients to predict disease progression and survival in metastatic and potentially even in early stage cancer patients [33-36]. Therefore, detecting, targeting, and controlling CTCs is believed to be a key factor in controlling metastasis and cancer [4]. Existing high resolution technologies are unable to detect CTCs; therefore alternative techniques are in demand. More recently CTCs have been successfully

identified in bone marrow, lymph nodes, and circulating blood with sensitive and specific assays [37, 38]. Bone marrow especially, appears to be a common homing organ for disseminated tumor cells. These cells are derived from carcinomas of different origins. When deposited in bone marrow, they could also act as the reservoir for disseminated tumor cells with potential to infect other distant organs [39]. Using a needle aspiration technique, bone marrow can be accessed through the iliac crest. Analyses of bone marrow samples play a big role as an indicator of the prognosis of minimal residual disease, small numbers of leukemic cells (cancer cells from the bone marrow) that remain in the patient. In some cases, detection of tumor cells in the bone marrow showed a greater clinical value for prognoses of disease in comparison to the CTC in blood [40].

Sequential and routine monitoring of prognosis of cancer patients are pivotal to disease prognosis. In such case, bone marrow needle aspiration is not an attractive technique due to its invasive nature, putting great limitations on sampling frequency. The bone marrow sampling process is invasive and can be an extremely painful and distressing experience causing anxiety. For children this experience can be even harsher and more terrifying [41-44]. Considering the inconvenience of bone marrow biopsy in regards to pain and recovery time, an alternative method has to be considered in the case of routine CTC testing. On the other hand sampling peripheral blood for CTC detection is a minimally invasive way in comparison [45]. Therefore there is a great deal of interest within the research community to evaluate the clinical utility of testing

for tumor cells in the blood instead of bone marrow for monitoring systemic therapy and prognosis of cancer patients [37].

The analysis of CTCs from blood samples is considered a real-time “liquid biopsy” for patients with cancer [18]. Capturing and detecting CTCs via different technologies that take advantage of their biological and physical properties by liquid biopsy can lead the way for personalized targeted therapies and unlock the opportunity for dynamic prescriptions according to the existing biomarkers and genotypes, hence significantly improving the quality of treatments [18, 46]. Since blood can be collected simply and in a minimally invasive manner, CTCs can potentially be easily obtained from small amounts of blood samples and provide the real time single cell level data for guided therapies [47, 48]. CTC as real time marker could be used as an indicator for disease progression and survivals [18]. However, the isolation, detection and quantification of CTC in blood is a very difficult task and faces technological hurdles due to rarity of these circulating tumor cells. For CTC marker to fulfil its role, development of CTC detection devices that can handle small sample volumes is crucial.

Cancer Cells including CTCs are originated from body’s own tissue in series of mutations [5]. Self-origin of these mutated cells present difficulties in distinguishing them from healthy cells, even masking them from the body’s own immune system [49]. CTCs are typically found in single digit numbers per milliliter of blood and are very similar to leukocytes in their dimensions, making it very difficult to detect using traditional microscopy techniques alone [45]. This presents a challenge to identify malignant cells among normal ones, making cancer diagnosis and therapies more

difficult. Studying cancer cell mutations, scientist have discovered over expression of certain proteins embedded in the cellular membrane at much higher levels than normal cells. In the case of carcinomas for example, CTC have the potential to be distinguished by over expressed epithelial cell membrane markers (receptor proteins). The specific membrane biomarkers can serve to identify CTC even at single-cell level [13].

Studying such biomarkers has enabled researchers to distinguish cancer cells from healthy tissue and even go as far as correlating them to specific cancer types. The biomarker overexertion and characteristics are unanimous in-between cancer tumors and their corresponding CTCs [50-54].

Large numbers of circulating epithelial cells have been detected in metastatic cancer patients, between 50 to 300,000 per mL of blood [55]. CTCs entail fraction of these circulating cells. Presence of CTC in blood has been reported anywhere from 1-10 to as high as 3,149 CTCs per mL of blood in metastatic cancer patients [56, 57]. The frequency of CTCs in blood is a strong indicator of the prognosis of cancer patients [33, 35, 56-60]. CTCs are systemic indicators and are a less invasive sampling option in comparison to local tumor biopsy, especially when accessing the tumor is not feasible [18, 55]. The information obtained from CTCs can determine the effectiveness of certain treatments, assist in more customized therapies, and give deep insights on patient survival, Figure 2 [34, 35, 56, 57, 61-64]. Therefore, understanding the principles behind CTC enrichment and the different methods for CTC capture and detection are of great interest. Table 1 summarizes the different approaches and methods for CTC enrichment, capture and detection.

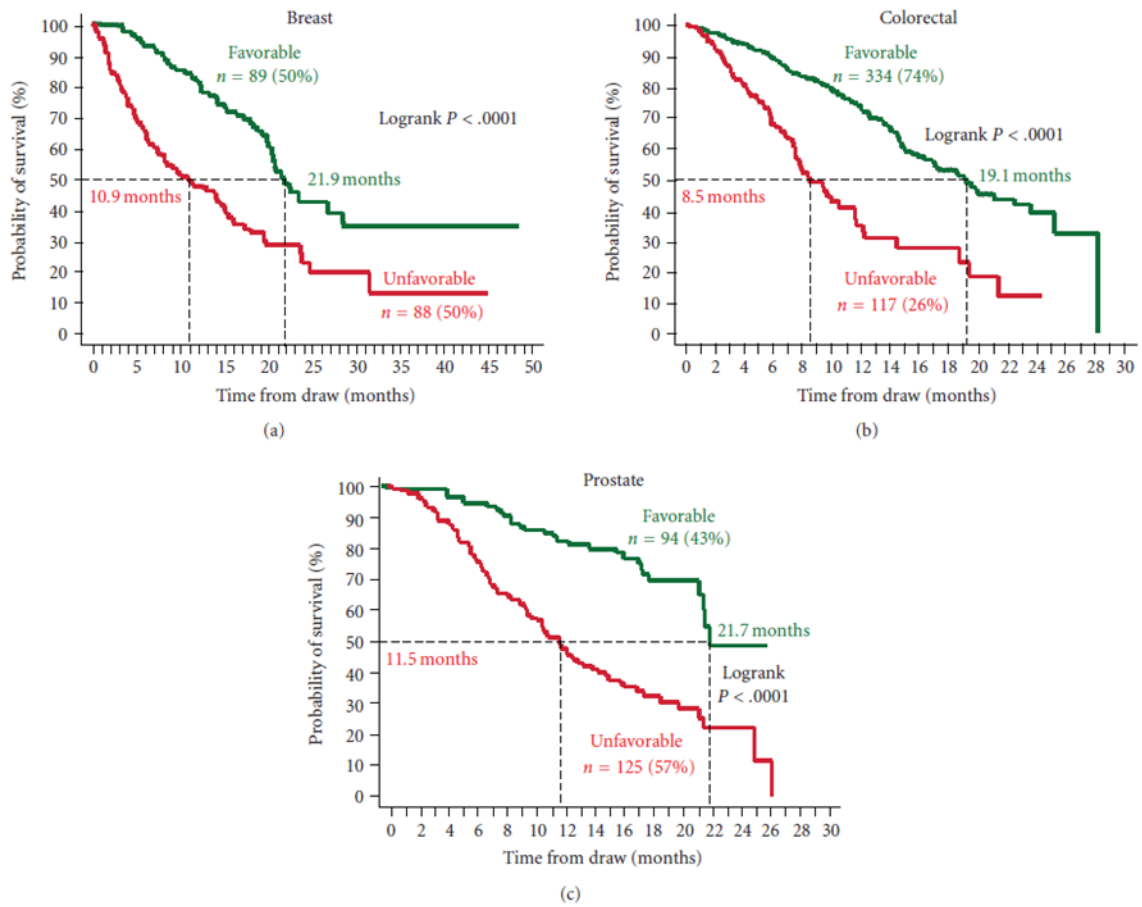


**Figure 2.** Kaplan Meier Analysis of overall survival for patients with metastatic breast cancer (a), metastatic colorectal cancer (b), and prostate cancer (c). Patients were divided into those with Favorable and Unfavorable CTC. The cutoff value between favorable and unfavorable CTC was  $\geq 5$  CTC/7.5mL blood for breast and prostate cancer and  $\geq 3$  CTC/7.5mL blood for prostate cancer [33, 57]. For example patient with 1 CTC/7.5 mL was labeled favorable.

**Table 1.** Summary of CTC isolation/detection technologies

Primary Method	Secondary Method	Principle of enrichment	Advantages	Limitations	Reference
<b>Immunomagnetic</b>	Nanostructure	Antibody based; aptamer based [65]	High intra and inter assay precision; standardized and semi-automatic, detection and capture	Cost, time, sample volume, labeling, microscope image analysis, capture or detection only; antigen dependent	[34, 65-72]
<b>Microfluidics</b>	Microstructure	Antibody based	Label-free, cell collection, molecular profiling, rapid	Antigen dependent, capture only	[73-80]
		Cell size and deformability	Label-free, allows gentle release, antigen independent	Capture only , Limited selectivity due to size overlap between CTC and WBCs, poor specificity; Limited to only CTC clusters (>2cells) [81]	[81-99]
		/Magnetic liposomes	Antigen independent, single platform	Capture only, label dependent, limited selectivity due to size overlap between CTC and WBCs, poor specificity	[100]
	Nanostructure	Antibody or aptamer based	CTC collection and isolation, stable	Capture only, can be antigen dependent, increased sensitivity decreases specificity to a degree	[101-114]
	Dielectrophoresis	Physical properties	Label-free, antigen independent	Capture only, depends on conductivity of CTC	[115, 116]
	Immunomagnetic	Antibody based and phenotype	Heterogeneity profiling of CTC, cell collection, integrated platform,	Capture only, antigen dependent; CTC degradation [117], detection only [118, 119]	[117-120]
	Microstructure and immunomagnetic	Antibody based	Single platform, automated, efficient	Capture only, sample volume, antigen dependent. , fluorescent imaging analysis dependent	[121-126]

**Table 1.** (continued)

	Immunomagnetic and impedance	Antibody based	Detection and capture, single platform	Antigen dependent	[127]
<b>Filtration</b>	Microstructure	Cell size and deformability	Label free, antigen independent, simple, fast, satisfies cell lysis, cell collection, and molecular profiling	Limited selectivity due to size overlap between CTC and WBCs, poor specificity; capture only.	[128, 129]
<b>Nanosubstrate</b>		Aptamer based	Capture, detection and release of multiple types of CTCs	Antigen based, depends on microscopy and flow cytometry techniques	[130]
		Antibody based	Tunable capture and release, cell collection; detection [131]	Capture only, can be antigen dependent, increased sensitivity decreases specificity to a degree	[131-133]
	Microfluidics	Antibody based	Surface capture and culture of CTC within device	Capture only, antigen dependent	[134]
<b>In vivo</b>	Functionalized wire/needle	Antibody based	In vivo, real time capture, no blood sample volume limitation	Antigen dependent, invasive, capture only, depends on immune staining and fluorescent imaging	[135-137]
<b>Cytometry</b>	Flow cytometry and fluorescent nanoparticles	Genotype	Detection of genetic marker of CTC, CTC culture	Require larger population of CTC (>100/mL of blood)	[138]
	Microfluidics and aliquoting	Antibody based	Cell collection, molecular profiling, rapid	Antigen dependent, fluorescence labeling	[139]
<b>Microcantilever</b>	—	Antibody based	Detection and capture	antigen dependent, limited sensor area for detection, sample volume limitations	[140]



## 1.2. PRINCIPLES OF ENRICHMENT FOR CTC

Different properties of CTCs distinguishing them from the surrounding normal hematopoietic cells have been targeted to develop a large panel of approaches for CTC enrichment technologies, Table 1. These techniques are divided into two main categories, separation based on physical properties (i.e. cell size, density, electric charge, elasticity and deformation) and biological properties of CTC (i.e. cell surface protein expression), Figure 3. Here we are going to discuss these approaches and understand their advantages and limitation.

### 1.2.1. PHYSICAL PROPERTY BASED SEPARATION OF CTC

The main advantage to physical property based approaches of CTC enrichment is that they allow for label-free separation of tumor cells. Physical property separation of CTC include: size based and dielectric based separation of CTC. More recently, cell membrane charge has also been explored for CTC separation in combination with existing size based separation techniques [100].

#### 1.2.1.1. SIZE BASED SEPARATION OF CTC

Size based approach leverages the size difference between tumor cells and the normal cell types found in blood. This technique can also be combined with other physical properties such as deformability and elasticity to enhance the enrichment results [82, 88-91, 129]. This approach is one of the first to arise as an alternative to affinity based techniques.

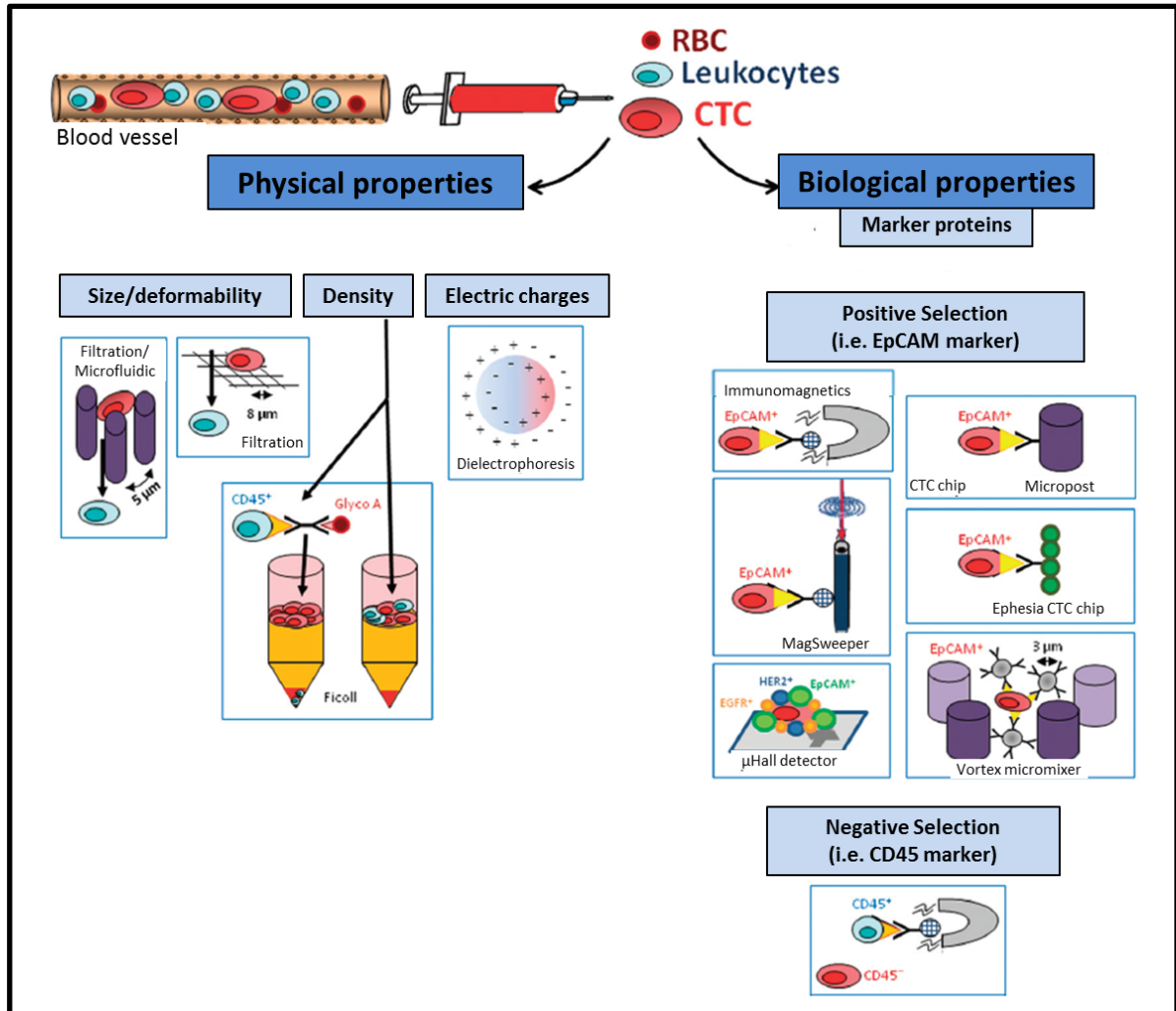


**Figure 3.** Isolation and enrichment of CTCs from blood of cancer patients is based on the physical or biological properties of CTCs [18]. Physical property based separation include size (membrane filter devices [128, 129]), deformability (microfluidics system in a chip [81-99]), electric charge (dielectrophoresis [115, 116]), and density (Ficoll centrifugation [58]). Biological based property isolation is based on: the expression of cell surface markers, (i.e. epithelial cell adhesion molecule (EpCAM)) for positive selection and CD45 for negative selection; anti-body (i.e. anti-EpCAM) or anti-CD45 antibodies conjugated with magnetic beads, for enriching CTCs in a magnetic field [34, 65-72]; anti-EpCAM antibodies on microposts or columns of nanobeads [73-80]; anti-EpCAM antibodies conjugated to 3 µm beads to increase the size of CTCs before filtration [141]; anti-EpCAM, anti-HER2/neu, anti-EGFR antibodies on different sizes of nanoparticles for capturing and detecting different CTCs [114].

In general, CTCs have larger cell diameter, 10-20  $\mu\text{m}$ , in comparison to normal red blood cells (RBCs), 4-6  $\mu\text{m}$ , and white blood cells (WBCs), 7-12  $\mu\text{m}$ , thus offering the possibility of size based separation of CTCs with high precision filtration [128, 142]. Initially sieve-like materials were used to demonstrate the possibility of tumor cell separation from blood [143]. Shortly after that more precisely engineered filters were microfabricated for the same purposed [83]. To further optimize this technique, polycarbonate membranes were used to produce arrays of consistently sized pores using ion beam etching, providing an ideal platform to optimize the performance of size based CTC separation [85, 144]. Using this material platform, isolation by size of epithelial tumor cells technique was developed for very sensitive enumeration of CTCs in patient samples [128, 145]. Furthermore, techniques such as fluorescence in situ hybridization (FISH) or polymerase chain reaction (PCR) were shown to be compatible with the platform and were utilized to perform gene based analysis on the captured CTCs. Separately, beads that would specifically bind to tumor cells were also used on some platforms to increase the cell diameters, thereby extending the size based enrichment approach to a wider range of CTCs, but in contrast this does introduce dependence on cell surface markers [141].

Microfluidics plays a big role in size based separation of CTC, this method had been introduced as a very promising alternative to traditional filtration methods. For example, the Microvortex fluidic platform, Figure 4, has achieved good levels of sensitivity and specificity, with purity values close to 95%, sensitivity of 93%, and reasonable capture efficiency. This platform uses trapping and inertial focusing of

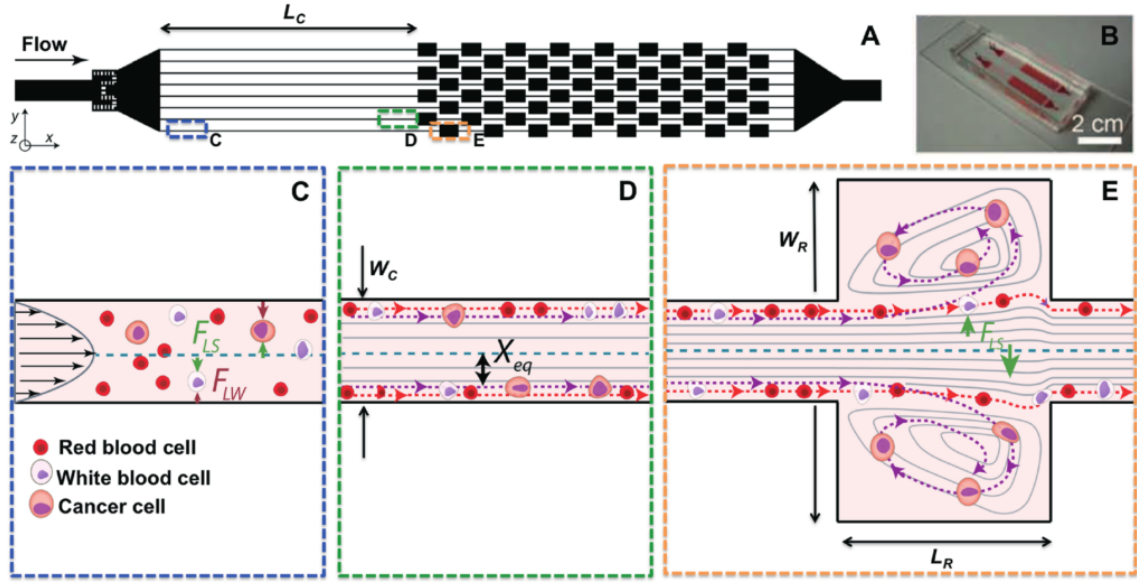


**Figure 4.** Microvortex chip design and principle. (A and B) show channels and reservoir arrangement ( $W_C = 40 \mu\text{m}$ ,  $H = 80\text{--}85 \mu\text{m}$ , and  $L_C = 4 \text{ mm}$ ). (C) Demonstrates the wall effect forces ( $F_{LW}$ ) and shear-gradient lift forces ( $F_{LS}$ ). (D) Shows the migration of cells to dynamic lateral equilibrium positions ( $X_{eq}$ ) and (E) trapping of CTC in reservoirs ( $W_R = 480 \mu\text{m}$  and  $L_R = 720 \mu\text{m}$ ) [96].

CTCs in microscale vortices, with fast processing times (0.375 mL/min) providing rapid means to isolation high purity samples of CTCs [96, 146].

In conclusion, size based separation of CTCs offers a unique platform for development of label free methods for isolation of viable tumor cells, which could also be compatible with post capture analysis techniques. However, this approach has selectivity limitation due to size overlap between CTCs and WBCs. A portion of all CTCs are smaller or the same size as WBCs, resulting in poor specificity and purity of the final enriched population [141].

#### 1.2.1.2. Dielectric Separation of CTCs

Another label free separation approach using the physical properties of CTC is by dielectrophoresis (DEP). Tumor cells can be separated from blood by exploiting the intrinsic dielectric differences between cell types. The total plasma membrane capacitance and conductance is reported by cell dielectric measurements using alternating field gradients. One can separate tumor cells from WBCs using the total capacitance. Applying DEP frequency of 60 kHz forces tumor cells to deplete from blood, meanwhile shifting the frequency to 15 kHz will result in to cells concentrating into fractions [115, 116].

Dielectrophoresis in combination with drag flow can fractionate the sample of different types of particles; this method is called dielectrophoresis field flow fractionation (depFFF), Figure 5. This method is able to recover up to 90% of the tumor cells spiked into blood and recovered cells can be cultured or molecularly analyzed [115, 116].

However, there are limitations to DEP for CTC separation applications. Cytoplasmic and membrane conductivities are susceptible to change over the course of the separation process. This can result in poor selectivity but by optimizing the separation periods one can minimize these variations and reduce cell-cell interactions.

#### 1.2.2. BIOLOGICAL PROPERTY BASED ISOLATION OF CTC

Approaches using biological properties of cells can significantly improve the sensitivity and specificity of CTC capture and analytical methods. Affinity based

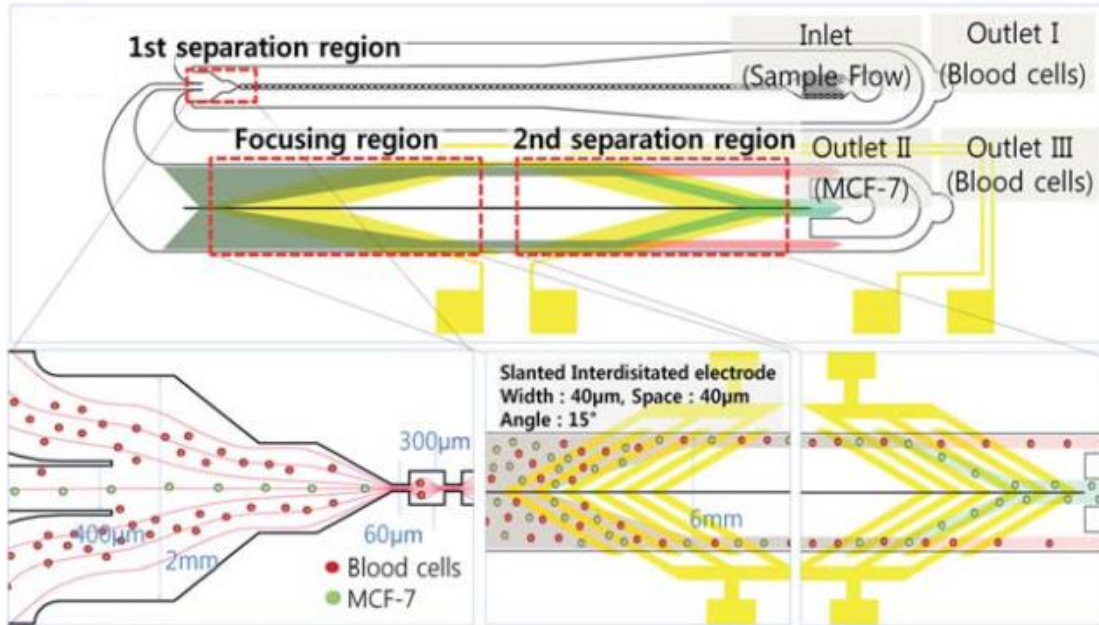


**Figure 5.** Schematic diagram of a microfluidic device for cancer cell separation using multi-orifice flow fractionation and DEP. In the first separation region, the relatively larger MCF-7 cells and a few blood cells pass through the center channel and enter the DEP channel, after which most blood cells exit through outlet I. In the focusing region, all cells experience a positive DEP force and then align along both sides of the channel. Finally, the second separation region selectively isolates MCF-7 cells via DEP [115].

methods such as antibody and aptamer capture approaches integrated into microdevices and nanomaterials have enhanced the capture efficiencies of CTCs in patient samples, allowing for detailed molecular level characterization of CTCs to be performed [142].

#### 1.2.2.1. ANTIBODY BASED IMMUNOAFFINITY ISOLATION OF CTC

An antibody provides a specific binding between itself and the antigen of interest. Antibodies have long been employed for investigating CTCs as a very effective tool for immunoaffinity isolation of tumor cells, due to antigen expression on

the surfaces of CTCs [147-156]. Such assays mainly use antibodies in positive selection procedures by targeting the antibody against tumor associated antigen or in negative selection by targeting the common leukocyte antigen CD45 [18].

Among positive selection procedures, epithelial cell adhesion molecule (EpCAM) plays a big role as a surface marker for CTC detection. EpCAM is over expressed in carcinomas such as breast, prostate, neck, head, lung, esophagus, liver, rectum, colon and pancreas tumor cells [147-156]. The down side to this marker is that capture efficiency is significantly reduced as EpCAM's overexpression is suppressed. Cells that undergo epithelial mesenchymal transition (EMT), express significantly less of EpCAM biomarker on their membrane therefore are less susceptible to stick to the antibodies as they break into the blood circulation [157]. Additionally, EpCAM methods are very effective for non-epithelial cancers such as sarcomas [45]. To address these limitations other proteins have been identified as an alternative membrane antigen target. As an example PSMA (prostate specific membrane antigen) has been identified as a transmembrane metallopeptidase which is widely expressed on prostate cancer carcinoma cells [158]. In the case for breast cancer carcinoma, human epidermal growth factor receptor 2 (HER-2) has been identified as a target antigen overexpressed on the tumor cell membrane [159]. Antibodies targeting cytokeratin (CK), intermediate filaments of epithelial cells, are used frequently as secondary means in immunocytology to distinguish the captured CTC from impurities in the sample such as WBCs which are CK negative and CD45 positive [14].

Where there is a lack of EpCAM expression, cocktails of antibodies against other epithelial cell surface antigens such as HER-2, mucin-1 (MUC1), and epidermal growth factor receptor (EGFR) are used [160].

#### 1.2.2.2. APTAMER BASED ISOLATION OF CTC

Aptamers are a category of oligonucleotides such as RNA, DNA, or some peptides which can specifically bind to proteins, similar to antibodies, and also ions or small molecules. Aptamers are similar to antibodies in function and at the same time are more advantages for biological applications in comparative [161, 162]. Therefore there has been an increasing shift toward aptamers in the recent years for biological applications.

Aptamers were first discovered as part of human immunodeficiency virus (HIV) and adenovirus research. During these studies, it was discovered that viruses use some short RNAs to bind to proteins with high specificity and affinity similar to immune binding of antibodies. In 1990 for the first time, Tuerk and Ellington's research groups reported a standard protocol for preparation of aptamers, which utilized a three step based systematic evolution of ligands by exponential enrichment [163, 164]. Aptamers show advantage over antibodies in high affinity and thermal stability, reversible denaturation, less batch variation, low cost and simplicity of operation, therefore a number of researchers have utilized aptamers for CTC isolation [102, 109, 165-168]. Tan and co-workers were first to report the application of aptamers for CTC enrichment in their microfluidic chip. Cancer cells were spiked into a control sample of  $10^6$  cells  $\text{mL}^{-1}$  and processed in aptamer coated microchannels. Their method



demonstrated 97% purity and 80% capture yield [109]. In their next attempt, Tan's group developed an S-shaped microfluidic chip to capture three leukemia cell lines in three regions respectively. In case of acute lymphoblastic leukemia cells and Burkitt's lymphoma cells the capture method show a purity of 97%, thereby indicating an notable specificity of aptamers to CTCs [109]. This shows a great potential to use multiple aptamers in combination with variety of CTC capture methods.

### 1.3. METHODS OF CTC ENRICHMENT AND DETECTION

In recent years, a variety of methods have been reported for enrichment and detection of CTCs. These methods include: immunomagnetic enrichment, microfluidic sorting, mechanical filtration, nanosubstrate based capture, in vivo, microcantilever, and dielectrophoresis. Utilizing one or more of the principles of enrichments discussed earlier, researchers have developed a number of methods, label dependent or independent, for capturing and or detecting CTCs as summarized in Table 1.

#### 1.3.1. IMMUNOMAGNETICS

One of the earliest and most commonly used methods to separate CTC from blood is immunomagnetic separation [58, 71, 169-176], Figure 6. Before the introduction of micro/nanoengineered platforms and devices, sample preparation for immunomagnetics separation consisted of taking the ethylene diamine tetra acetic acid (EDTA) treated blood of patients and first centrifuging it in density gradient solution. After this step the blood sample is separated into three main components of plasma, red blood cells, and buffy coat (containing WBCs and CTCs).

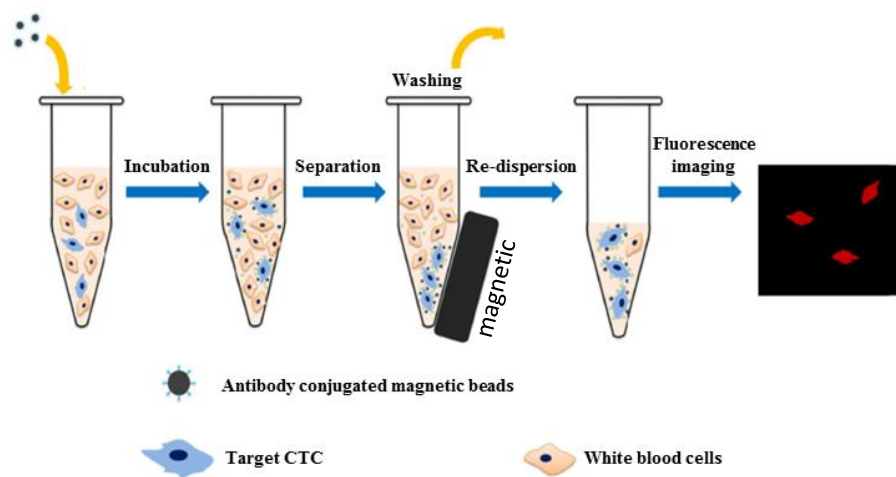


**Figure 6.** Schematic illustrating the CTC capture using antibody conjugated magnetic bead and fluorescence imaging [65].

After preliminary enrichment of targeted cells, microbeads modified with antibody (i.e. anti-EpCAM) are incubated in the sample to specifically bind to the targeted cell membrane protein marker (i.e. EpCAM receptor). Finally by applying a magnetic field to the sample, target cells bound to the magnetic microbeads are harvested and separated [171, 172]. This method can be effective in capturing CTCs with good specificity by combining the principles of cell density gradient and cell affinity. However, the immunomagnetic separation method is labor intensive, requires large expensive facilities, a technical operator, and a long processing time which can affect the CTC capture result and cell loss by repeated pipetting and container to container transfer of the sample as part of the process.

Veridex CellSearch is a semi-automated system and is the only Food and Drug Administration (FDA) approved platform for the prognosis of patients with metastatic

breast, colorectal, and prostate cancer. This platform takes advantage of the immunomagnetic system with an addition of fluorescence microscopy. After the enrichment of the cells using the microbeads, sample are further processed by fluorescently staining of CKs (positive marker), the common leukocyte antigen CD45 (negative marker), and nuclear dye (4',6-diamidino-2-phenylindole, or DAPI). The stained samples are then prepared for fluorescence microscopy enhanced image analysis. CTCs are distinguished from background WBCs based on the positive and negative fluorescence markers ( $CK^+$ ,  $CD45^-$ , and  $DAPI^+$ ) [34, 66, 69]. Another more recent method utilizing the same principle is the MagSweeper, which positively enriches for CTCs expressing EpCAM and allows their subsequent molecular analysis [70].

### 1.3.2. MICROFLUIDICS

Since the early 2000s, microfluidic devices have been a center of focus for CTC enumeration for cancer diagnostics. For such applications, microfluidic devices have taken advantage of physical and biological principles of CTCs to demonstrate a powerful method for efficient cell isolation and focused proteomic/genomic analyses [177-179]. Microfluidic devices are generally integrated with biomolecular probes (i.e. antibodies or aptamers) to form a functionalized surface to capture specific cells from a flowing medium such as unprocessed blood containing CTCs. After isolation and capture of target CTC, further analyses is done using optical and electrical methods to determine number of isolated cells, type of biological signals, and the characteristics of cells [73, 74, 115, 177, 180, 181]. One of the more prominent groups in microfluidics'

field, Nagrath and co-workers, developed a micropost based microfluidic device (CTC-chip) in 2007 to isolate CTCs, Figure 7. The surface of the microposts were functionalized with anti-EpCAM antibodies to isolate CTCs from unprocessed blood samples of patients with various cancer types such as prostate, breast, lung pancreatic, and colon cancer. They were able to isolate 1-100 CTCs per mL of blood with 50% purity, identifying CTC in 115 of 116 samples from patients with various cancer types. In the smaller group of patients under systematic treatment, the number of CTCs captured were correlated with the clinical prognosis of the disease [73]. Although microfluidic devices enhanced with biological probes have shown great promise, they still present difficulties in retrieving captured cells from the device for implementing cell analysis. Additionally, there have been demonstrations of CTC isolation using microfluidic method solely based on physical properties of CTCs, addressing some of the limitations with molecular probe based microfluidic devices, eliminating the need for antibodies and aptamers. By creating a microfluidic system such as microvortex and microspiral, researchers have taken advantage of physical differences (i.e. cell size) between CTCs and healthy blood cells to achieve CTC capture and isolation. Even though such methods are attractive due to their independence from molecular probes such as antibodies, but they have poor specificity and limited selectivity due to size overlap between some CTCs and WBCs [81-99].

Microfluidic platforms have overcome the limitations of conventional cell isolation techniques such as immunomagnetic sorting of CTC. Microfluidic methods have proven to be cost and labor efficient, easy and simple to use, have short

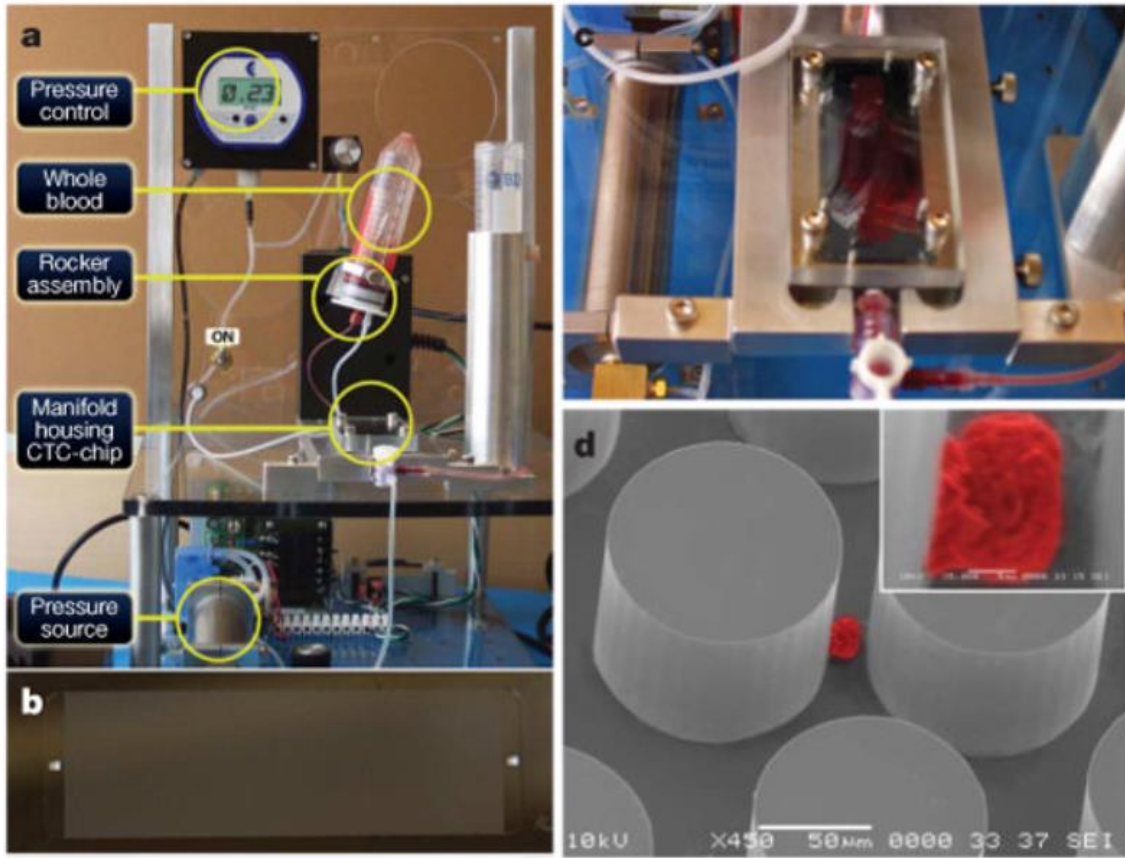


**Figure 7.** CTC-chip for isolation of CTCs from whole blood using a microfluidic device. (a) The sample is continually mixed on a rocker, and pumped through the chip using a pneumatic-pressure-regulated pump. (b) The CTC-chip with microposts etched in silicon. (c) Whole blood flowing through the microfluidic device. (d) Scanning electron microscope image of a captured NCI-H1650 lung cancer cell spiked into blood (colored red). The inset shows a high magnification view of the cell [73].

processing time, and no preprocessing requirements [182]. However, microfluidic methods still need to become more efficient in sample purity and specificity and are dependent on secondary methods such as fluorescent image analysis for detection and CTC analysis [28].

### 1.3.3. FILTRATION

Filtration method for isolation of CTCs is advantageous because of its independence from immunoaffinity isolation techniques [183]. Therefor eliminating the need for knowing the specific surface markers of all CTC types such as EpCAM [184]. This method of CTC isolation is based on cell size and takes advantage of the fact that CTCs in general have a larger size than blood cells, enabling separation of large tumor cells through filtering membranes independent of specific binding to antigens, which are prompt to miss cells with little or no expression of such biomarkers [82, 83, 85, 89, 91, 128, 185, 186].

In 2000, isolation by size of epithelial tumor cells (ISET) was the first protocol to demonstrate the filtration based method using commercialized filtration membrane morphology analysis. In this study, Vona and co-workers illustrated a significant difference in cell size between cancer cell lines, 10-20  $\mu\text{m}$ , and normal blood cells, RBCs: 4-6  $\mu\text{m}$  and WBCs: 7-12  $\mu\text{m}$  [128]. Similarly, a 2D parylene membrane microfilter device was developed by Zheng and co-workers to isolate and electrolyze the CTCs. Under this work, they demonstrate processing samples of prostate cancer cell lines spiked in Dulbecco's phosphate buffered saline (DPBS) and human peripheral blood at 3.75 mL / min, achieving 90% recovery rate. This was achieved by using a microfilter with highly dense and uniformly distributed pores [83]. In clinical specimen assays, this method showed detection of CTCs in 51 out of 57 of patients with metastatic breast, colon, prostate, and bladder cancer, while the CellSearch system only detected CTCs in 26 out of the same 57 patients [85]. Even though the isolation

efficiency is satisfactory, high stress and damage from the edges of the pores to cells during filtration process compromises the viability of the captured CTCs, prohibiting further cell and molecular analysis of captured cells. To address such issues with filtration method, Zheng and co-workers later improved their design by introducing a 3D microfilter to promote viable isolation of CTC [84], Figure 8. This 3D design minimized the stress concentration on the cell membrane without significantly sacrificing processing time or volume. However, high throughput and flow rate of filtration scheme causes clogging of the filtration structure resulting in higher fluid stress on cells potentially causing damage to cells and reducing the viability.

Size based filtration method remains an attractive high throughput approach for CTC capture, independent from surface markers and cancer cell type. However, the fundamental limitation to filtration methods still remains. CTCs are heterogeneous, and

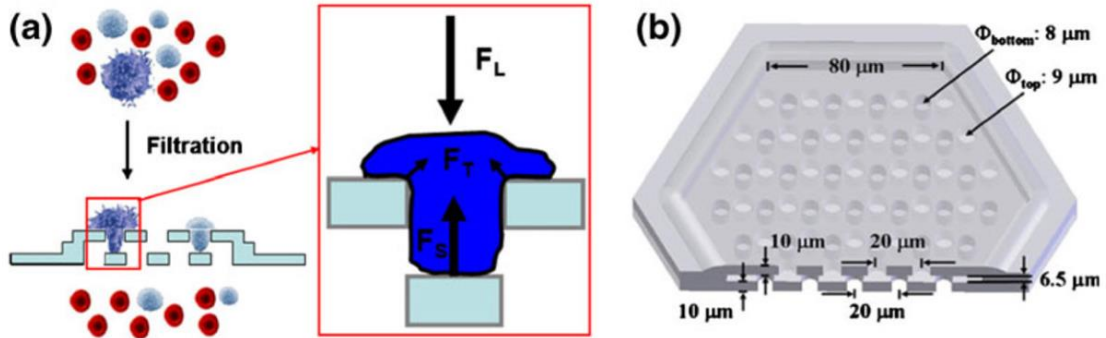


**Figure 8.** 3D microfilter device for viable CTC enrichment from blood. (a) Shows the filtration process and forces on a trapped cell.  $F_L$ : force caused by fluidic pressure from top.  $F_S$ : supporting force from bottom membrane.  $F_T$ : tension stress force on plasma membrane. (b) Device design of a single hexagon-shaped microfilter patch [84].

have a large size range (4-30  $\mu\text{m}$ ), overlapping with leukocytes causing potential loss of sub population of CTCs and effecting specificity and purity [18].

#### 1.4.4. NANOSUBSTRATE

More recently, researchers have extensively explored nanostructured surfaces (i.e. nanopits, nanofibers, and nanogrooves) and their integration with cells in terms of proliferation, differentiation, alignment and migration [187-191]. Nanostructures better promote protein adherence to surfaces due to a larger surface area resulting in better surface functionalization [192]. Nanostructures promote and facilitate cell attachment, adhesive forces are improved further more by antigen-ligand binding between cells and substrate [193-199].

Increasingly nanostructure substrates (i.e. nanowires, nanotubes, nanopillars and nanotextured polydimethylsiloxane (PDMS)) have been integrated into microfluidic platforms to improve CTC capture in microfluidic devices used for CTC isolation [103, 105, 107, 110, 167, 200]. Tseng and co-workers developed a NanoVelcro chip based on an array of nano-silicon-needles, Figure 9. They functionalized the nanosurface of the needles with antibodies, targeting CTC surface markers such as EpCAM and showed improved adhesion of CTCs to the capture substrate [103, 200, 201]. Additionally, nanomaterials such as electrospun  $\text{TiO}_2$  nanofibers, polymer nanodots, and carbon nanotubes have been optimized and tested for CTC capture [108, 110, 133].



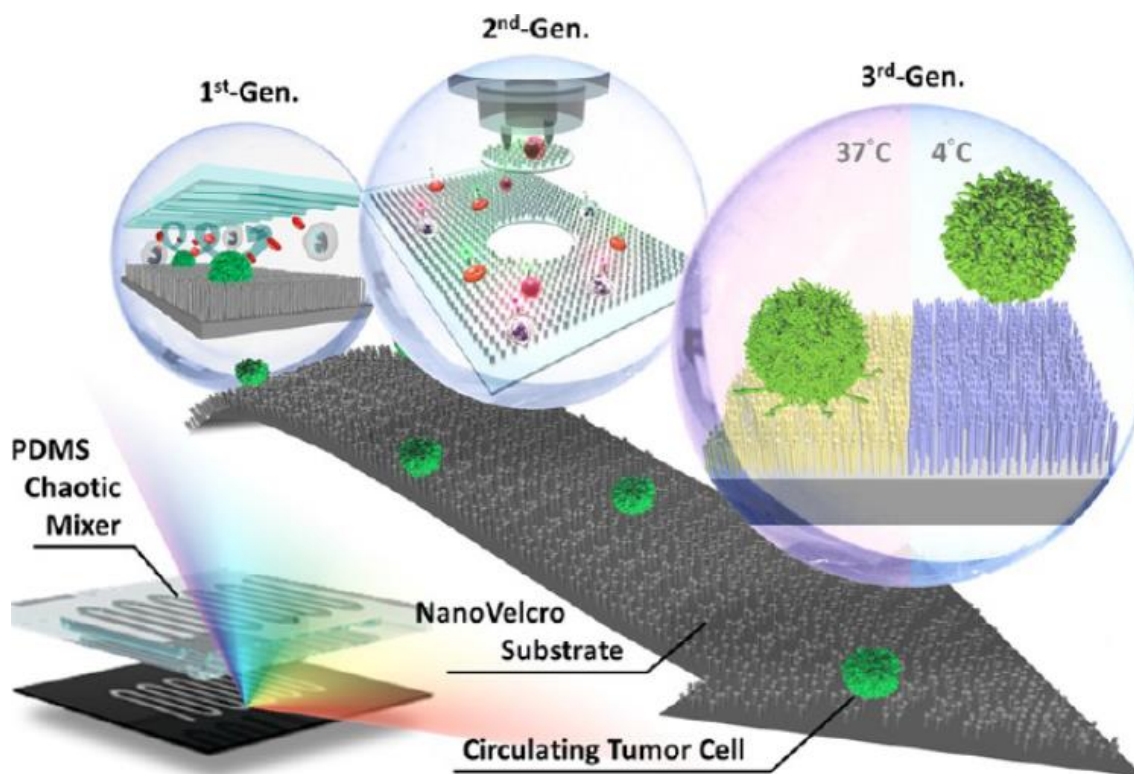


**Figure 9.** NanoVelcro chip. Schematic overlooking the first, second, and third generation of the device. This device takes advantage of nanosubstrates and microfluidics to capture isolate and release CTCs for further analysis [201].

### 1.3.5. IN VIVO

Majority of research has focused on ex-vivo analysis of CTCs, meanwhile a number of researchers have investigated the in vivo monitoring of these tumor cells [135-137].

Mouse model studies, showcased a real time in vivo CTC monitoring by injecting fluorescent ligands that specifically bind to tumor cells and then using a flow-cytometry-like technique to monitor cells in blood vessels [202]. They were able to

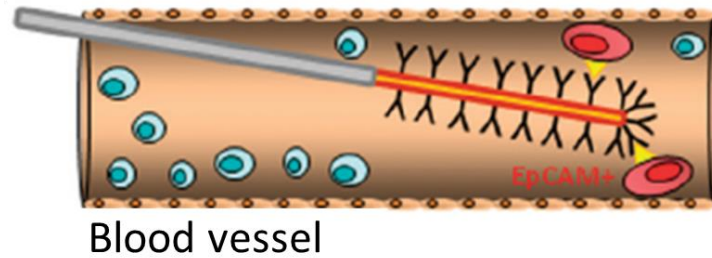


**Figure 10.** Stainless steel seldinger guidewire functionalized with anti-EpCAM antibodies to capture CTC inside the patients vein, in vivo approach [18].

detect CTCs weeks before metastatic disease became evident, showing great prognostic potential for such approach. In another novel approach, a stainless steel medical seldinger guidewire (FSMW) was functionalized with anti-EpCAM and was inserted into the vein on the patient for half an hour to capture CTCs, Figure 10. 24 lung or breast cancer patients were tested with this in vivo approach and captured cells were analyzed using immunofluorescence [135].

Such techniques have the potential to provide direct means to monitor CTCs levels in real time. However, such approach can prove to be highly challenging due to dynamics of blood-borne cells and biocompatibility of such invasive techniques complicating the analysis.

#### 1.3.6. MICROCANTILEVER

Microcantilevers have long been used as label-free biosensors, by converting biological signals into mechanical deflections that can then be detected using electrical, magnetic and optical methods [203-209]. In general, cantilevers are structured with one

end fixed and the other end free similar to a diving board and are usually fabricated from silicon, silicon oxide, or silicon nitride. Overall, cantilevers are classified into two basic groups of static and resonance mode. In static mode operation, deflection of the free end of the cantilever caused by biomolecular interactions on cantilever surface is observed. On the other hand, resonant mode demonstrates a change in the vibration frequency of the cantilever due to addition of biological mass, such as cells, to the surface of the cantilever. This change in vibration frequency can be measured using optical means to quantify the mass [210]. Variety of cantilever biosensor system based on biomolecular probe surface functionalization haven been developed in the past decade to detect various biological targets such as E-coli [205], cancer biomarkers [208], kinases and myoglobin's [211], glucose [212], *Listeria innocua* [204] , *Bacillus subtilis* spores [213], RNA [214], vaccinia virus particles [206].

Recently, Kaur *et al.* reported a real time detection of breast cancer cells using peptide functionalized microcantilever arrays, Figure 11. In this work, they reported selectively detecting CTCs using peptide moiety in conjunction with a microcantilever array system. Cantilevers were functionalized with peptide 18-4, cancer specific peptide, and showed efficient capture and detection of cancer cells in spiked human blood samples with a capture yield of 80% [140]. This novel approach present potential for capturing and detecting cancer cells using nanomechanical cantilever platform. However, this system has limited sensor surface area limiting the number of CTCs that can be detected to 50-100 cells.

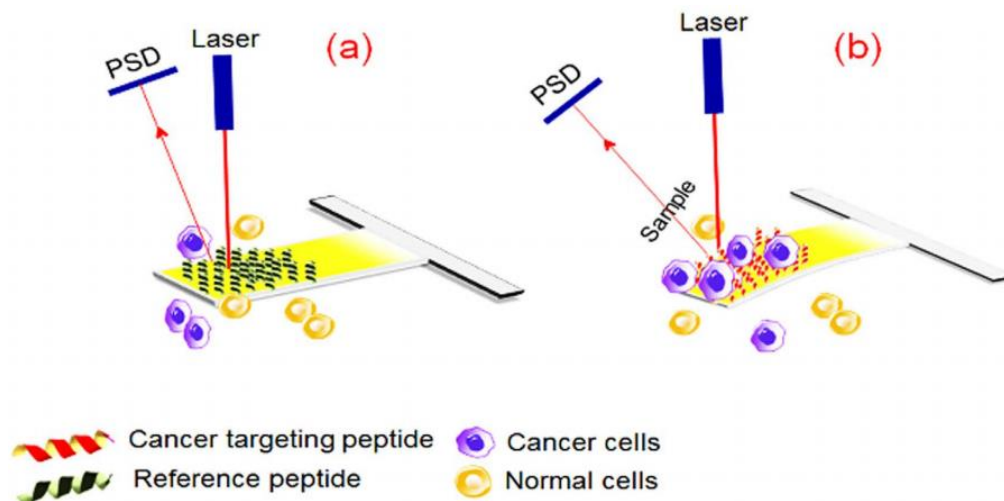


**Figure 11.** Schematic showing principle of microcantilever sensor operation. (a) Microcantilever coated with non-specific reference peptide, shows no response in form of a deflection to the presence of normal cells or CTCs. (b) Microcantilever functionalized with cancer targeting peptide demonstrates a strong response in form of a deflection as CTCs interact with the cantilever [140]. Position sensitive device (PSD).

### 1.3.7. COMMERCIALY AVAILABLE CTC DEVICES

Advance methods of CTC capture combine two or more methods of CTC enrichment and detection techniques to identify these cells. In a single integrated platform, combinations of principles of detection are utilized for a more novel and effective approach [116-127]. In a most recent effort, Han and co-workers demonstrated an electrical detection method for circulating tumor cells by taking advantage of nanoparticles, graphene nanoplates (GNPs), and using a microfluidic device in combination with impedance cytometry. Here, they presented a two-step cascade discrimination lab on a chip device for electrically identifying CTCs from the enriched blood samples. CTC device enriches rare CTCs from millions of background

blood cells using lateral magnetophoresis and then uses impedance cytometry to electrically identify CTCs, modified with GNPs, based on their electrical impedance. To improve the accuracy of electrical discrimination, GNPs were used as a highly conductive material for modifying surface conductivity of CTCs, resulting in 500-fold enrichment of CTCs using this device [127].

In the recent years, there have been number of integrated platforms that have found their way to the market and are commercially available technologies for CTC enrichment, Table 2. However, the only U.S. Food and Drug Administration (FDA) approved method for detection of CTCs is the Veridex CellSearch system [14]. CellSearch system uses magnetic nanoparticle and fluorescent dye technology to analyze 7.5 mL of blood for CTC, Figure 6. Blood sample is first processed by a centrifuge gradient process to separate buffy coat from RBCs and plasma. EpCAM conjugated magnetic microbeads are then mixed into the processed blood to bind to the EpCAM positive CTCs. Magnetic field is applied to isolate CTCs from the peripheral blood. Lastly, captured cells are fixed with 4% paraformaldehyde, immunostained with fluorescently labeled anti-CK, anti-CD45, and DAPI, and enumerated by automated cell image capture and analysis. CTCs are identified by satisfying the following criteria: low eccentricity, size greater than 5  $\mu\text{m}$ , a visible nucleus (DAPI<sup>+</sup>), positive staining for CK, and negative staining for CD45 [57]. This System can detect 85% of CTCs in a sample with 95% confidence, although its detection limit at its lowest range is  $1.2 \pm 0.4$  CTC per 7.5 mL sample [56]. The CellSearch system is considered as the benchmark standard in the industry and is also used in research as an investigative tool

**Table 2.** Commercially available technologies for CTC enrichment.

products	techniques	specifications	Reference
The CellSearch® System (Janssen Diagnostics)	Immunomagnetic separation (EpCAM-coated beads) Fluorescence imaging	Sensitivity: $\geq 2$ CTCs in 7.5 mL of whole blood Recovery: $>80\%$ in cells	[56]
AutoMACS® Pro separator (Miltenyi Biotec)	Immunomagnetic separation (EpCAM-coated beads)	Sensitivity: $19 \pm 24$ CTCs per 5 mL Recovery: $>61\%$ at each spiking level Throughput: approximately 2 hours	[215]
IsoFlux™ systems (FLUXION)	Immunomagnetic separation (EpCAM-coated beads)	Sensitivity: $\geq 5$ CTCs per 7.5 mL blood Recovery: 80% each cell line	[216]
ISCT (Isolation by Size of Epithelial Tumor Cells) (rare cells)	Size-based filtration: 8 $\mu$ m porous membranes	Sensitivity: 1 CTCs per 10 mL of blood Recovery: — Throughput: CTC separation from blood in 3 minutes	[217]
Parsortix system (Parsortix)	Wier-type step filter: size and deformability	Sensitivity: ability to process up to 20 ml of whole blood Recovery: capture of $>60\%$ CTCs in samples	[218]
RNAscope® (Advanced Cell Diagnostics)	Multi-fluorescent RNA in situ hybridization (FISH)	Sensitivity: detecting CTCs in 47% of patients in 5 ml of blood Recovery: $71\% \pm 12\%$ ( $n = 17$ ) Throughput: 5–10 hours (with $\sim 2$ hours hands-on time)	[219]
CytoTrack CT4 (Cytotrack)	Conventional CD/DVD technology Flow cytometry & Scanning microscopy	Sensitivity: scanning procedure performed in 10–15 minutes per sample Recovery: the recovery rate of 10, 33, and 100 tumor cells in a blood sample is 55%, 70%, and 78%, respectively Throughput: scan 100 million cells in just one minute	[220]
ApoStream® (Apocell)	Dielectrophoresis field-flow assist	Sensitivity: sample suspension collection volume: $\sim 1.5$ mL (starting blood volume: 50 $\mu$ l–10 ml) Recovery: — Throughput: —	[221]

for understanding the metastatic process [57, 64, 222].

While the CellSearch system represented a breakthrough in CTC separation technology both in principle and clinical applications but it is ultimately dependent on magnetic bead staining, fluorescent molecular labeling, and imaging. This method of processing requires sophisticated equipment, multistep processes, technician specialist and time, resulting in high operation cost and therefore limited application in real-patient situations. Meanwhile great number of cells are lost as part of this multi-processing technique limiting sample purity, sensitivity, and the final yield of the device [45]. Likewise, other commercially available techniques that are not yet FDA approved suffer from similar downsides. Methods utilized in bulk of these detection techniques employ molecular biology technology integrating labeling step and subsequent optical imaging step to detect target molecules. Therefore they also suffer from the same or similar downsides as the CellSearch system.

Labels are molecules that specifically bind to another molecule, i.e. antibodies, aptamers. These targeting molecules are tagged with dye or other indicator such as fluorescent dyes, enzymes, and quantum dots [223]. Labeling systems typically require extensive sample preparation and sophisticated optical imaging devices. Therefore label-free techniques are of great interest. Label-free systems that can match the high accuracy of existing standard molecular labeling technology have the potential to significantly lower the cost and complexity of these systems, thus increasing the accessibility.

The ideal CTC isolation technology should be sufficiently versatile to capture a heterogeneous population of cells. This requires high specificity, sensitivity, portability, and small size for clinical setting and point-of-care testing. Further, the ideal CTC detector should be gentle to ensure cell viability, able to capture and count the number of CTC at a rapid pace (<1 hour) with high throughput, consume only a small volume of blood and have minimum sample preparation or purification steps. To minimize the loss of CTC and to increase yield, it is important that such platform avoids enrichment steps. Finally, the ideal CTC platform should also have inexpensive, simple, and repeatable fabrication process, have the ability to interpret biological information such as different types of biomarkers, genetic mutations in tumor DNA, and any other information that reflects the biological process occurring during metastasis.

Considering all of the above, the development of the ideal CTC platform is far from reality and more work in this field is needed to satisfy the true clinical needs for CTC detection. Nanotechnology and nanoscale engineering is projected to impact this field significantly and overcome current limitations associated with CTC capture and analysis. Small size of nanoparticles and their high surface-area-to-volume ratio provides the capacity to address the problems of insufficient capture efficiency and low purity [199].

Nanomaterials such as carbon nanotubes, graphene oxide, nanopillars, and nanowires can be manufactured to a high degree of precision by advance microfabrication technologies (i.e. photolithography, ion etching, and chemical vapor deposition) and modified by customized chemistries, such as pyrenebutanoic acid,



succinimidyl ester (PASE) affinity to carbon nanotubes through  $\pi$ -stacking, to fit desired applications. Their simple incorporation with microfluidics to facilitate prototyping is also of great advantage. As it advances, the field of nanotechnology is projected to be the future of rare cell separation [224].

In general, the objective of this dissertation is to investigate a novel carbon nanotube micro-array device based on ultra-thin CNT films for label-free sensing of proteins, and capture and discrimination of CTCs.

- We begin in Chapter 2 with an overview of the physical properties of carbon nanotubes. We describe the structure of nanotubes and methods for fabricating them. We then provide background into the carbon nanotube field effect transistors and their utilization as sensing tools. Lastly, we reviewed existing carbon nanotube based approaches for sensing and their biological applications.
- Chapter 3 details our approach for developing a platform of carbon nanotube micro-arrays based on ultra-thin films using a very cost effective simple method. We begin with characterizing the nanotubes utilized for this purpose, studying their physical and electrical properties. Next, we discuss the methods behind fabrication and characterization of CNT ultra-thin films and micro-array devices. Finally, we describe our measurement setup for collecting characterization data and electrical measurements presented here and in the next chapters.

- In Chapter 4, we describe a unique approach for non-covalent functionalization of CNT surface. We demonstrate our ability to functionalize the surface of the nanotubes with proteins, such as antibodies, and capture nanoparticles on the surface of the CNT using the proposed functionalization technique. Furthermore, we characterize the sensing capabilities of our CNT micro-array devices described in Chapter 3 and their response to ionic charges.
- In Chapter 5, we investigate the application of nanotube devices for digital profiling of cancer biomarker. Showing proof of concept for label-free detection of targeted biomarker, further validating the successful functionalization protocol developed in Chapter 4 and biosensing capabilities of our CNT devices. Here we also discuss the factors behind the change in electrical properties of a CNT device due to protein/analyte interaction with the nanotubes.
- Chapter 6 presents the ability to improve upon the sensing capabilities of our CNT devices by utilizing an aptamer molecule instead of an antibody as part of CNT surface functionalization and targeting antigens. Aptamers, with their smaller molecular structure and higher affinity present a promising potential to improve biosensors, closing the Debye length. The ultrasensitive 1 pg/mL label-free sensing of IL-6 biomarker molecule is showcased as an example of aptamers based sensing capabilities on our platform. In conclusion, we discuss our decision to elect antibody platform for cell capture studies due to availability and robustness.

- In Chapter 7, we for the first time demonstrate using CNT ultra-thin film micro-array devices for capture and digital profiling of cancer cells. Here, we present the ability to capture and profile spiked circulating tumor cells in phosphate buffered saline on nanotube devices utilizing label-free techniques. This is done by targeting HER-2 and EpCAM receptors on SKBR-3 and MCF-7 cells using antibody molecule functionalized CNTs.
- Additionally, in Chapter 8 we demonstrates label-free capture of breast cancer cells spiked in buffy coats using carbon nanotube micro-arrays. We demonstrate identifying the captured cells on the device using immunofluorescence confocal microscopy. We also, present a novel classifier based on dynamic time warping statistical analysis to distinguish specific vs. non-specific interaction of captured cells on the device with great statistical confidence, based on the electrical signal captured from the device.
- In Chapter 9, we further investigate the clinical utility of our CNT device. Here, we examine the interaction between carbon nanotube devices and living spiked cancer cells in whole blood. In our initial observation, in which 170 devices are tested with 4 specific and 13 nonspecific control groups, the specific interaction present an increase in device signal, conductance. When plain blood or non-cancerous cell spiked blood is injected on the device, however, we observe no change or decrease in the device conductance. Following up, we utilized the statistical classifier discussed in Chapter 8 and observed a significant difference between SKBR-3, cancerous, spiked blood samples from plain and MCF-10A,

non-cancerous, spiked blood's electrical signal, targeted by HER-2 antibody.

Additionally, using optical imaging and image analysis, we present capturing all spiked cells, relative to device geometry, and their geometrical properties. For the first time, we report a unique arrangement of blood cells and spiked cells on the CNT device as part of the sample droplet image analysis, showing direct contact between spiked cancer cells and the CNT device surface. Using confocal microscopy and immunofluorescent technique, we identified captured CTCs on the surface of the device after end of testing. Finally, we discuss the possible origins of this signal, as well as questions about this interaction that remains to be answered.

- Chapter 10 concludes the dissertation, here we summarize the results in this thesis and provide several suggestions regarding future direction of this work.

## CHAPTER 2 BACKGROUND

### 2.1. CARBON NANOTUBES (CNT)

In 1991, Iijima for the first time reported carbon nanotubes when he discovered multi-walled carbon nanotubes (MWNTs) in carbon-soot made by an arc-discharge evaporation method at Fundamental Research Laboratories (NEC Corp.) [225]. Two years later in 1993, he observed single-walled nanotubes (SWNTs) [226]. Since then, carbon nanotubes (CNT) have become one of the most actively researched materials, opening whole new fields of study in physics, chemistry and materials science. CNTs possess a unique combination of properties, such as small size (1-50 nm diameter and length of up to several mm) [227], low density (similar to graphene), high stiffness, high strength, and a broad range of electronic properties from metallic to p- & n-type semiconducting [228]. In the past quarter century, a significant amount of work has been done to reveal the unique structure, mechanical, electrical, electro-mechanical and chemical properties of CNT and its potential applications in electronics, sensing, and actuating to name a few [229]. Such applications include electron sources in field emission displays [230], reinforcing elements in high-strength composites [231], small X-ray sources, ultra-sharp and resistant local probes [232], components of future nanoscale electronics [233], gas sensors [234], and biosensors [235].

Carbon nanotubes (CNT), more specifically SWNT, are the basic form of a graphene sheet rolled over into a cylinder, Figure 12. Typically, SWNTs have diameter of 1-2 nm. This narrow diameter distribution, results in SWNTs to often bundle up in

form of crystalline ‘ropes’ in which single tubes are held together by van der Waals interaction [236]. On the other hand MWNT consist of multilayer cylinders with an interlayer spacing that can range from 3.42 Å to 3.75 Å, depending on the diameter and number of shells composing the tube [237]. As the interlayer spacing in graphite is 3.35 Å, one can assume similar weak interaction between individual shells in MWNTs. Diameter of MWNTs are in the range of 10-50 nm [227]. The lengths of both types of CNTs, SWNTs and MWNTs, can be as short as few hundred nanometers and as long as hundreds of microns or even centimeters [229].

#### 2.1.1.1. MOLECULAR BOND STRUCTURE

CNT is a cylindrical molecule composed of carbon atoms in hexagon pattern that repeat itself periodically in space, Figure 12 (B). Each carbon atom is covalently bonded to its three neighboring carbon atoms. CNT’s structure is mainly due to the process of  $sp^2$  hybridization [238]. This structure is consisting of one s-orbital and two p-orbitals combined to form three hybrid  $sp^2$ -orbitals at  $120^\circ$  to each other within a plane, Figure 13. This covalent bond is referred to as  $\sigma$ -bond and is a very strong chemical bond which plays a significant role in the remarkable mechanical properties of CNT. Additionally,  $\pi$ -bond is the out-of-plane bond that is relatively weaker than  $\sigma$ -bond but plays an important role in the interactions between SWNTs in bundles and the layers in MWNTs. It is important to note that the bonding in CNT is not purely  $sp^2$  because of the curving the graphene sheet undergoes as it forms a tube resulting in re-hybridization in the  $\sigma$  and  $\pi$  orbitals, yielding and admixture [239].

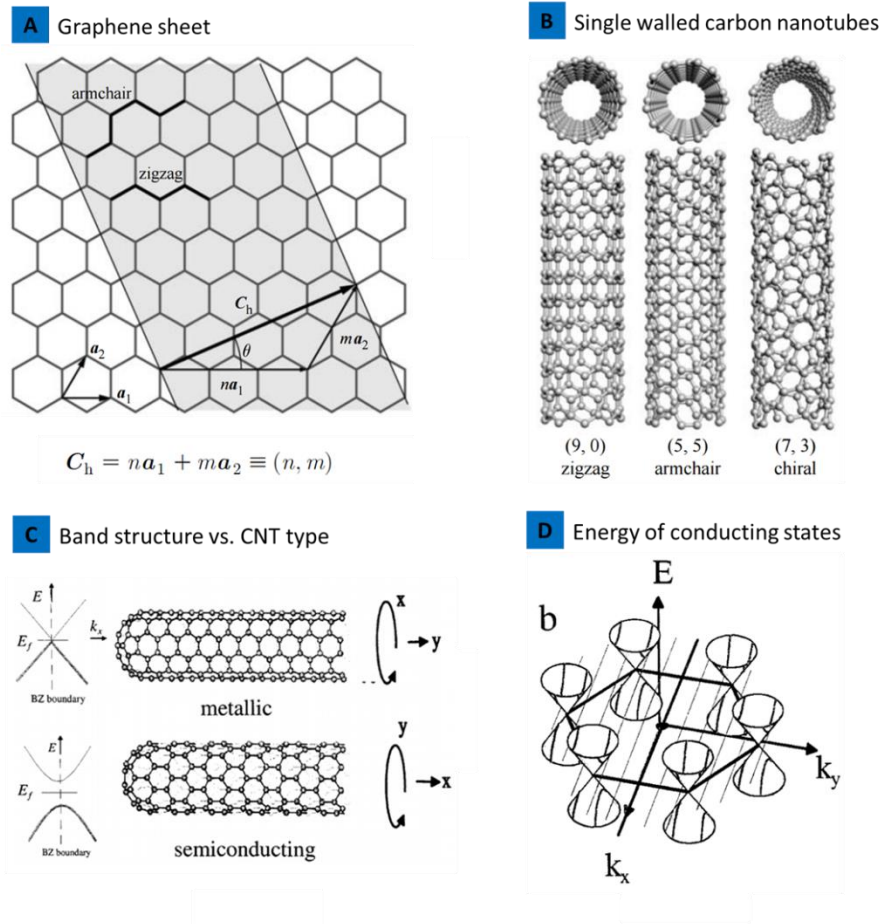


**Figure 12.** Graphene lattice and construction of a carbon nanotube (CNT) and their band structure (A) honey comb structure of graphene lattice sheet, a CNT can be constructed by rolling up a graphene sheet. The chiral vector  $C_h$  points from the origin to the point which is rolled up to the origin, here,  $C_h = 3a_1 + 2a_2$ , so this is known as an  $(n, m) = (3, 2)$  nanotube [228]. (B) shows an illustration of rolled up zigzag, arm-chair, and chiral single walled carbon nanotubes (SWNTs) [228]. (C) Rolling a graphene sheet into a nanotube quantizes the wave states perpendicular to the nanotube axis, resulting in 1-D slices through the 2-D band structure. Depending on the way the tube is rolled up, the results can be either a metallic or Semiconducting SWNT [240]. (D) The allowed electron states in a CNT are determined by the intersections between the allowed wavevectors and the graphene band structure, which, near the fermi energy,  $E_F$ , is well-approximated by a series of cones [240].

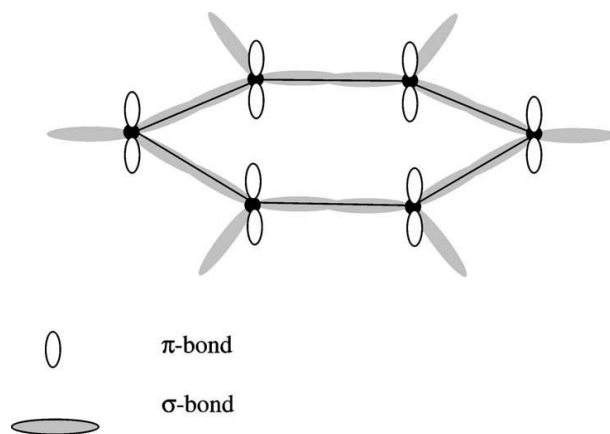


**Figure 13.** Schematic showing the basic hexagonal bonding structure on a graphene sheet. Carbon nuclei shown as filled circle,  $\pi$ -bonds are out-of-plane, and  $\sigma$ -bonds connect the carbon nuclei in-plane [239].

#### 2.1.2. PRODUCTION OF CNT

Nanotubes are produced in several different ways. By generating and cooling down a carbon plasma between two graphitic electrodes in an inert atmosphere, one can produce high quality nanotubes [225]. Lasers can also be used to ablate a graphitic target to form carbon plasma [236]. Catalytic decomposition and chemical vapor deposition (CVD) are other methods used for producing nanotubes. Here, various hydrocarbons such as methane or acetylene mixed with nitrogen or hydrogen in the presence of catalysts are used [241]. The CVD approach is of an advantage for producing controlled nanoscale structures with integrated CNTs, because of the possibility of controlling the growth of nanotubes by patterning the catalyst on a base substrate, i.e. silicon wafer [242]. Additionally, this method is also capable of producing CNTs in industrial quantities [243]. However, the main disadvantage to



CVD method is the higher concentration of defects that affects CNTs stiffness [244] and tensile strength [245, 246].

### 2.1.3. CHIRALITY

Figure 12 shows the real-space lattice and reciprocal lattice of graphene, as well as the construction of a metallic and Semiconducting CNT and its band structure.

Graphene sheet is folded to create CNT in multiple different fashions. The real-space crystal is a two-dimensional honeycomb lattice of carbon atoms with lattice vectors

$$\vec{a}_1 = \left( \frac{a\sqrt{3}}{2}, \frac{a}{2} \right) \text{ and } \vec{a}_2 = \left( \frac{a\sqrt{3}}{2}, -\frac{a}{2} \right), \text{ where the lattice constant is } a = 2.46 \text{ \AA}.$$

As shown in Figure 12 (A), a  $(n, m)$  nanotube structure is obtained when a beginning and the end of a  $(n, m)$  lattice vector in the graphene plane join together, making each CNT to have uniquely defined chiral vector  $C_h$ , where  $C_h = na_1 + ma_2$  [247]. The  $(n, m)$  indices at the backbone of the nanotubes determine its diameter and also its ‘chirality’. When the tubes are arranged in  $n = m$  or  $(m, m)$  fashion with the atoms around the circumference in an arm chair pattern they are called ‘arm-chair’ tubes, Figure 12 (A & B). “arm-chair” CNT is always metallic. On the other hand,  $(n, 0)$  nanotubes are called ‘zigzag’ as they appear in their atomic configuration along the circumference on a side view, Figure 12 (A & B). The other types of nanotubes are referred to as chiral, with the rows of hexagons spiraling along the nanotube axes, Figure 12 (B). Zigzag and chiral CNTs can be either metallic or semiconducting depending on their  $(n, m)$  structure.

#### 2.1.4. ELECTRICAL PROPERTIES AND BAND STRUCTURE

CNTs have very interesting electrical properties that originate from their core material, structure, and size. CNT are made of graphene which has high intrinsic electron mobility due to its lack of lattice defects as compared to most other semiconductor materials and its unique linear dispersion relation [248]. Small diameter of SWNTs results into quantization of electron wave vectors along the circumferences. The angle of orientation of the CNT's lattice relative to its axis (known as the chiral angle) can determine its diameter and chirality, making it semiconducting (with a moderate bandgap around 0.5 eV, semiconductor, or a small bandgap around 0.01 eV, small-gap semiconductor) or metallic [249]. The electrical properties of both semiconducting and metallic CNTs can rival or exceed the best materials known [250].

SWNTs have impressive electrical performances, for example high quality SWNTs can have a mobility value larger than  $10,000 \text{ cm}^2\text{V}^{-1}\text{S}^{-1}$  and mean free path longer than  $1 \text{ }\mu\text{m}$  [251]. Additionally, nanotubes can have minimum capacitance coupling with gates when made into field effect transistors (FETs). As a result, researchers have demonstrated SWNT FETs operating at up to 50 GHz [252].

CNT is also a unique optoelectronic material due to the unique band structure and its one dimensionality. Onsets of subbands are a possibility as part of CNT's electron density of states and a series of singularities. Thereby, CNT can efficiently absorb lights of a wide spectrum as it is a semiconductor with multiple bandgaps [253, 254]. Finally, the doping level of nanotubes can be modulated electrostatically with

high spatial resolution to generate electrons and holes at different regions unlike the chemical doping requirements in traditional semiconductor devices [255].

Since a CNT is a cylindrical graphene sheet, it has a very similar band gap structure to that of graphene. The band structure of graphene was first calculated by Wallace in 1947 using the tight-binding approximation, in which one assumes that interactions between carbon atoms only cause perturbations to electrons in atomic wave functions [256]. Later, Wallace's calculations were improved by including the overlap of atomic wave functions of different atoms [247, 257] and also considering third-nearest-neighbor interactions [258].

Graphene sheet itself is semimetallic with a zero band gap. In this case, conduction and valence bands touch each other on graphene sheet at the six corner points of the first Brillouin zone resulting in electrons filling the states at the highest energy (Fermi's energy) [240], Figure 12 (D). Arm-chair (m, m) CNT are always metallic because the electronic states, parallel lines in k space continuous along the tube axis and quantized along the circumference, always cross the corner points of the first Brillouin zone, Figure 12. The (n, m) nanotubes with  $n - m \neq 3 \times \text{integer}$ , are semiconducting. The energy gap scales with the tube diameter as  $1/d$  is on the order of 0.5 eV for SWNT with typical diameter  $d = 1.4$  nm. The energy gap for the semiconducting nanotubes is dependent on the diameter and can be calculated by the following equation:

$$E_{gap} \approx \frac{2\gamma_0 a_{C-C}}{d} \quad (1)$$

where  $\gamma_0$  is the C-C tight-binding overlap energy,  $\gamma_0 \approx 2.7 \text{ eV}$ , [258] and  $a_{C-C}$  the nearest-neighbor C-C distance (0.142 nm) and  $d$  the diameter [259]. Both Odom *et al.* [260] and Wildoer *et al.* [259] in 1998 experimentally verified the link between physical and electronic structure of CNTs using scanning tunneling microscopes (STMs) by measuring the chiral angle and diameter of individual SWNTs, allowing  $(n, m)$  to be determined. They also measured the electronic properties of each tube, including the band gaps of semiconducting nanotubes, and their results agreed with the theoretical equation presented above.

For  $n - m = 3 \times \text{integer}$ , nanotube with electron states landing on the corner of the first Broulloin zone would be semimetals but depending on the diameter it can become small-gap semiconductors because their band gap scales with  $1/d^2 \sim 10 \text{ meV}$  and  $d \sim 1.4 \text{ nm}$  due to a curvature induced orbital rehybridization effect [257]. The band structure of nanotube is also modified by stain [261] and was experimentally confirmed by Minot *et al.* [262]. The band diagram becomes even more complicated when defects and interactions with a substrate are introduced. For sensing applications, however, the important fact is simply that nanotubes are semiconducting, and not the exact size of their band gap.

### 2.1.5. MECHANICAL PROPERTIES

CNTs are among the strongest and most resilient material known to exist in nature. The Young's modulus of nanotubes is  $\sim 1$  TPa and is five times higher than that of steel [263]. The theoretical limit to the maximum tensile stress one material can sustain before failure is 130 GPa [264], for MWNTs this value was reported to be  $\sim 63$  GPa at its largest point [265]. One can compare this value to tensile strength of steel which is less than 1 GPa. At the same time, nanotubes are extremely light. Considering CNT's extreme mechanical properties, there was even a proposal to build a space elevator using SWNT ribbons [266]. However, there are huge fundamental and practical challenges standing in the way of this project for the time being.

Mechanical properties of CNT discussed above, coupled with its electrical conductivity has inspired researchers to integrate SWNTs into nanoelectromechanical systems. For example, Sazonova and co-workers demonstrated an electrically actuated tunable oscillator using SWNTs [267]. There also have been efforts in the industry to take advantage of CNT's unique properties; a company called Nantero is working toward commercializing large density and high speed random access memories based on suspended nanotubes that can be modulated by external voltages to switch between two states.

### 2.1.6. CHEMICAL AND BIOLOGICAL PROPERTIES

CNTs are chemically stable and biologically compatible. This is due to the fact that they are chemically inert, especially when no defects are present. For example, studies have shown that SWNT FETs can operate in aqueous solutions [268, 269].

SWNTs are extremely sensitive to environment because of their molecular-scale size and the fact that all the atoms in single wall carbon nanotube are oriented on its surface, therefore any change in the surface of these atoms can affect their electron transport properties. This makes SWNTs an ideal materials to make detectors that are capable to reach single-molecule level sensitivity [270, 271].

Potential applications of CNT are not just limited to sensors. On top of being chemically stable, SWNTs have large surface to volume ratio which has made them an interesting material as electrodes in electrochemistry research. SWNTs have been used as electrodes [272] or nucleate sites for nanoparticle growth [273]. The high surface area SWNTs are being researched as a candidate for hydrogen storage [274]. For biological applications, SWNTs have been used as drug delivery vehicles to bring chemicals into cells [275]. Even though there are concerns with toxicity of CNT but there have not been a great evidence of such concerns. In one study, Liu and co-workers showed that injected SWNTs can be excreted out the bodies of mice within a couple months, during this time no toxic effects were observed in the subject mice [275].

#### 2.1.7. PROPERTIES BASED ON SMALL SIZE AND DIAMETER

The small diameter of SWNTs is one of their big advantages. This is very useful for example with atomic force microscopy (AFM) as the lateral resolution is limited by the size of the scanning tip. Wong and co-workers attached a MWNT to a conventional AFM tip and used it to interact with sample surface in order to improve resolution capability of AFM [276]. Additionally, they chemically modified the end of a SWNT

tip with functional groups to do chemical force microscopy [277]. The small size of nanotubes makes it possible and easier to study chemical bindings between specifically one pair of receptor and target protein.

Electron emitters are another application utilizing the small size of nanotubes. SWNTs have a very small cross section, this enables electrical field around the tip to reach very high value when a potential is applied between SWNTs and the ground. Therefore electrons tunnel out due to high electrical field. This unique emission characteristic can be used to extract electrons to generate light at different wave lengths (i.e. visible light for television or very low wavelengths of light for applications in portable and high resolution X-ray machine) [278].

Here, we reviewed only a number of applications of nanotubes based on their unique characteristics. One can imagine number of more potential applications for SWNT as researchers are still exploring different possible applications in different fields.

## 2.2. CARBON NANOTUBE FIELD EFFECT TRANSISTORS (CNT-FET)

The first reported semiconducting SWNT based transistor was fabricated by Tans *et al.* in 1998. This device had a similar geometry as the CNT-FET device illustrated in Figure 14. The CNT bridges two metal electrodes, referred to as source and drain in transistor terminology. CNT conductance can be determined by applying a small voltage bias ( $V_{DS}$ ) across the nanotube and measuring the resulting current ( $I_{DS}$ ). CNT is laid on a dielectric surface, such as  $SiO_2$ , separating it from a conducting back

gate, like doped silicon substrate. Within such geometry, one can measure the conductance of a semiconducting CNT as a function of voltage applied to the back gate ( $V_G$ ), Figure 14 (B). CNT stays well conductive at low  $V_G$  and shuts off at high  $V_G$ . Threshold voltage of a transistor device is referred to as a voltage at which the transistor turns off; in this case it is around 5 V.

This behavior can be understood by looking at the band diagram for a semiconducting CNT, Figure 14 (C). The conductance of a semiconducting CNT at a given gate voltage is dependent on two main factors, one is the position of the Fermi level at the contacts, and two its position for the bulk of the nanotube.

The metal contact's work function is the main determinant of the Fermi level at the contacts. Gold, palladium, or platinum are the main metals used for contacts, the Fermi level typically lies below the valence band end for these metals, causing *p*-type conduction at  $V_G = 0$  through the unoccupied valence states, as shown in the middle panel of Figure 14 (C). Different techniques are used to promote *n*-type transistor behavior at  $V_G = 0$ , such as contacting the CNT with a material like calcium that has a lower work function than the nanotubes [279]. It is important to note that the *p*-type behavior at  $V_G = 0$  is also related to the adsorbed oxygen on the CNT when exposed to air and the charges on the oxide surface, therefore annealing the device in vacuum to remove the oxygen will also result in *n*-type transistor behavior [280].

The Fermi level position for the bulk of CNT is determined by the applied voltage gate. Electrons are pushed away from the CNT and into the contacts as the gate



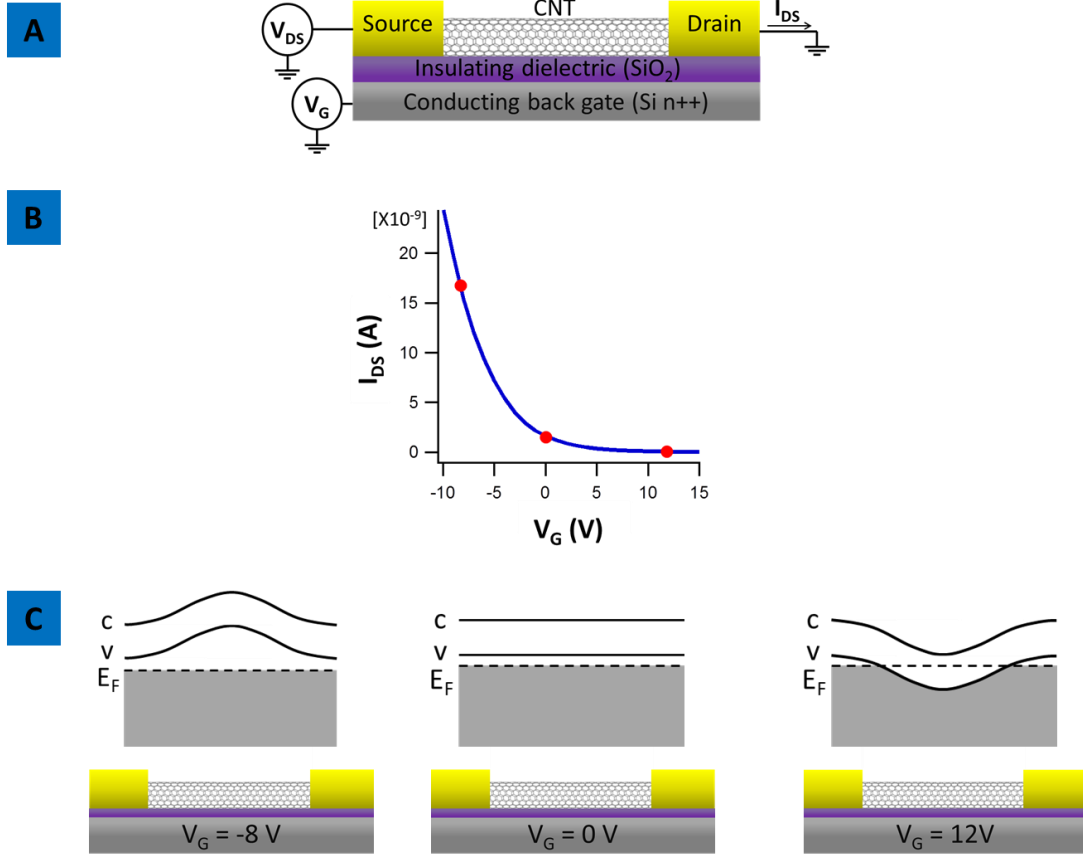


**Figure 14.** Schematic of a typical carbon nanotube field-effect transistor (CNT-FET). (A) side view of a back-gated CNT-FET. Metal electrodes are contacted on either end of the CNT, allowing one to apply a source-drain voltage bias  $V_{DS}$  across it and to measure its conductance as a function of the back gate voltage  $V_G$ . The CNT is insulated from the gate by a dielectric material, typically SiO<sub>2</sub>. (B) Conduction of a semiconducting CNT as a function of gate voltage ( $V_G$ ). (C) Band diagram of CNT for different gate voltages (marked with red dots in the  $I_{DS}$  vs.  $V_G$  curve (B)) as a function of position along the nanotube axis. At  $V_G = -8$  V, the Fermi level is deeper in the valence band, therefore allowing for higher conduction. At  $V_G = 0$  V, the Fermi level typically lies below the valence band edge due to the work function of the metal contact, as a result CNT is conducting. At  $V_G = 12$  V, the Fermi level lies in the band gap, in this case turning the transistor off.

voltage is decreased; this is due to Fermi energy going deeper into the valence band (unless the voltage is screened by the metal contacts), thus increasing conduction, as shown in the left panel of Figure 14 (C).

The Fermi level can be raised into the conduction band if the gate voltage is raised high enough,  $V_G > 15$  V for the device in Figure 14, and conduction can take place when electrons tunnel from the valence band at the contacts to these conduction band states. This is even more apparent with MWNTs as the inner tubes are not affected with oxygen in the air and preserve their *n*-type nature. As the result of the tunnel barrier, the *p*-type conduction at low  $V_G$  is larger than *n*-type conduction at high  $V_G$ . This *n*-type conduction in air was rarely observed for the devices prepared for the experiments in this thesis as SWNT were used for the majority of the work presented. It is important to note that the *n*-type conductance effect was observed sometimes when electrolyte solution gating was applied, we will discuss this effect later in this chapter when investigate electrolyte-gated CNT-FET.

Capacitance between the CNT and the gate can be employed to determine the number of electrons added to the CNT for a given  $V_G$ . The capacitance consists of two main components:  $C_E$ , the classical electrostatic capacitance between CNT and the gate which depends on the geometry and dielectric properties between the CNT and the gate, and  $C_Q$ , which depends on the CNT density of states, this is dependent on some energy that is required to add an electron to the next available state in the CNT. One can ignore the quantum capacitance of the back gate by approximating it as a perfect

metal. In this case the total capacitance would be the series combination of those components, eqn. 2, so the CNT charging is dominated by smaller capacitance.

$$C = (C_Q^{-1} + C_E^{-1})^{-1} \quad (2)$$

For example, a CNT separated from a back gate by a 200 nm thick SiO<sub>2</sub> layer, with a dielectric constant  $K = 4$ , has a electrostatic capacitance per length of  $C_E \approx 3 \times 10^{-17}$  F/ $\mu$ m, on the other hand the quantum capacitance can be estimated as  $C_Q \approx 4 \times 10^{-16}$  F/ $\mu$ m, as one can see the electrostatic capacitance will dominate the total capacitance [281].

### 2.2.1. ELECTROLYTE-GATED CNT-FET

Electrolyte-gated CNT-FET enables studying CNT with biochemical systems based in solution. In 2000, Kruger and co-workers first showed the MWNTs can be used as FET in an electrolyte environment [268]. Later in 2002, Rosenblatt *et al.* demonstrated the same results for SWNTs [269]. These researchers illustrated gating the CNT-FET devices through a wire placed in the solution instead of gating the CNT by applying a voltage to a back gate. Schematic in Figure 15 illustrates this setup.

To better understand this set up we first need to become more familiar with the properties of electrolyte solution and its electrical characteristics.

#### 2.2.1.1. ELECTROLYTE SOLUTION PROPERTIES

To best understand the electrical processes that occur in solution, one must have a thorough understanding of chemistry and chemical reactions covering topics such as

electrochemistry, physical chemistry, and interfacial science. For detailed introduction to these topics, the reader is directed to references such as Bard and Faulkner (2001) [282], and Harned and Owen (1958) [283]. However, here we will summarize and reduce these topics as much as possible and focus on the details more fundamental to the scope of this thesis.

Conducting solutions or electrolytes include a wide range of constituent ions and solvents. Aqueous electrolytes were the main focus for the works in this thesis, most commonly Phosphate-buffered saline (PBS), which consist of NaCl (137 mmol/L), KCl (2.7 mmol/L), Na<sub>2</sub>HPO<sub>4</sub> (10 mmol/L), and KH<sub>2</sub>PO<sub>4</sub> (1.8 mmol/L) [284]. NaCl is the most dominant component in these electrolyte solutions. NaCl in a solid crystal form does not conduct electricity, but when dissolved in water it separates into Na<sup>+</sup> and Cl<sup>-</sup> ions as the polar water molecules surround each element and break their ionic bonds. The dissolving of NaCl in water produces ions with charge  $\pm 1$  or otherwise known as 1:1 salt. Charged ions floating around, enables NaCl solution to conduct electricity just like a metal with free electrons.

The resistivity of a bulk electrolyte can generally be used to approximate its electrical properties [285]. The concentration of conducting ions plays a big role in the solutions conductivity, for example, 1 mM NaCl has  $\rho = 81 \text{ } \Omega\cdot\text{m}$  while 100 mM NaCl solution has  $\rho = 0.9 \text{ } \Omega\cdot\text{m}$ . The equivalent conductivity ( $\Lambda$ ), with units of  $\text{m}^2/\text{ } \Omega\cdot\text{mol}$ , for a variety of electrolytes is provided in the “CRC Handbook of Chemistry and Physics”. Therefore, the conductivity can be expressed as  $\sigma = \Lambda \cdot c_0$ , where the resistivity is  $\rho =$

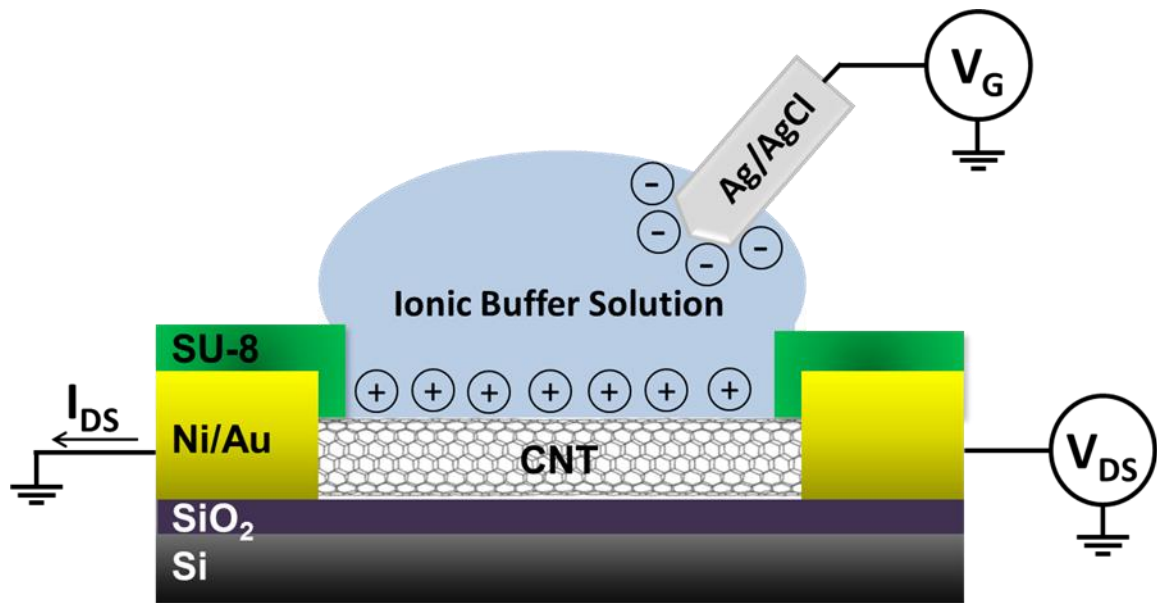


**Figure 15.** Schematic of an electrolyte-gated CNT-FET. Similar to Figure 14, CNT is contacted by metal electrodes (Ni/Au) on each side, allowing one to take conductance measurements. The gate voltage  $V_G$  is applied by a wire (i.e. Ag/AgCl reference) that is in contact with the electrolyte solution (i.e. ionic buffer solution). The voltage applied affects the CNT via ions in the electrolyte solution. For example, if voltage is applied to make the wire positively charged, the negative ions will get attracted to form a double layer. SU-8 polymer layer acts as an insulator to separate the charges in the electrolyte solution from the contacts, therefore only directly gating the CNT.

$1/\sigma$  and  $c_0$  is the bulk salt concentration. For example, NaCl (0.5-100 mM) the  $\Lambda = 107\text{-}126 \times 10^{-4} \text{ m}^2/\Omega\cdot\text{mol}$ , and for most other solutions the  $\Lambda \approx 100 \times 10^{-4} \text{ m}^2/\Omega\cdot\text{mol}$ , ranging from  $50\text{-}425 \times 10^{-4} \text{ m}^2/\Omega\cdot\text{mol}$  [286]. Due to similarity of  $\Lambda$  in most electrolyte solutions used in this thesis, we can estimate the resistivity using the following equation:

$$\rho \approx \frac{100}{c_0[\text{mM}]} \Omega \cdot \text{m}. \quad (3)$$

In this case we can continue using the length  $l$  and cross-section  $A$  to estimate the resistance of a section of solution,  $R_{\text{soln}} = \rho l / A$ .

#### 2.2.1.2. MODEL OF ELECTROLYTE-GATED CNT

There have been different approaches to model electrolyte-gated CNT and its response to the environment [287-289]. McEuen and co-workers, came up with a model based on the ratio of the oxidized to reduced molecules ( $[\text{Ox}]/[\text{Red}]$ ), i.e. potassium and sodium ferrocyanide respectively [288]. They developed a quantitative model to understand the expected threshold voltage shift of the CNT-FET response by utilizing Nernst equation, which gives the chemical potential of the electrons in a solution of redox-active molecules with formal potential  $E^0$  as:

$$\frac{\mu_i}{e} = E^{0'} + \frac{kT}{ne} \ln \frac{[\text{Ox}]}{[\text{Red}]} \quad (4)$$

where  $k$  is Boltzmann's constant,  $T$  is the temperature,  $n$  is the number of electrons transferred, and  $e$  is the electron charge. Then by substituting this expression into:

$$\bar{\mu}_i = q\varphi + \mu_i \quad (5)$$

where  $\bar{\mu}_i$  is the electrochemical potential, which is the electrostatic ( $\varphi$ ) and chemical ( $\mu_i$ ) potentials. This integration expresses the voltage,  $V_G$ , applied to the gold electrolyte-gate wire as:

$$V_G = \frac{\bar{\mu}_i}{e} = \varphi + \left[ E^{0'} + \frac{kT}{ne} \ln \frac{[Ox]}{[Red]} \right] \quad (6)$$

In this case, if the nanotube behaves as a reference electrode and senses only the electrostatic potential,  $\varphi$ , then the shift in the threshold voltage,  $\Delta V_{th}$ , is the change in  $V_G$  needed to produce the same  $\varphi$ , which is just the change in  $\bar{\mu}_i/e$ . In this case,  $n$  is fixed at 1, therefore, the expected threshold voltage shift is written as:

$$\Delta V_{th} = \Delta E^{0'} + (59.2 \text{ mV}) \log \left[ \frac{[Ox]}{[Red]} \right] \quad (7)$$

It was concluded that oxide molecules, i.e. potassium ferricyanide, result in a positive shift in threshold voltage,  $V_{th}$ , and redox molecules, i.e. sodium ferricyanide, cause a negative shift in the threshold voltage,  $V_{th}$ .

### 2.3. CARBON NANOTUBES (CNT) FOR SENSING AND BIOLOGICAL APPLICATIONS

SWNTs are exclusively consist of surface atoms as part of their impressive electrical properties making them very sensitive to adsorbents [234, 290]. The sensitivity of CNT to adsorbents has been advantageous for sensing applications.

Electrical changes in CNT can be evaluated in resistor, transistor, or capacitor structures. As a result, SWNTs have been incorporated as sensing elements for various types of molecules, such as toxic chemical vapors and bio-macromolecules [270, 291-293]. The surface modification and treatment of CNT, covalently or non-covalently, has enabled targeting specific free molecules and even proteins on surface of cell membranes, receptors [133, 294, 295]. Here we will review number of works that used CNT for applications such as gas sensing, biosensing, and capturing/tagging of molecular complexes.

### 2.3.1. CNT FOR GAS SENSING

In 2000, Kong *et al.* for the first time demonstrated nanotube sensing experiment in Hongjie Dai's Stanford laboratory. In this experiment they exposed a back-gated nanotube transistor to  $\text{NO}_2$  gas and observed an increase in threshold voltage  $\Delta V_{th} \approx 4 \text{ V}$ , while exposure to  $\text{NH}_3$  caused a decrease in threshold voltage  $\Delta V_{th} \approx -4 \text{ V}$ , Figure 16 [290]. In summary, a non-functionalized semiconducting SWNT exposure to gases causes the entire  $I_{DS}$  vs.  $V_G$  response curve to be translated with respect to  $V_G$ , which was described as a shift in the threshold voltage of the device. This change in the case for  $\text{NO}_2$  is due to the fact that  $\text{NO}_2$  is a strong oxidizer, attributing to the increase in threshold voltage and charge transfer from the CNT to  $\text{NO}_2$  molecules, or in other words p-doping the CNT. On the other hand,  $\text{NH}_3$  has a lone electron pair that it can donate, n-doping the CNT. However, based on their density-functional theory calculations they showed no affinity between  $\text{NH}_3$  molecules and the



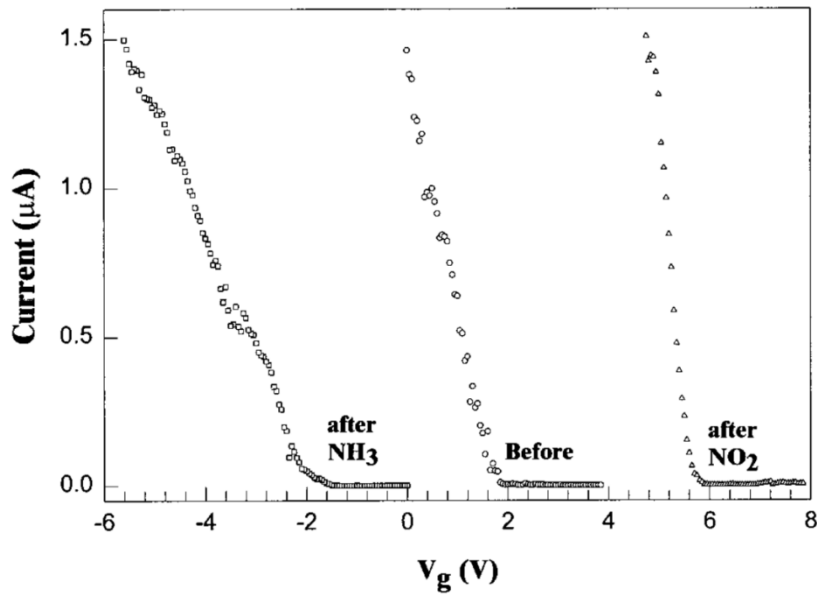


**Figure 16.** Chemical gating effects to the semiconducting SWNT by gaseous  $\text{NH}_3$  and  $\text{NO}_2$ . Each gas causes a large threshold voltage shift in the  $I_{\text{DS}}$  vs.  $V_{\text{G}}$  curve. The measurements with these gases were carried out successively after sample recovery [290].

CNT, therefore they suggest that it is indirectly affecting the CNT through the  $\text{SiO}_2$  substrate or through preadsorbed oxygen on the CNT.

Similar n-doping effects from other amine compounds was again observed by Kong and Dai [296]. Bradley from Nanomix Inc., confirmed the previous results. Here, he used CNT devices in which the metal contacts were covered with  $\text{SiO}_2$  and showed that the effect is not related to these contacts [297]. Using the previous result, Liu *et al.* modulated the band structure of SWNTs spatially by covering parts of the CNT and letting the exposed area be doped by gaseous  $\text{NO}_2$  or  $\text{NH}_3$  [298]. Later, Novak *et al.* showed an application of this sensing mechanism by demonstrating the ability to

specifically detect dimethyl methyl phosphonate (DMMP), an electron donor similar to the nerve agent gas sarin, by coating the CNT with a chemoselective polymer film [299]. With this device, he observed a shift in the threshold voltage  $\Delta V_{th} \approx -2 V$ .

Additionally, electronic properties of bare CNTs have shown extreme sensitivity to oxygen. In ultrahigh vacuum, CNTs are n-type, but they become p-type when in air or in pure oxygen environments [234]. Initially, this was ascribed to charge transfer from CNT to adsorbed O<sub>2</sub>, but Cui and co-workers later suggested that the O<sub>2</sub> instead changes the energy alignment at the metal-nanotube contacts [300].

A shift in CNT's voltage threshold was also shown in response to alcohol vapors such as ethanol [301]. Later Snow and his colleagues demonstrated kind of CNT vapor sensing experiment that looks at the change in the capacitance between the CNT and the silicon back gate, instead of just studying the conductance response. Here they reported 10-100 times larger change in capacitance than the corresponding change in conductance, when CNT was exposed to most vapor [302]. As part of these studies, they concluded that the adsorbed gas molecules form a polarizable layer that increases the nanotube capacitance which scales roughly with molecular dipole moment [303]. They additionally reported that the change in signal is dominated by adsorption at defect sites and they can increase sensitivity by introducing defects by controlled oxidation [304].

### 2.3.2. CNT FOR BIOSENSING

The promising studies using CNT for sensing gaseous molecules has led the researchers to further investigate the potential and application of CNT for sensing other molecules. The majority of these efforts have focused on biological sensing applications to potentially optimizing existing sensors, making them fast, low cost, and sensitive using CNT technology. Biosensing techniques are currently dominated with complex and multiple processes involving optical detection, techniques using only electrical measurements are presenting to be a great alternative overcoming many of the current challenges.

CNTs have comparable diameter, size, and carrier density to the size and surface-charge density of bio-macromolecules, therefore chem-resistor or transistor structures based on CNTs can be utilized as ultrasensitive transducers in biosensors [293, 305-307]. Biomolecules, such as proteins and DNA, can bind to the surfaces of SWNTs by  $\pi$ - $\pi$  stacking, hydrophobic interactions, and even amino-affinity of CNTs to alter the conductance of CNT thin films [308]. This opens the possibilities for CNTs to present themselves as efficient material for label-free detection of biomolecules [309, 310]. Additionally due to these same properties, CNT's surface can be functionalized with organic and biomolecules (i.e. linker molecules with antibodies) for more specific interaction with target biomolecules and proteins [270, 311]. Utilizing such strategies, CNTs have been used to detect different biomolecules, such as DNA, proteins, enzymes, and neurotransmitters [293].

Koehne *et al.* demonstrated detection of DNA targets using aligned MWNTs in low-density nanoelectrodes within SiO<sub>2</sub> matrix [312]. MWNTs forming glassy carbon electrode were also used for enhanced detection of DNA hybridization [313]. In addition, SWNTs DNA sensor based on conductance change was also developed based on hybridization of DNA conducting onto gold electrodes [314], Figure 17.

Kim *et al.* demonstrated detecting target prostate specific antigens (PSA) protein, a common biomarker for prostate cancer, by linking PSA antibodies to a SWNT-FET, Figure 18 (A). They were able to increase the sensitivity of the device by putting spacer molecules between the covalent linkers that were bound to antibodies, by decreasing surface coverage. The extra space between antibodies allowed for more flexibility so the interaction could occur within the Debye length. Yu *et al.* also showed CNT based method for PSA detection. He demonstrated multi-label strategy using secondary antibodies attached to MWNTs and horseradish peroxide (HRP) labels for sensitive detection of PSA, Figure 18 (B) [315]. Here, SWNTs forest with PSA antigens attached to them were assembled on a conductive substrate. Sandwich immunoassay in form of capturing PSA antigens by the primary and secondary antibodies were measured by adding a mediator and hydrogen peroxide to activate the peroxidase cycle that resulted in increasing current under constant voltage. Bovine serum albumin (BSA) and Tween-20 were used to control nonspecific binding by blocking the immunosensor during signal amplification step. 1-(3-(dimethylamino) - propyl)-3-ethylcarbodiimide hydrochloride (EDC) and N-hydroxysulfosuccinimide

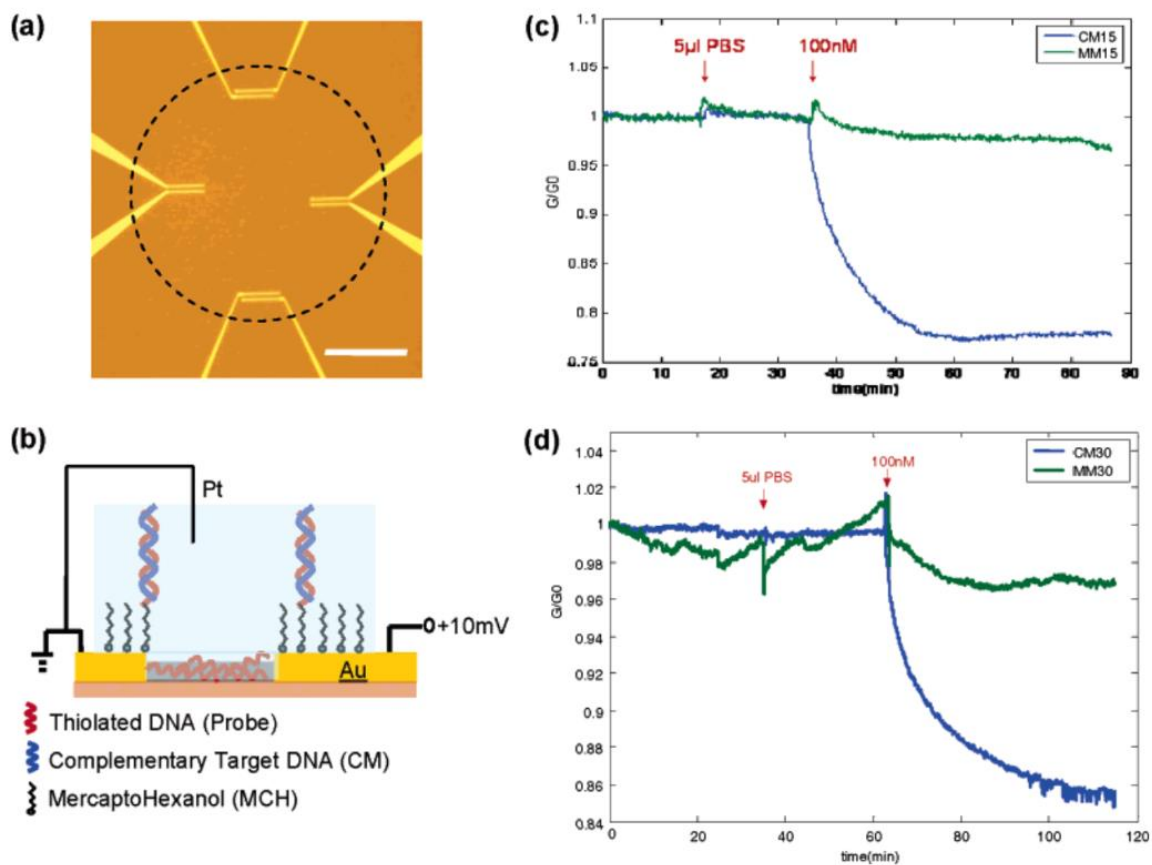


**Figure 17.** CNT DNA sensor and sensing mechanism, (a) optical image of the central region of a single sensor chip with four SWNT devices (scale bar 200  $\mu\text{m}$ ). (b) Schematic illustration of a single device during electrical measurement. Complementary ssDNA oligos hybridize to thiolated ssDNA coimmobilized with mercaptohexonal (MCH) on the gold electrodes. Real-time monitoring of 15mer (c) and 30mer (d) DNA hybridization in PBS, pH 7.4, is shown. The conductance of a nanotube device functionalized with thiolated ssDNA exhibits selective response to the addition of complementary ssDNA showing decrease in conductance at the time of sample addition [314].

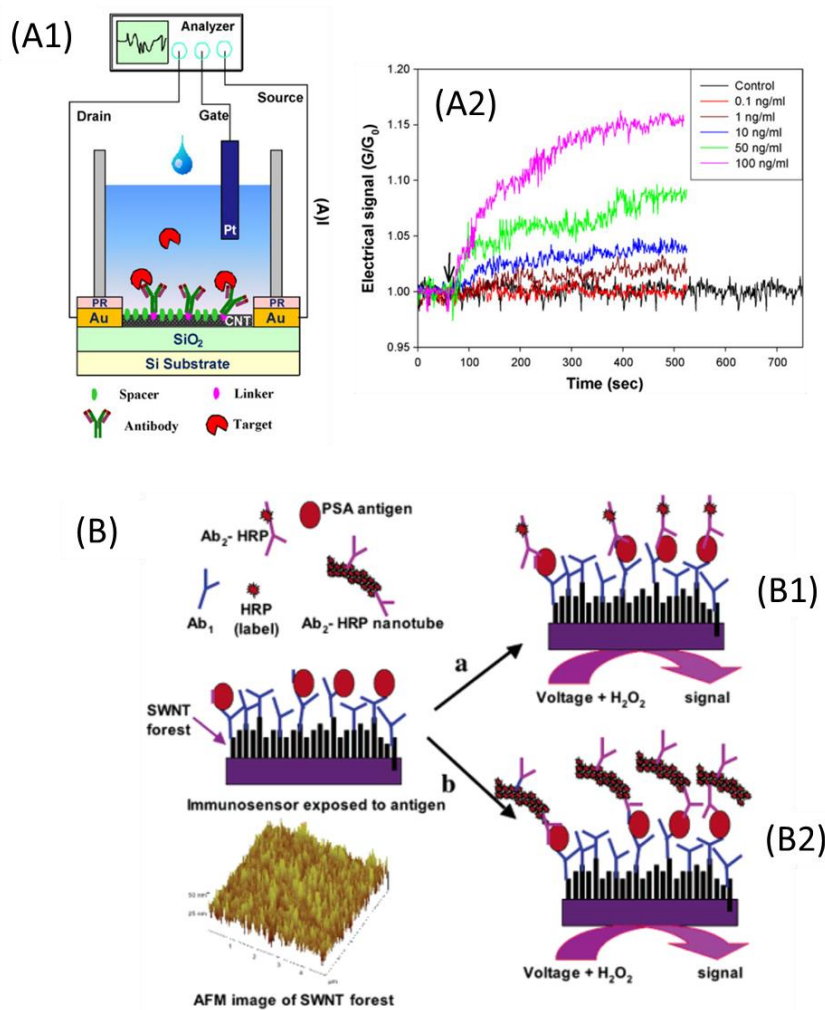


**Figure 18.** (A1) Schematic diagram of a CNT-FET for protein detection. Antibody is bound to the CNT and binding to the target electrostatically gates the transistor, causing a change in conductance of the CNT. (A2) The electrochemical signal, plotted as normalized conductance, is shown when different concentrations of prostate specific antigen (PSA) are introduced to the device (arrow). Concentrations as low as  $1\text{ ng mL}^{-1}$  can be detected [316]. (B) Immunoassay detection principle using CNTs to immobilize multiple labels and secondary antibodies for signal amplification. HRP catalyzes  $\text{H}_2\text{O}_2$  and generates electrons for amperometric based measurement. (B1) conventional single HRP labeled secondary antibody (B2) multiple HRP and secondary antibody on carbon nanotube for signal amplification [315]

(NHSS) were used here to link and attach the primary and secondary antibodies on the CNTs through amide bonding.

CNT has also been utilized for sensing enzymes. In one example, Yang *et al.* fabricated an enzyme sensor on an electrode where aligned CNT were grown [317]. Platinum (Pt) nanoparticles were used on CNT electrode and chitosan-cadmium sulfide quantum dots were used to immobilize glucose oxidase (GOx) on the top. Oxidation/reduction peaks were observed only when Pt nanoparticles were present with a detection limit around 50  $\mu\text{M}$ . Dekker's group developed an enzyme-coated CNT platform as single molecule biosensor [270], Figure 19 (A). They demonstrated the use of individual semiconducting SWNTs as versatile biosensors. Linking molecule was used to attach GOx to the CNT sidewall. Enzyme coated CNT acted as a pH sensor with large and reversible changes in conductance upon changes in pH. This device showed a step like response that can be monitored in real time as glucose is added to the substrate of GOx, suggesting the capability of measuring enzymatic activity at the level of single nanotube.

Additionally, CNT-immunosensors have shown to be able to trap whole cells by targeting known proteins on the cell membrane. Panchapakesan *et al.* used SWNTs interconnects between patterned metal electrodes for the detection of live breast cancer cells. When the cells were captured by the specific antibodies on the SWNTs a decrease in conductance was detected. A small change in conductance was observed for control cells, but the cancer cells produced a larger decrease [295]. However, exclusion of non-specific binding will need to be improved. In another study, CNT-FET approach was

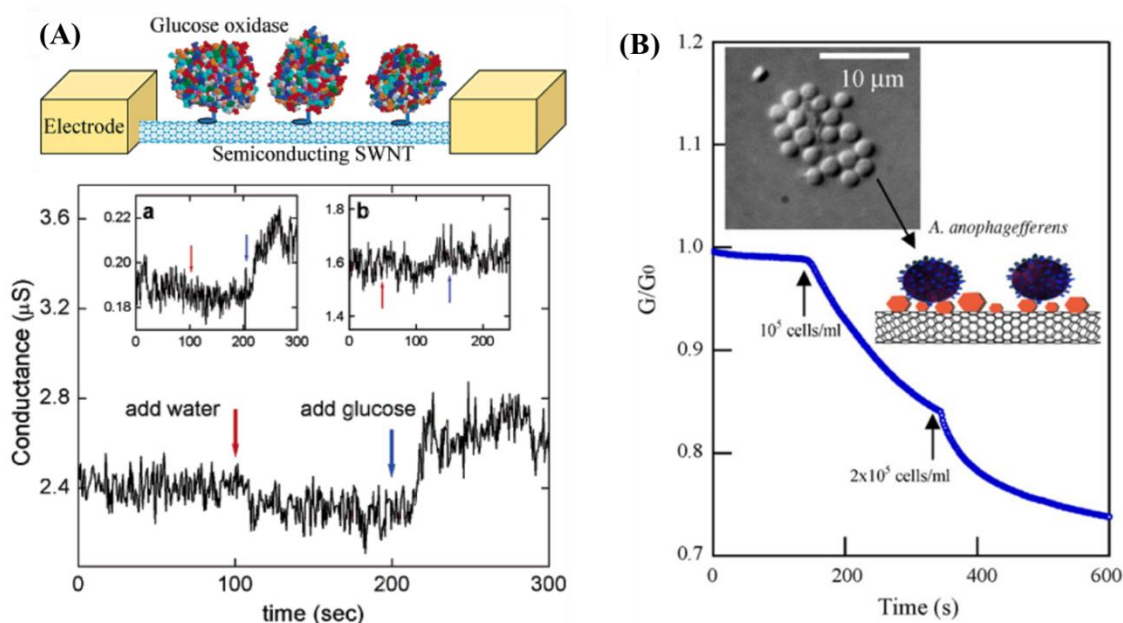


**Figure 19.** (A) Top panel shows a schematic picture of two electrodes connecting a semiconducting SWNT with GOx enzymes immobilized on its surface. (A) Bottom panel shows real time electronic response of the glucose, the substrate of GOx. Milli-Q water sample was added to the liquid at 100 sec (red arrow), and at 200 sec 0.1 mM glucose in milli-Q water was added to the liquid (blue arrow). The conductance of the GOx-coated SWNT is observed to increase upon addition of glucose to the liquid. Inset (a) shows the same measurement on a second device where the conductance was a factor of 10 lower. Inset (b) displays the same measurement on a semiconducting SWNT without GOx. As expected, no conductance increase is observed here [270]. (B) Shows the cell detection by metal-cluster-decorated CNT biosensor. The normalized conductance plot here shows the change in signal during exposure to *A. anophagefferens*. The insert at top is an optical image of *A. anophagefferens*. The inset at the middle shows a schematic illustrations of cells on the devices with metal-clusters [318].



used for cell detection. Here, CNTs were decorated with metal cluster and then metal electrodes were deposited [318], Figure 19 (B). The device was functionalized with monoclonal antibodies for *A. anophagefferens*, an alga cell, and a change in gate conductance was detected when the algae cells bound to the surface of the device, cells could be detected at concentrations of  $10^4$  cells mL<sup>-1</sup> with time response of 10 s. Here also, the non-specific binding remains the biggest limitation.

In a different approach, the Wang group sensed cancer cells by detecting differences in ferricyanide detection after adsorption of cells [319]. Their electrode was a TiO<sub>2</sub>/MWNT paste that was applied to a carbon paper electrode. Surprisingly, a 10-fold higher signal for ferricyanide was observed at the electrode after leukemia cells were bound. The enhancement was attributed to ferricyanide being attracted to the hydrophilic cells whereas it may have been repelled by the hydrophobic TiO<sub>2</sub>/MWNT surface. However, no non-cancerous or other types of cancerous cells were tested, so it is not known if this technique is really selective for specific cancer cells. Without a molecular recognition element, it is doubtful that a simple adsorption experiment would be able to selectively detect only cancer cells.

### 2.3.3. CNT FOR OTHER BIOLOGICAL APPLICATION

CNT has also been used for non-sensing biological applications, such as drug delivery, and cancer targeting and therapeutics [294, 320-322].

Liu *et al.* introduced functionalization of SWNT by chemically partitioning the surface of nanotubes to attach various species non-covalently for potential drug

delivery applications [320]. To obtain aqueous soluble SWNTs, nanotubes were first functionalized with PEG derivatives. The unoccupied sites on the prefunctionalized SWNTs were used to bind with cancer chemotherapy drug, doxorubicin (DOX). Release of DOX drug was also studied by varying the pH for controlled delivery of molecules bound on CNTs.

Xiao *et al.* utilized SWNTs to develop an antibody-CNT complex for detection and destruction of cancer cells, using two unique optical properties of CNT (strong Raman signal and near-infrared (NIR) absorbance), in an in vitro model consisting of HER-2-expressing SKBR-3 cells and HER-2-negative MCF-7 cells [321]. The anti-HER-2 was covalently conjugated to carboxylated SWNTs and targeted at cancer cells. Raman spectroscopy showed significantly greater signal coming from HER-2-positive cancer cells vs. control HER-2-negative cells. NIR irradiation was performed at 808 nm wavelength for 2 min and results showed selective destruction of complex-treated breast cancer cells without harming receptor-free cells.

Shao *et al.* utilized SWNT functionalized with antibodies specific to breast cancer cells to carried out phototherapy [294]. SWNTs were selectively targeted at cancer cells through selective binding of antibodies specific to the cancer cells. Applying infrared photons at ~ 808 nm wavelength led to the destruction of these cancer cells due to the concentration of the SWNTs present at the site. In the case of non-specific antibodies treated with SWNTs, 80% of the cells remained alive. The SWNT and antibody conjugation was achieved through amide bonding using 1-

pyrenebutanoyl succinimide. Polyethylene glycol was then used to insulate the surface of the SWNTs from nonspecific interactions.

CNTs have shown great promise for biological applications. In this thesis, we will utilize CNTs to develop a micro-array platform for biosensing and cancer cell capture applications based on SWNT ultra-thin films.

#### 2.3.4. DISCUSSION AND ANALYSIS

In this section we examined many examples of chemical and biological sensing with carbon nanotube transistors. These sensors are divided into two different device architectures, both utilizing carbon nanotubes that connect the source and drain electrodes, and have been developed and explored by various groups working in this area. In one device architecture, a single nanotube connects the source and the drain, example seen in Figure 19 (A). Such devices have been utilized for biosensing, and they offer excellent sensitivity [323]. There is, however, substantial variation between the different devices that are fabricated; such variation reflects the (geometry-dependent) variation in the electronic characteristics of individual nanotubes as discussed earlier in this chapter. In addition, the interface between the nanotube and the metallic contact, Schottky barrier, may vary substantially from device to device. In alternative device architecture, the devices contain a random array of nanotubes functioning as a conducting channel, example seen in Figure 19 (B). Current flows along several conducting channels that determine the overall device resistance. In this configuration, the device operation depends upon the density of nanotubes. For a dense array, screening of the gate voltage by the conducting nanotube is important, in a

fashion similar to gate voltage screening due to a metal layer deposited on the device. For a rarified array, such screening is not significant and the array can serve as the source-to-drain conducting channel. It is expected that arrays close to and on the conducting side of the two-dimensional structure will have appropriate transistor characteristics. Under such circumstances screening effects are expected to be small, but conduction is still provided by the nanowire network. Therefore, ultra-thin single layer, continuous, conducting nanotube array network are of great interest. Devices with nanotube network conducting channels, while less sensitive than single nanotube devices, offer reproducibility and manufacturability. Due to the reproducible and manufacturable nature of carbon nanotube array network, we have elected this architecture containing a random array of nanotubes functioning as a conducting channel to fabricate our carbon nanotube micro-array devices for the purposes of this thesis. This also enables us to fabricate larger active nanotube array area suitable for cell capture, which would not be possible with single nanotube architecture.

In both device architectures, the parameter that is used for detection is dependent on the source-drain current,  $I_{DS}$  (for a fixed source–drain voltage  $V_{DS}$  and gate voltage  $V_G$ ). The change in conductance of nanotube or nanotube array as a result of analyte interaction can be explained in two general ways: the carrier mobility can be decreased, causing a suppression of conductance at all gate voltages,  $G_{new}(V_G) = G_{old}(V_G)/a$ , or the carrier density can be changed, causing a shift in the conductance with respect to gate voltage,  $G_{new}(V_G + \Delta V_{th}) = G_{old}(V_G)$  [307]. The former is

commonly seen in experiments with functionalized nanotube sensors, but almost all experiments with non-functionalized nanotubes result in the latter signal.

A change in carrier density in a nanotube can be caused either by electron transfer from the analyte to the nanotube or by capacitive gating, in which the analyte changes the local electric field [324]. When a total charge  $\Delta q$  is transferred to the nanotube, it will cause a threshold voltage shift  $\Delta V_{th}$  given by  $\Delta q = C\Delta V_{th}$ , where  $C$  is the combination of the electrostatic and quantum capacitances. In the second case, the analyte changes the carrier density not by directly transferring electrons to or from the nanotube, but by changing the electrostatic potential near the nanotube, which pulls more electrons onto the nanotube from the contacts (or vice versa); this effect changes the nanotube conductance in the same way as gating the transistor through a back gate or through the electrolyte, as discussed in Section 2.2. On the other hand change in carrier mobility is caused by potential scattering of charge carriers by the scattering potential created by analyte, reducing or increasing the carrier mobility thereby the conductance [307].

All of the experiments reported in this thesis, however, were performed with nanotubes lying on an  $\text{SiO}_2$  surface, and Artyukhin *et al.* [324] have shown that this complicates the capacitive gating signal, making it more difficult to originate the change in signal. However, we can still assume the change in CNT electrical property is a combination of change in carrier mobility and carrier density.

## CHAPTER 3

### CHARACTERIZATION AND METHODS

In this chapter the design, fabrication and characterization of the CNT films, micro-arrays devices, and the testing platform setup will be reviewed in detail.

The fundamentals behind the design and fabrication methods will be reviewed as part of the three generations of the CNT device micro-arrays. This is consisting of fabrication and characterization of CNT thin films, explaining the vacuum filtration process and the protocol for generating an ultra-thin film. In regards to micro-array CNT devices, we will review device design parameters and microfabrication protocol. Next, we will present the characterization of physical (i.e. absorbance, transmittance, and Raman spectroscopy) and electrical (i.e. sheet resistance, mobility, on-off ratio) properties of CNT, thin films and micro-array devices. Here, we will review the effect of CNT film concentration, network density, on CNT device electrical property, utilizing percolation theory, and elect the working concentration for the objectives of this thesis. Finally, the testing platform on which the CNT devices were tested on will be described here.

### 3.1 CNT DEVICE DESIGN AND FABRICATION

The CNT devices are a simple two-terminal design at their core, with a carbon nanotube thin film network connecting the source and drain nickel-gold (Ni/Au) electrodes on each end, on top of a silicon/silicon-dioxide (Si/SiO<sub>2</sub>) substrate. The electrodes are then covered and insulated with a photoresist polymer, SU-8, as illustrated in Figure 20. The prototyping of a CNT device includes preparing a CNT thin film and transferring it on a silicon wafer substrate followed by multiple photolithography and reactive ion etching steps as part of microfabrication process. In this section we will review this process from start to finish.

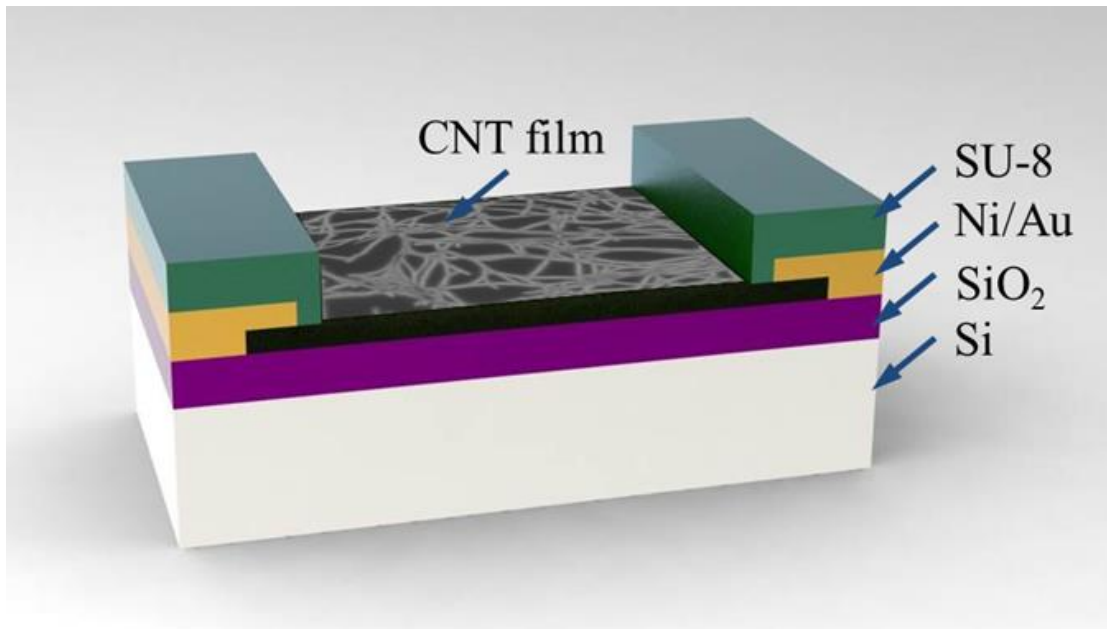


**Figure 20.** Schematic of a basic structure of carbon nanotube (CNT) device after microfabrication process. CNT film bridging the two source and drain Ni/Au electrodes on top of a Si/SiO<sub>2</sub> substrate. Source/drain electrodes are covered and insulate with a photoresist polymer later, SU-8.

### 3.1.1 VACUUM FILTRATION AND CNT-NETWORK FORMATION

The first step in the process of making a CNT device is assembling the carbon nanotube thin film network. In the last chapter we described why we have elected to fabricate our CNT micro-arrays using nanotube arrays instead of single nanotube architecture, as they are more reproducible, manufacturable, and allow for larger active CNT area suitable for cell capture. The ideal CNT array network would be made of purely semiconducting nanotubes with universal chirality. This would be consisting of defined number of aligned single wall carbon nanotubes connecting the source and drain electrodes, forming a single layer directionally aligned nanotube film. This ideal array of nanotubes would have all the CNTs exposed to the surface with zero underlying conductive channels. This ideal CNT network would give the most reproducible and sensitive results. In an attempt to produce a nanotube array network closest to its ideal form, we have utilized vacuum filtration method which enables us to close down on many of these parameters, such as semiconducting nanotube purity, almost single layer film, and reproducibility as a function of CNT film mass.

Vacuum filtration is one of the most preferred methods for making macroscopic and transparent randomly oriented/highly aligned carbon nanotubes thin films and transistor devices [325]. The film can be formed by using stock solutions of known concentrations. Vacuum filtration of SWNT suspension creates a concentration gradient due to the fluid velocity across the membrane [326]. With appropriate bulk solution concentration and fluid velocity, one can form either isotropic or highly oriented nanotube films [326]. The CNT network is formed as the filtration action elevates



CNT concentration near the membrane [327, 328]. While vacuum filtration has been used, in general, to make randomly oriented bucky papers, recent work by our group has demonstrated the isotropic-nematic transition of semiconducting nanotube films at ultra-low concentrations than what was thought to be achievable [326]. These semiconducting nanotube films are finding applications as thin film transistors with high mobility and ON/OFF ratio's [326], nanotube liquid crystal elastomer based light-driven actuators [329] and as chemical and biological sensors as presented in this thesis. Our films were very low concentrations (1–6  $\mu\text{g}$ ) and most of our films were isotropic with 2–6  $\mu\text{g}$  sample concentrations, partially transitioning into the nematic domains [326]. Also, the nanotube network in these films are mostly single layers laying on the substrate as shown in the scanning electron microscope (SEM) image in Figure 21 (D and E).

Based on the solvents used and CNT solution concentration, different network structures of nanotubes can be achieved, isotropic to highly oriented nematic, Figure 21 (D and E). High weight percentage ( $5 \times 10^{-5}$  wt-%) CNT solutions suspended in aqueous surfactant solutions can produce networks with nematic domains and at lower concentration ( $2 \times 10^{-6}$  wt-%) uniform isotropic network of CNT forms [326]. In this research our interest is in the ultra-thin, single layer, continues isotropic semiconducting SWNT-networks. Our objective is to have a uniform conductive network that exposes all the nanotubes on the surface and minimizes the current flow of under layers. In this section we will review the protocol for making the optimum ultra-

thin CNT film that has been used for the experiments of this thesis, unless specified otherwise.

To form a CNT thin network films, an in-house vacuum filtration system was used, Figure 21 (A). First a carbon nanotube source is acquired, in this case a 99% weight, IsoNanotubes-Semiconducting single wall carbon nanotube mixture was purchased from NanoIntegris Inc. (Menlo Park, CA). Nanotubes are listed at 1.2-1.7 nm diameter (1.4 nm mean diameter) and 300 nm to 5 microns length ( $\sim 1 \mu\text{m}$  mean length). Nanotubes were suspended in an aqueous surfactant solution at  $0.01 \text{ mg mL}^{-1}$  and used as received. Dilutions of CNT suspension were prepared. For example, for preparing a  $2 \times 10^{-6}$  wt-% film, 200  $\mu\text{L}$  of the stock solution, 2  $\mu\text{g}$  of CNT, was added to 85 mL DI water and  $\sim 15 \text{ mL}$  of 1% wt/v sodium dodecyl Sulfate (SDS) (sigma-Aldrich, Cat. No. 436143) to achieve 2  $\mu\text{g}/100 \text{ mL}$  concentration. Prepared solution was sonicated for 15 minutes. The 100 ml solution is then vacuum filtered over a nitrocellulose membrane, 0.05  $\mu\text{m}$  pore size and 90 mm diameter (Millipore, Cat. No. VMWP09025), then rinsed with 25 mL of isopropanol and 300 mL of water. This method self-regulates the deposition rate of nanotubes on the membrane to produce an evenly distributed network [326], Figure 21 (B). The network is then pressed onto a 4 inch (100 mm diameter) silicon wafer, 500  $\mu\text{m}$  thick, with dry oxidized layer (300 nm thickness), Purewafer Inc., for 30 minutes. Next the wafer is transferred onto an acetone vapor bath which dissolves the membrane, leaving behind the CNT film attached on the wafer. After this step CNT film transfers onto the Si wafer, Figure 21 (C). Next the wafer with the film on top is rinsed in liquid acetone and methanol baths

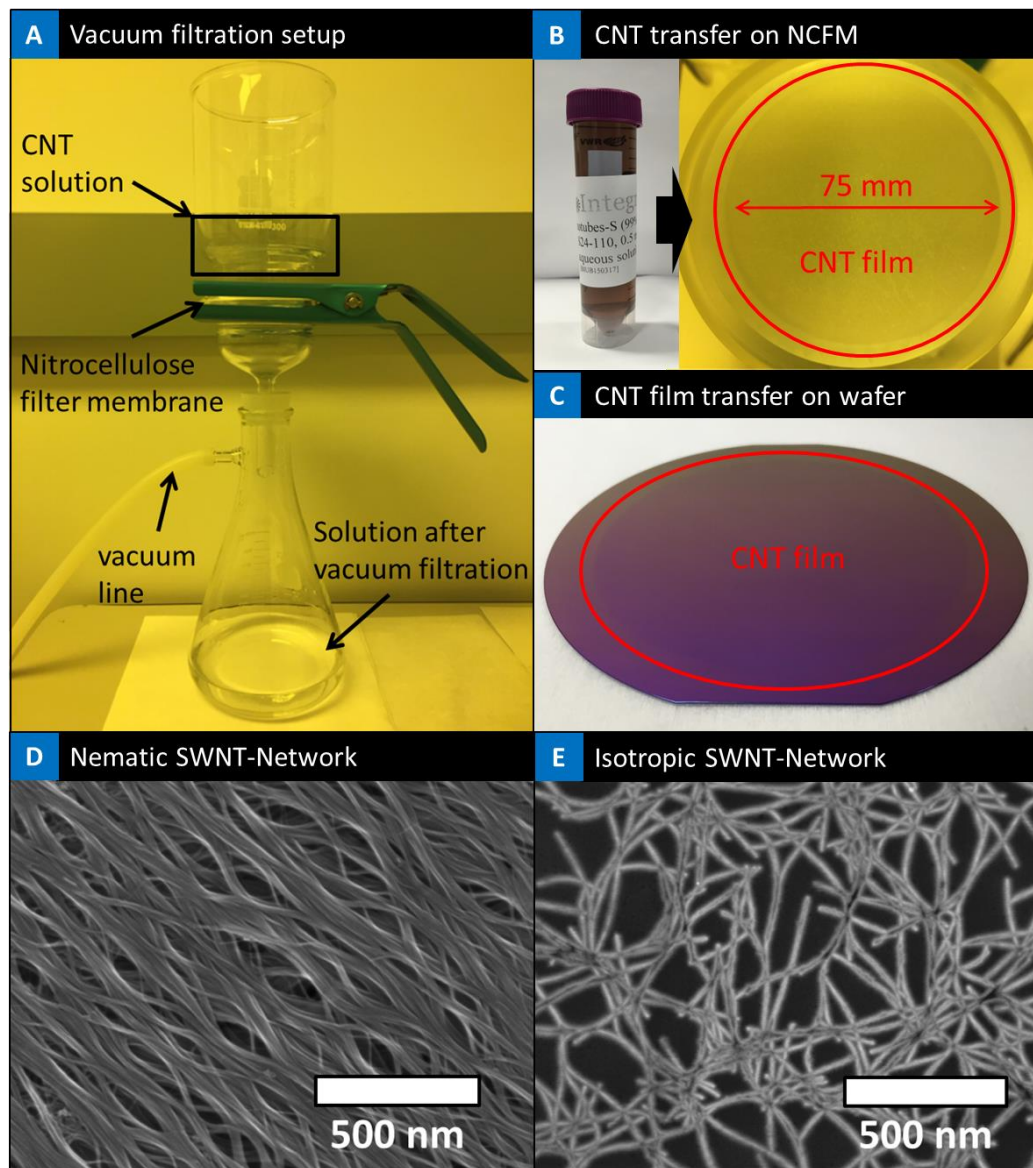


**Figure 21.** CNT film fabrication process. (A) Vacuum filtration setup, (B) CNT stock solution before dilution, left side. CNT transferred onto nitrocellulose filter membrane (NCFM) after vacuum filtration (red circle), right side. CNT film diameter after filtration = 75 mm. (C) Shows the CNT film transferred onto 4" Si/SiO<sub>2</sub> wafer after acetone vapor bath step, red circle. SEM images (D and E) showing the structure of two different CNT films in the nano-scale on Si/SiO<sub>2</sub> wafer after the completion of CNT film fabrication process. (D) Shows a nematic and (E) Isotropic CNT film network.

for 15 minutes each. Finally the CNT film suspended on silicon wafer is placed in DI water bath overnight. The rinsing and baths processes remove any residual filter membrane and remaining surfactant molecules. Similar protocol can be utilized processing CNT suspended in organic solvent solutions (i.e. ethanol, and isopropanol).

For simplicity, from here on in this thesis the concentration of CNT used in each film will be referred to as the total CNT mass used in that CNT film, as the area of the film is constant throughout at  $4418 \text{ mm}^2$ ,  $d = 75 \text{ mm}$ , the only varying component is the CNT mass. For example the CNT film described in the protocol in this section would be referred to as a  $2 \text{ }\mu\text{g}$  CNT film, since the total CNT mass making the film is  $2 \text{ }\mu\text{g}$ . The area of the CNT film is related to the dimensions of the filter membrane,  $90 \text{ mm}$  diameter, that capture the nanotubes during the vacuum filtration process. As the filtration setup fixture covers the edges of the membrane, the actual diameter of the active area of filter membrane capturing the nanotubes is  $75 \text{ mm}$ , Figure 21 (B), which is a constant and fixed for all CNT film samples described in this thesis.

### 3.1.2. CLEAN ROOM PROCESSING

The silicon wafer with the CNT film on top is next taken to microfabrication cleanroom facility, University of Louisville Micro/Nano Technology Center, to be further processed to fabricate CNT micro-array devices, illustrated in Figure 20. The microfabrication process consists of patterning the CNT film, depositing metal electrode, and covering the metal electrodes with photoresist polymer, Figure 22. In the case of the back gated CNT-FET, an additional step is added to etch a window through

the SiO<sub>2</sub> into the body of a doped Si substrate. The silicon wafers used for back gated devices were similar to all other wafers used here, in addition they were p-type boron doped, < 0.005 resistivity.

Patterning of the CNT film, electrodes, and insulating layer are done by photolithography in a Class 100 cleanroom. SC1813 photoresist is used to mask the nanotube film areas needed for the device elements. Table 3 presents the specific setting at which SC1813 photoresist is spun on the wafer using a standard spin-Coating system. Next the sample is soft baked for 60 seconds at 90 °C before getting exposed to

**Table 3.** Spin-Coater setting for SC1813 photoresist.

<u>Step</u>	<u>Ramp(RPM/s)</u>	<u>Speed(RPM)</u>	<u>Time(s)</u>
1	100 RPM/s	450 RPM	2s
2	1000 RPM/s	4140 RPM	10s
3	1000 RPM/s	0 RPM	0s

UV light (10 mW/cm<sup>2</sup> at 365 nm) on a mask aligner for 8 seconds. The wafer is then developed in MF-319 until excess photoresist has been removed entirely, exposing parts of the CNT film.

Exposed nanotubes are etched away in a march reactive ion etcher for 90 s at 200 W power with oxygen plasma. The excess nanotubes are removed and wafer is rinsed and cleaned off the photoresist using acetone, methanol, and DI water. After drying the wafer, SC1827 photoresist is again used to mask the electrode patterns in the same fashion as above. Electrodes consist of a 15 nm Ni adhesion layer and a 90 nm Au

layer, and are deposited by sputtering in a Leskar PVD 75 system, 300 W DC power. The excess Au/Ni layer is lifted off in acetone bath. Next, to further improve the CNT film sheet resistance and CNT-metal contact resistance, wafers are annealed for 2 hours at 250 °C inside a vacuum oven. Lastly, devices are covered with SU8-2005, a 5 µm thick photopolymer layer. Table 4 shows the specific setting at which SU8-2005 photoresist is spun on the wafer using a standard spin-coating system. After this step

**Table 4.** Spin-Coater setting for SU8-2005 photoresist.

<u>Step</u>	<u>Ramp (RPM/s)</u>	<u>Spin Speed (RPM)</u>	<u>Time (s)</u>
1	100	500	10
2	300	3000	30
3	1000	0	0

wafer is soft baked for 4 minutes at 95 °C and then exposed in the mask aligner (10 mW/cm<sup>2</sup> at 365 nm) for 15 seconds. Post-exposure bake is done next, 4 minutes at 95 °C. The wafer is developed in SU-8 developer to remove excess photoresist. Lastly wafer is hard baked at 150 °C for 5 minutes. A window over each of the nanotube sensor elements is developed but the electrodes remain insulated beneath the SU8. Schematic in Figure 22 illustrates the device fabrication process from start to finish.

Series of wafer arrays were processed further by opening a window through the silicon dioxide into the p-type doped silicon body by a standard buffered oxide etch technique. This was done to analyze the CNT-FET characteristics of the CNT device through back-gating in addition to liquid gating the CNT device using an ionic buffer and the Ag/AgCl reference electrode.

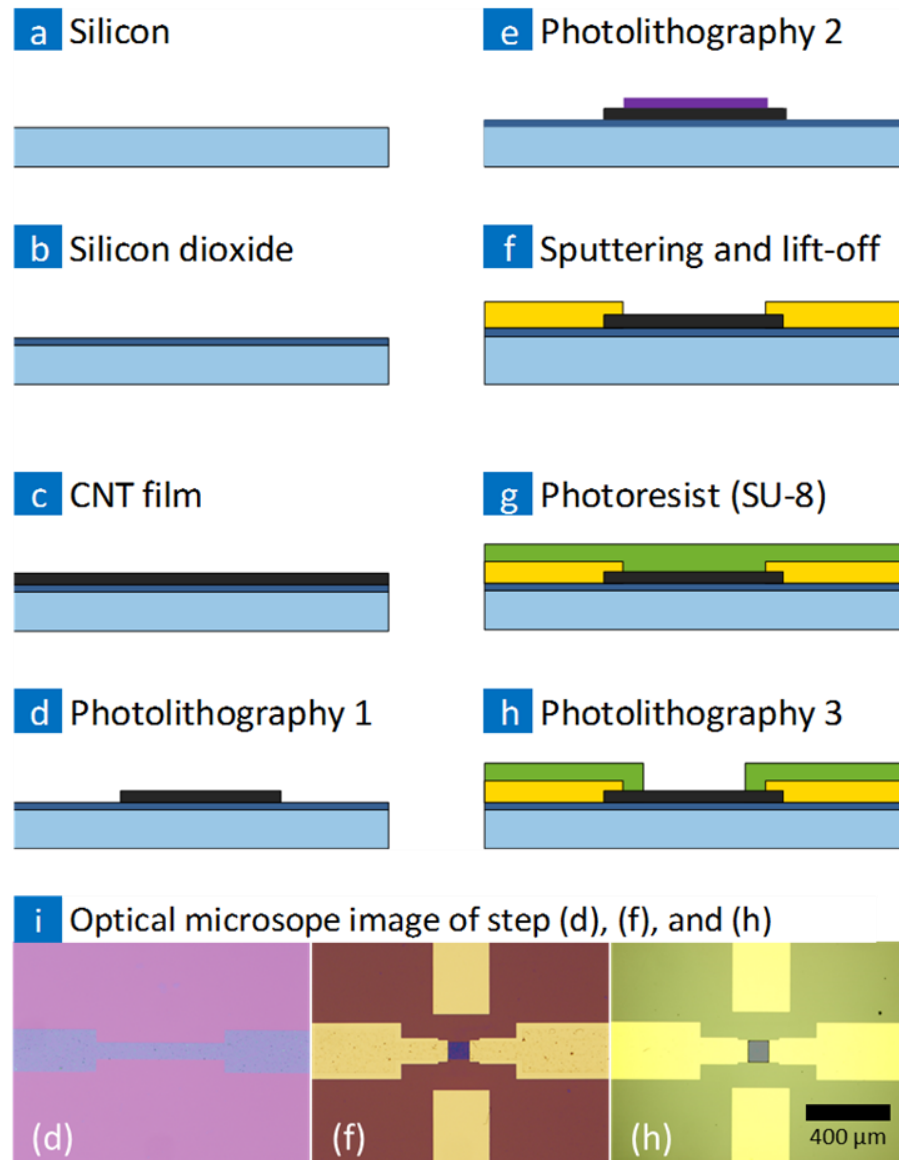


**Figure 22.** Micro-array device micro-fabrication process. (a) 4" silicon wafer. (b) Dry-thermal oxidation. (c) CNT film transfer. (d) First photolithography step followed by patterning CNT film, Reactive-ion etching. (e) Second photolithography for patterning electrodes. (f) Sputtering Ni/Au and lift-off, in yellow. (g) SU-8 photoresist is spun on top of wafer, in green. (h) Third photolithography step is performed to open window through SU-8 layer and expose the CNT network. (i) Shows an optical microscope image of devices at the end of photolithography 1 (d), sputtering left-off (f), and photolithography 3 (h) steps.

### 3.1.3. CNT DEVICE GENERATION I, II, AND III

Three fundamental factors that need to be addressed in designing the ideal sensor for detection and capture are: Settling time, sensitivity and selectivity. Settling time is the time it takes the analyte to diffuse to the CNT surface or for a cell to settle on the active area of a sensor. As the device active area increases, the settling time decreases resulting in a quicker detection of the target. With cells the size of the active area can have a direct impact on cell capture as an active area smaller than the cell itself,  $< 20\ \mu\text{m}$ , will eliminate the chance of cell-sensor interaction diverging settling time to infinity. The second factor, sensitivity is defined by the least number of targets to initiate a signal. In this case the number of targets needed to generate the same signal from the device increases with increasing device geometry, active area. As one can see, smaller device geometry will increase sensitivity; however, also increasing settling time which can be of a disadvantage. Lastly, selectivity, the ability to respond to a particular target without interference from others, is fundamental and if not addressed the other two factors lose their significance.

To accommodate for the objectives of this thesis, three generations of devices were designed and developed for small and large count cell capture and for protein detection, Figure 23. The nature of the fabrication of all three generations of CNT devices are similar as described in the previous section. The only difference is the dimensions to accommodate for settling time and sensitivity of the device with respect to the specified target.

Generation I is consisted of 60 devices on a single 4" wafer, Figure 23 (A). The



CNT window on these devices is 100X80  $\mu\text{m}$ . The parameters were optimized for single and small concentration cell capture. The device area was minimized to its limit with respect to cell size,  $\sim 20 \mu\text{m}$ , to increase sensitivity; however, cell concentration had to be increased for these devices to accommodate for settling time. Generation I devices were both used for cell capture and CNT film characterization. At these dimensions, generation I device can capture up to  $\sim 1\text{-}25$  cells on a single device.

Generation II CNT devices were an upgrade to generation I, Figure 23 (B). By optimizing the design, number of the devices increased to 76 per 4" wafer from 60. Additionally, the CNT window is significantly larger at 3000X3000  $\mu\text{m}$  to improve settling time and increase the number of cells that can interact with the active area. This device was specifically designed to accommodate for high cell count, for samples with high concentration of cells such as blood samples. In this design each device has the potential to interact with up to  $\sim 30,000$  cells at one time. However, such large increase in device geometry and active area impacts the sensitivity of the device. As a result even though more cells can be captured but more cells need to interact with the device to generate the same signal as generation I devices. This generation of devices was used for cell capture only with blood samples described in Chapter 9.

Generation III of CNT devices were designed with protein sensing as the main objective, Figure 23 (C). Proteins are much smaller in size than cells and diffuse through the solution and onto the active area much more efficiently, therefore they don't require a large sensing surface area. The CNT window was miniaturized

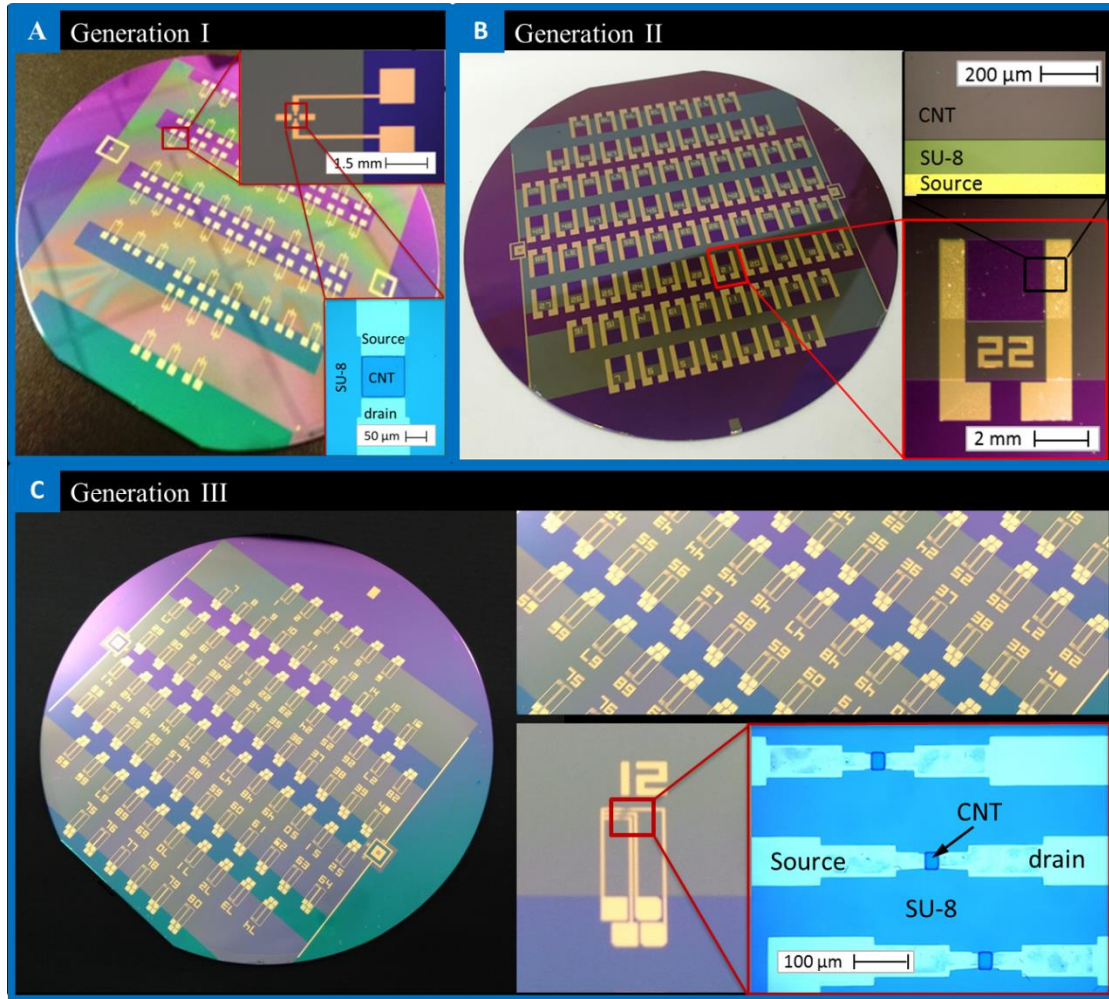


**Figure 23.** Generation I, II, and III of CNT devices, all are microfabricated on 4 inch silicon wafer. (A) 60 devices per wafer, CNT window on each device is 100X60 μm. (B) 76 devices per wafer, CNT window on each device is 3000X3000 μm. (C) 80 devices per wafer, three sensors per device for a total of 240 sensors. CNT window on each sensor is 20X20 μm.

accordingly to  $20 \times 20 \mu\text{m}$ . Each device is consisting of three sensors, sharing a common drain electrode. Overall, there are 80 devices per 4" wafer in this design with three sensors on each device, totaling in 240 sensors per 4" wafer. This generation of devices was used for protein sensing experiments presented in Chapter 5 and 6.

### 3.2. CNT ULTRA-THIN FILM

As discussed in Section 3.1.1, depending on the concentration of CNTs and the solvent type they are suspended in the quality and the structure of the CNT film can vary significantly, Figure 24. For the purposes of this thesis, CNTs were suspended in two types of solutions, organic solvent and surfactant base solution. It was observed that CNTs dispersion in micro scale is much better in aqueous surfactant solution, 1% wt-v sodium dodecyl sulfate (SDS), in comparison to organic solvents such as ethanol, isopropanol, and dimethyl-formamide.

In aqueous surfactant solution, as the concentration of CNT is increased, liquid crystal CNT starts to form in the solution. This phase translates itself into the CNT films, showing nucleation of nematic sites in the isotropic fabric of the films. These nematic regions grow with the increasing concentration of CNT till eventually converting the whole film, converting it from isotropic to nematic film. Nematic phase films show local alignments of CNTs. Ben King and Xiaoming Fan investigated the potential and the alignment of these nematic liquid crystal (LC) based CNT films for photomechanical and transistor applications [326, 329].

Vacuum filtration of nanotubes in aqueous surfactant solution formed nematic

domains on the filter membrane surface and exhibited local ordering [330]. Work done by our group on the similar nanotubes showed the transmittance versus sheet resistance measurements of such films resulted in optical to dc conductivity of  $\sigma_{\text{opt}}/\sigma_{\text{dc}} = 9.01$  indicative of purely semiconducting nanotube liquid crystal network. High  $I_{\text{on}}/I_{\text{off}}$  ratios from 10–19,800 and electron mobility values  $\mu_e = 0.3\text{--}78.8 \text{ cm}^2 (\text{V-s})^{-1}$ , hole mobility values  $\mu_h = 0.4\text{--}287 \text{ cm}^2 (\text{V-s})^{-1}$  were reported. High  $I_{\text{on}}/I_{\text{off}}$  ratios were observed at low order parameters and film mass. A Schottky barrier transistor model was consistent with the observed transistor characteristics here. Electron and hole mobilities were seen to increase with order parameters and carbon nanotube mass fractions. A fundamental tradeoff between decreasing on/off ratio and increasing mobility with increasing nanotube film mass and order parameter is therefore concluded. Increase in order parameters of nanotubes liquid crystals improved the electronic transport properties as witnessed by the increase in  $\sigma_{\text{dc}}/\sigma_{\text{opt}}$  values on macroscopic films and high mobilities in microscopic transistors. Fan *et al.* using these LC-CNT films in polymer composite demonstrated a unique and reversible photomechanical response using near infra-red light.

LC-CNTs have great potential in soft photochromic actuation, energy conversion and photo-origami applications to name a few, but they are also consisted of relatively thick ropes of multiple CNTs in multi-layer fabric network. For the purposes of this thesis, we are interested in maximizing the exposure of CNT surface and minimizing conduction channels under the surface, for higher efficiency in cell and protein capture and sensing. In this situation, we are interested in very thin, single later,

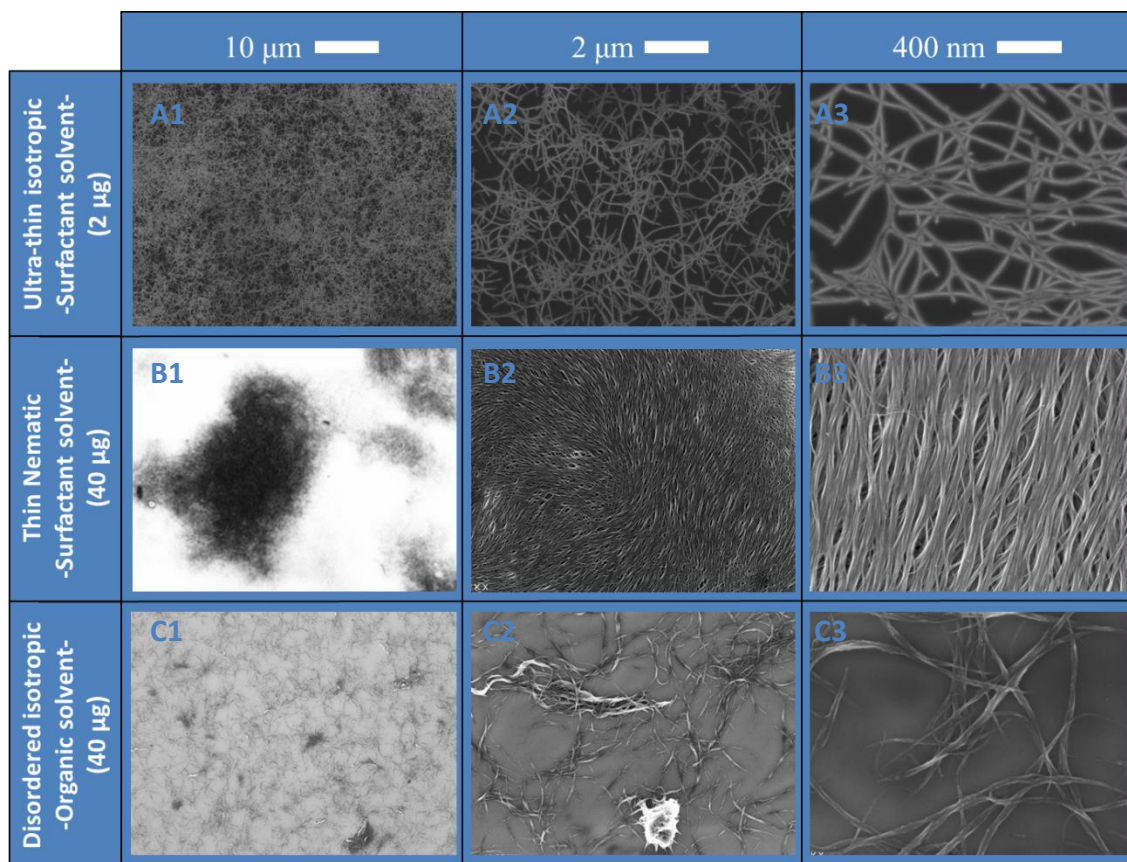


**Figure 24.** SEM images of three different unique CNT film structure, (A) ultra-thin isotropic, (B) thin nematic, and (C) disordered isotropic. (A and B) are products of CNT suspended in aqueous surfactant solutions. CNT suspended in these solution produce an ultra-thin CNT films at very low concentration (A), i.e. 2  $\mu\text{g}$ . These films are ~10-50 nm thick and uniform. Increasing the concentration of CNT in aqueous surfactant solution results in a much different nematic CNT films. Nematic nucleation of CNT films occur as concentration increases, dark region of (B1). Resulting in locally aligned CNT on the film (B2 and B3). CNT films made from CNT suspended in organic solvents are very much different in micro and nano scale. Large mass of CNTs in these films are trapped in tangled ropes that can get as thick as 1  $\mu\text{m}$  or larger, (C2). As a result of this effect, much greater CNT mass is required to achieve a uniformly conductive film, i.e. 40  $\mu\text{g}$  vs. only 2  $\mu\text{g}$  for aqueous solution suspension. As a result, great fraction of these nanotubes are hidden and not exposed to the environment.

uniform, continuous, and conductive film that expose the maximum CNT surface area. Number of CNT films were made and studied at different concentrations and using different solvents, as summarized in Figure 24, to finally achieve the optimum ultra-thin CNT films used for the purposes of this thesis.

Ultra-thin films were achieved using a very small concentration of CNT suspended in aqueous surfactant solution that were vacuum filtered on a membrane to generate an almost single layer CNT film, Figure 24, as described in Section 3.1.1. These films were consistent in their uniformity, thickness less than 50 nm, in comparison to films achieved from organic solvent solution that have tangled CNT ropes in large masses with varying film thickness, from 100 to over 1000 nm. In the case of CNT suspended in organic solvent, because majority of the CNT mass is trapped in tangled ropes, much larger CNT mass is required,  $>40\text{ }\mu\text{g}$ , to achieve a conductive uniform film. Much more uniform and even, ultra-thin films were achieved with CNT suspended in aqueous surfactant solution at much lower concentration,  $2\text{ }\mu\text{g}$ , as shown in Figure 24. In the next section we will review the effect of different film concentrations from surfactant based CNT suspensions on final CNT device characteristics.

### 3.3. MEASUREMENT SETUP

In this section we will describe the platform on which all the electrical readings and characterizations were conducted on. The platform was set up on S-1160 Signatone probe station. Agilent 4156C Semiconductor Parameter Analyzer equipped with a custom LabVIEW interface was used for monitoring the sensors and data collection,

Figure 25 (A). Computer running the LabVIEW program connected to the parameter analyzer through a National Instruments card (PCI-GPIB), allowed for direct communication to the instrument. Three EM shielded triaxial cables connected the three SMU ports on the back of the parameter analyzer to each of the three micro probes stationed on the probe station. Each triaxle cable was converted to a coaxial cable using an EM shielded adaptor right before connecting to the probe to minimize noise. Each SMU port connected to an individual probe and was programmed to either apply a specified source and gate voltage (DC voltages) or read the drain current, Figure 25 (A). Bias voltage was applied through the source probe electrode and the source-drain current,  $I_{SD}$ , was recorded for the duration of the test using the Agilent 4156C parameter analyzer. The accuracy of the semiconductor parameter analyzer is 1 femtoamps (fA), while most of the readings taken from the CNT devices are in the nanoamps (nA) region suggesting a very sensitive and accurate level of signal collection. The entire probe station assembly is placed on an optical table that is vibration isolated using air on all four legs. A metal box covers the entire assembly to avoid electromagnetic interference. The non-dry samples with a sample droplet were maintained inside a humid changer, Figure 25 (B), which preserved humidity level of the chamber by  $H_2O$  soaked cotton balls carefully placed inside the petri dish, preventing the evaporation of the droplet sample during device functionalization and testing. The testing set up for devices with sample droplet is demonstrated in Figure 25 (C), showing the probes contacting the electrodes through an opening on a modified humid chamber and Ag/AgCl reference electrode applying gate voltage via the sample



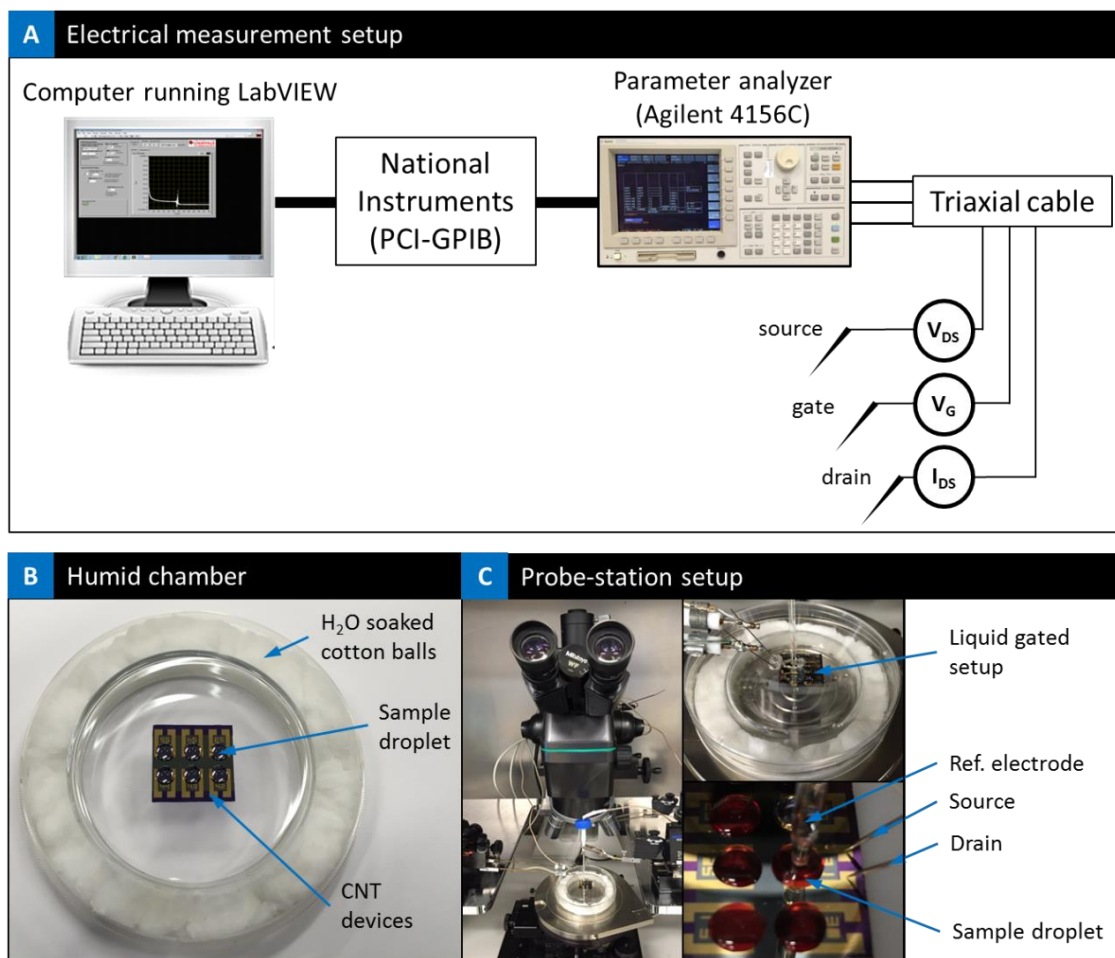


**Figure 25.** (A) Schematic demonstrates the electrical measurement setup. A DC bias voltage,  $V_{DS}$ , and gate voltage,  $V_G$ , was applied and the current  $I_{DS}$  passing through the drain was measured using the parameter analyzer while the LabVIEW program was used to control the parameters on the parameter analyzer and save the data to the computer. (B) Shows the humid chamber used to store devices with sample droplets during functionalization and testing to prevent the evaporation of the droplet. This was achieved by controlling the humidity inside the chamber using  $H_2O$  soaked cotton balls carefully placed on the outer edge of the chamber. (C) Showing the probe-station setup, including the vibration isolated base, optical microscope, and the three probes. This set-up specifically demonstrates the platform for liquid gated testing, devices with sample droplets, using a modified humid chamber allowing probe access to the device.



droplet, liquid gating. Throughout the testing the devices were maintained inside a humidified chamber to prevent evaporation of the sample droplet. This set up and the ability of parameter analyzer to apply spectrum of voltages independently to each channel/probe and record output signal with great percisioun and accuracy allowed for collecting spectrom of data from the CNT devices including resistance, current vs. time with and without gating,  $I_{DS}$  vs.  $V_{DS}$ , and  $I_{DS}$  vs.  $V_G$  voltage sweeps namely.

For all the conductance readings presented in Chapters 5, 6, 7, 8, and 9, 100 mV DC bias was applied to the drain-source electrods, while 0 V was applied via the Ag/AgCl refrance electrode. The film resistance data presented in this chapter were a simple two terminal readings, via 100 mV source-drain bias.

### 3.4. DEVICE CHARACTERIZATION

In this section we will review the characteristics of carbon nanotubes used for this thesis, CNT films, and finally the CNT micro-array devices.

#### 3.4.1. CHARACTERIZATION OF CARBON NANOTUBES (CNT)

To better undrestand the fundamentals of the devices, series of characterizations were done on the underlying carbon nanotubes used for fabricating the CNT devices here. Initially the Iso-Semiconducting Nanointegris carbone nanotubes were first studied by AFM, SEM, Raman spectroscopy, and Spectrophotometry . In these studies size, shape, quality, absorbanse, transmittance, and the band gap of the CNT were investigated.

The highly purified 99% wt ISO-Semiconducting single wall carbon nanotubes

purchased from NanoIntegris Inc. were analyzed by spectrophotometry. The optical absorbance and transmittance results are illustrated in Figure 26 (A and B). The transmittance is modulated from 0% to 29% at 400 nm and continues to rise to its peak of 50% at 620 nm wavelength Figure 26 (A). These results correlates with previous findings of similar nanotubes [325]. Absorbance diagram, Figure 26 (B) shows the transition regions for semiconducting nanotubes, S33 transition between ~450-630 nm. and S22 transition between ~900-1000 nm, confirming the semiconducting nature of the nanotubes as reported by the manufacturer and aligned with past reports [331].

Figure 26 (C) presents the Raman spectroscopic micrograph of the nanotube network suggesting a very large G band ( $1590\text{ cm}^{-1}$ ), in plane vibration of  $\text{SP}^2$  bonds; small D band ( $1340\text{ cm}^{-1}$ ), defective band, and large 2D band ( $2673\text{ cm}^{-1}$ ), twice D band and also known as G' band in graphene. This suggests extremely low amorphous carbon content. Further, we also measured the  $I_G/I_D$  ratio for several networks, measured  $I_G/I_D \sim 30$  suggesting a low density of defects and suitable for high-quality sensing applications. Radial breathing mode (RBM) mode was observed at  $\omega_r=174\text{ cm}^{-1}$ , interaction of the CNT diameter with the laser. Using the simple formula for calculating CNT diameter,  $d_{\text{CNT}} = 248 / \omega_{\text{RBM}}$ , we calculated the diameter of these nanotubes to be ~1.4 nm, similar to what was reported by the manufacturer. The Iso-semiconducting nanotubes had iodine as specified by the manufacturer (5% by mass using neutron activation analysis) in the form of iodixanol. This was observed in the shift in radial RBM mode  $\omega_r=174\text{ cm}^{-1}$  suggesting iodine doped nanotubes due to poly iodide ions or  $\text{I}_3^-$  and  $\text{I}_5^-$  in the RBM mode at the same excitation wavelength [332]. The

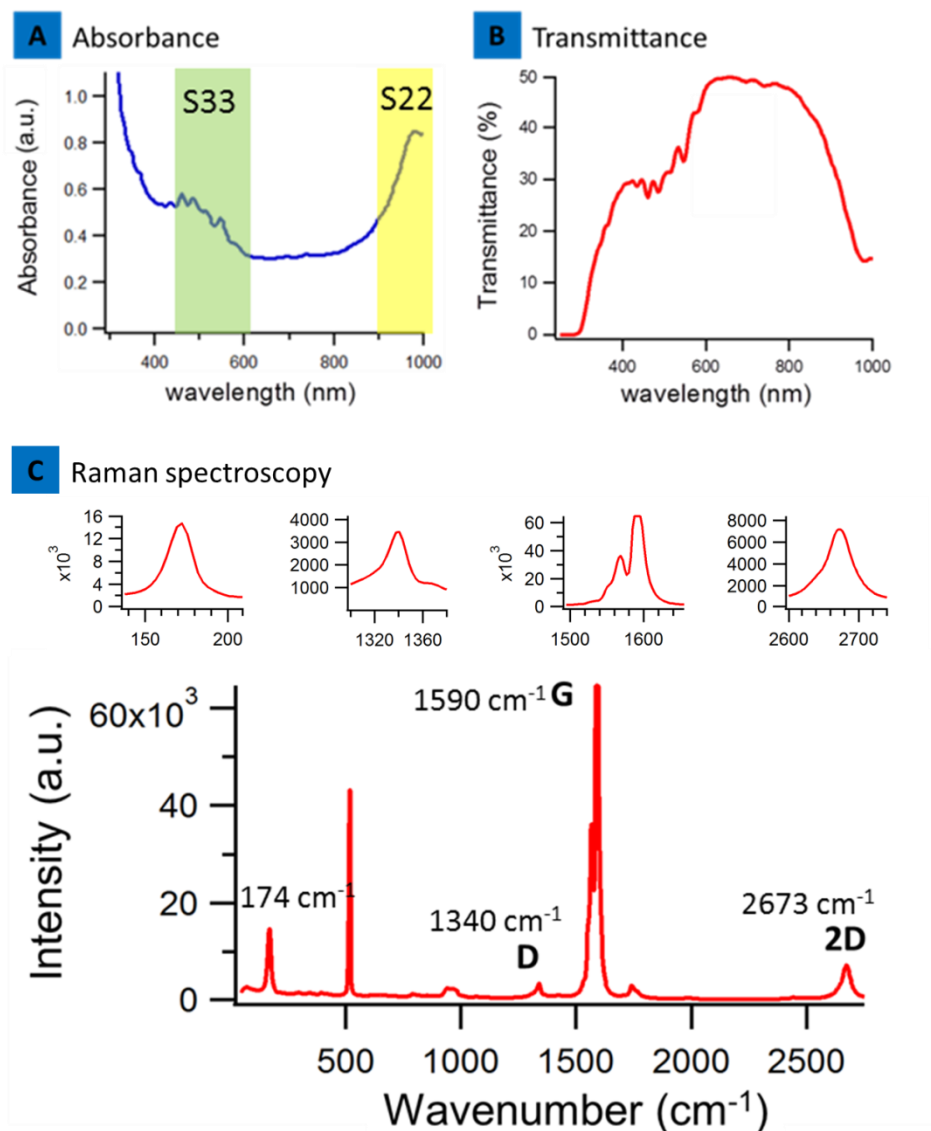


**Figure 26.** (A) Optical absorbance of Iso-semiconducting SWNT showing the S33 (~450-630 nm) and S22 (~900-1000 nm) transition peaks. (B) Transmittance of Iso-Semiconducting SWNT in aqueous surfactant solution. (C) Raman spectrum of Iso-Semiconducting SWNT film on silicon wafer showing a large G band, small D band and 2D band. The  $I_G/I_D \sim 30$  was observed in these nanotubes.

iodine also decreased the tangential mode to  $1590\text{ cm}^{-1}$  in these samples as compared to pristine nanotube samples ( $1593\text{ cm}^{-1}$ ) in line with past reports [333].

Figure 27 shows the SEM and AFM image of the ultra-thin ISO-Semiconducting SWNT network ( $2\text{ }\mu\text{g}$  CNT film). These SWNTs are listed to have diameter of 1.2-1.7 nm on supplier's datasheet. This narrow diameter distribution, results in SWNTs to often bundle up in form of crystalline 'ropes' in which single tubes are held together by van der Waals interaction as presented in AFM. This effect is vivid on AFM image, as the nanotubes bundles have a width ranging from 10 to 50 nm, Figure 27 (B), and height of  $\sim 4$  to 8 nm, Figure 27 (C). This indicates that SWNTs bundling to ropes effect is present here. Based on the CNT dimensions we can estimate approximately 20 nanotubes per bundle on average. Additionally, knowing the nanotube diameter we can calculate the bang gap of the nanotubes based on eqn. 1 presented in Chapter 2. For semiconducting nanotubes with diameter ranging from 1.2 to 1.7 nm, calculated bandgap ranges from  $\sim 0.4$  to  $0.6\text{ eV}$ .

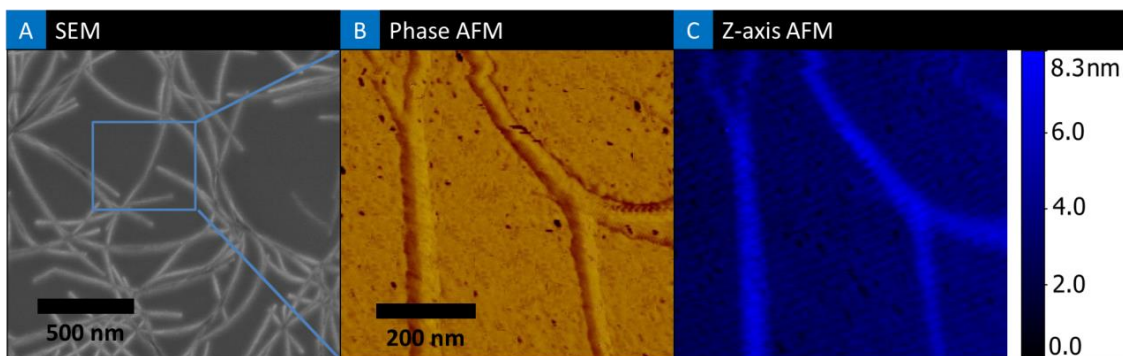


**Figure 27.** (A) SEM and (B and C) AFM images of ultra-thin SWNT network.

### 3.4.2. DEVICE AND THIN FILM CHARACTERIZATION

Following CNT devices fabrication, numbers of devices were prepared using different CNT concentration films on generation I device platform with source and drain electrode window of 100 by 80  $\mu\text{m}$ . These devices were then investigated for their electrical properties based on imbedded CNT films. The properties of devices made with nematic films are presented in Figure 28. Properties for devices fabricated with ultra-thin isotropic films are presented in Figure 29. In these two panels, SEM image of the devices made from different nanotube film concentrations are shown. In these images CNT film bridging the source and drain electrodes are shown, in addition the high resolution image of the CNT network of each film is also presented. CNT devices were made with two, nematic, and four, isotropic, CNT films at different concentrations, devices were tested for their electrical properties before and after annealing. It is observed that as the concentration increased so did the network density. For ultra-thin films, at the film concentration of  $\sim 1 \mu\text{g}$ , the nanotube-nanotube contacts were not established at some points, and this is reflected in their high electrical resistance. For samples with higher concentrations, 2-6  $\mu\text{g}$ , uniform network density was observed. CNT devices based on nematic films had even lower device resistance as expected, since there are more conducting nanotubes bridging the electrodes. But these devices are not single layer and are consisted of multiple CNTs in rope form in multi-layer structure that are not of interest for the objectives of this thesis as described earlier. We, therefore, used 4 and 6  $\mu\text{g}$  films with more directional nanotubes for our studies in this thesis with optimized electrical properties. The film electrical resistance

before and after annealing was measured as presented in Figure 28 (B) and Figure 29 (B). Annealing at 250 °C decreased the resistance of the devices universally. It was observed that the decrease in electrical resistance of the device with annealing was directly related to the concentration of the nanotube films. Devices made with 1 µg films registered a larger decrease in electrical resistance of ~95%, compared to devices with larger film concentrations (~57% and ~47% decrease in resistance for 2 µg and 4 µg respectively). The large decrease in electrical resistance after annealing suggests healing and refining of nanotube network structure to enable stable electrical pathways associated with the device. Figure 28 (C) and Figure 29 (C) present the distribution of nanotube device resistance, for 14 and 58 devices, suggesting narrow distribution of network resistance in the  $10^6$ - $10^7$  Ω range, showing repeatability which is suitable for further sensing applications. Table 5 presents the summary of the 4 point probe (1 mm probe spacing) measurements for the sheet resistance before and after annealing and final device resistance. The average resistances after annealing for nematic films were  $1.77 \times 10^6$  Ω for 10 µg film and  $8.32 \times 10^4$  Ω for 40 µg. While the low concentrations (1 and 2 µg) yielded highly rarefied nanotubes and much higher decrease in electrical resistance as suggested with annealing, it was difficult to always get a conductance reading due to lack of connection between all the nanotubes in low concentration nanotube devices. Therefore, we optimized our devices for 4 and 6 µg nanotube films to provide stable network connectivity; these concentrations were used for all the studies henceforth presented unless specified otherwise.

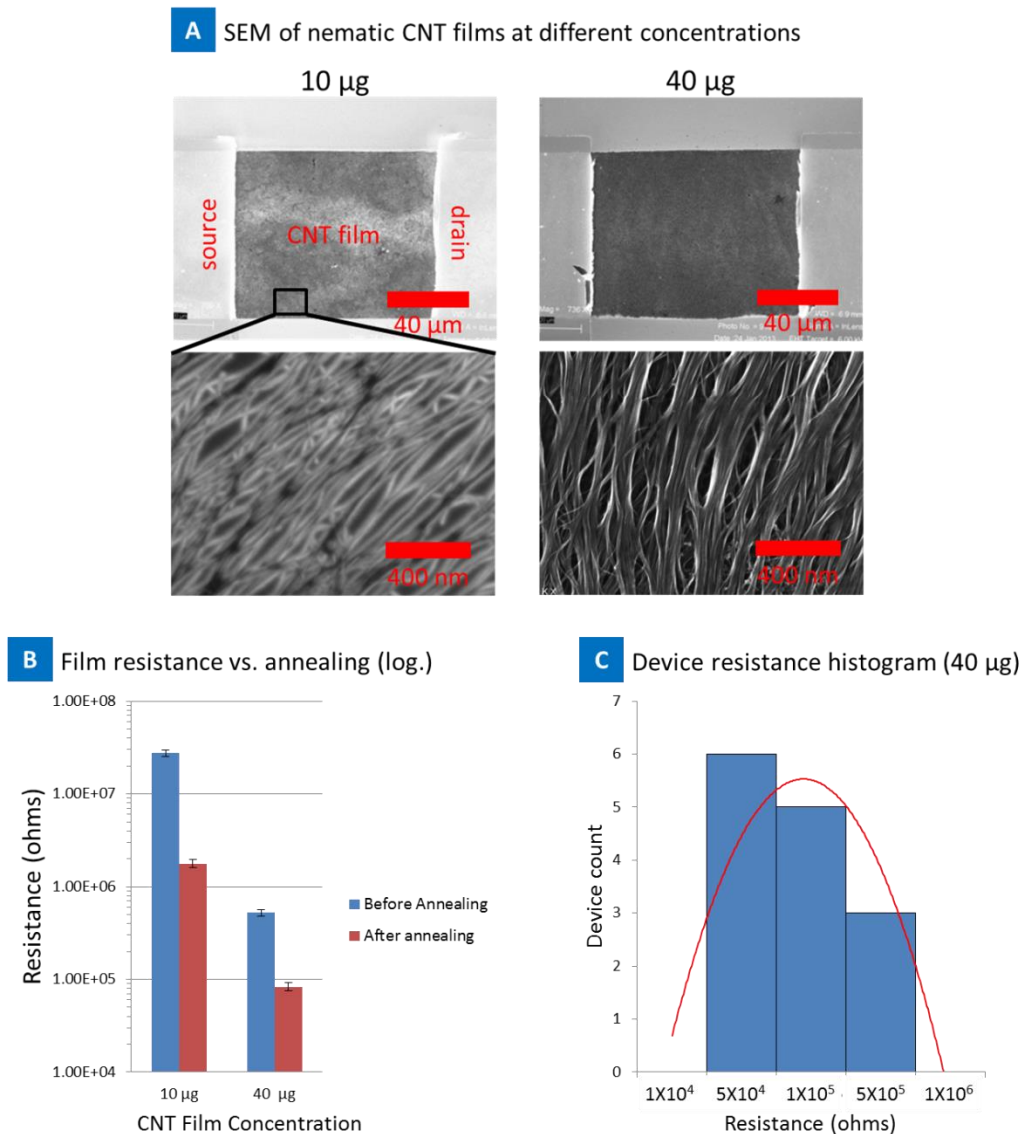


**Figure 28.** Electrical resistance of CNT devices fabricated from nematic films. (A) SEM image of the actual device fabricated from 10 and 40  $\mu\text{g}$  CNT films and their corresponding high resolution images of the CNT network; (B) film resistance before and after annealing at 250  $^{\circ}\text{C}$ ; (C) histogram suggesting high degree of control in device resistance over 14 devices.

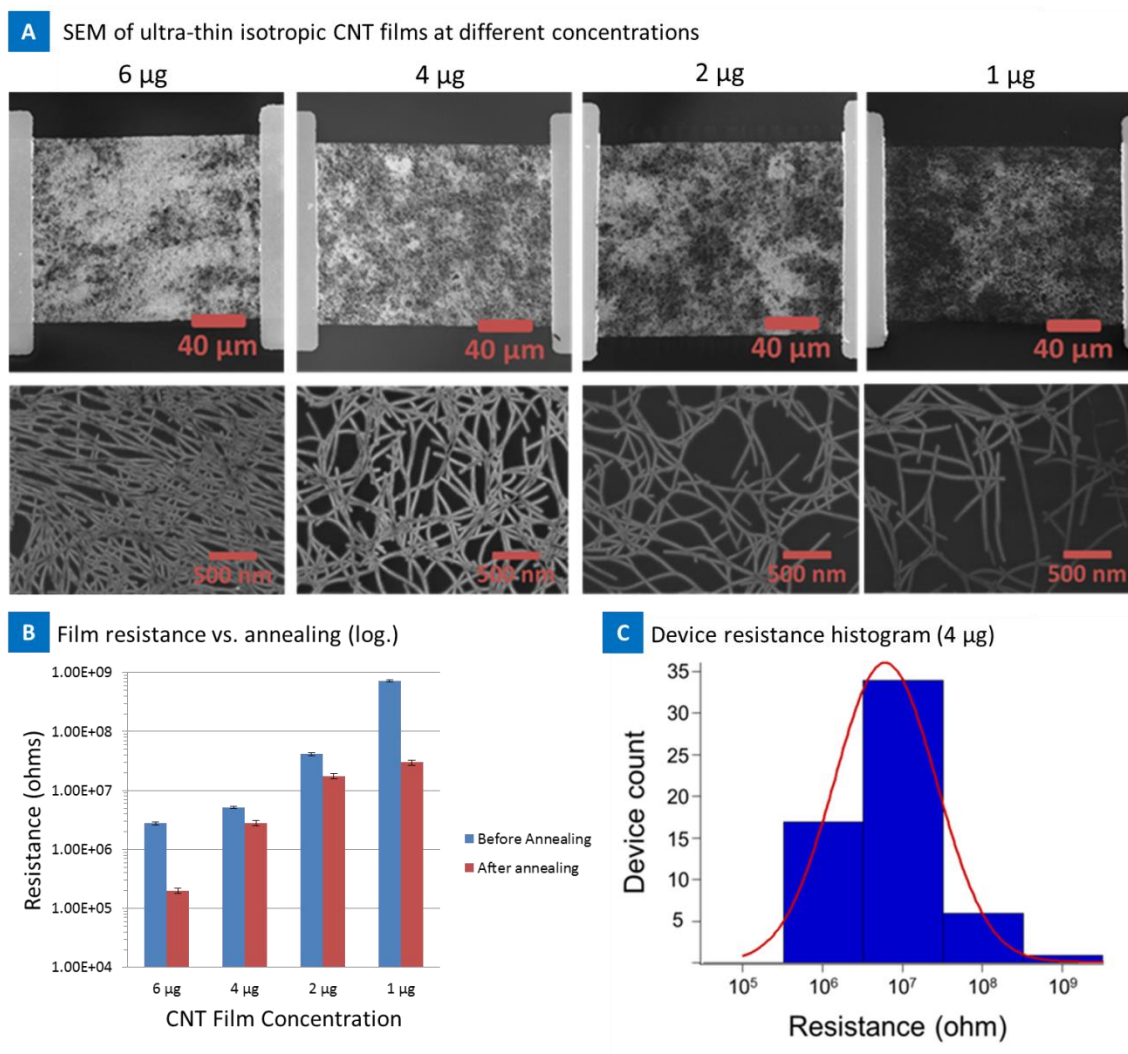


**Figure 29.** Electrical resistance of CNT devices fabricated from ultra-thin isotropic films. (A) SEM image of the actual device fabricated from 6, 4, 2, and 1  $\mu\text{g}$  CNT films and their corresponding high resolution images of the CNT network; (B) film resistance before and after annealing at 250  $^{\circ}\text{C}$ ; (C) histogram suggesting high degree of control in device resistance over 58 devices.



**Table 5.** Average film resistance summary

CNT Film Concentration	6 $\mu\text{g}$	4 $\mu\text{g}$	2 $\mu\text{g}$	1 $\mu\text{g}$
Sheet resistance before annealing ( $\Omega/\text{sq.}$ )	9.21E+06	4.16E+06	3.30E+07	5.82E+08
Sheet resistance after annealing ( $\Omega/\text{sq}$ )	6.66E+05	2.25E+06	1.41E+07	2.40E+07
CNT Film Resistance after annealing ( $\Omega$ )	2.00E+05	5.20E+06	4.12E+07	7.28E+08
% Drop In Resistance After Annealing	<b>92.76%</b>	<b>45.92%</b>	<b>57.38%</b>	<b>95.88%</b>

In a typical traditional FET sensor, there are conduction channels underneath the surface that give rise to a large background noise. Having only one conduction channel on a nanotube surface can raise the sensitivity even higher and increase the on-off ratio. This is why we have elected ultra-thin CNT film at 4-6  $\mu\text{g}$  levels for these studies.

### 3.4.3. PERCOLATION THEORY VS. CNT FILM MASS

Percolation theory studies the formation of conducting pathways in different dimensions, using objects of various geometries. In one model, a random array of long conducting sticks were used to study the formation of conducting channels across a material [334]. We utilized this variation of percolation theory to model the conductance of our arrays as a function of CNT film mass. Ultra-thin, uniform SWNTs films of varying densities have been prepared and fabricated into CNT devices. The film resistance is fit into percolation theory as a function of CNT mass.

Figure 29 shows SEM images of four different samples that have been prepared by filtering a 1, 2, 4, and 6  $\mu\text{g}$  total mass of CNT, respectively, through the filter membrane. Several features can be noted in these images. First, though not shown here, images taken at various spots along the film, sometimes separated by as much as 5 cm,

show no noticeable difference in film characteristics, indicative of the spatial uniformity of the film. Also, the nanotubes, at these concentrations, appear randomly oriented with no preferential directions, allowing application of the percolation theory of a random distribution of conducting “sticks”. Notice, however, that in these networks, each “stick” is actually a small bundle of nanotubes, because nanotubes tend to be attracted to each other through van der Waals interactions as discussed in Section 2.1. We count each bundle of nanotubes as one “conducting stick” (CS). Percolation theory requires only that the CS has a length that is much greater than its diameter (the aspect ratio of the bundles is still of order 100). By manually counting the number of CS present in several images, we arrive at the average density (CS per area) for each CNT film mass. CNT film with  $M = 1 \mu\text{g}$  is  $5 \text{ CS}/\mu\text{m}^2$ ,  $M = 2 \mu\text{g}$  is  $11 \text{ CS}/\mu\text{m}^2$ , and  $M = 4 \mu\text{g}$  is  $21 \text{ CS}/\mu\text{m}^2$ . As expected, the CS density is proportional to the mass of CNT applied to the filter; i.e., if more nanotubes are used, a denser film results. Using this fact, the mass of CNT used to make each film can be directly converted into a CS density, using the conversion factor of  $5 \text{ CS}/\mu\text{m}^2 \mu\text{g}$ .

Before measuring the DC conductivity of the CNT film in the percolation region, we used generation 1, 2, and 3 devices to verify that all resistances measured were due to the CNT in the network and not due to the gold/CNT interface at the contacts. To measure the contact resistance, same CNT film mass,  $2 \mu\text{g}$ , was used to fabricate all three generation of devices, allowing for variation only in the separation distance between the contacts (width between contacts was not held constant). The

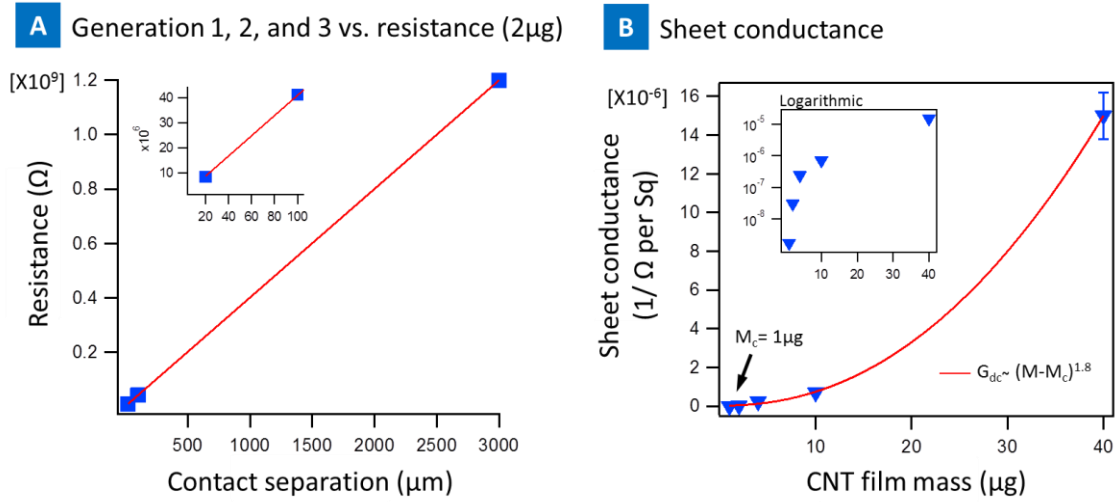


**Figure 30.** (A) Shows the measured CNT film resistance versus the source drain distance of generation 1, 2, and 3 CNT devices, for films of the same density. All three generations have unique constant separation distance, generation 1: 100  $\mu$ m, generation 2: 3000  $\mu$ m, and generation 3: 20  $\mu$ m. inner box shows a zoom in on generation 1 and 3. (B) Demonstrates the sheet conductance versus CNT film mass in  $\mu$ g, inner box shows the data in logarithmic form.

resistance between contacts of all three devices was then measured, and plots made of the resistance vs the contact separation (generation 1: 100  $\mu$ m, generation 2: 3000  $\mu$ m, and generation 3: 20  $\mu$ m); a typical plot is shown on Figure 30 (A). The plot shows that the resistance of the network at 100  $\mu$ m channel length, generation 1, is  $\sim 5$  times larger than the 20  $\mu$ m channel length, generation 3, and  $\sim 29$  times smaller than 3000  $\mu$ m, generation 2. This linear relationship indicates that the resistance is dominated by the CNT film, with only small contributions from the nickel-gold/CNT interface at the contacts.

For the percolation study, several CNT devices were made on identical CNT films, varying only the CNT mass (and therefore the CNT density), similar to what is presented on Figure 28 and Figure 29. CNT devices with identical metal contacts were prepared to produce a CNT channel 80  $\mu\text{m}$  in width (W) and 100  $\mu\text{m}$  in length (L), generation 1 design. A standard two-probe measurement was made to measure the DC resistance (R) between the two metal contacts. To be comparable with other works, resistance was converted to sheet resistance ( $R_{\square}$ ), which is defined as  $R_{\square} = R(W/L)$ . Figure 30 (B) shows a plot of sheet conductance G (defined as  $1/R_{\square}$ ) vs CNT film mass (proportional to CNT film density).

Standard percolation theory predicts that the density dependence on the conductivity is given by

$$\sigma \propto (N - N_c)^{\alpha} \quad (8)$$

Here,  $\sigma$  refers to the conductivity in three dimensions and the sheet conductance G in two dimensions, N is the CS density, and  $N_c$  is the critical density corresponding to the percolation threshold. For the random distribution of the CS model [335], the critical density is given by

$$l\sqrt{\pi N_c} = 4.236 \quad (9)$$

Here,  $l$  is the length of the CS. Equation 8 holds close to the transition; while well above the critical density, one expects to enter a region of linear dependence on density.

The critical exponent,  $\alpha$ , depends only on the dimensionality of the space; for a film in two dimensions, theory predicts  $\alpha = 1.33$ , while in three dimensions  $\alpha = 1.94$  [336].

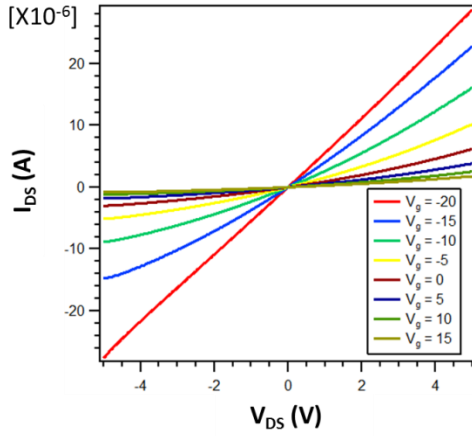
The Figure 30 (B) shows a fit of eqn. 8 to our data in the percolation region, using a critical volume value of 1  $\mu\text{g}$ . The best fit to our data yields an experimentally measured value of  $\alpha = 1.8$ , which is close to but somewhat higher than theory predicts. There are several reasons why the measured and theoretical values would differ. First, critical exponents hold in the limit that one approaches the critical point. Since our measurement must encompass a range of points around the critical point, the exponent is not guaranteed to be exactly  $4/3$ . In fact, as we approach the critical point, including fewer and fewer points in our fit, the exponent converges to  $4/3$ . Discrepancies may also arise because our CNT film is not perfectly two-dimensional, and one could be observing some crossover into three dimensions, where the critical exponent ( $\alpha$ ) is 1.94. Additionally, the channel width varies from different device generations. Theory also does not account for the fact that all the CNT used here are semiconducting. The resistance of metallic-metallic tube interconnects has been shown to be less than the resistance of semiconducting junctions, due to the presence of a Schottky barrier [337]. In this case conductance is limited by the Schottky barriers. However, as the network density increases, more CNT pathways are formed, yielding an increase in conduction with film density that is not accounted for by standard theory. Prior experiments on CNT found  $\alpha$  values of 1.2 [338], and 1.3 [339] for three dimensional CNT composite films and 1.5 [334] for two dimensional ultra-thin film. These previous findings are substantially different compared to theoretical prediction of  $\alpha = 1.33$ , in two

dimensions, and  $\alpha = 1.94$  in three dimensions. It is important to note that all the previous studies used a mixture of metallic and semiconducting CNT. For the CS model of a random distribution of sticks, theory predicts the value of the critical density  $N_c$ , given as eqn. 9. Assuming an average nanotube length of  $1\ \mu\text{m}$  (verified by SEM images and manufacturers data sheet), we calculate a theoretical critical density of  $5.7\ \text{CS}/\mu\text{m}^2$ , using eqn. 9. Using the data obtain by counting the SEM images of films made at the critical volume of  $1\ \mu\text{g}$ , we measure a density of  $5\ \text{CS}/\mu\text{m}^2$  at the critical point. The discrepancy between the data and theory can be accounted for by counting errors, or by nanotubes on the film that are not resolvable by the SEM, thus causing undercounting of the CS density.

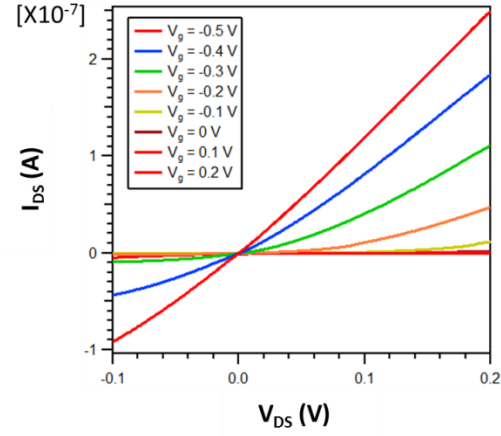
Furthermore we can verify our formula for calculating the number of “conducting sticks” (CS) per unit of area as function of CNT film mass. This ratio was presented earlier in this section as  $5\ \text{CS}/\mu\text{m}^2\ \mu\text{g}$ . One can calculate the number of CS and thereby number of CNTs per unit of area. Earlier in Section 3.4.1 we explained how SWNTs come together to bundle and form ropes and based on nanotube dimensions and our observations under AFM we estimated each rope, CS as referred to here, to be made up of  $\sim 20$  nanotubes on average. Accordingly, we are able to back calculating the film mass of the film based on the number of estimated CNTs observed under SEM and compare it to the actual CNT mass used to make the film experimentally.

The weight of any SWNT ( $W_{\text{sw}}$ ) of diameter  $d$  and length  $L$  can be calculated from the surface area of the graphene sheet [340]:

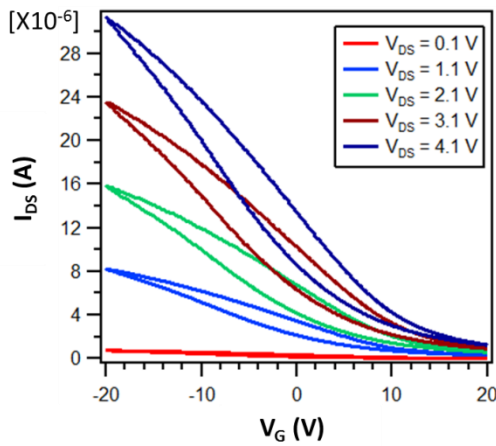
**A** P-type silicon back-gate



**B** Ag/AgCl reference electrode gate



**C** P-type silicon back-gate



**D** Ag/AgCl reference electrode gate

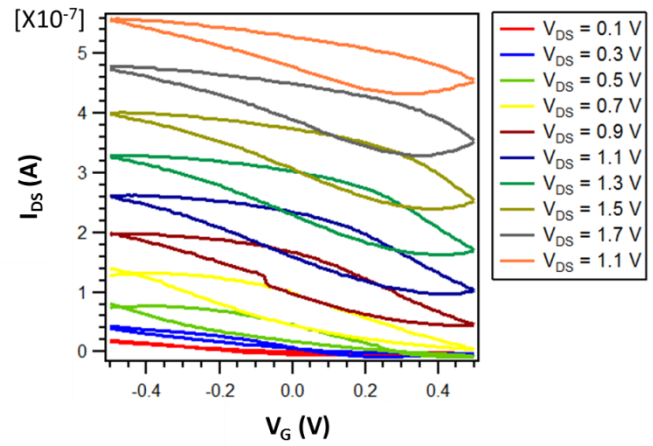


**Figure 31.** Electrical properties of CNT-FET devices ( $6 \mu\text{g}$ ) under dry conditions with a p-type back-gate (A and C) and under phosphate buffer solution with Ag/AgCl reference electrode (B and D). A & B show the  $V_{DS}$  sweep and C & D present the  $V_G$  sweep characteristic of the CNT-FET devices.

$$W_{sw} = \frac{1}{1315} \pi L d \quad (grams) \quad (10)$$

We estimated the weight of the SWNTs we used here to be  $W_{sw} = 2.866 \times 10^{-18} \text{g}$  ( $d=1.2 \text{ nm}$  and  $L= 1 \text{ }\mu\text{m}$ ). Next we calculated the number of SWNTs on a  $4 \text{ }\mu\text{g}$  film to be  $1.77 \times 10^{12}$ , knowing the  $5 \text{ CS}/\mu\text{m}^2 \mu\text{g}$  ratio, area of the film,  $4.42 \times 10^9 \mu\text{m}^2$ , and CS to SWNT ratio, 1:20. Finally using the total number of nanotube and their individual weight, we estimated the CNT film mass using our model to be  $\sim 5 \text{ }\mu\text{g}$ , which is very close to the actual  $4 \text{ }\mu\text{g}$  measured experimentally. This level of accuracy is impressive, 80%, knowing the magnitude and complexity of the system. Error is also expected with the number of variables and degrees of freedom within the system and also with assumptions made earlier.

#### 3.4.4. CNT DEVICE FET CHARACTERISTICS

After microfabrication of CNT-FET devices, back-gated and Ag/AgCl reference electrode gated three terminal devices were characterized for their FET characteristics (i.e. mobility, and on/off ration).

Figure 31 (A and C) presents the characteristics of the CNT-FET under dry conditions with a p-type back-gate, Figure 31 (B and D) presents the characteristics of the CNT-FET in buffer solution with a Ag/AgCl reference electrode gate. The source to drain current ( $I_{DS}$ ) versus source to drain voltage ( $V_{DS}$ ) at different gate voltages is presented in Figure 31 (A and B). The source to drain current ( $I_{DS}$ ) versus gate voltage ( $V_{DS}$ ) at different source to drain voltages ( $V_{DS}$ ) is presented in Figure 31 (C and D).



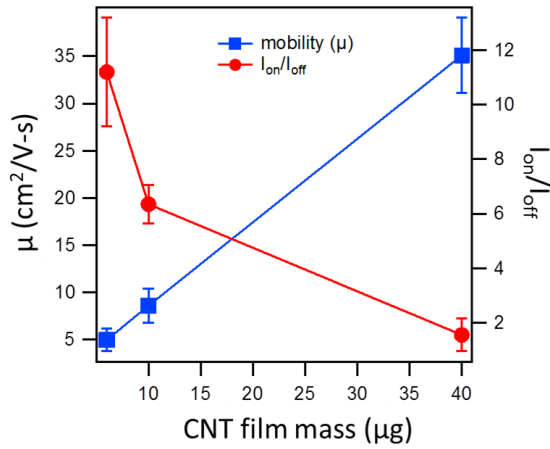
The source to drain current decreased with increasing positive gate voltage. This suggest the device works as a p-type semiconductor, aligned with our expectation described in Chapter 2. We explaine this behavior in detail in Section 2.2. No leakage is seen at positive voltage the current is almost zero suggesting superior p-type transistor compared to past reports where there was still a significant drain current at zero and increasingly positive gate voltage [341].

Field effect mobility was calculated as:

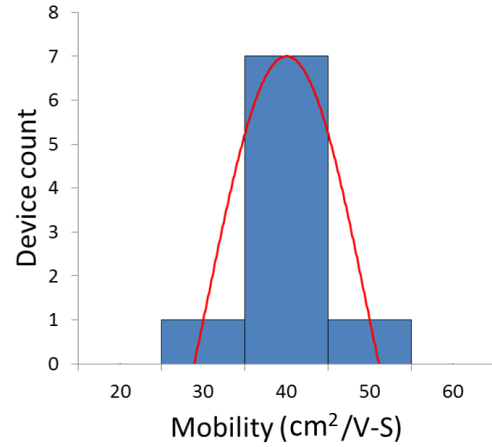
$$\mu_{FE} = \frac{L^* g_{MAX}}{W^* C_{ox}^* V_{SD}} \quad (11)$$

where  $L$  is channel length,  $W$  is channel width,  $g_{MAX}$  is maximum transconductance (taken from the negative transfer curve slope),  $C_{ox}$  is gate capacitance per unit area defined as  $C_{ox} = \frac{\epsilon_{ox}}{t_{ox}}$  (F/cm<sup>2</sup>), where dielectric constant of the oxide  $\epsilon_{ox} = 3.9\epsilon_o$  (permittivity of free space or air  $\epsilon_{ox} = 8.85 \times 10^{-14}$  F/cm), and  $t_{ox}$  is the oxide thinkness.  $V_{SD}$  is the source drain voltage. The results of the mobility calculation are presented in Figure 32 (A and B) as a fuction of CNT film mass. It is obvious that mobility increases as CNT mass increases, film density increases. With these devices, mobility ranged from 4.95 cm<sup>2</sup>/V-s for a 6 µg film to 35.1 cm<sup>2</sup>/V-s for a 40 µg film. Additionally,  $I_{on}/I_{off}$  were also calculated for CNT device through back-gating, Figure 32 (A), and electrolyte liquid-gating, Figure 32 (C). A droplet of electrolyte solution (1X phosphate buffered saline) was placed over the device surface and an Ag–AgCl reference electrode was inserted into the droplet and connected to the gate terminal. On-off ratio by backgating ranged from 1.55 to 11.2, for 40 µg and 6 µg films, and for

**A** Back-gated mobility and on-off ratio



**B** Device mobility histogram (40  $\mu\text{g}$ )



**C** Top-liquid-gated on-off ratio

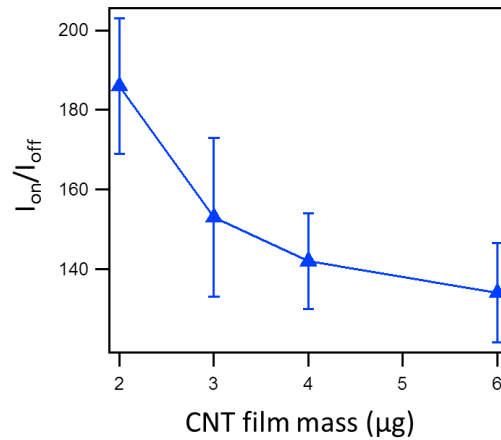


**Figure 32.** Transistor properties versus film mass: (A) presents mobility and on-off ratio of a back-gated CNT device in one plot, we can see that mobility is reversely related to on-off ratio. (B) Presents the mobility range for 40  $\mu\text{g}$  film. (C) presents the on-off ratio for a top-liquid-gated CNT device, gate is applied by Ag/AgCl reference electrode through electrolyte solution (1X PBS).

top liquid gated it ranged from 134 to 186, 6  $\mu\text{g}$  and 2  $\mu\text{g}$  films, increasing as the CNT film mass decreases. The mobility and on-off ratio trends, as a function CNT film mass, correlate with past reports for these nanotubes [326].

Our CNT-FET is also definitely superior compared to past reports on using CNT-FET with antibody fragments which used a mixture of metallic and semiconducting nanotubes resulting in poor on/off ratios' [342]. This point is important and needs to be emphasized as the whole sensing principle relies on the charge introduced at the nanotube channels either reducing or increasing the conductance with introduction of charged proteins. Leakage currents or poor on/off ratio's can thus affect the sensing reliability if one needs to detect such ultra-low concentrations of charged molecules. Thus we can be confident in our experiments that at  $V_G = 0$  V, we can suggest that the increase or decrease in conductance with introduction of proteins or other molecules is as a result of binding alone and not as a result of the currents in the substrate.

After observing the CNT device properties in this section, one can see that the overall conductance is limited by the intertube resistance of 100 M $\Omega$ , about four orders of magnitude larger than the resistance of the tube themselves, 10 k $\Omega$  [334]. This same ratio is also obtained if one compares the mobility of single nanotube (100,000 cm<sup>2</sup>/Vs) [343] with that of network ( $\sim 10$  to 100 cm<sup>2</sup>/Vs). This same effect was also observed in another study by Hu *et al.* [334]. In conclusion, we can see that to generally increase device performance for future application of these CNT devices one needs to address the intratube resistance of nanotubes.

## CHAPTER 4

### CNT DEVICE FUNCTIONALIZATION AND SENSOR CHARACTERISTICS

To enable CNT device specific interact and capture of proteins such as receptor proteins on cell membrane, surface modification of CNT is required. Such modification usually is done with a linker molecule connecting the nanotube with an antibody or aptamer of interest, which can specifically bind to a target protein. It is important to conjugate these molecules and protein to the surface of the nanotube non-covalently without altering the molecular structure of CNTs to preserve their electrical properties. In this chapter we will review the functionalization process of CNT devices. Here we will present studies which verified the success of the functionalization process using different techniques. In addition, CNT devices were characterized for their sensor characteristics using ion molecules.

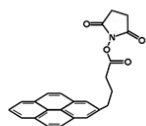
#### 4.1. CNT FUNCTIONALIZATION

As discussed previously in Section 2.1, SWNTs are molecular wires that exhibit interesting structural, electrical, mechanical, and electromechanical properties. SWNTs are unique among solid state materials in that every atom is on the surface. Therefore, surface chemistry could be critical to the physical properties of SWNTs and their applications. Thereby, the ability to functionalize the surface of SWNTs in noncovalent ways to preserve the  $sp^2$  CNT structure and thus their electrical properties is very important. SWNT sidewall functionalization is important to soluble nanotubes, self-assembly on surfaces, and chemical sensor. For the objectives of this thesis, CNT functionalization plays a big role for capturing free proteins and cells.

Chen *et al.* reported a very effective and simple approach for noncovalent functionalization of CNT surface using 1-pyrenebutanoic acid, succinimidyl ester (PASE) linker molecule which can attach to CNT surface on one end and bind to amine group on proteins (i.e. antibodies and other molecules with active amine groups) on the other end conjugating them to the nanotube surface [344], Figure 33. Even though there are other methods of CNT functionalization such as carboxyl groups [345, 346] and hydroxyl groups [347] (covalently), but PASE functionalization remains an very attractive robust non covalent functionalization method for biosensing applications [348]. PASE irreversibly adsorbs onto the inherently hydrophobic surface of SWNTs in an organic solvent such as methanol or dimethylformamide (DMF), Figure 33 (B). The pyrenyl group, being highly aromatic in nature, is known to interact strongly with the basal plane of graphite [349, 350] and sidewalls of SWNTs via  $\pi$ -stacking [344]. The PASE molecule includes a pyrene fragment which consists of four condensed six-membered aromatic rings. This fragment interacts with the CNT surface with a non-bonding  $\pi$ -  $\pi$  interaction. The pyrene and succinimidyl fragments are connected in PASE by an alkyl chain whose structure is highly flexible, the distance between the pyrene molecule and the nanotube surface is about 3.2 Å [351]. As a result, the succinimidyl ester groups are functionalized to SWNTs, succinimidyl ester groups are highly reactive to nucleophilic substitution by primary and secondary amines that exist in abundance on the surface of most proteins. This process includes a nucleophilic substitution of N-hydroxysuccinimide by an amine group on the protein, resulting in the formation of an amide bond [344], Figure 33 (A). Using this technique, we were

### A PASE reaction with amine groups

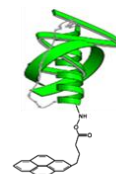
1-Pyrenebutanoic Acid  
Succinimidyl Ester (PASE)



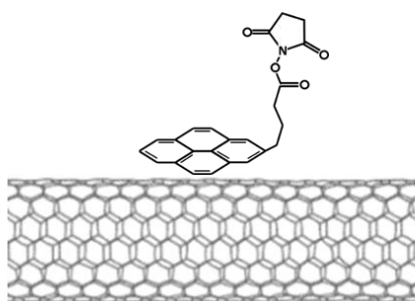
Biomolecule with  
amine groups



Biomolecule  
conjugated PASE



### B PASE $\pi$ -stacking on CNT



### C PASE-biomolecule on CNT

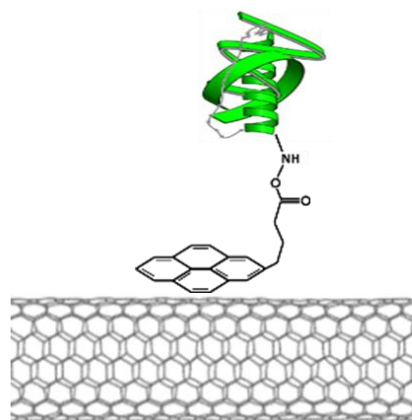


**Figure 33.** (A) 1-Pyrenebutanoic Acid, Succinimidyl Ester (PASE) reacting with the amine groups on a biomolecule (i.e. protein) to form an amine bond resulting in a PASE-biomolecule complex. (B) PASE irreversibly adsorbing onto the sidewall of SWNT via  $\pi$ -stacking. (C) Amine groups on a biomolecule reacting with the anchored succinimidyl ester to form amide bonds to immobilize PASE-biomolecule complex on CNT surface.

able to immobilize a wide range of biomolecules such as antibodies, aptamers, and free proteins on the sidewalls of SWNTs with high specificity and efficiency, Figure 33 (C), which we will review in more detail in this section.

#### 4.1.1. GENERAL CNT FUNCTIONALIZATION PROTOCOL

Depending on the specific study, CNT thin film or CNT devices were functionalized with a specific biomolecule by 1-pyrenebutanoic acid, succinimidyl ester (PASE) linker molecule to meet the objectives of the study. The pyrene rings of PASE molecule (AnaSpec, Cat. No. 81238) adsorb onto carbon nanotube sidewalls by  $\pi$ -stacking. The ester on the other end of the molecule provided an attachment point for antibodies. PASE was dissolved in methanol at 1 mM. Devices were incubated in the PASE solution for 2 h at room temperature, and then rinsed with methanol three times. Devices were then incubated with the proper biomolecule (i.e. antibodies), at a defined concentration and suspended in buffer solution such as 1X PBS, for 2 h at room temperature. After incubation, devices were rinsed in a fresh buffer solution, for example 1X PBS, three times. For protein or cell studies, next Tween20 was used to block unfunctionalized/bare nanotube sidewalls to minimize non-specific interactions. Devices were incubated with 0.5% v-v Tween20 suspended in buffer solution (1X PBS) for 2 h at room temperature. After incubation, devices were rinsed in 1X PBS solution, and then incubated in a droplet of 1X PBS in a humid chamber at 4 °C for further studies.

## 4.2. GOLD NANOPARTICLES (NP) STUDIES

In exploring the use of such multiplexed nanotube devices for measuring differential cellular response and capture, the functionalization of antibodies that are specific to the receptors, their coverage on the surface, and their eventual interaction with the cellular receptors and free biomolecules producing an electrical signal must be understood in depth. To get to this understanding, it is important to understand and confirm the functionalization protocol, the backbone of all these studies, described in the previous section. In this section we demonstrate step by step verification of the functionalization process, PASE onto CNT (Figure 34), biomolecules (i.e. streptavidin and antibodies) on to PASE (Figure 35 and Figure 36), and finally the interaction of free biomolecule with the functionalized CNT complex (i.e. streptavidin functionalized CNT with biotin, Figure 35), using conjugated gold nanoparticles (NPs) for visual verification, via SEM imaging, of functionalization process and demonstration of NP capture on CNT surface via specific interaction.

### 4.2.1. GOLD NPs FUNCTIONALIZATION METHOD

Similar to general functionalization protocol described earlier in this section, devices were prepared and functionalized. Instead of using a biomolecule with an amine group, an antibody conjugated gold NPs (Nanopartz, Cat. No. C11- 15-TX-50), amine-polymer conjugated gold NPs (Nanopartz, Cat. No. C11- 15-TA-50), or streptavidin conjugated gold NPS (Nanopartz, Cat. No. C11- 15-TS-50) were used to functionalize with the PASE linker molecule. The NPs, 15 nm in diameter, were diluted 1:250 in 1X PBS and incubated on top of the device for 2 h. Finally, devices were



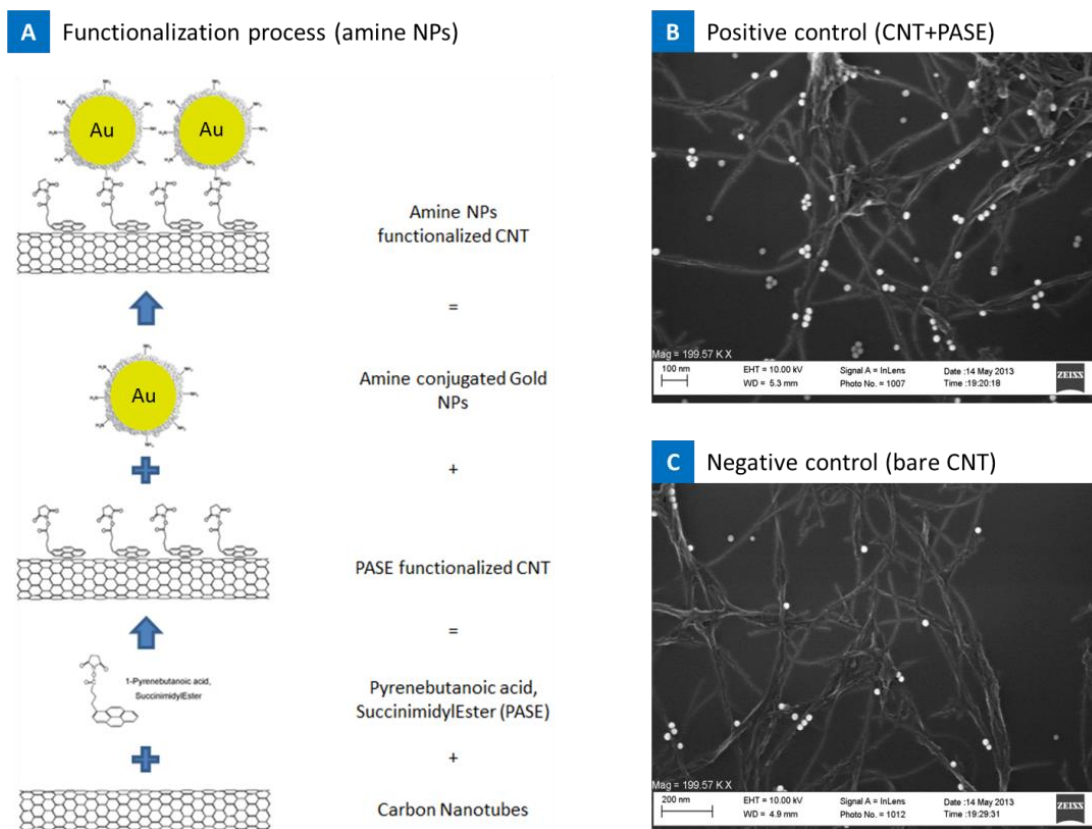


**Figure 34.** Functionalization of PASE. Demonstrating the successful functionalization of PASE molecule onto CNT side walls, by binding of amine polymer conjugated gold NPs to the side walls of PASE functionalized CNT. (A) Schematic showing the Schematic of the PASE functionalization protocol and binding of amine NPs onto CNT surface by PASE linker molecule. (B and C) SEM images of CNT devices after NPs functionalization. (B) SEM image of positive control, PASE functionalized CNT, amine conjugated NPs are clearly binding to the PASE functionalized CNTs. (C) SEM image of negative control, bare CNT, showing no significant interaction between amine conjugated NPs and the bare CNT surface.

rinsed with 1X PBS three time and samples were taken for SEM imaging.

#### 4.2.2. RESULTS

In the first study, PASE functionalization of CNT and binding of amine conjugated NPs, the prepared SWNT devices were functionalized with PASE molecule. The pyrene rings of the 1-pyrenebutanoic acid, succinimidyl ester (PASE) adsorb on to the sidewalls of the SWNT through  $\pi$  stacking and produce a stable nanotube-PASE composite. The ester on the other end of the PASE provides the attachment site for the amine group. The amine polymer conjugated NPs bind to the ester end of PASE after incubation for 2 hrs. Schematic in Figure 34 (A) visualizes this functionalization process. The results from PASE functionalized and bare CNT clearly verify the presents of PASE on the CNT sidewalls and its effect on the attachment of amine polymer, thereby NPs, to the CNT surface via PASE, Figure 34 (B and C).

In the next study, the functionalization process of PASE onto CNT was followed up by functionalization of streptavidin molecule to PASE forming a streptavidin-PASE-CNT complex, Figure 35 (A). Biotin has a high affinity binding to streptavidin which is a protein with active amine groups [352]. Biotin conjugated NPs were used to bind to streptavidin on CNT surface and verify the successful functionalization process of streptavidin-PASE-CNT complex. The results for biotin NPs incubated with functionalized and bare CNT is presented in Figure 35 (C and D).

We demonstrated the functionalization of PASE molecule onto the CNT side walls and attaching biomolecules with amine group to the PASE forming a CNT

functionalized surface complex. Furthermore, we showed the ability to attach a free protein to the CNT complex by specific interaction, streptavidin biotin.

Finally we show the successful functionalization of antibodies to the surface of the CNT using similar functionalization protocol. The prepared SWNT sensors were functionalized with anti-EpCAM antibodies through a pyrene linker molecule. The pyrene rings of the 1-pyrenebutanoic acid, succinimidyl ester (PASE) adsorbed on to the sidewalls of the SWNT. The ester on the other end of the PASE provides the attachment to the antibodies as presented in Figure 36 (a) schematic. Antibody conjugated gold nanoparticles (15 nm) were targeted to the PASE functionalized nanotubes and imaged in a SEM to assess their binding to nanotube. The antibody conjugated nanoparticles were observed to be arranged on the nanotube side wall as presented in Figure 36 (b). A negative control experiment was conducted by targeting antibody conjugated gold nanoparticles to bare nanotube surface without PASE functionalization to the nanotube surface. The results in Figure 36 (c) conclusively suggest that antibody functionalized nanoparticles attached to the nanotube side wall by binding to PASE while no functionalization occurred between bare nanotubes and antibody conjugated nanoparticles without the presence of the PASE linker molecule. Overall the PASE conjugation was proven to provide a stable platform for all protein and cell sensing and capture needs of this thesis. The efficiency of streptavidin–biotin conjugation chemistry, Figure 35, and Au-amine-polymer-conjugation chemistry, Figure 34, were compared with antibody–PASE functionalization in Figure 36 (d).

As a result of these studies, it was found that the antibody–PASE

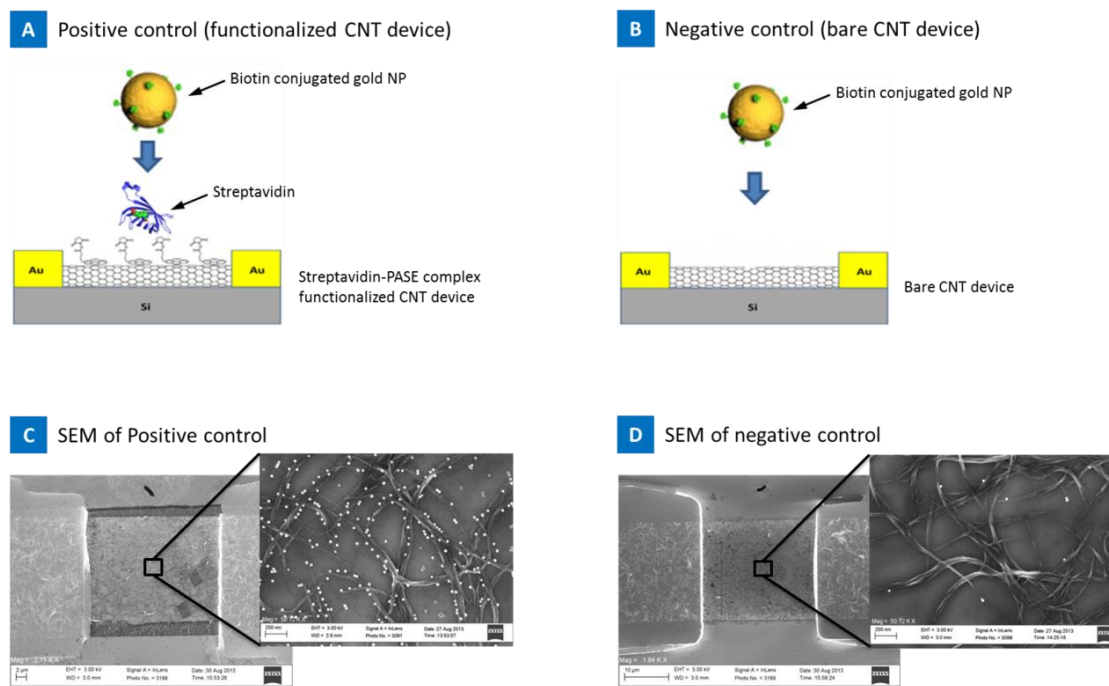


**Figure 35.** Functionalization of streptavidin. Demonstrating the successful functionalization of streptavidin onto CNT by PASE molecule, by showing the specific binding of biotin conjugated gold NPs to the side walls of streptavidin functionalized CNT. (A) Schematic showing the interaction of biotin conjugated NPs with the functionalized CNT surface. (B) Schematic showing the bare CNT presenting no binding site for biotin conjugated NPs. (C and D) SEM images of CNT devices after NP functionalization. (C) SEM image of positive control (A), biotin conjugated NPs are clearly binding to the streptavidin functionalized CNTs. (D) SEM image of negative control (B) showing no significant interaction between biotin conjugated NPs and the bare CNT surface.

functionalization gave the most promising results with  $\sim 76$  particles per  $\mu\text{m}^2$ , followed by streptavidin–biotin conjugation chemistry of  $\sim 71$  particles per  $\mu\text{m}^2$ , followed by Au-amine-polymer functionalization of  $\sim 21$  particles per  $\mu\text{m}^2$ . Non-specific controls yielded about  $\sim 1$ – $6$  particles per  $\mu\text{m}^2$ . Standard deviation of the particle count by each method was plotted suggesting high degree of control and reproducibility of the functionalization and attachment of antibody to the PASE molecule. The devices presented here had channel length of  $100\ \mu\text{m}$  and width of  $80\ \mu\text{m}$ . Assuming 1 antibody site per particle, this would translate into 608,000 sites for antibody binding to PASE for the entire device. Similarly, for the streptavidin–biotin chemistry, this would translate into 568,000 binding sites and for the amine-polymer-Au nanoparticle functionalization protocol, this would translate into 168,000 binding sites. For non-specific controls this would translate into 8000–48 000 binding sites. Typically, a cancer cell surface has 250,000 receptors overexpressed all over the surface compared to normal cells which has less than 10,000. With 608,000 sites, this is a ratio 2.4 antibody available per receptor for interaction. Based on these results, functionalization protocol developed here is very suitable for free protein and cell capture.

#### 4.3. CNT DEVICE SENSOR CHARACTERISTICS

As a result of the functionalization studies in the previous section, it was demonstrated that the CNT devices developed here can also be investigated for sensor application. It was shown that the functionalized CNT complex can be customized with different complex biomolecules and antibodies to interact, bind and capture targeted specific proteins and nano particles. This characteristic is essential for any biosensor. In

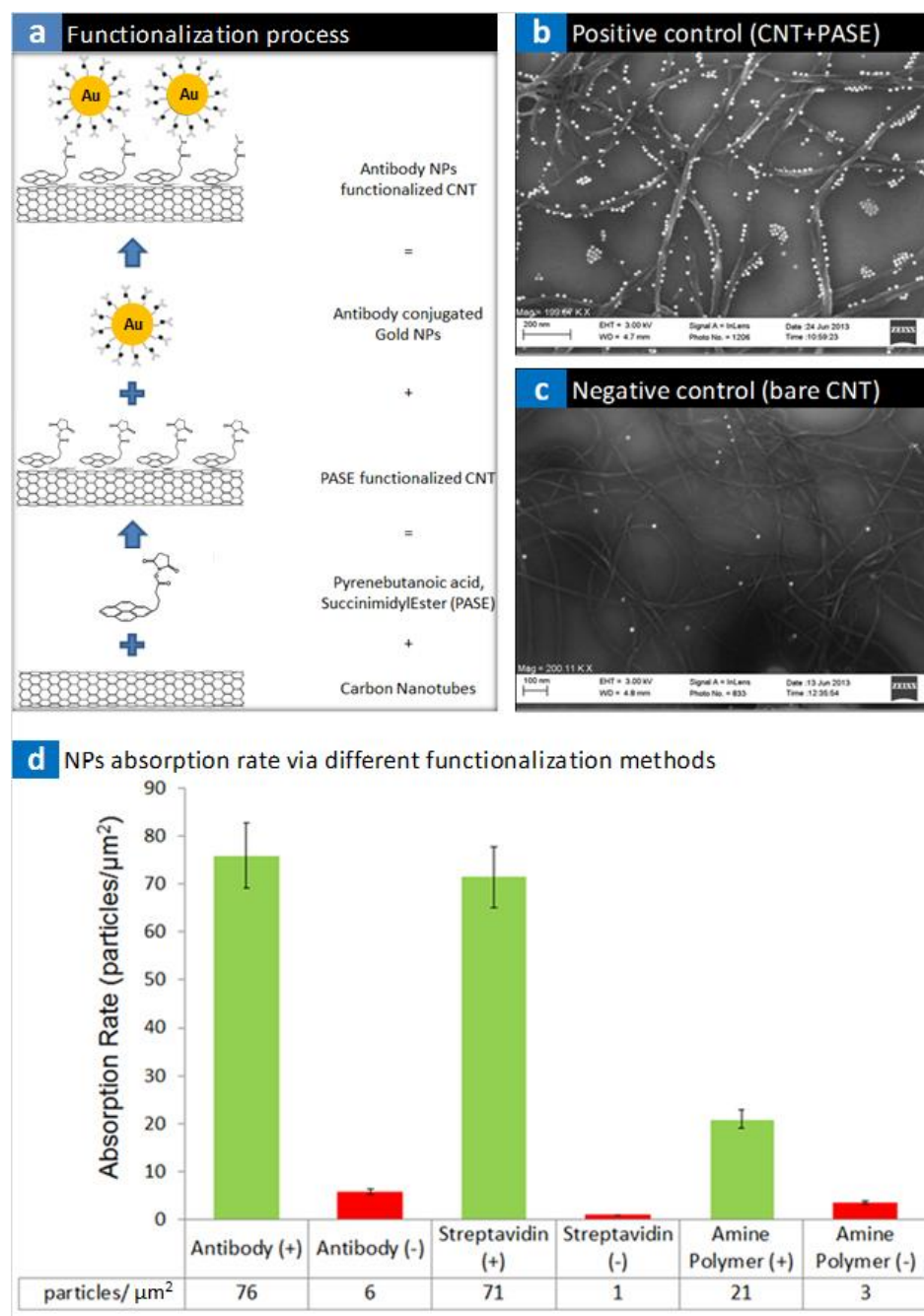


**Figure 36.** Functionalization of antibodies. (a) Schematic of the PASE functionalization protocol; (b) SEM image of positive control suggesting high degree of antibody functionalization; (c) SEM image of negative control suggesting no functionalization; (d) comparison of different functionalization protocols including PASE–antibody, streptavidin–biotin and amine–polymer-NP conjugation.

this section we will review the studies done on how introduction of free charges to the surface of the CNT device can affect its electrical properties. The source of charge potential affecting the CNT in a solution can be induced by free ion injected in the solution or carried by proteins binding to the CNT surface. In this section we will utilize ionic solutions to characterize the properties of CNT device as sensors.

#### 4.3.1. UNDERSTANDING SEMICONDUCTING CNT FOR CHEMICAL SENSING

Understanding the network structure and how they behave reproducibly is highly important in assessing complex biochemical reactions. Towards this, series of experiments were conducted in  $\text{Hg}^{2+}$  and  $\text{NH}_4^+$  ions to understand the change in electrical characteristics of the bare CNT devices.  $\text{HgCl}_2$  in DI water was prepared to create  $\text{Hg}^{2+}$  ions with concentrations ranging from 30 pM to 13  $\mu\text{M}$ . Similarly,  $\text{NH}_4\text{OH}$  in DI water was prepared to create  $\text{NH}_4^+$  with concentrations ranging from 300 nM to 1.5 mM. Figure 37 (a) presents the real time monitoring of both  $\text{NH}_4^+$  and  $\text{Hg}^{2+}$  ions with each spike is a measure of increasing concentration from 300 nM to 1.3mM for  $\text{NH}_4^+$  ions and 30 pM to 13  $\mu\text{M}$  for  $\text{Hg}^{2+}$  ions respectively. Surprisingly, we found that both  $\text{Hg}^{2+}$  and  $\text{NH}_4^+$  ions increased the conductance of the nanotube network as the concentration of ions increased. It is seen that for some intermediate concentrations, the amplitude of the spike decrease suggesting saturation of the sensor but they are also seen to recover as the amplitudes increase with time at higher concentrations. This is clearly observed in  $\text{Hg}^{2+}$  ion sensing. In past  $\text{Hg}^{2+}$  has been shown to increase the conductance of nanotube device [353], while  $\text{NH}_4^+$  ions decreased the conductance of the device [354]. The increase in conductance with concentration for both  $\text{Hg}^{2+}$  and

$\text{NH}_4^+$  ion are as a result of doping. Typical electron-acceptor dopants such as  $\text{I}_2$ , and  $\text{Br}_2$  are expected to transfer electrons from the carbon  $\pi$  states in the tubes to the dopant molecules, creating an increase in hole carriers in the SWNTs [333]. This can increase the conductivity due to charging when positively charged molecules such as  $\text{NH}_4^+$  and  $\text{Hg}^{2+}$  interact with the nanotube thereby increasing the current of the p-type nanotube. The shift in the RBM and G mode of the Raman spectrum presented, Figure 26 (C), also agrees with the presence of iodine as dopant in these nanotubes. An interesting result is that our doped nanotube devices did take the level of detection of both  $\text{Hg}^{2+}$  and  $\text{NH}_4^+$  ions to  $\sim 30$  pM and  $\sim 300$  nM respectively, which is significantly higher in sensitivity compared to past reports on pristine nanotubes where the limits of detection has been shown to be  $\sim 10$  nM for  $\text{Hg}^{2+}$  [355]. Voltage sweeps as presented in Figure 37 (b) shows a shift in threshold voltage towards more positive  $V_G$  suggesting p-type behavior. The real time  $\text{Hg}^{2+}$  and  $\text{NH}_4^+$  chemical sensing therefore correlates well with the voltage sweeps. Figure 37 (c) presents the change in  $I_{DS}$  versus  $V_G$  for different concentrations of  $\text{Hg}^{2+}$  and  $\text{NH}_4^+$  ions. As the concentration increases, so does the current suggesting an increase in hole carrier density for both types of ions. A  $\Delta G/G_0$ , normalized conductance, versus  $\log [A]$  is presented in Figure 37 (d) suggesting a Langmuir-adsorption isotherm with a linear response centered around  $[A] = 1/K$ . The higher ( $\Delta G/ G_0$ ) for our doped nanotubes (y-axis) presented here in the Langmuir adsorption isotherm compared to past networks of mixed metallic and semiconducting nanotube [353] also suggests the increased sensitivity of the iodine doped semiconducting nanotube sensors and lower limits of detection. The mechanism of



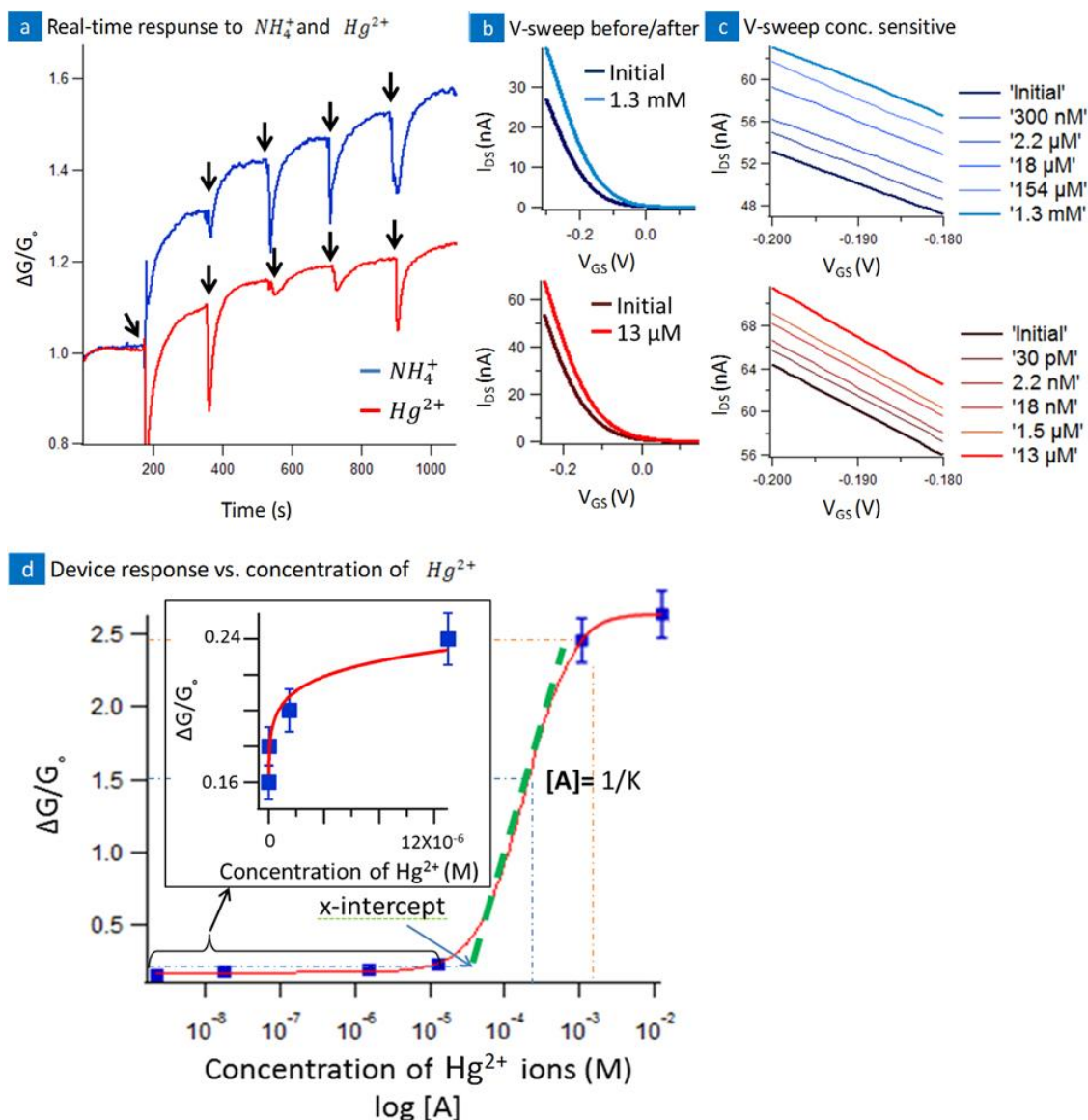


**Figure 37.** Understanding semiconducting nanotube network. (a) Real time response of device to concentrations of  $\text{NH}_4^+$ , 300 nM to 1.3 mM, and  $\text{Hg}^{2+}$ , 30 pM to 13  $\mu\text{M}$ , ions; (b) voltage sweep before and after exposure to  $\text{NH}_4^+$  and  $\text{Hg}^{2+}$  ions; (c) concentration sensitivity of voltage sweep for  $\text{NH}_4^+$  and  $\text{Hg}^{2+}$  ions; (d) normalized signal conductance versus concentration of  $\text{Hg}^{2+}$  ions suggesting Langmuir adsorption isotherm. The inset shows the percentage sensitivity versus concentration for  $\text{Hg}^{2+}$ . Similar results were seen for  $\text{NH}_4^+$  ions suggesting same sensing mechanism.

sensing ions for both  $\text{NH}_4^+$  and  $\text{Hg}^{2+}$  is therefore due to an increase in carrier density of iodine doped nanotubes. The same increase in conductance for the same type of charge also suggests similar mechanism and predictable sensor response of the doped nanotubes sensor devices. One application of these iodine doped nanotube networks with 30 pM sensitivity for  $\text{Hg}^{2+}$  could be in screening drinking water ( $\text{Hg}^{2+}$  ions set by most governmental EPA is  $\sim 10$  nM [355]).

In the next chapter we will build on the findings here and utilize the CNT devices for capturing and sensing free proteins.

#### 4.3.2. $\text{Hg}^{2+}$ AND $\text{NH}_4^+$ ION EXPERIMENTATION METHODS

$\text{HgCl}_2$  (Sigma-Aldrich, Cat. No. 215465) in DI water was prepared to create  $\text{Hg}^{2+}$  ions with concentrations ranging from 30 pM to 13  $\mu\text{M}$ . Similarly,  $\text{NH}_4\text{OH}$  (Sigma-Aldrich, Cat. No. 338818) in DI water was prepared with concentrations ranging from 300 nM to 1.5 mM. Array of un-functionalized bare devices were prepared with initial 5  $\mu\text{l}$  droplet of DI water suspended on top. 100 mV source drain bias and 0 V gate voltage applied by reference Ag/AgCl electrode. Device current was monitored as ion concentrations were increased on the devices every 180 s. In addition voltage-sweep readings were taken after addition of each ion concentration.

#### 4.3.3. LANGMUIR ISOTHERM MODEL FOR BIOSENSORS

After conducting ion sensing with the CNT device, we can propose theoretical model to predict the set parameters, where the target molecules are adsorbed onto the CNT surfaces via the Langmuir isotherm process and the conductance of the sensor

transducer via capacitive coupling or charge transfer. Figure 38 shows a schematic diagram depicting the experimental setup and Figure 37 (d) shows the ion data fitted to the theoretical model for the CNT network sensors.

For the theoretical model, we assume that analyte “A” in bulk solution was adsorbed onto a finite number of binding sites “B” on the CNT surfaces following a Langmuir isotherm model, Figure 38. In the Langmuir isotherm model, it is assumed that analyte molecules in solution bind to a finite number of binding sites on solid substrates, and the analyte molecules in solution and those bound to the binding sites form an equilibrium. In the case of specific biosensors based on CNT FETs, specific receptor molecules fixed on CNT surfaces work as binding sites [270]. Let  $[A]$ ,  $[B]$ ,  $[AB]$ , and  $[B]_{\max}$  represent the concentration of analytes in bulk solution, the surface density of binding sites on CNT networks, the surface density of adsorbed analyte molecules, and the maximum surface density of binding sites on CNT networks, respectively. Then, the surface density of adsorbed analytes can be expressed following a Langmuir isotherm, Figure 37 (d), as:

$$[AB] = [B]_{\max} \times \frac{[A]}{[A] + 1/K} \quad (12)$$

with equilibrium constant  $K = k_1/k_{-1}$ , where  $k_1$  and  $k_{-1}$  are the association and dissociation constants, respectively [355]. Since CNTs respond to analytes only within the distance of Debye length in ionic solutions due to the screening effect, [342] we can assume that the sensor response of our sensors is mostly due to the analytes adsorbed onto the CNT channels.

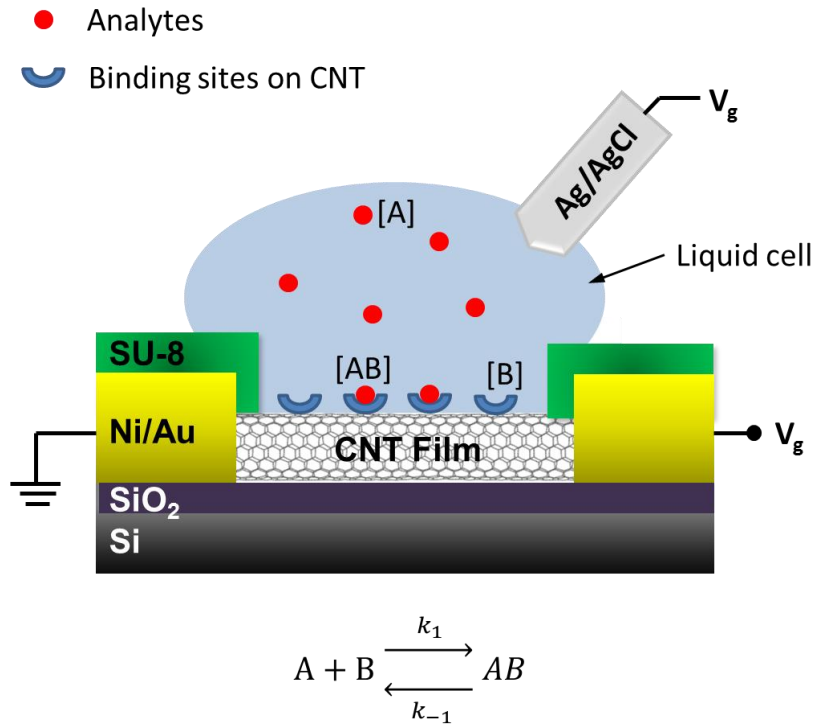


**Figure 38.** Schematic diagram depicting the measurement and the bases for the theoretical model. Showing the CNT device as described in Chapter 3 with a liquid droplet on top containing the analytes [A]. CNT film is functionalized with the binding sites [B]. [AB] shows the binding of analyte to the binding site on CNT surface.

CNT network-based channels are usually composed of multiple CNTs overlapping on each other to form junctions. In this case, we can expect rather diffusive charge transport due to the short mean free paths. Thus, we can ignore any coherent gating effect and assume that the current change  $\Delta I$  in the channel is affected by the adsorbed analyte concentration [AB] on CNT surfaces via electric coupling like

$$\Delta I = G_L \times \Delta V_A \approx g_L V_{ds} \times \frac{\Delta q_A}{C_0} \quad (13)$$

$$\begin{aligned}
&= g_L V_{ds} \times \frac{q_A [AB]}{C_0} \\
&= g_L V_{ds} \times \frac{q_A}{C_0} [B]_{max} \times \frac{[A]}{[A] + 1/K}
\end{aligned}$$

where  $G_L$  represents the liquid gate transconductance;  $\Delta V_A$  the liquid potential change around the CNTs caused by the adsorbed analyte molecules;  $g_L$  the normalized transconductance defined by  $g_L \approx G_L/V_{ds}$ ;  $\Delta q_A$  the total electric charge contributed by the adsorbed analyte molecules to the CNTs;  $q_A$  the electric charge contributed by the unit surface density of the adsorbed analyte molecules to the CNTs; and  $C_0$  is the coupling constant between the analyte molecules and CNT surfaces [342].

Based on previous reports, electric field gating [269] and direct charge transfer [308] are the most common mechanisms about how charged analytes near the CNT surface can affect the conductance of CNT network channels. For CNT devices  $q_A$  and  $C_0$  are determined by the type of analytes and should not be affected by the CNT device structures [342].

From eqn. 13, the sensor response, defined as the conductance change ( $\Delta G = \Delta I/V_{ds}$ ) with respect to initial conductance  $G_0$ , becomes

$$\frac{\Delta G}{G_0} = \frac{g_L}{G_0} \times \frac{q_A}{C_0} [B]_{max} \times \frac{[A]}{[A] + 1/K} \quad (14)$$

It is worth mentioning several important aspects of this equation. First,  $\frac{g_L}{G_0}$  represents the electrical characteristics of the CNT device and should be independent of the analyte species. It can be estimated by simple electrical measurement on the CNT device without performing actual sensing experiments. Second,  $\frac{q_A}{C_0} [B]_{max}$  and K represent the electric coupling and the adsorption properties of the analyte molecules onto CNT-based sensor surfaces, respectively. Considering  $[B]_{max}$  as a constant, both can be determined only by the analyte type and do not depend on the CNT device structures or nanotube chirality.

In a previous report Lee *et al.* reported that the sensor response can be expressed in a linear form to logarithmic concentration in certain range of concentration [356]. Accordingly, for this linear region we can write

$$\frac{\Delta G}{G_0} \sim \frac{1}{4 \log_{10} e} \left( \frac{g_L}{G_0} \right) \times \frac{q_A}{C_0} [B]_{max} \times [\log_{10}[A] + \log_{10}[e^2 K]] \quad (15)$$

by setting  $x = \log_{10}[A]$  and  $y = \Delta G/G_0$ , we can arrive to the following equation

$$y \sim \alpha [x - y] \quad (16)$$

where

$$\alpha \left( \equiv \frac{1}{4 \log_{10} e} \left( \frac{g_L}{G_0} \right) \times \frac{q_A}{C_0} [B]_{max} \right) \quad (17)$$

this way  $y(\equiv -\log_{10}(e^2 K))$  represent the slope and x-intercept of the sensor response graph, respectively, as indicated in Figure 37 (d). This model is effective, but it is important to note that slightest variation in CNT film distribution may cause a slight variation of surface binding site density and channel conductance of the CNT devices. Furthermore, even for the devices with uniform CNT density, the conductance of the devices shows some distribution due to the variation of the network connectivity as reported by other researchers also [357].

The model explained above can be used to validate the experimental results. The measured response from the CNT device were plotted to the logarithmic concentration of analytes, and the linear region was fitted using eqn. 16, as presented in Figure 37 (d). The equilibrium constant  $K$  can be estimated from the x-intercept  $y \equiv -\log_{10}(e^2 K)$  of the fitting curve.  $K$  is defined as  $[A] = 1/K$ , with  $[A]$  obtained from the center point of the fitting curve, as shown on Figure 37 (d). In this case,  $K$  (equilibrium constant) value for  $\text{Hg}^{2+}$  analyte was estimated to be  $K = 5 \times 10^3$ .

## CHAPTER 5

### CNT DEVICES FOR CAPTURE AND SENSING OF CANCER BIOMARKER PROTEINS

Following CNT device characterization and functionalization, in this chapter we will investigate the capability of the CNT device micro-arrays for capturing and profiling electrical signature of free proteins. In our first attempt here, we will analyze the effect of the streptavidin biotin binding on the CNT surface and its effect on CNT's electrical properties, namely conductance and voltage threshold. Following the successful functionalization protocol of streptavidin on the CNT surface using PASE molecule and capturing biotin conjugated gold nanoparticles on the surface of the CNT through the high-affinity interaction and binding of streptavidin and biotin. Next we will apply the same logic based on our antibody functionalization protocol, discussed in detail in Chapter 4, to capture and profile digital signature of cancer biomarker protein epithelial cell adhesion molecule (EpCAM).

#### 5.1. INTRODUCTION

Single wall carbon nanotubes are ideal candidates for label-free sensing; every atom is on the surface hence their electronic properties are very sensitive to the surrounding charge environment [226]. Many reports have described carbon nanotube sensors for detection of free proteins [344, 358, 359], DNA [360-362], viruses [363, 364] and even cancer cells [133, 365, 366]. For many of these, the sensing mechanism is the gating effect of the target proteins as they bind to the antibodies, bringing them near the CNT within the Debye length of the fluid,  $\sim 1$  nm in 1X PBS [367, 368].



## 5.2. RESULTS

### 5.2.1. DETECTION OF BIOTIN ON CNT DEVICES

In this section we report the study of biotin interaction on a streptavidin functionalized CNT device. Biotin-streptavidin interactions are chosen to demonstrate the first CNT device system on our platform because they are well studied binding partners that interact with very high affinity [352]. We compare two sets of CNT device: a) CNT devices that are functionalized with streptavidin using PASE linker molecule, and b) CNT devices that are not functionalized, bare CNT. We will compare the electrical signature of the devices as a function of change in current vs. time.

The functionalized devices were exposed to 1ng/mL biotin (Sigma Aldrich, Cat. No. B4501) in 1X PBS. The result of this experiment is shown in live conductance readings in Figure 39 (A). We observe that the change in conductance is equal or less than 2% for negative controls, not functionalized bare CNT devices, and greater than 2% for positive controls, CNT devices functionalized with streptavidin, showing an increase in device current as a result of a biotin interaction with streptavidin on CNT surface. Additionally, the changes in the voltage sweep of the devices were also recorded. The bare devices (red line) and streptavidin functionalized devices (green line) were exposed to 1ng/mL biotin in 1X PBS. Voltage sweep was taken before and after the biotin target molecule injection on the device. The result of this experiment is shown in Figure 39 (B).

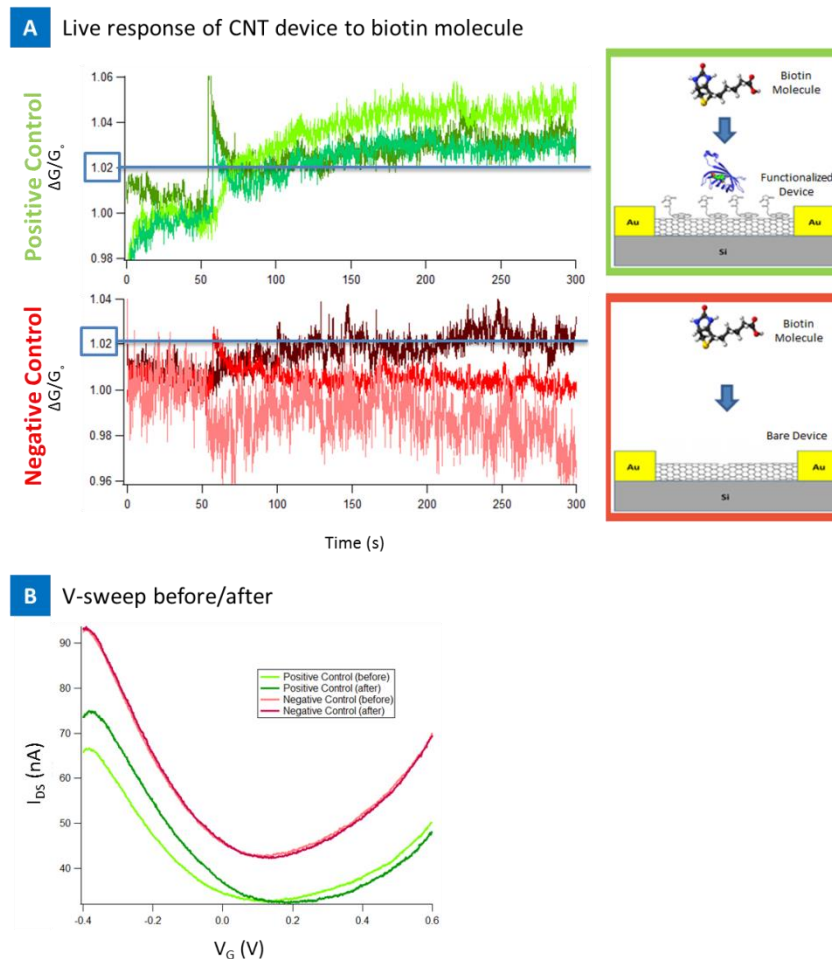


**Figure 39.** (A) Normalized live response of six CNT devices, three functionalized with streptavidin (positive control in green) and three not functionalized bare CNT devices (negative control in red). 5  $\mu\text{L}$  of biotin solution, 1 ng/mL in 1X PBS, was added to each device at 60 seconds and the electrical current of the device was recorded for the remaining 240 seconds. The functionalized devices current increased after biotin introduction suggesting negatively charged biotin molecules interacting with CNT surface while, the bare devices show no significant change thereby no specific interaction. Schematics in the right hand side of the figure illustrated the device functionalization state and its interaction with biotin molecule. (B) Shows the V-sweep response for before and after biotin introduction to the device. Functionalized positive control device, in green, shows a shift in the positive direction, correlating with the live current reading while negative control, in red, shows no change.

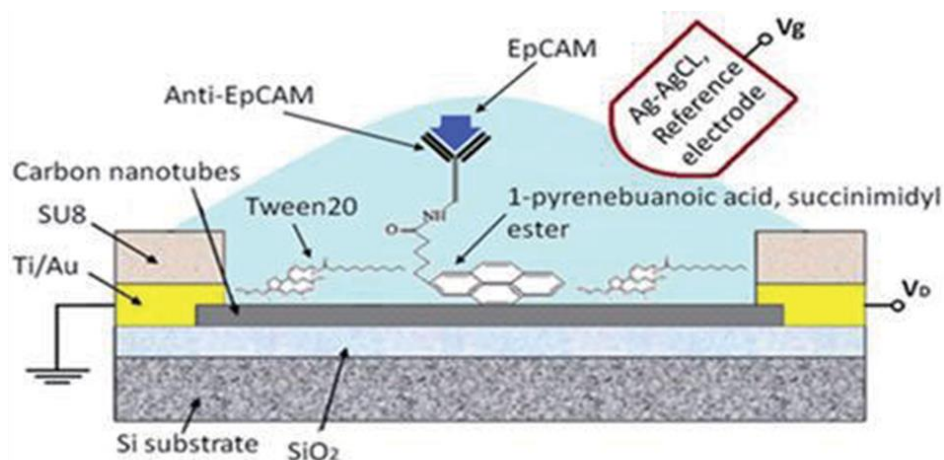
### 5.2.2. DETECTION OF FREE EpCAM ON CNT DEVICES

Figure 40 and Figure 41 presents the results from three terminal devices on molecular EpCAM. Liquid gating, as shown in Figure 40 (A), Ag/AgCl electrode was used to apply gate voltage. In this study, we first attempted to ascertain shift in gate voltages due to specific versus non-specific interactions. Therefore, we used free proteins due to the simplicity of interactions. Figure 41 (A) Demonstrates the testing without antibody, IgG and anti-EpCAM. It is seen that for anti-EpCAM, there is a shift in the gate voltage after the addition of EpCAM indicated by blue line. Figure 40 (B) and Figure 41 (B) presents the ability to monitor each step (including PASE, anti-EpCAM functionalization, Tween 20 blocking and finally EpCAM). It is seen that exposure of EpCAM proteins caused a decrease in threshold voltage values decreasing the nanotube conductance due to interaction. This is the mechanism of sensing of proteins. Up to 1 ng/ml was detected using such device as shown in Figure 41 (C). The graph in Figure 41 (C) clearly shows the shift in gate voltage for different concentrations from 1 ng/ml to 1000 ng/ml done consecutively. This also suggests that the device does not get saturated over range of clinical concentrations (diagnostic gray zone: 4 ng/ml for Prostate-specific antigen (PSA) [289]).

### 5.3. CONCLUSION AND ANALYSIS

In this chapter we demonstrated the biosensing capabilities of the CNT devices via streptavidin-biotin interaction and with antibody-biomarker interaction, EpCAM cancer biomarker. We showed detection of 1ng/mL of biotin and free EpCAM protein in the PBS solution environment. The nature of this interaction and its effect on CNT's

**A** Schematic of sensing mechanism



**B** CNT device history as a function of V-sweep

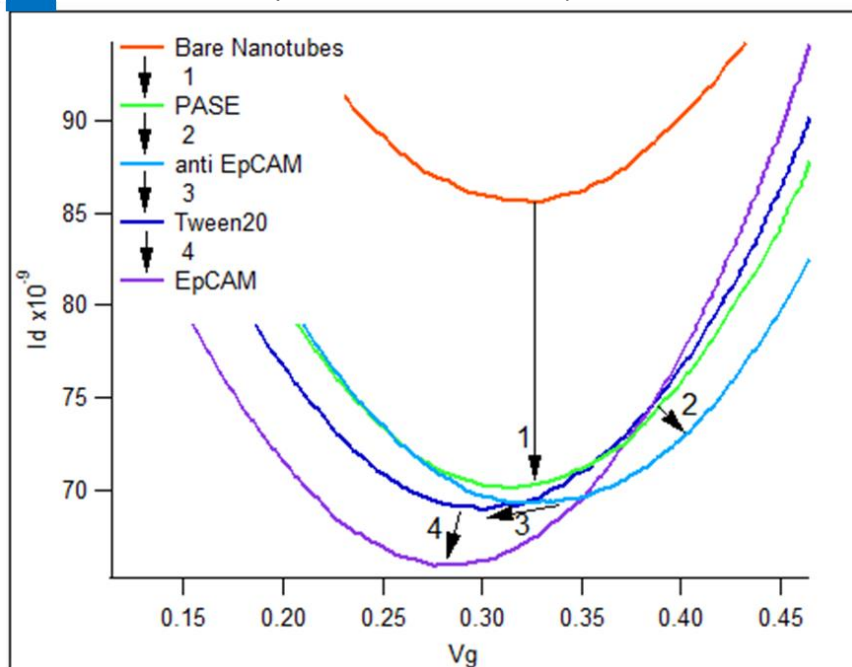


**Figure 40.** (A) The schematic of a protein/CTC detection scheme. The entire device except the active nanotube layer is sealed off using SU8 polymer. (B) CNT device history from bare to functionalization process and introduction of EpCAM molecule is presented in one graph as a function of V-sweep.

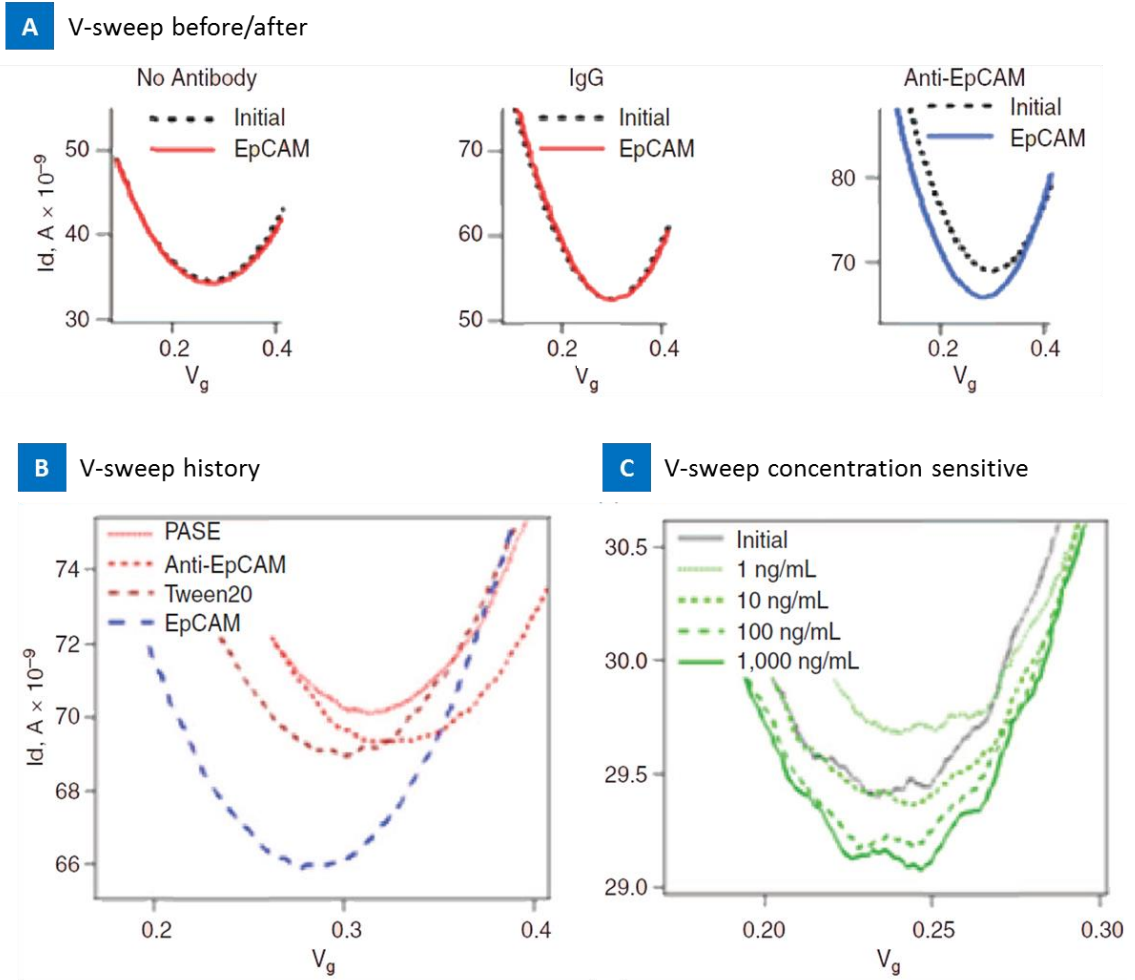


**Figure 41.** (A) Showing the typical V-sweep for three groups of devices, from left to right, not functionalized, IgG functionalized, and anti-EpCAM functionalized. In each case, initial sweep before EpCAM protein introduction and after sweep post EpCAM ( $1\mu\text{g/mL}$ ) introduction to the device is presented. Both not functionalized and IgG functionalized showed no change with the introduction of EpCAM but anti-EpCAM functionalized showed a shift. (B) CNT device history from bare to functionalization process and introduction of EpCAM molecule is presented in one graph as a function of V-sweep. (C) Presents concentration dependent device response, showing detection of molecular EpCAM up to  $1\text{ ng/mL}$ .

electrical property, modifying the device conductance and threshold voltage, can be explained in two general ways: the change in carrier mobility and carrier density as described in Section 2.3.4. We clearly demonstrated a shift in device conductance and threshold voltage as a function of analyte interaction with the CNT. Based on our observations we can assume that the change in device electrical property is a result of specific interaction of free protein with the CNT surface and change in carrier density of the nanotubes as discussed in Section 2.3.4. In the next chapter we will further investigate the biosensing capabilities of the CNT devices using aptamer molecules as a substitute for antibodies.

## 5.4. EXPERIMENTAL

### 5.4.1. CNT DEVICE FABRICATION

CNT thin film was assembled on a silicon/silicon dioxide wafer, 400 nm wet oxide, and micro-arrays were fabricated as described in Section 3.1. CCVD synthesized, single wall/double wall CNT mixture (99% weight) was purchased from Cheap Tubes Inc., 1-2 nm outer diameter and 3-30  $\mu\text{m}$  length. CNTs were suspended in IPA at  $\sim 45 \mu\text{g/mL}$  and sonicated for 90 min. The solution was then diluted to  $\sim 3.5 \mu\text{g/mL}$  and sonicated for 3 hours to completely disperse the nanotubes. 40  $\mu\text{g}$  CNT film was generated using this solution, Figure 24 (C). Generation 3 device design was used for these experiments.

### 5.4.2. CNT DEVICE FUNCTIONALIZATION

CNT devices were incubated with 1-Pyrenebutanoic acid, succinimidyl ester (PASE) linker molecule for 2 hours. Next, they were incubated with streptavidin

(Sigma Aldrich, Cat. No. S4762) or anti-EpCAM antibody (Millipore, Cat. No. OP187) accordingly, at 10  $\mu\text{g/mL}$  in 1X PBS, for 2 hours at room temperature, forming a CNT-PASE-streptavidin complex. Finally, a surfactant, Tween20, was used to block functionalized nanotube sidewalls or PASE sites to minimize nonspecific interactions. The devices were incubated in 0.5% Tween20 for 2 h at room temperature. At the end, devices were covered by a droplet of 1X PBS and stored in a humid chamber at 4  $^{\circ}\text{C}$  for further testing. For greater detail of the functionalization process please refer to Chapter 4.

#### 5.4.3. EXPERIMENTAL SET-UP

Experimental set up is previously described in Section 3.3. The testing protocol started with a hydrated device, and a 5  $\mu\text{L}$  droplet of 1X PBS which was placed immediately after functionalization. The bias was applied and the sensor was monitored for the initial 1-3 minutes, then 5  $\mu\text{L}$  droplet of sample solution was pipetted directly into the standing 5  $\mu\text{L}$  droplet. Devices were monitored for 120-360 seconds after each addition of a new sample solution. The total duration of one test varied from 180 to 1980 seconds. To compare results among devices,  $I_{\text{SD}}$  data were normalized to obtain the  $\Delta G/G_0$  values for conductance.  $V_G$  sweeps were recorded on each device before and after injection of the target sample.

## CHAPTER 6

### ULTRASENSITIVE AND LABEL-FREE SENSING OF IL-6 BASED ON PASE FUNCTIONALIZED CARBON NANOTUBE MICRO-ARRAYS WITH RNA- APTAMERS AS MOLECULAR RECOGNITION ELEMENTS

#### 6.1. INTRODUCTION

When using antibodies as recognition elements, the large size of the antibody can enable the target protein to interact outside the space charge layer or the Debye length of the sensor. This could reduce the sensitivity and specificity of the biosensor. Thus, antibody binding fragments [342], and aptamers [341] have been proposed for sensing very small concentrations of proteins. In the past nanotube-aptamer technology has been used to detect the binding of thrombin, IgE, and VEGF [369-371]. Previously researchers demonstrated IL-6 detection using antibody-nanotube systems with multiple label and amplification strategies [372-374]. Here for the first time we demonstrate label-free nanotube micro-array platforms using PASE conjugated aptamers for detection of IL-6 protein, an important cancer biomarker.

##### 6.1.1. APTAMERS

Aptamers are analogous to antibodies in their range of target recognition and variety of applications; here we will review several key advantages over their protein counterparts. Aptamers are self-refolding, single-chain, and redox-insensitive. They also lack the large hydrophobic cores of proteins and thus do not aggregate. They tolerate, or recover from, pH and temperatures that proteins do not [375]. Aptamers are easier and more economical to produce, especially at the affinity reagent scale. In stark contrast to peptides, proteins and to some small chemicals, oligonucleotides, DNA



aptamers are made through chemical synthesis, a process that is well defined, highly reproducible, sequence independent and can be readily and predictably scaled up. Their production does not depend on bacteria, cell cultures or animals [375]. In contrast to antibodies, toxicity and low immunogenicity of particular antigens do not interfere with the aptamer selection. Further, highly custom or “orphaned” targets can be addressed rapidly and cheaply [375]. Aptamers in general are capable of greater specificity and affinity than antibodies [376]. Additionally, they can easily be modified chemically to yield improved, custom tailored properties. For instance, reporter and functional groups and PEG can easily be attached to the aptamer in a deterministic way. More specifically for the purposes of studies in this chapter, aptamers were modified with PASE functional molecule. Aptamers can also even be combined with antibodies if necessary [377, 378].

Aptamer’s small size leads to a high number of moles of target bound per gram, and they may improve transport properties allowing cell specific targeting and improved tissue penetration [379-383]. They are much more stable at ambient temperature than antibodies yielding a much higher shelf life, and they can tolerate transportation without any special requirements for cooling, eliminating the need for a continuous cold chain. As result, aptamers are attractive alternatives to replace antibodies for sensing applications in the long run.

#### 6.1.2. INTERLEUKIN-6 (IL-6)

Interleukin-6 (IL-6) is a multi-functional cytokine characterized as a regulator of immune and inflammatory responses [384, 385]. IL-6 plays a crucial role in tumor

microenvironment regulation in number of cancers namely breast, oral, prostate, and pancreas cancers to name a few [386-392]. Higher levels of IL-6 in the blood of patients have been associated with advanced/metastatic cancers [386, 393-395]. Overexpression of IL-6 receptor has also been shown in cervical cancer cells [396]. Such findings have increased the interest in development of anti-IL-6 therapeutics to target many of related diseases [397-401]. In this environment an efficient, simple and reliable diagnostics technique would be of significant interest and nanotube micro-arrays can be equipped for sensitive detection of IL-6 biomarker.

Detection of IL-6 is only applicable at low concentrations, 12-300 pg/ml, for practical clinical utility in metastatic cancers [394, 402-405]. Electrochemical sensing of IL-6 has been reported using different methods namely gold nanoparticles, carbon nanotube forest electrodes and ferrocene loaded polyelectrolyte nanoparticles [372-374]. Detecting very small amounts of biomarkers using CNT-FETs has been a challenge due to the complication that relative large size of antibodies creates in regards to Debye length. The effect on the mobile charge on the material is not realized if the target molecule is placed Debye length away from the surplus charge [406], which can be the case in the ionic environment that the CNT-FET biosensors operate in for biological applications with reference to the antibody size. To solve this issue aptamers have been used for biosensing of immunoglobulin E (IgE) using CNT-FETs and showed improvement in sensor performance compared to an antibody coated nanotube channel under similar conditions [341]. Using aptamers we have demonstrated the ability to detect IL-6 at concentrations as low as 1 pg/ml by using

**A** IL-6 aptamer PASE complex

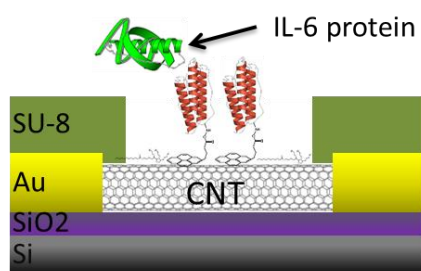
1-Pyrenebutanoic Acid  
Succinimidyl Ester (PASE)

IL-6 aptamer

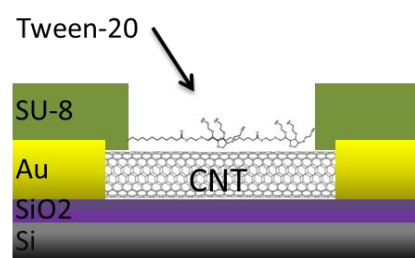
PASE conjugated  
IL-6 aptamer



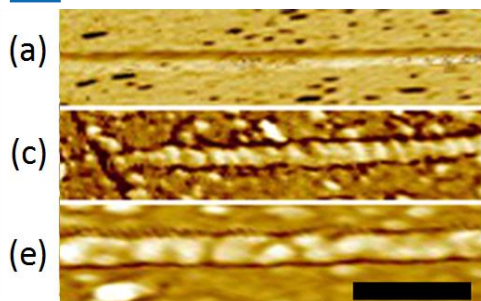
**B** IL-6 aptamer functionalized CNT



**C** Tween-20 functionalized CNT



**D** AFM phase image



**E** AFM z-axis image

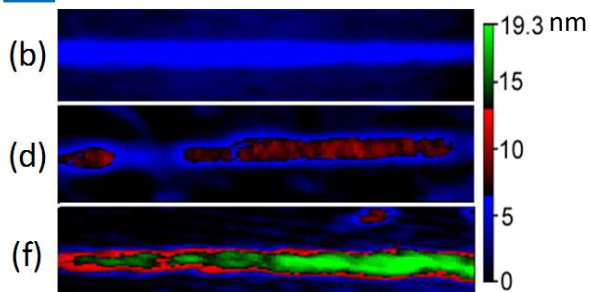


**Figure 42.** Schematic showing, (A) the reaction of PASE onto aptamer, (B) PASE conjugated aptamer functionalized CNT structure and aptamer interaction with IL-6 protein on the surface of the CNT. (C) Schematic illustration of the blocking of CNT surface with tween-20 molecule. (D and E) AFM image showing a phase image, (D), and Z-Axis image, (E), of bare CNT, (a) and (b), functionalized CNT with IL-6 aptamer, (c) and (d), and IL-6 protein binding to aptamer/CNT structure, (e) and (f). Images were obtained using dry tapping mode (Nanosurf NaioAFM system). Scale bar = 100 nm.

nanotube micro-arrays.

## 6.2. RESULTS

In this chapter, we demonstrate the detection of ultra-low levels of IL-6 protein using PASE conjugated IL-6 aptamer functionalized on the nanotube channels. The RNA-aptamer specific to the IL-6 protein was used as the recognition element. The pyrene rings of the 1-pyrenebutanoic acid, succinimidyl ester (PASE) adsorb on to the sidewalls of the SWNT through  $\pi$  stacking [344]. The PASE conjugated IL-6 aptamers composite (Length: 32 nts, Base Pair Biotechnologies, Cat. No. 575702; 5' - NH<sub>2</sub> modification) was adsorbed on to the side wall of the SWNT transistor to produce a stable nanotube-PASE-aptamer composite as presented in Figure 42 (A). The amine group on the PASE provides an attachment site for the NH<sub>2</sub> modified aptamers similar to past reports [341]. Atomic Force Microscopy (AFM) was used to image the bare nanotubes, PASE-aptamer functionalized nanotube and the binding of IL-6 on the functionalized nanotube surface. Figure 42 (D and E) presents the Z-axis and the AFM phase image of bare nanotubes (blue), PASE-aptamer conjugate adsorption to the nanotube side wall in red and the IL-6 binding to the functionalized CNT surface, in green. The phase image visually distinguishes the bare nanotube, Figure 42 (a), from nanotube surface with aptamer, Figure 42 (c), and aptamer-IL-6 complex, Figure 42 (e). Z-axis AFM image color codes the CNT surface as a function of its height. Figure 42 (b), shows the bare nanotube height at ~6 nm. Figure 42 (d), shows a similar nanotube after aptamer functionalization, here we can observe a change in texture and height, ~9 nm, of the nanotubes. The ~3 nm increase in CNT height after aptamer

functionalization is in scope with expected aptamer size, 1-3 nm diameter sphere (~14,000 Da) provided by supplier (Base Pair Biotechnologies). Finally, Figure 42 (f) demonstrate functionalized nanotube surface after injection of IL-6 target protein (10 pg/mL), here we can see the interaction and binding of the IL-6 protein to the IL-6 aptamer on the surface of the CNT as a function of its height, ~ 19 nm, and texture. These results shows that the surface height of the CNT increased by about 10 nm as a result of this specific interaction. The green color of the IL-6 binding shows almost complete coverage on the nanotube surface suggesting the devices may have high sensitivity based on PASE-functionalization protocol. As a result of these AFM studies we can suggest that the functionalization protocol and specific targeting of IL-6 protein was a success.

SWNT devices were fabricated using vacuum filtration of carbon nanotubes and device processing inside a clean room [133]. Figure 43 presents the wafer scale image of the 240 element array of nanotube network sensors, generation 3. The sensor arrays were developed using a combination of vacuum filtration of carbon nanotube network film onto oxide coated wafers followed by multiple photo-lithography and reactive ion etching as described in Section 3.1. Our films were low concentrations (4  $\mu\text{g}$ ) and most of our films were isotropic and also mostly single layers laying on the substrate as shown in the SEM image of Figure 43 (F). Figure 44 presents the characteristics of the CNT-FET in buffer solution. The source to drain current ( $I_{\text{DS}}$ ) versus source to drain voltage ( $V_{\text{DS}}$ ) at different gate voltages is presented in Figure 44. The source to drain current decreased with increasing positive gate voltage. This suggest the device works

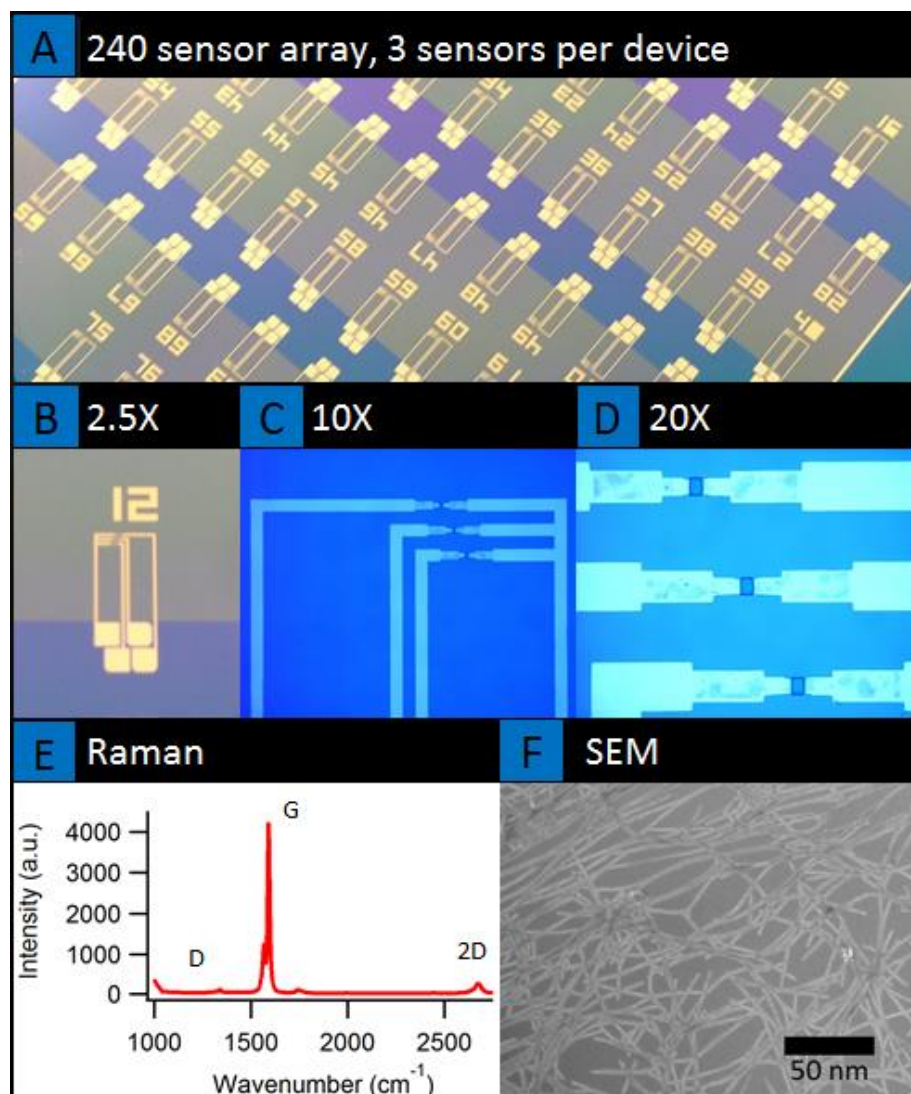


**Figure 43.** Device characterization showing optical images of the sensor array platform, (A, B, C and D), Raman characterization (E) and SEM image (F) of the CNT film imbedded within the sensors.

as a p-type semiconductor in 1X PBS. No leakage is seen at positive voltage the current is almost zero suggesting superior p-type transistor compared to past reports where there was still a significant drain current at zero and increasingly positive gate voltage [341]. Our CNT-FET is also definitely superior compared to past reports on using CNT-FET with antibody fragments which used a mixture of metallic and semiconducting nanotubes resulting in poor on/off ratios [342]. This point is important and needs to be emphasized as the whole sensing principle relies on the charge introduced at the nanotube channels either reducing or increasing the conductance with introduction of IL-6 protein. Leakage currents or poor on/off ratio's can thus affect the sensing reliability if one needs to detect such ultra-low concentrations. Thus we can be confident in our experiments that at  $V_G = 0$  V, the increase or decrease in conductance with introduction of protein is as a result of binding alone and not as a result of the

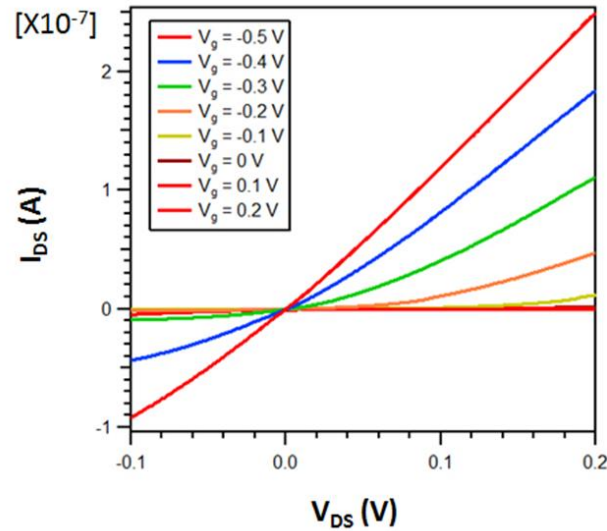


**Figure 44.** Electrical properties of CNT-FET devices before PASE-aptamer functionalization in phosphate buffer solution (1X PBS, pH 7.4).

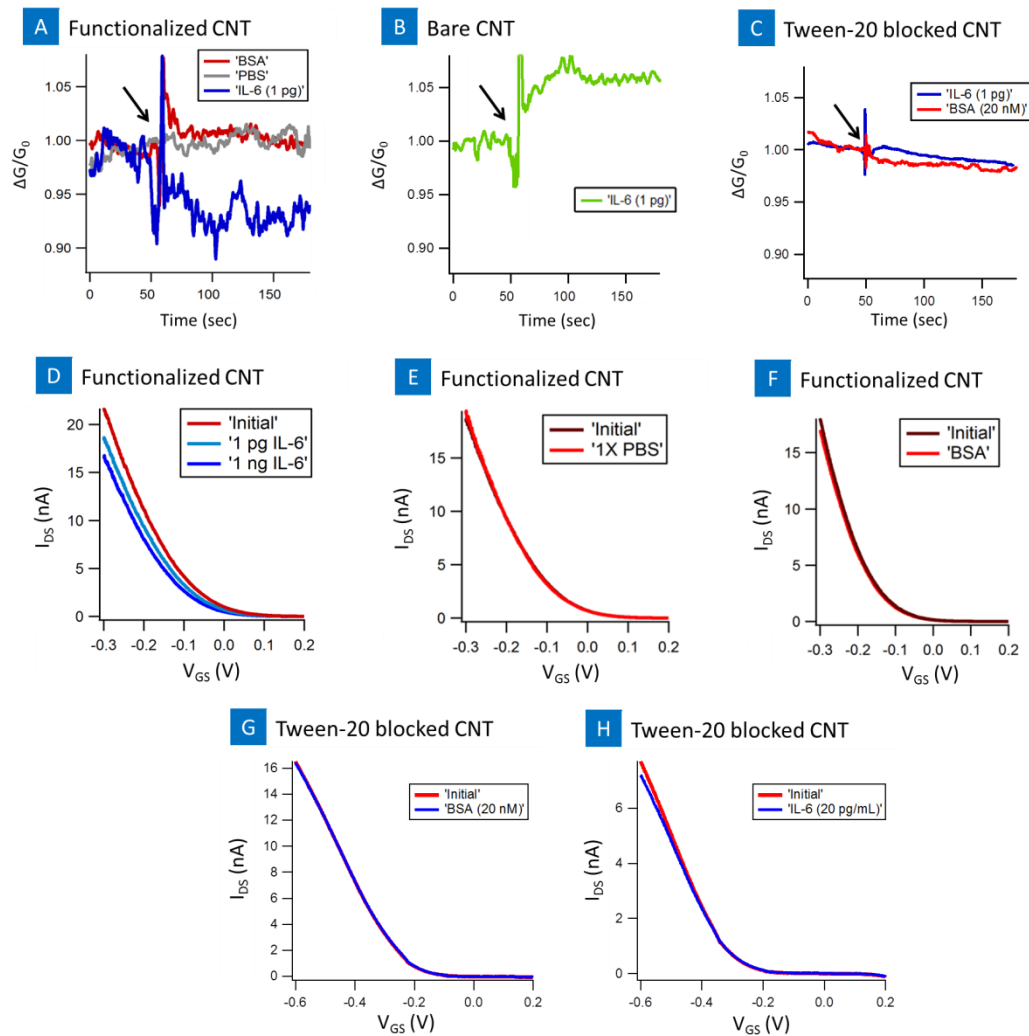
currents in the substrate.

Figure 45 (A and B) presents the real time sensing of IL-6 protein (BioLegend, Cat No. 575704) on the PASE-aptamer functionalized nanotube. First 5  $\mu\text{L}$  droplet of 1 mM  $\text{MgCl}_2$  1X PBS was placed on the functionalized device. The change in conductance was recorded followed by introduction of 1 pg/ml of IL-6. As soon as IL-6 was introduced, the conductance decreased and reached a saturation value as shown in blue color line of Figure 45 (A). Introduction of plain PBS or BSA on the functionalized surface showed little/no change and is shown in red and grey lines.

Figure 45 (B) presents the time dependence of the normalized conductance on introducing 1 pg/mL IL-6 to the bare unfunctionalized nanotube channel. The increase in conductance of the CNT-FET was clearly observed after introduction of 1 pg/mL of IL-6 onto bare CNT-FET without aptamers. Since IL-6 were non-specifically interacted with the bare CNT channels, the entire molecule must be placed inside the Debye length. IL-6 was negatively charged under our experimental conditions (pH 7.4), which was relatively higher than the isoelectronic point of IL-6 ( $\text{pH(I)} \sim 6.96$ ). The increase in conductance is therefore expected as the negative charge on the IL-6 is equivalent to applying a negative gate voltage, assuming capacitive gating effect [341].

Figure 45 (C, D, and E) presents the transistor device characteristics for PASE aptamer functionalized nanotube device. All the devices were p-type with average  $I_{\text{on}}/I_{\text{off}}$  of  $\sim 180$  and the nanotubes were semiconducting carbon nanotubes [133]. On introduction of PBS as well as BSA controls on the functionalized nanotube surface there was no significant shift in the  $I-V_G$  curve. However, on introduction of 1 pg/ml of





**Figure 45.** (A-C) Sensor response of the CNT-biosensor at source-drain bias of 0.1 V and at the gate bias of 0 V. (A) indicates the response after the introduction of 20nM BSA (red line), 1mM MgCL2 1X PBS (gray line), 1pg IL-6 target protein (blue line) to functionalized CNT-biosensor and (B) 1 pg IL-6 target protein to bare unfunctionalized CNT-biosensor (green line). (C) Shows response of tween-20 blocked CNT-biosensor to IL-6 protein (blue line), and BSA (red line). Arrow indicates the point of sample injection. (D-H) Before and after  $I_{DS}$ - $V_{GS}$  characterization of IL-6 aptamer functionalized CNT-biosensor with (D) 1 pg and 1 ng IL-6 protein injection, (E) blank 1mM MgCL2 1X PBS samples, and (F) 20 nM BSA. (G and H) show  $I_{DS}$ - $V_{GS}$  response of tween-20 blocked CNT-biosensor to BSA (G), and IL-6 protein (H).

IL-6 and 1 ng/ml of IL-6 on two different devices with similar initial characteristics, there was a change in the  $I-V_G$  curve. The  $I-V_G$  curve shifted down with increasing concentration suggesting positively charges by IL-6 decreased the conductance of the nanotube device. This is equivalent to applying a positive gate voltage and has been seen in previous reports [341]. The conjugated negatively charged IL-6-aptamer was placed inside the electrical double layer in the buffer solution, local positive charge in IL-6 molecules in the Debye length was detected as a decrease in conductance [341]. The specificity of the device is observed from the controls where both PBS and BSA showed no response of the nanotube sensor. Thus the results suggest that non-specific binding was successfully suppressed using aptamer functionalized nanotube surface.

Figure 46 (A) presents the real time response of the nanotube sensor from 1 pg/ml to 10 ng/ml of the IL-6. Each concentration of the IL-6 was seen with a characteristic spike as well as decrease in conductance as seen in all the experiments before. The change in normalized conductance ratio of the device went from 1.0 to less than 0.80, suggesting interaction between IL-6 protein and aptamer-PASE functionalized CNT and screening of the nanotube surface as a result of this interaction. The device saturated beyond 100 ng suggesting all the binding sites were depleted above these concentrations on the device and thus a saturated response. Figure 46 (B) presents the sensitivity as a function of concentration. The linear range at low concentration suggest sensitivity for 1-100 pg which could be useful for biomarker testing.

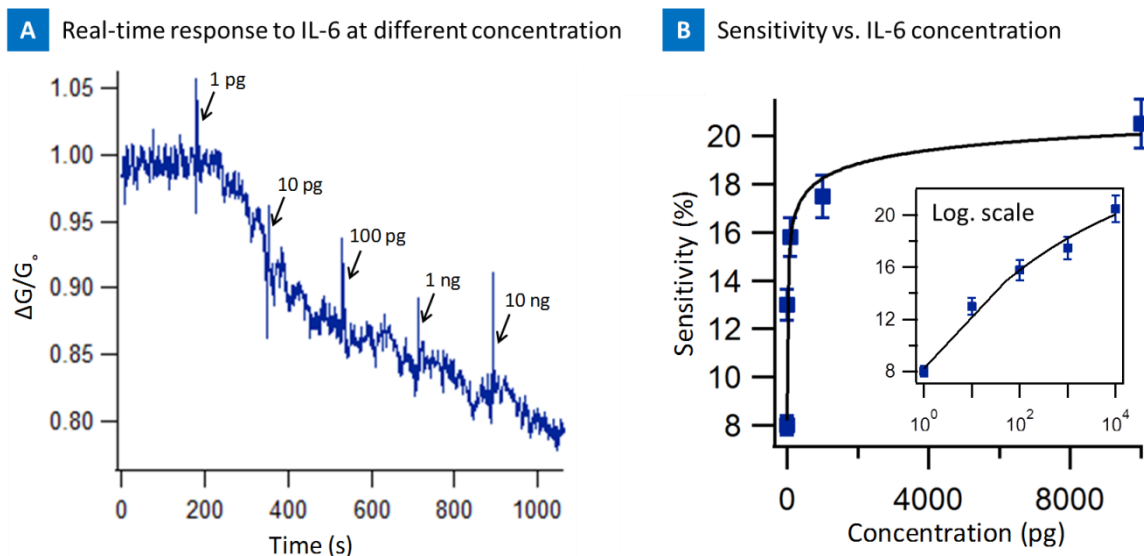


**Figure 46.** (A) Time dependence of normalized source-drain current of the CNT-biosensor at the source-drain bias of 0.1 V and at gate bias of 0 V after the introduction of IL-6 target protein at various concentrations onto the IL-6 aptamer functionalized CNT-biosensor. Arrows indicate the points of IL-6 target protein injection. (B) The Sensitivity of IL-6 aptamer CNT-biosensor as a function of IL-6 protein concentration (1pg to 10 ng /mL)

### 6.3. DISCUSSION AND CONCLUSIONS

The ability to detect IL-6 at low concentrations in serum can have implications in the clinic. IL-6 levels in serum >12 pg/ml have been correlated with large tumor size and elevated Serum-C Reactive Protein (CRP) levels for colorectal cancers [407]. In another study, patients with undetectable levels of IL-6 in the serum had a mean CRP level of 27 mg/liter, whereas it was 43 mg/liter for patients with detectable IL-6 levels (~300 pg/ml) [408]. Patients with IL-6 levels >300 pg/ml exhibited CRP levels of 117mg/liter [408]. IL-6 is detected in blood due to the secretion of IL-6 from the

cancer cells and thus very low detection thresholds can lead to life saving measures.

In the past the gold nanoparticle immunosensor gave a detection limit (DL) of 10 pg /mL of IL-6 in 10  $\mu$ L calf serum [372]. The sensitivity of SWNT forest immunosensor was 0.5 pg/ml as their lowest detection level for the same assay protocol, however here multi-label detection techniques were used which is still disadvantages and inferior compared to our label-free technique [373, 374]. Our nanotube-FET with 1 pg/ml sensitivity is thus capable of achieving 10 pg/ml sensitivity in serum. These are our next steps in being able to use these micro-arrays in unaltered blood that can detect both levels of IL-6 and circulating tumor cells. The big question that is not yet answered: is there a correlation between levels of IL-6 and CTCs in blood which could be indicative of the metastatic condition. Past reports have shown increased level of serum IL-6 in some patients with lung cancer has been reported previously and shown to be part of an inflammatory response [409]. Detecting both CTCs and IL-6 simultaneously would require an assay where both can be detected easily with minimal sample preparation and testing. The nanotube micro-arrays with the PASE functionalization protocol thus pave the way to detect these two important targets for diagnosis, treatment and progression of cancer.

To conclude, we have presented an approach to detect an important cancer biomarker namely IL-6 using semiconducting nanotube channels. IL-6 in the level of 1 pg/ml to 10 ng/ml was detected successfully using a PASE conjugated IL-6 aptamer as the molecular recognition element. The nanotube micro-array is thus capable of capturing cancer cells using antibodies and detecting IL-6 using aptamers. An assay

that could detect both proteins and cells simultaneously can lead to an understanding between the serum levels of IL-6, CRP levels and the number of CTCs in blood.

## 6.4. MATERIALS AND METHODS

### 6.4.1. DEVICE FABRICATION

The sensors are a three-terminal design. Each device shares a common source, and each has separate drain electrodes, generation 3. A carbon nanotube network connects the source and drain Ni/Au electrodes and the electrodes are covered by an insulating layer of SU8 photopolymer. Gate voltage is applied through an external Ag/AgCl reference electrode. 4  $\mu$ g film preparation and microfabrication of generation 3 devices are described in detail in Chapter 3.

### 6.4.2. DEVICE FUNCTIONALIZATION

CNT biosensors were functionalized with 1-Pyrenebutanoic Acid Succinimidyl Ester (PASE) conjugated IL-6 aptamers (Base Pair biotechnologies, Cat. No. ATW0077) at 20  $\mu$ g/mL in 1mM MgCl<sub>2</sub> 1X PBS buffer solution for 2 hours at room temperature. Devices then were functionalized with tween-20. Devices were rinsed three times in 1mM MgCl<sub>2</sub> 1X PBS and were stored with 5  $\mu$ L droplet of 1mM MgCl<sub>2</sub> 1X PBS for testing. For greater detail of the functionalization protocol please see Chapter 4.

### 6.4.3. TESTING

Bare non-functionalized and IL-6 aptamer functionalized devices were prepared. Both batches of devices were tested with 2  $\mu$ L droplets of 1mM MgCl<sub>2</sub> 1X

PBS (blank buffer solution), BSA (20 nM in buffer solution) and IL-6 target protein (1 pg to 10 ng/mL in buffer solution) individually.

100 mV source-drain bias and 0 V gate bias applied across the sensor and the source drain current,  $I_{DS}$ , was monitored vs time. 2  $\mu$ L droplet of sample solution, 1mM  $MgCl_2$  1X PBS, BSA, or IL-6 protein was pipetted directly into the standing 5  $\mu$ L 1mM  $MgCl_2$  1X PBS droplet on top of the devices. The change in current flow was monitored for the next three minutes. Devices were tested on a Signatone probe station platform using an Agilent 4156C semiconductor parameter analyzer with a Lab View Software. The entire probe station assembly is placed on an optical table that is vibration isolated using air on all 4 legs. A metal box covers the entire assembly to avoid electromagnetic interference. The probes are connected to the parameter analyzer using a triaxial cable that is EM shielded. Throughout the testing the devices were maintained inside a humid chamber to prevent evaporation of the sample droplet. For more detail on testing set-up please see Section 3.3.

## CHAPTER 7

### NANOTUBE DEVICES FOR CAPTURE AND DIGITAL PROFILING OF CIRCULATING TUMOR CELLS

#### 7.1. INTRODUCTION

Circulating Tumor Cells (CTCs) were first discovered in 1869 in blood of patients suffering from metastatic disease by Australian physician Thomas Ashworth using optical microscopy [10]. Current understanding is that these CTCs are thought to mediate spread of cancer at distant sites including lung, liver, bone and brain. CTCs are shed by primary and metastatic cancers in the range of 5-77,200/ml [410]. Recent clinically approved techniques for CTC detection include Veridex from Cell Search [411], CTC chip [33], and ADNA test [73, 412]. While these methods are impressive none of them are handheld point of care device where the test can be administered in clinic and results obtained in few minutes both for CTCs and cancer biomarkers. Therefore, with this objective in mind, we present our approach on development of nanotube devices for detection of both protein biomarkers, presented in Chapter 5, and CTCs using nanotube devices.

In this chapter, we will examine the interaction and response of the CNT micro-array devices to living cells, extending the results presented in the previous chapter on free protein interaction with devices; here we will more specifically examine the interaction of the receptor proteins on cell membrane with the functionalized nanotube surface. As seen in Figure 47, a living cell membrane is much more complicated than a free standing protein. In a cell, the bilayer contains a complicated structure of membrane proteins/receptors that are of critical importance for cellular functions such

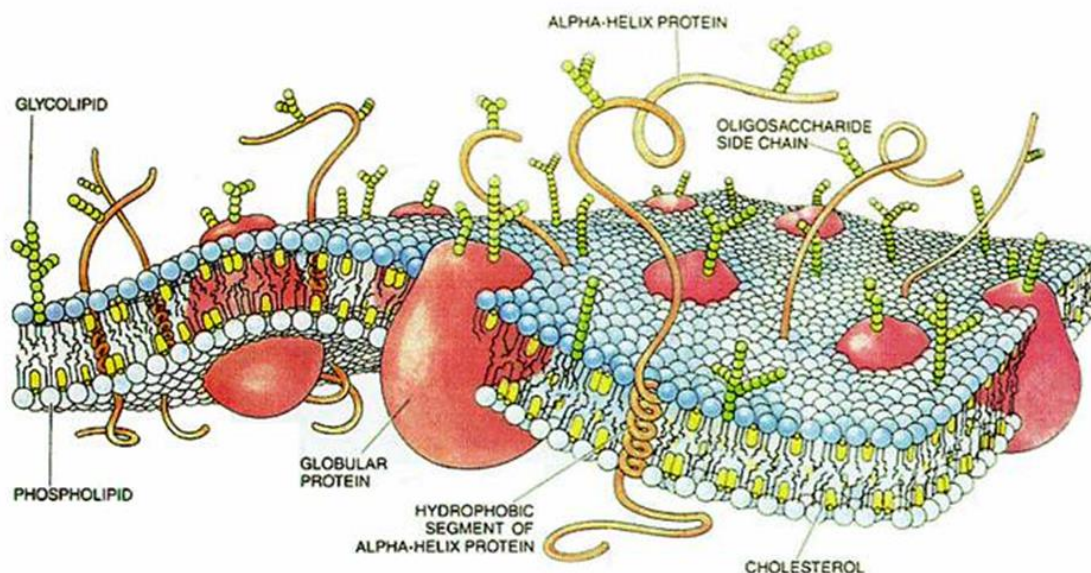


**Figure 47.** Illustration of a cell membrane [413]. The plasma membrane is composed of many proteins, receptors, and channels embedded in a fluid bilayer of phospholipids.

As communication with other cells, adhesion to external structures, and exchange of nutrients and wastes. It would be exciting to be able to locally capture the receptor protein structure on the cell membrane, by targeting tens of thousands of over expressed receptors that are present on the cancer cell membrane (i.e. EpCAM and HER-2), and anchoring the cell on the surface of the CNT through this interaction.

## 7.2. CELL CULTURE

Three breast adenocarcinoma cell lines, MCF-7, MCF-10A and SKBR-3 (ATCC, Cat. No. HTB-22; CRL-10317; HTB-30) were prepared for cell culture studies in this thesis. The general culture, preparation, and characterization of these cells



reviewed in this section apply to all cell studies from here on: spiked cells in 1X PBS buffer solution (Chapter 7), buffy coat (Chapter 8), and blood (Chapter 9).

Michigan Cancer Foundation-7 (MCF-7) is an adherent breast cancer cell line isolated in 1970 from a 69-year-old Caucasian woman. MCF-7 cells were extracted from an invasive primary ductal carcinoma breast tumor and over expresses EpCAM receptors [414].

Michigan Cancer Foundation-10 A (MCF-10A) is a non-tumorigenic epithelial cell line derived from adherent breast tissue cells from a 36 years old Caucasian female [415].

SKBR-3 is an adherent cell line isolated by the Memorial Sloan-Kettering Cancer Center in 1970. This cell line was derived from a 43 year old Caucasian female mammary gland, breast tissue, by pleural effusion due to an adenocarcinoma originating in the breast. The SKBR-3 cell line over expresses the HER-2 gene product including HER-2 membrane receptors [416].

The breast adenocarcinoma cell lines, MCF-7, MCF-10 A and SKBR-3 (ATCC, Cat. No. HTB-22; CRL-10317; HTB-30), were received frozen and cultured under conditions as recommended by the supplier, MCF-7: Eagle's Minimum Essential Medium (ATCC Cat. No. 30-2003), SKBR-3: McCoy's 5a Medium Modified Medium (ATCC Cat. No. 30-2007), and MCF-10A: MEGM kit (Lonza/Clonetics Corp. Cat. No. CC-3150) with the proper additives as recommended by ATCC and 10% fetal bovine serum (FBS), inside a cell culture incubator at 37 °C, 5% CO<sub>2</sub>, and 95% air, Figure 48.

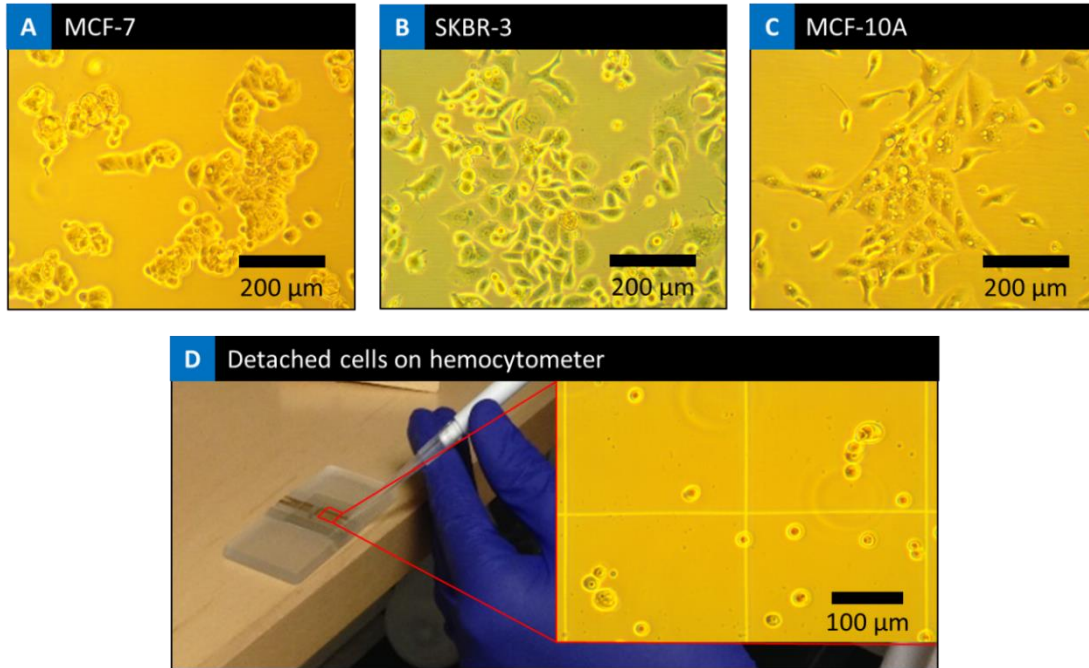


**Figure 48.** (A, B, and C) optical microscope image showing the cells cultured at ~80% confluency. Cells are detached at this point to be counted and prepared for testing. (D) Shows an optical microscope image of the detached SKBR-3 cells (right) on a hemocytometer counting device (left).

These immortal cell lines were subcultured and cryopreserved to be used for all the cell experiments in this thesis.

#### 7.2.1. IMMUNOFLUORESCENT STAINING AND CONFOCAL MICROSCOPY

MCF-10A cells are non-tumorigenic and are EpCAM negative. MCF-7 and SKBR-3 are EpCAM positive cell lines. SKBR-3 is additionally positive for HER-2 [417]. IgG is negative all across three cell lines. Series of immunofluorescent staining and confocal microscopy studies were done to confirm the overexpressed receptors mentioned above with all the cells used for the objectives of this thesis.

SKBR-3, MCF-10A, and MCF-7 cell lines were each suspended on a separate coverslip. The coverslips were prepared and stained with anti-EpCAM primary antibody, anti-mouse IgG-TR Texas Red conjugated secondary antibody, and DAPI according to the standard immunofluorescent staining protocol. Confocal laser scanning microscopy images were obtained on a Nikon Eclipse T. with coverslip corrected objective focused at 600X. Three images were obtained for each event through separate channels of DAPI, Texas Red, Alexa Green, and bright field accordingly. Merged images were created within the Nikon software as necessary. Results of these studies are presented in Figure 49, showing presence of DAPI on all three cell lines confirming a present of intact nucleus and viability of the cells. Additionally, MCF-7 and SKBR-3 cells are positive for EpCAM and MCF-10A is negative.

In a separate study, SKBR-3 and MCF-7 cells were also stained for IgG, stained with secondary antibody Texas Red, and cytokeratin, stained with secondary antibody Alexa Green, Figure 50 (A), showing positive results for cytokeratin and negative for IgG on both cell lines. MCF-10A was also stained for IgG, stained with secondary antibody Alexa Green, Figure 50 (B), and showed negative results. Thereby we can conclude carcinoma cells used here were positive for cytokeratin and all cell lines used in studies for this theses were negative for IgG, aligned with previous reports [417].

In a separate study, SKBR-3 cells were investigated for overexpressing HER-2 receptor. In this study SKBR-3 and MCF-10A, negative control, were both stained for HER-2 and DAPI and the results are presented in Figure 51. These results confirmed the over expression of HER-2 on SKBR-3 and its negative presence on MCF-10A cells.

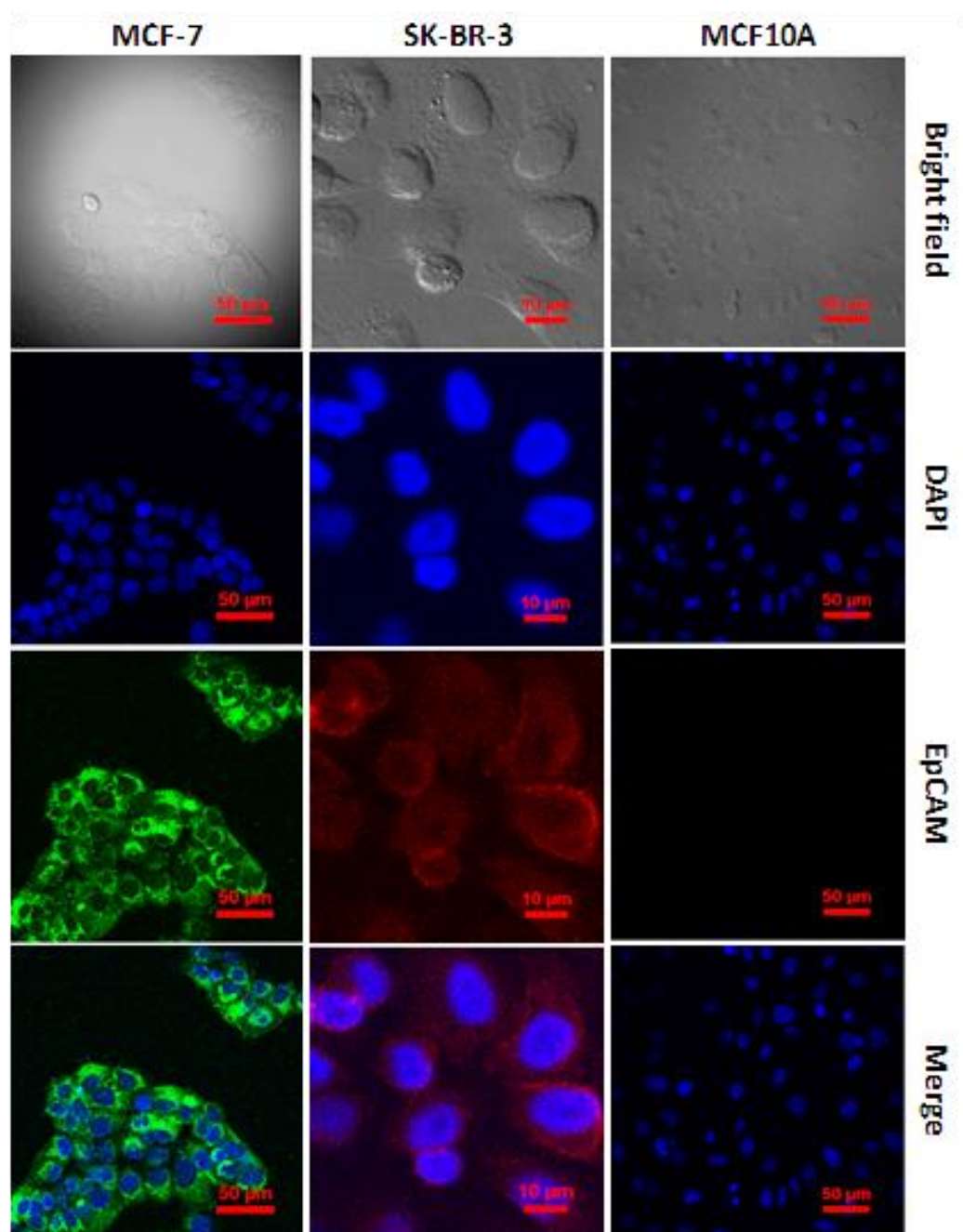


**Figure 49.** Confocal microscopy images of MCF-7, SKBR-3, and MCF-10A cell lines immunostained for EpCAM and DAPI. MCF-7 and SKBR-3 cells are positive for both EpCAM (in red or green) and DAPI (in blue) while MCF-10A cells are negative for EPCAM.

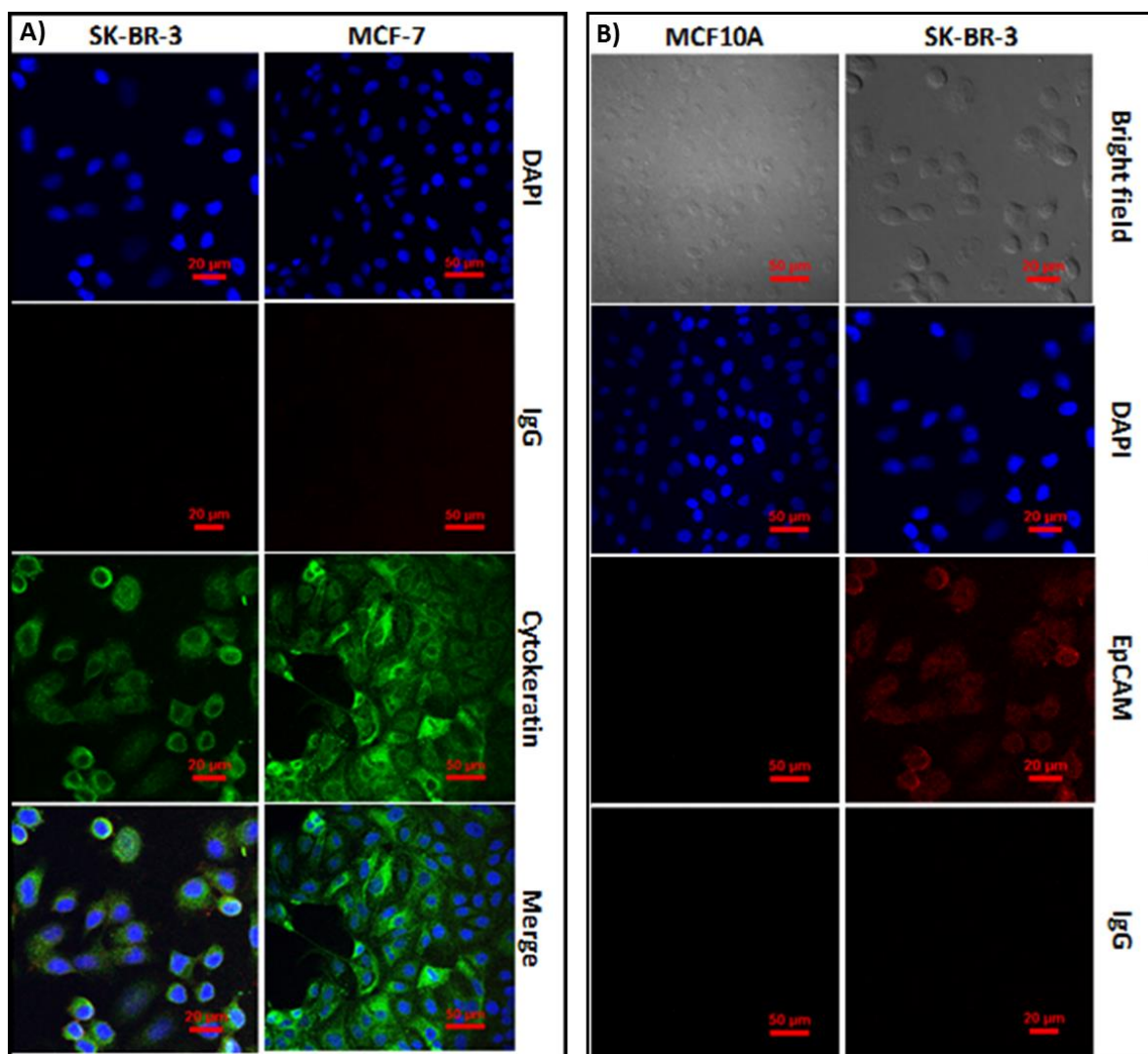


**Figure 50.** Confocal microscopy images of SKBR-3, MCF-7, and MCF-10A. (A) Presents SKBR-3 and MCF-7 cells immunostained for DAPI, IgG, and cytokeratin. SKBR-3 and MCF-7 cells are positive for cytokeratin (in green), and DAPI (in blue) while negative for IgG. (B) SKBR-3 and MCF-10A cells immunostained for DAPI, EpCAM, and IgG. EpCAM is positive for SKBR-3 and negative for MCF-10A, both cell lines are negative for IgG. IgG shows to be a universal negative control across cell lines.

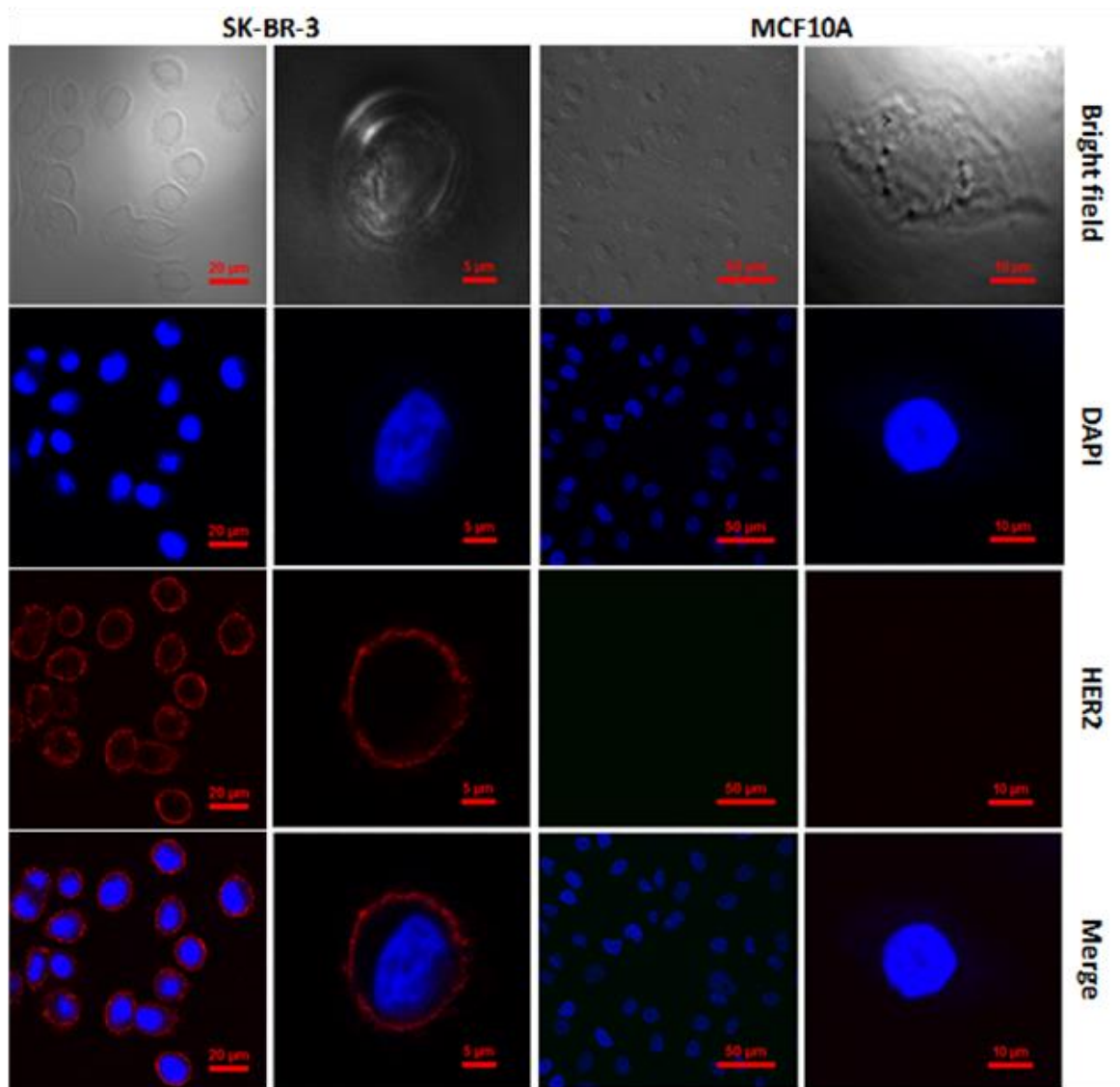


**Figure 51.** Confocal microscope image of the SKBR-3 and MCF-10 cells immunostained for DAPI and HER-2. SKBR-3 is positive for HER-2 and DAPI. MCF-10A is negative for HER-2 and positive for DAPI. First and third columns present culture of cells and second and fourth row demonstrate single cell staining.

### 7.2.2. CELL CULTURE PREPARATION FOR TESTING

Cells were grown in a culture medium for 3-4 days to reach ~80% confluence, Figure 48 (A, B, and C). The cells were then detached using Accutase solution (Sigma, Cat. No. A6964), cell detachment solution of proteolytic and collagenolytic enzyme, centrifuged and re-suspended in 1X PBS, counted using a hemocytometer, Figure 48 (D), and prepared at a proper concentration.

For the purposes of the studies in this chapter, MCF-7, SKBR-3, MCF-10A cells were each separately prepared at 10,000 cells/ $\mu$ L in 1X PBS buffer solution. The prepared concentrations of cells were used for testing the CNT devices for cell capture and detection as discussed in the results section.

### 7.3. RESULTS

Figure 40 (A) presents the schematic of the device for testing. The nanotube devices that were produced using vacuum filtration followed by film transfer, lithography, etching, and post processing were functionalized with PASE and antibody. The silver (Ag)/silver chloride (AgCl) reference electrode was used as the third gate electrode. The entire device except the active nanotube layer is sealed with an SU8 polymer. Figure 52 (A) presents optical image of the testing platform of the first-generation, wafer with 60 devices, also presented in Figure 23 (A), and Figure 52 (B) shows an optical microscope close up image of the device with the spiked sample on top. The active area of the single device is 100 X 80  $\mu$ m to enable the capture and detection of cells. Figure 52 (C) shows a confocal image of a single cell on the device,

indicating the viability of the cell and showing the active EpCAM receptors on the cell membrane at the time of testing.

### 7.3.1. NANOTUBE DEVICE ARRAY TESTING IN CELL CULTURES

Cellular detection with these devices is less understood and also quite rare because of the heterogeneity of the cell surface. CNT -immunosensor detection of cells via their surface markers has only been reported with devices containing nanotubes immobilized in a 1- $\mu\text{m}$  gap between electrodes. A decrease in conductance was attributed to straining of the nanotube due to the attachment of the cell [208]. To test larger, more clinically relevant cell samples and volumes, we have developed CNT micro-array devices with an 8000  $\mu\text{m}^2$  area thin film per device. The CNTs are functionalized with anti-EpCAM mouse monoclonal antibodies. EpCAM is a well-studied cancer biomarker, which functions in mediating homophilic cell–cell adhesions [295]. EpCAM was chosen as a model system because it is present in nearly all adenocarcinomas and squamous cell carcinomas [54, 418]. In the development of the sensors, we observed that gas molecules in the air were doping the CNT and obscuring the sensor readings. We corrected for this and tested these sensors with EpCAM-positive and EpCAM-negative cells and identified a unique electrical signature for the two different cell types.

Testing in different cell lines yielded highly intriguing results on the measurement of normalized electrical conductance  $\Delta G/G_0$  over various cell lines. In these experiments several cell lines namely normal breast cell line (MCF-10A), breast cancer cell lines (SKBR-3 and MCF-7) were used. Anti-EpCAM antibodies were used



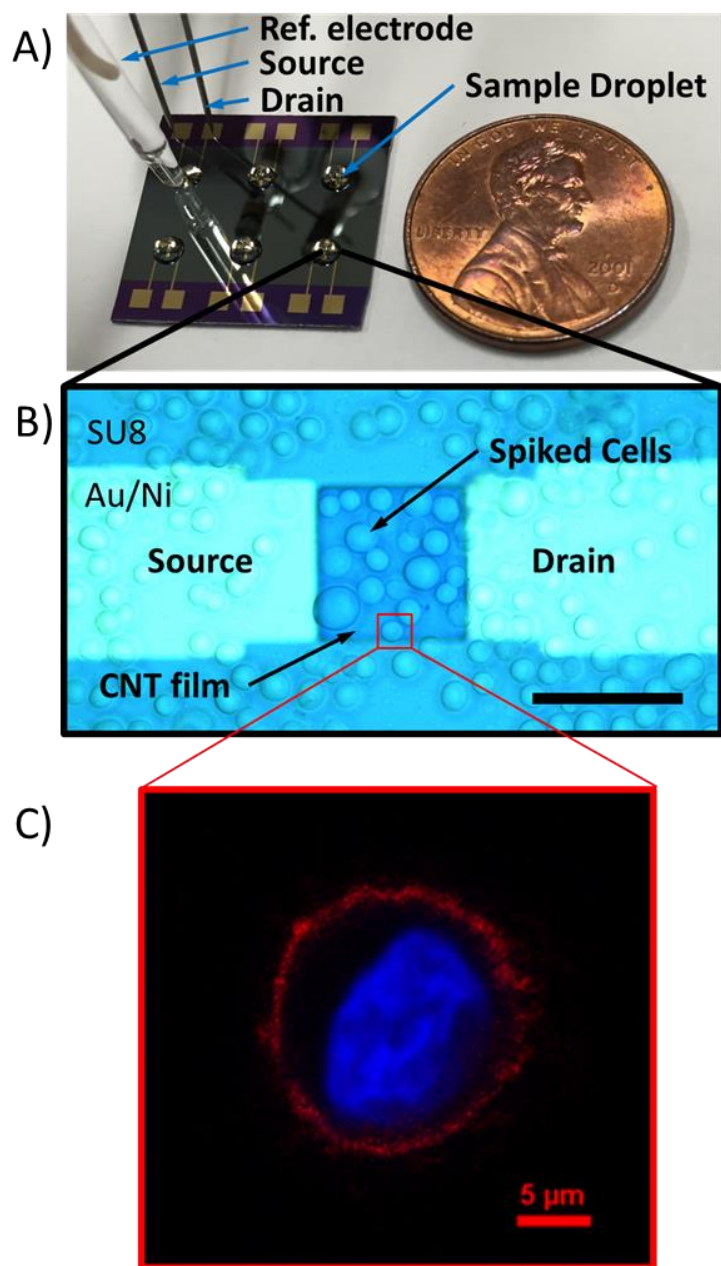


**Figure 52.** (A) Showing the CNT device testing set up with source, drain, and reference electrodes in contact on the device during testing on microarray chip. (B) Optical microscope image of a sensor device with a spiked SKBR-3 cancer cell sample droplet, scale bar 100  $\mu\text{m}$ . (C) Confocal image of a SKBR-3 cancer cell on the device stained for EpCAM, in red, and DAPI, in blue.

as specific control while anti-IgG antibody was used as non-specific control. Both SKBR-3 and MCF-7 overexpress EpCAM while MCF-10A normal cells do not, as described in Section 7.2. Surprisingly, two differential signals were generated between positive and negative controls. The positive controls such as targeting EpCAM on SKBR-3, Figure 53 (a), and MCF-7, Figure 53 (b), produced characteristic spikes in the electrical signatures with positive slopes that stabilized after few seconds. It is also noted that the stabilized conductance levels even after 60 seconds are higher than initial value before the sample addition suggesting an irreversible change in the electrical signature or forward reaction kinetics for the formation of the antibody-receptor complex. Similarly, the negative controls namely targeting EpCAM in MCF-10A, Figure 53 (c), and targeting IgG in all the cells, Figure 53 (d), and even PBS produced similar spikes with negative slopes and stabilized after several seconds. It is also noted that the final conductance after cell addition was higher than the initial conductance value and stabilized at that value. In determining the statistical significance, the average slope of ~0.5 seconds following the inflection point was calculated for each signal. Both data sets were determined to be random and of equal variance. A final  $p$  value of  $0.0011 < 0.05$  was calculated showing a statistically significant difference between all positive and negative controls as presented in Table 6. It should be noted that the positive controls consisted of two different cell lines MCF-7 and SKBR-3 targeted for EpCAM mentioned as G1 and G2 respectively in Table 6. Similarly the negative control consisted of EpCAM-MCF-10A, and IgG-(MCF-7, MCF-10A, and SKBR-3) mentioned as G3 and G4. The  $p$  values in the Table 6 suggest that there is a significant

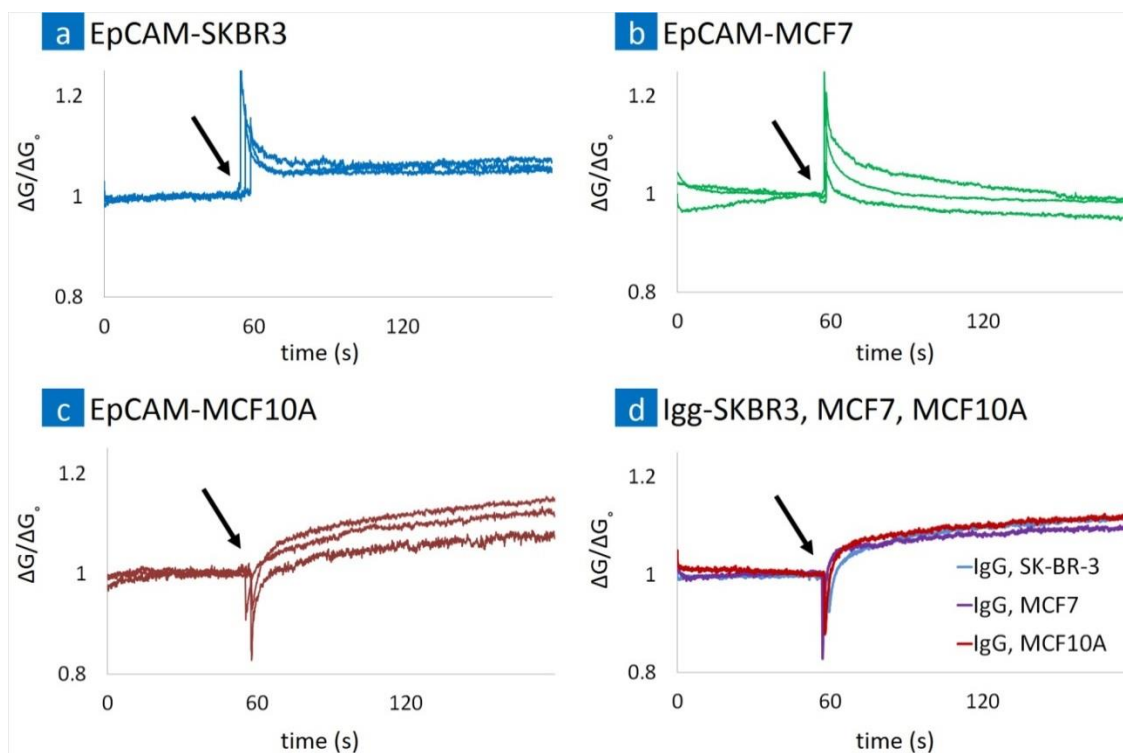


**Figure 53.** Testing in Cell Cultures: (a) Normalized device conductance of anti-EpCAM functionalized device with SKBR-3 cancer cells; (b) Normalized device conductance of anti-EpCAM functionalized device with MCF-7 cancer cells; (c) Normalized device conductance of anti-EpCAM functionalized device with MCF-10A normal cells; (d) Representative graph of normalized device conductance of anti-IgG functionalized device with SKBR-3, MCF-7 and MCF-10A cells.

**Table 6.** Statistical comparison between specific and control signals in cell cultures.

	Specific		Non-specific	
	G1: EpCAM-SKBR3	G2: EpCAM-MCF7	G3: EpCAM-MCF10A	G4: IgG-(SKBR3, MCF7, MCF10A)
Calculated slopes	0.0249	0.0498	−0.0471	−0.1761
	0.1205	0.0296	−0.0279	−0.0432
	0.0414	0.0943	−0.0258	−0.1197
Average	0.0623	0.0579	−0.0336	−0.1130
Std. deviation	0.0417	0.0270	0.0095	0.0544
<i>p</i> value	G1 versus G2 :			0.9072
	G1 versus G3 :			0.0340
	G1 versus G4 :			0.0225
	G2 versus G3 :			0.0107
	G2 versus G4 :			0.0164
Final <i>p</i> value	G3 versus G4 :			0.1120
	Specific versus non-specific			<b>0.0011</b>

statistical difference between specific and non-specific electrical signatures based on the slope of the conductance after sample injection. It is also observed that within the same group, the *p* values do not reflect a significant difference suggesting natural partitioning of specific and non-specific signals. This suggests that the nanotube sensor is capable of differentiating between two different cell populations which are similar except for their surface markers. The similar results over a wide range of cell lines and antibodies suggest specific interactions gave rise to characteristic spikes in electrical signatures due to their cooperative binding of antibodies to their receptors on the cell membrane. The ability to distinguish between cancerous and non-cancerous cell populations based on their surface markers with statistical significance in fast manner as presented here is thus a significant accomplishment for any nanotube thin film sensor. On-chip confocal microscopic analysis without removing cells could potentially lead to no CTC loss. A typical chip surface can have anywhere between 1 and 25 cells landing on the surface, and all of them can be counted easily. However, doing that in blood may be difficult, and this type of device could be useful for buffy coats where all

RBCs are removed before testing. Integrating such a device as demonstrated here with isolation protocols could enable handheld isolation and detection of CTC. However, these devices are also useful for cancer biomarker testing at the level of 1 ng/ml (below the diagnostic gray zone) as described in Chapter 5 and 6.

#### 7.4. KOHLRAUSCH-WILLIAMS-WATTS (KWW) FUNCTION MODEL

Kohlrausch Williams Watts (KWW) function is a stretched exponential function and the most popular function applied to fit the time-domain relaxation data [419]. Kohlrausch first proposed the stretched exponential in 1854 to describe the relaxation of charge from a glass Leiden jar [420]. Investigating the nature of specific and non-specific interactions, CNT micro-array devices demonstrated specific and non-specific interaction electrical signature that was fitted as per the KWW function for specific interaction:

$$\Delta G_{specific} = 1 + \exp \left[ - \left( \frac{t}{\tau} \right)^\beta \right] \quad (18)$$

and non-specific interaction [419]:

$$\Delta G_{non-specific} = 1 - \exp \left[ - \left( \frac{t}{\tau} \right)^\beta \right] \quad (19)$$

Figure 54 (A) presents the normalized,  $\Delta G/G_0$ , drain current,  $I_{DS}$ , signal of specific and non-specific controls fitted to the KWW functions for both specific and non-specific interaction respectively. The time constants were observed at  $\tau_{specific} = 1.094$ , for specific, and  $\tau_{non-specific} = 20.99$ , for non-specific interaction. The difference

in time constant ( $\tau$ ) is a great indicator showing a signature difference between specific and non-specific signals. Specific interaction is seen with interaction exponent  $\beta_{\text{specific}} = 0.1558$  and for non-specific interaction  $\beta_{\text{non-specific}} = 0.2878$ . The stretched exponential function contains just two free parameters: the “equilibration” time  $\tau$  and the fractional “interaction” exponent  $\beta$ , which satisfies  $0 < \beta \leq 1$ . Figure 54 (B) presents the modeling of the signal response for specific and non-specific interaction based as a function of interaction coefficient,  $\beta$ . The upper limit of  $\beta = 1$  corresponds to simple exponential decay or mild interaction, while lower values of  $\beta$  are indicative of a more complicated non exponential interaction process or multi-cell interaction, as the conductivity of the device is greatly manipulated and has to be due to large change in free energy that one can correspond to number of cells interacting with the device. Results here suggest that potentially one can correlate the  $\beta$  factor to number of cells interacting to the device and define it as coefficient multiplication of the number of cells on the device.

We monitored and recorded the number of cells on each device after the end of each test, no direct correlation with  $\beta$  coefficient, intensity of the  $I_{\text{DS}}$  signal, was observed with respect to the number of cells observed on each device. However, this does not rule out our original hypothesis completely, the number of cells interacting with the device can be different at the time of interaction and the time of microscopic observations as there was a few minutes of gap in-between. Also, not all the cells observed on top of the device could be interacting with the device. A more robust method is needed to control the number of cells on each device; perhaps using a piezo-

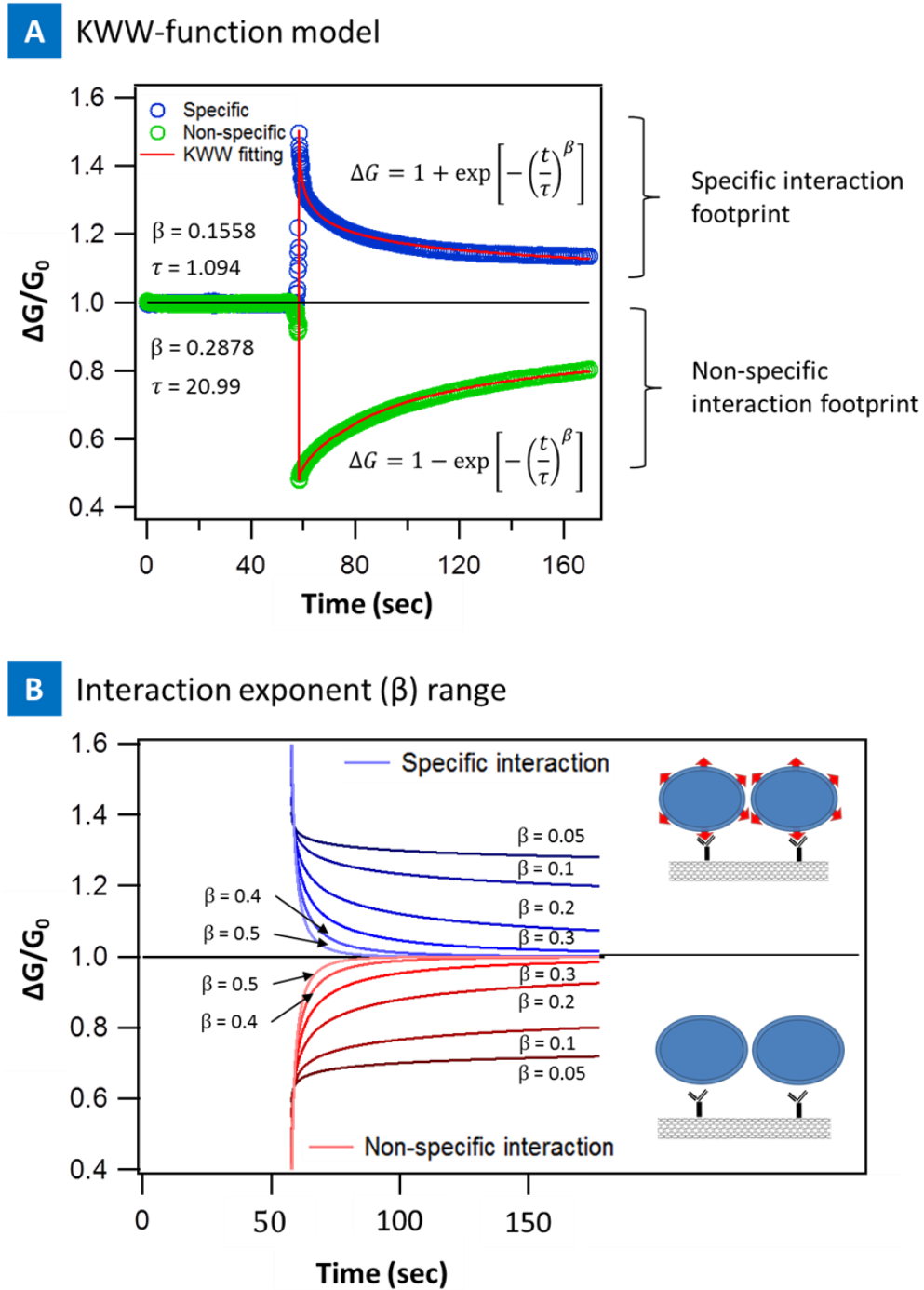


**Figure 54.** Principle of electrical signal response of CNT micro-array devices. (A) Specific and non-specific interactions. (B) Interaction exponent modeled for range of  $\beta$  for both specific and non-specific signal.

controlled manipulator to pick up individual cells and place them on the device can help gain a higher understanding of this interaction and the device response.

## 7.5. CONCLUSIONS

CTC detection and analyses in blood or body fluids may provide insights into the progression of cancer and treatment effectiveness. CTCs are only in the range of  $10^{-7}$  to  $10^{-3}$  among normal blood cells, making them rare [411]. The current CTC detectors are based on a mechanical cell sorting devices, which uses magnetic and shear forces inside a microfluidic channel to isolate cells. This chapter presents an electronic device that could be developed for point-of-care testing of CTCs. There are several significant challenges to be addressed, however, before full realization of the present device for CTC detection, which, once fully developed, could be a more powerful approach and may provide higher information content both on proteins and cells and therapeutic response. The device-related difficulties such as dispersion of individual nanotubes within the network for higher sensitivity, lithographic patterning, and density of nanotubes in devices, functionalization protocols, oxygen adsorption on the tubes, and cellular interaction within the Debye length can affect sensor conductance. With progress in device development, we have shown a 60-element array for the development of a point-of-care diagnostics type of device for cancer biomarkers and CTC. Using a PASE functionalization technique and testing with cells showed specific versus nonspecific binding with up to 95% confidence intervals with an average of 5–25 cells per sensor surface in 5  $\mu$ l of fluid. Instead of adding 1 ml of fluid to microfluidic device, fractionating the 1 ml body fluid into 5  $\mu$ l drops can result in



potentially no loss of CTCs during the testing process. However, they would require 200 devices that are individually addressable electronically. An application-specific integrated circuit could potentially interrogate all of the sensors and give a read out within few minutes, which could include a gamut of information from proteins, circulating tumor DNA, mRNA, and CTCs. Further, reaction chambers on chip for reverse transcription polymerase chain reaction can potentially analyze CTCs for specific gene sequences. These could be a part of the entire clinical process involving surgery, chemotherapy, radiation, and hormonal therapy. The nanotube platform is versatile, and hundreds of sensors patterned using clean-room processing techniques enable a different philosophical approach in detecting cancer biomarkers and CTCs and could potentially be a powerful tool for clinic in the future.

## 7.6. EXPERIMENT

### 7.6.1. CARBON NANOTUBE SENSOR FABRICATION

The CNT devices are a simple two-terminal design with liquid gating capability, each wafer include 60 devices (generation 1), Figure 23 (A). The structure and fabrication methods for the micro-array devices are previously described in Section 3.1. Catalytic chemical vapor deposition (CCVD)- synthesized, single-wall/double-wall CNT mixture (99% weight) purchased from Cheap Tubes Inc., 1–2-nm outer diameter and 3–30- $\mu\text{m}$  length, were used for these experiments. The nanotubes were suspended in isopropyl alcohol (IPA) at  $\sim 45\text{ }\mu\text{g/mL}$  and sonicated for 90 min. The solution was then diluted to  $\sim 3.5\text{ }\mu\text{g/mL}$  and sonicated for 3 h to completely disperse the nanotubes. 11.5 mL of the suspension was then further diluted with 85 mL of IPA and vacuum

filtered over a cellulose membrane, 0.22- $\mu\text{m}$  pore size. This method self-regulates the deposition rate of nanotubes on the membrane to produce an evenly distributed network,  $\sim 40\text{ }\mu\text{g}$  film, Figure 24 (C). The network was then transferred onto an oxidized (400-nm thickness) silicon wafer and taken for microfabrication, Section 3.1.

#### 7.6.2. CNT FUNCTIONALIZATION

The finished CNT sensors were functionalized with the antibody, via a pyrene linker molecule, and Tween-20 as previously described in Section 4.1. After functionalization, devices were incubated in a 2- $\mu\text{L}$  droplet of PBS inside a humid chamber at 4  $^{\circ}\text{C}$  before testing.

#### 7.6.3. EXPERIMENTAL SET-UP

Experimental set up is previously described in Section 3.3. The testing protocol started with a hydrated device, and a 2  $\mu\text{L}$  droplet of 1X PBS which was placed immediately after functionalization. The bias was applied and the sensor was monitored for the initial 60 seconds, then 5  $\mu\text{L}$  droplet of cancer cell spiked or plain PBS sample solution was pipetted directly into the standing 5  $\mu\text{L}$  droplet. Devices were monitored for 120 seconds after each addition of a new sample solution. The total duration of one test was 3 minutes long. To compare results among devices,  $I_{SD}$  data were normalized to obtain the  $\Delta G/G_0$  values for conductance.

## CHAPTER 8

### LABEL-FREE CAPTURE OF BREAST CANCER CELLS SPIKED IN BUFFY COATS USING CARBON NANOTUBE ANTIBODY MICRO-ARRAYS

#### 8.1. INTRODUCTION

Commercially available nucleic acid microarrays allow sensitive identification of thousands of DNA sequences simultaneously [421-425]. However, they cannot capture many changes in cellular response and function in many cases which are carried out by proteins. The cellular proteomic profiles, which is directly relevant for disease detection, label-free high-throughput diagnostics has, however, remained a challenge and sample handling to get a complete proteomic profile is also challenging and enormous in some cases [426].

Techniques that have been developed for protein analysis include: flow cytometry [427], fluorescent reporting of antigen–antibody binding [428], time-of-flight mass spectroscopy [429], electrophoretic separation [430], label-free detection of changes in surface mechanical properties due to antigen–antibody binding using micro-cantilevers [208], change in electronic properties using silicon nanowires [431] and carbon nanotubes due to biomarker interaction [432]. The cellular proteomic analysis that is important for auto-immune diseases, label-free devices are rare [365]. Some of these devices have focused on understanding how device properties change on cellular attachment or detachment after growth on the substrates and the drug interaction [433].

Recent progress in area of isolation of rare cells has used different techniques namely immunomagnetic methods [33], microfluidic chips [434, 435], laser scanning

cytometry [436], and nano-Velcro array [437] to name a few and has created the need for capturing and molecular profiling of cells based on their biomarkers for targeted therapy. While these above mentioned devices have used large volumes of blood (~7.5 ml) to isolate circulating cancer cells using microfluidic devices, magnetic devices for fine needle aspirates (1  $\mu$ l) has also been reported to capture and analyse single cells [438], thereby showing the importance of capturing cells and profiling their biomarkers in small and large volume samples. Current technologies namely ELISA or Western blots for measuring protein concentrations are painstakingly slow and need skilled personnel for accurate results. Therefore, devices that can capture single cancer cells in highly complex medium such as blood/buffy coats in rapid, low cost and high throughput fashion with the capability to profile them for their biomarker can result in significant clinical impact.

In this study we present capture of breast cancer cells spiked in buffy coats using carbon nanotube micro-arrays functionalized with anti-EpCAM antibodies and their stratification based on their electrical signatures using classifier based on Dynamic Time Warping (DTW). Epithelial Cell Adhesion Molecule (EpCAM), is a mesenchymal marker that is overexpressed in all epithelial cancer cells [439, 440]. EpCAM is overexpressed in carcinomas and also is upregulated in metastases thereby making it a highly valuable diagnostic marker [441]. A multiplexed micro-array of nanotube sensors functionalized with anti-EpCAM antibodies enables measurement of electrical signatures of specific and non-specific interactions as characteristic spikes in conductance versus time data. These signatures are then analyzed using Dynamic Time

Warping (DTW) technique to develop heatmap with integrated dendrogram to enable classification of the electrical signatures and relate it to their sample condition (MCF-7 spiked buffy or plain buffy), for the ease of reference, we call cases and controls. The experiments demonstrated “spikes” in electrical device signatures in cell cultures and cancer cells spiked in buffy coats with natural partitioning between plain buffy coats and spiked buffy coats using nanotube-antibody arrays. To predict classification between cases and controls, the training set data indicated ~100% sensitivity, ~90% specificity, and ~96% accuracy in classifying devices that corresponded to un-spiked and spiked buffy coats based on their electrical signatures. A blinded test to classify case and control samples revealed ~91% sensitivity, ~90% specificity, and ~86% accuracy. Staining of captured cells on the device based on electrical signatures using confocal microscopy revealed the overexpression of EpCAM with each device capable of capturing anywhere from 1-25 cells per device suggesting single cell sensitivity. Our demonstration of the combination of multiplexed micro-arrays, sensitive nanotube elements and statistical data mining enables a new line of thought in developing devices for isolation of cells based on their mesenchymal biomarker profiles both in fine needle aspirates and for large volume samples in isolation and analysis of circulating tumor cells. The study presented in this chapter was approved by the University of Louisville Institutional Review Board, IRB#10.0428, and the IRB at Worcester polytechnic Institute, IRB#00007374.

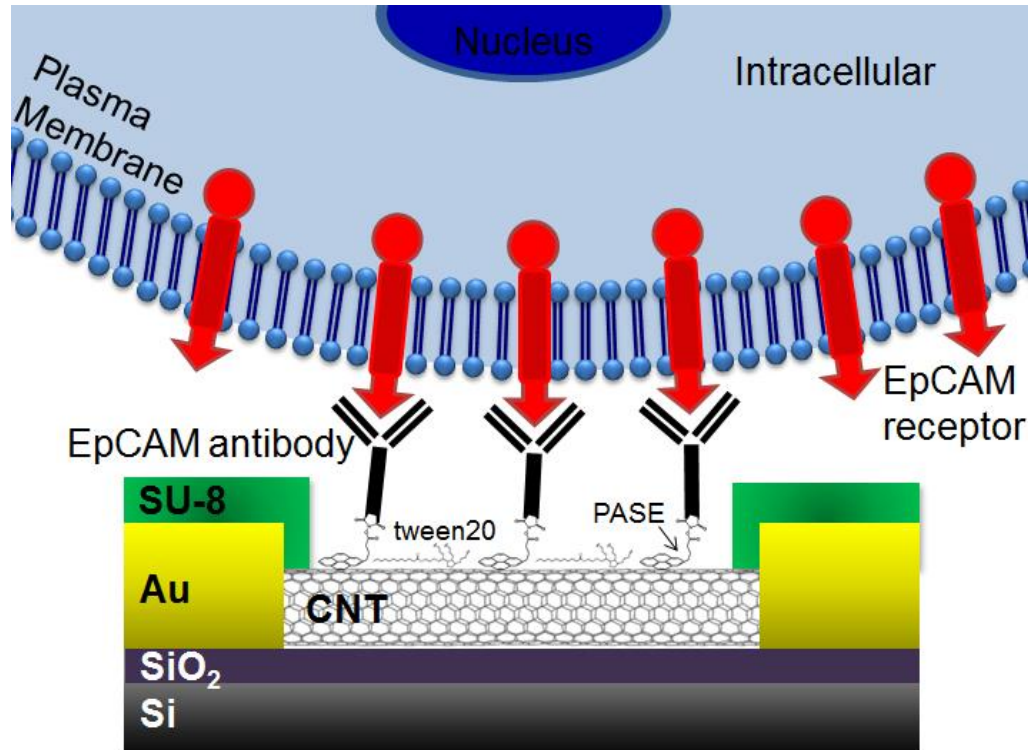


**Figure 55.** Schematic of Sensing Mechanism: Cooperative binding of anti-EPCAM antibodies to their corresponding receptors in cells on top of nanotube biosensors creates “spikes” in electrical conductance.

## 8.2. RESULTS

Figure 55 presents the schematic of the sensing technique. Biomolecular reactions are driven thermodynamically by the reduction in free energy of the system. For specific interactions, the reduction in free energy should be higher than non-specific interactions as presented in equation 20 [442]. It is this thermodynamic advantage of specific interactions that is the hall mark of living systems which enables a high degree of control in biological processes. Otherwise, non-specific interactions would prevail resulting in loss of cellular specificity and directionality in function

[442]. One can use a spectrum of energy domains to transduce the change in the free energy of the specific interactions into mechanics, electricity, thermal or magnetism [442]. While label-free sensors have been developed for measuring ultra-low protein concentrations as mentioned before, the measurement of specific versus non-specific binding events in cells as electrical spikes in a fast manner and the ability to stratify them rapidly are rare. If such cellular arrays that are fast, label-free and one that can detect specific versus non-specific interactions at the level of single cells and relate the electrical signatures to their biological condition using advanced classifiers developed, could revolutionize the disease paradigm for isolation and analysis of rare cells.

$$\Delta G_{specific} \gg \gg \Delta G_{non-specific} \quad (20)$$

Since the reduction in free energy is universal for specific and non-specific pairs, we hypothesize that this should be true for detection of specific versus non-specific interactions in cells. Extracellular overexpressed receptors namely EpCAM interacts with their corresponding anti-EPCAM antibodies on the nanotube surface. The cooperative specific interaction of thousands of extracellular receptors with specific antibodies on nanotube surface creates spikes in the normalized electrical conductance versus time [366]. Non-specific samples such as plain buffy coats also create such spikes in the electrical conductance versus time data with differences in their slopes. The philosophy behind this work is whether such spikes in the signals could carry meaningful information about the sample condition/interaction that could be indicator of disease status.

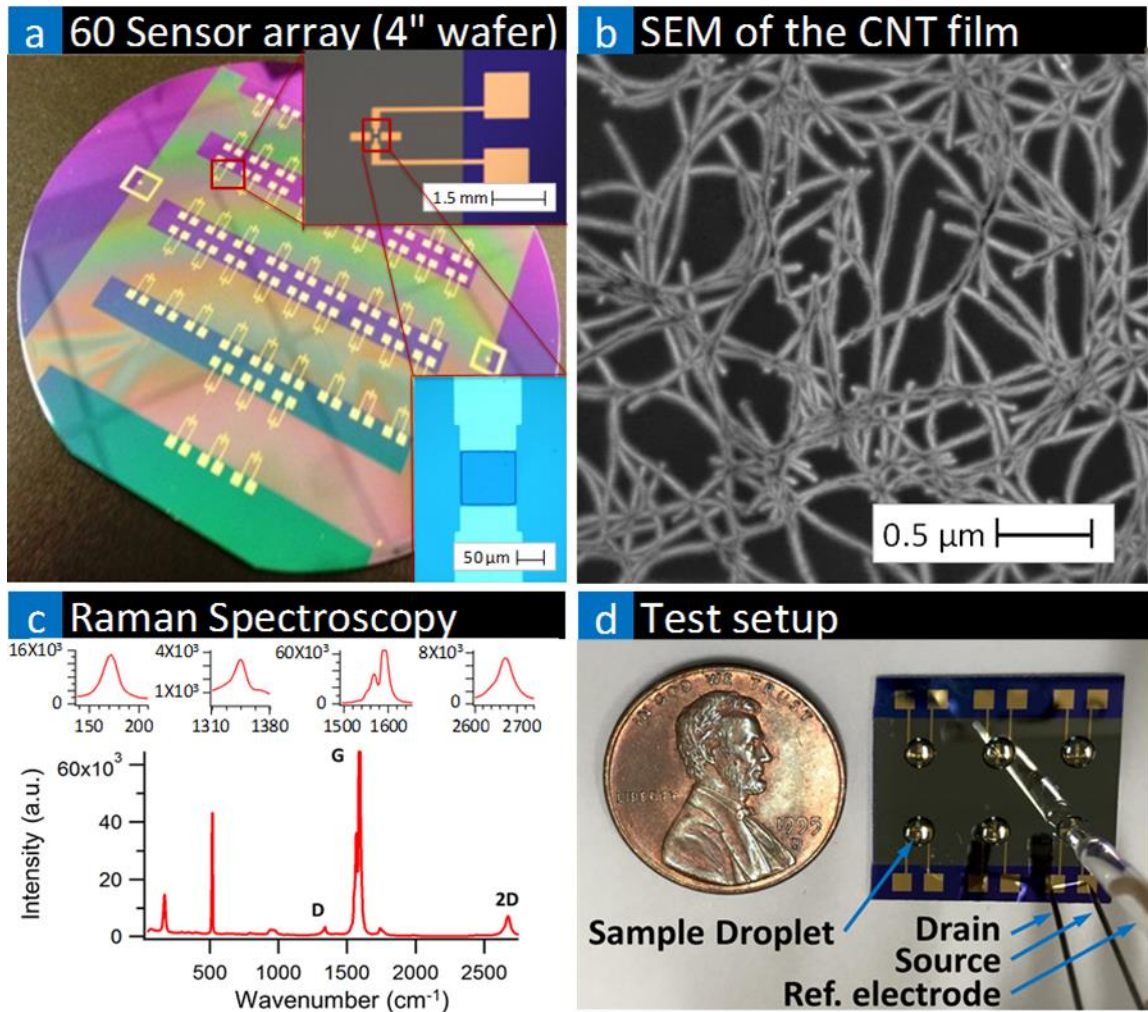
### 8.2.1. FABRICATION OF NANOTUBE SENSOR ARRAYS

Figure 56 (a) presents the wafer scale image of the 60 element array of nanotube network sensors. The sensor arrays were developed using a combination of vacuum filtration of carbon nanotube network film onto oxide coated wafers followed by multiple photo-lithography and reactive ion etching, covered in detail in Chapter 3. CNT films used here were very low concentration (4  $\mu\text{g}$ ) isotropic and also mostly single layers laying on the substrate as shown in the SEM image of Figure 56 (b).

Figure 56 (c) presents the Raman spectroscopic micrograph of the nanotube network suggesting a very large G band ( $1590\text{ cm}^{-1}$ ), small D band ( $1340\text{ cm}^{-1}$ ) and large 2D band ( $2673\text{ cm}^{-1}$ ). This suggests very low amorphous carbon content. Further, we also measured the  $I_G/I_D$  ratio for several networks measured  $I_G/I_D \sim 30$  suggesting a low density of defects and suitable for high-quality sensing applications. The Iso-semiconducting nanotubes had iodine as specified by the manufacturer (5% by mass using neutron activation analysis) in the form of iodixanol. This was observed in the shift in radial RBM mode  $\omega_r = 174\text{ cm}^{-1}$  suggesting iodine doped nanotubes due to poly iodide ions or  $\text{I}_3^-$  and  $\text{I}_5^-$  in the RBM mode at the same excitation wavelength [332]. The iodine also decreased the tangential mode to  $1590\text{ cm}^{-1}$  in these samples as compared to pristine nanotube samples ( $1593\text{ cm}^{-1}$ ) in line with past reports [333]. Figure 56 (d) shows an array of devices and compares them to a penny with the source, drain, reference Ag/AgCl electrode and sample droplet all in one set-up.

4  $\mu\text{g}$  CNT films were used for all the studies henceforth presented. Full characterization of these films and devices are reviewed in detail in Chapter 3.





**Figure 56.** Device Characterization: (a) Optical image of the wafer with 60 devices manufactured using photolithography, metal deposition and etching; (b) scanning electron micrograph of carbon nanotubes; (c) Raman spectrum of semiconducting carbon nanotubes showing a large G band, small D band and 2D band. The  $I_G/I_D \sim 30$  was observed in these nanotubes; (d) Test set up showing 6 devices on a chip and compares it to a penny. The source, drain and reference electrodes are observed.

### 8.2.2. ANTIBODY FUNCTIONALIZATION

In exploring the use of such multiplexed nanotube devices for measuring differential cellular response, understanding the functionalization of antibodies that are specific to the receptors, their coverage on the surface and their eventual interaction with the cellular receptors producing an electrical signal must be understood in depth. The prepared SWNT sensors were functionalized with anti-EpCAM antibodies through a pyrene linker molecule, as described in detail in Chapter 4. Overall the PASE conjugation provided a stable platform for all sensing in cell cultures and buffy coats.

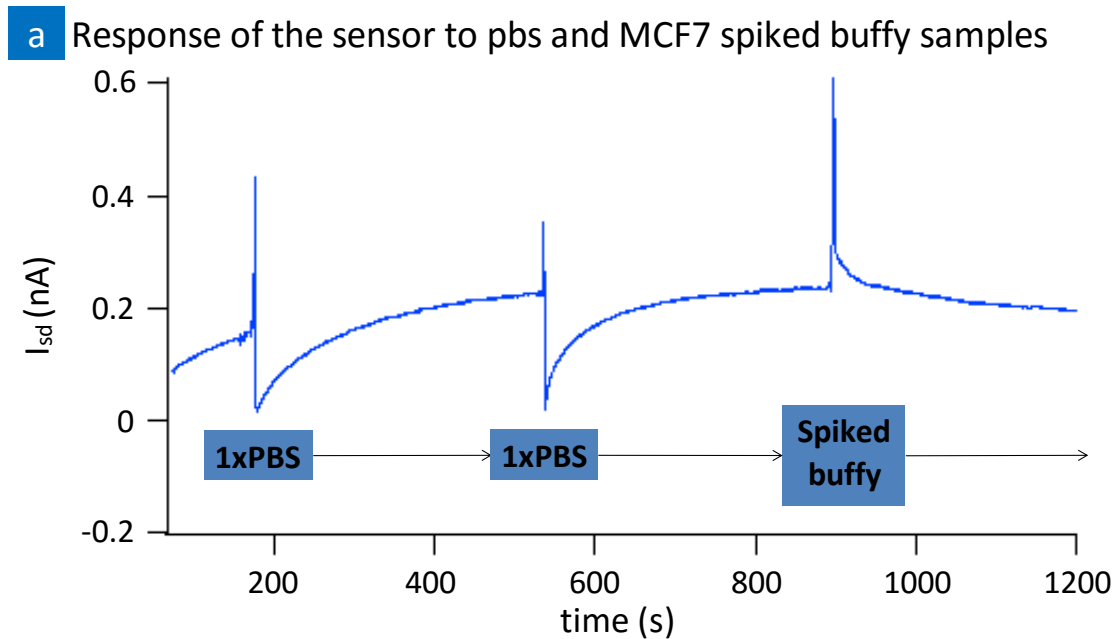


**Figure 57.** Representative graph of the testing protocol. First drop of 5-10  $\mu$ l PBS is added to the sensor followed by wait period of several hundred seconds, followed by second PBS drop followed by wait period of several hundred seconds followed by addition of spiked buffy or plain buffy coat. This ensures the sample is behaving the same way over a time period before addition of the actual sample.

### 8.2.3. TESTING IN BUFFY COATS AND DEVELOPMENT OF A STATISTICAL CLASSIFIER FOR LIQUID BIOPSY

If nanotube thin film sensors were to be used for any diagnostic/prognostic value in the clinic, testing in more complex medium such as buffy coats/blood would be necessary. The ability to capture cancer cells and analyze their biomarkers in complex medium both in large and small volumes can have profound translational impact. Biosensors that produce electrical signals or other time series data present a unique challenge for researchers attempting to use such sensors to classify biological samples. The analysis of such data is complicated by undesirable variation in the time domain between samples of the same class in addition to variability in the characteristic patterns that may be shared between samples of the same class. Further, use of such complex medium such as buffy coats with white blood cells and other proteins makes it highly complicated and cannot be simply differentiated based on simple time domain electrical signatures. Currently, there exists no statistical classifiers for “liquid biopsy” samples for both small and large volumes of samples.

We used ANOVA balanced design to reduce any systematic variability. Factors in ANOVA design includes medium (Bare, IgG, and EpCAM) and three types of samples (PBS: control 1, Buffy: control 2 and Spiked Buffy: case) with fixed number of replicates. With the same design two data sets were generated for training set and then for test set. As summarized in Cambon *et al.*, [443, 444], there are different approaches to classification of higher dimensional data sets based on biosensor signals. In the recent past, group classification of cervical cancer versus control samples were done based on differential scanning calorimetry thermograms. The excess specific heat

capacity versus temperature were measured from both cervical cancer sample and control samples. These were then classified using a parametric classifier with 96.7% classification rate. Compared to the newly developed parametric method, the I-RELIEF method that is commonly used to classify higher dimensional data sets only showed a classification rate of 73.3% [445]. Here, we use Dynamic Time Warping (DTW) for classification as the biosensor signals and patterning techniques are quite different.

To demonstrate the ability of the devices to discriminate between buffy and spiked buffy signals, we used a training-test approach to building a k-nearest neighbor classifier using DTW [446]. The training data consisted of ten buffy coat samples and 17 spiked buffy coat samples. k-fold cross-validation parameter selection was conducted using tenfold cross-validation on 10,000 bootstrapped samples from the training set of 27 signals for which the class (buffy vs spiked buffy) was known. The tuning parameters selected were those that minimized the mean and variance of the misclassification rate. Once tuning parameters had been selected, 22 test signals (of class unknown to the personnel constructing the classifier) were classified using a DTW distance-based k-nn classifier using the training signals as reference signals. The test set misclassification rate, classifier sensitivity, and classifier specificity were then used as criteria to measure the success of the devices in discriminating between positive and negative samples. To evaluate if devices could differentiate between MCF-7 positive samples and MCF-7 negative samples, both were tested utilizing the devices. The negative samples consisted of a buffy coat sample from the biorepository without

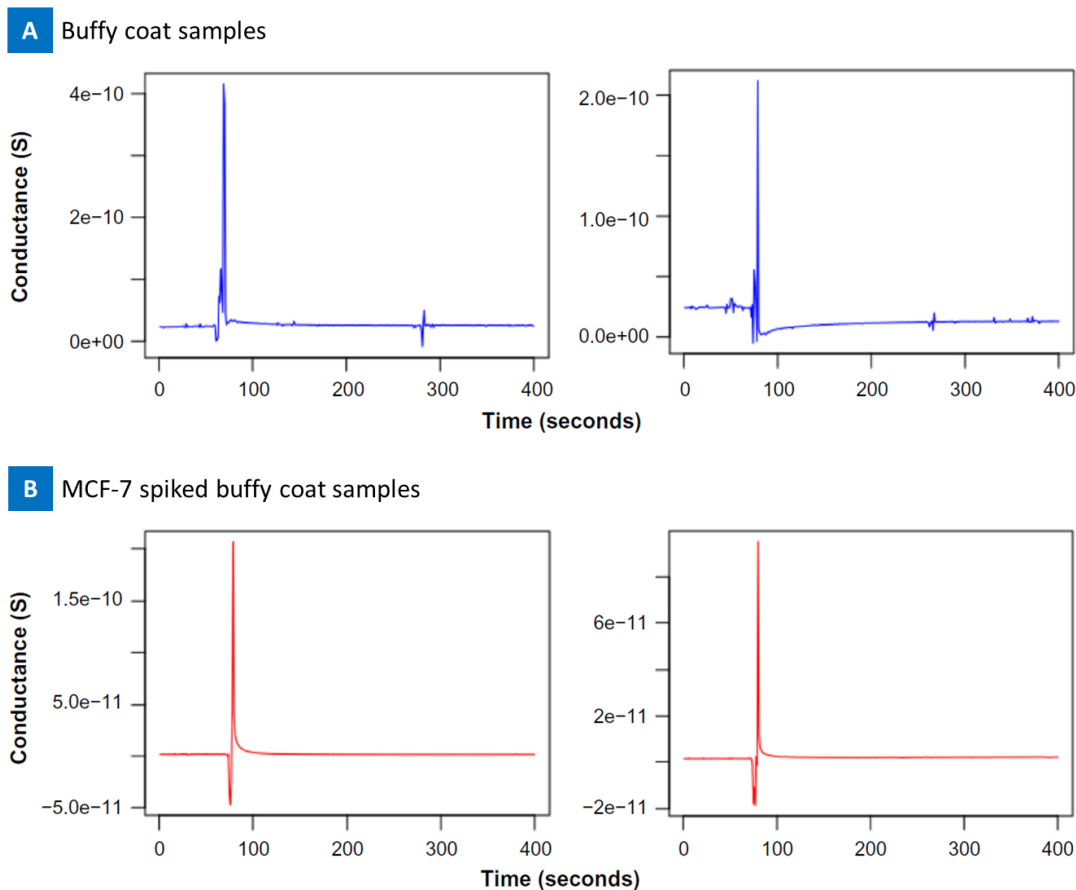


**Figure 58.** Plots of representative electrical signatures from samples used in construction of a k-nn DTW distance-based classifier for breast cancer surface marker profiling. (A) Two plain buffy coat samples. (B) Two spiked buffy coat samples.

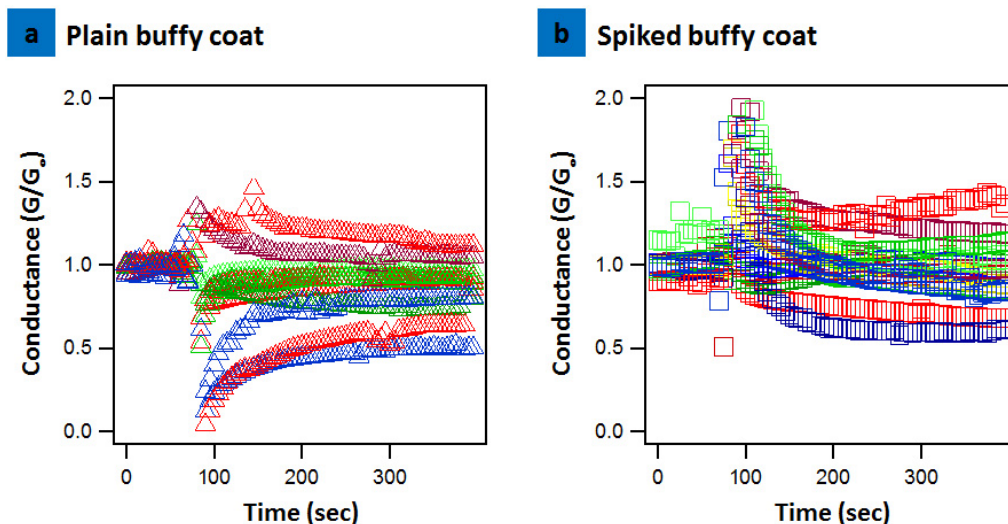
the presence of breast cancer cells. The positive samples consisted of the same buffy coat sample that was spiked with MCF-7 breast cancer cells (10,000/ $\mu$ l) as a proof of concept. The drain current from the nanotube devices was recorded continuously throughout each experiment. A representative figure of the testing protocol is presented in Figure 57 and two MCF-7 positive and two MCF-7 negative samples are depicted in

Figure 58. The resulting data consisted of time series with characteristic “spikes” occurring after the application of the sample as shown in Figure 59 for the training set.

#### 8.2.4. CONSTRUCTION OF THE CLASSIFIER

A set of training signals from the devices was used for selecting the optimal tuning parameters for the classifier. An independent set of mixed signals was then classified using the classifier. Sensitivity, specificity, and the misclassification rate of the classifier on the test set were then used to evaluate performance.

To describe the construction of the classifier, we first introduce some notation. We represent a device signal as a time series,  $y = [y_t, t \in T]$ , where  $T$  is a finite set that indexes time. To indicate that the signal is the  $i^{\text{th}}$  replicate from the  $j^{\text{th}}$  group (Buffy vs. Spiked buffy) we use the notation  $y_{i,j}$ . Before a classifier could be constructed, the raw signals were processed so that the signals had comparable a sampling rate, length, and intensity. The signals  $y_{i,j}$  were first averaged so that each signal had the same sampling rate of one sample per second. The signal was then truncated by removing series values between the first value and five seconds after signal most extreme peak—resulting in a new  $t_0$  for each signal. Experimental variation in the timing of the replicate drops contacting the device resulted in non-uniform length time indices. For length standardization, the signals were then truncated at 253 seconds. The final processing step was mean and variance standardization so that each signal had mean 0 and variance 1.



**Figure 59.** Merge of sensor arrays with statistical classifiers in training set: Normalized conductance versus time data from the arrays grouped into two categories. (a) Plain buffy coat; (b) buffy coat spiked with MCF-7 cells.

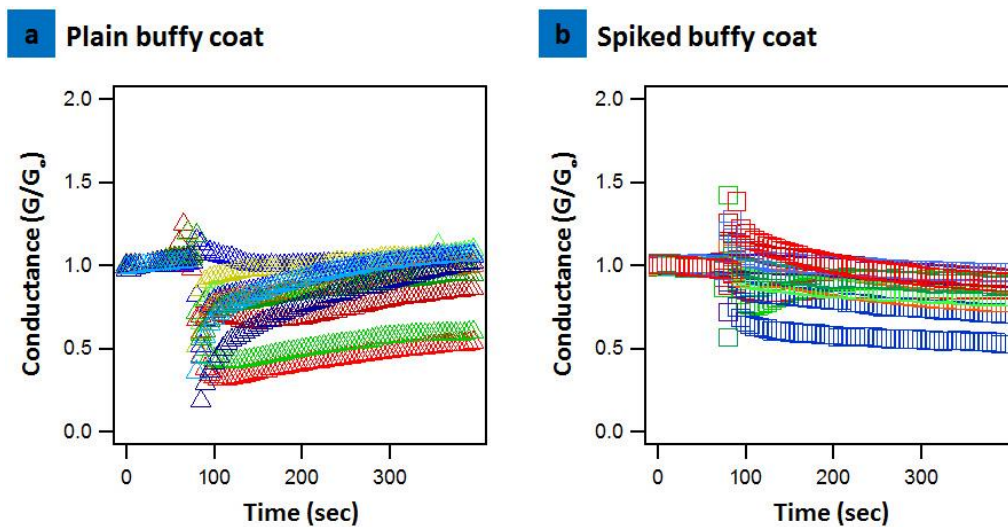


**Figure 60.** Merge of sensor arrays with statistical classifiers in blinded set: Normalized conductance versus time data from the arrays grouped into two categories. (a) Plain buffy coat; (b) buffy coat spiked with MCF-7 cells.

To compare signals and develop a classifier, a measure of signal similarity is needed. The technique employed to develop a similarity measure in this analysis is known as Dynamic Time Warping (DTW) [447-452].

DTW is a method of aligning two-time series so that a traditional distance metric (such as the Euclidean metric) can be used as a measure of similarity. To measure the similarity between two signals  $y_1$  and  $y_2$ , we compute two matrices  $\Delta \in \mathbb{R}^{m \times n}$  and  $\Gamma \in \mathbb{R}^{(m+1) \times (n+1)}$ . The first matrix  $\Delta$  has entries representing the pairwise distances between points in the series, that is:

$$\delta(t, t') = d(\mathbf{y}_{1,t}, \mathbf{y}_{2,t'}) \quad (21)$$

where  $d$  is a distance metric. For this analysis we chose to use the Euclidean distance metric. Once this distance matrix was defined, we determined the elements of  $\Gamma$  using a recurrence relation that weights steps through a cumulative distance matrix. Two formulations for this matrix were considered using the following recursions:

$$\begin{aligned} \gamma_1(i, j) &= \min\{\delta(i, j) + \gamma_1(i-1, j), \delta(i, j) + \gamma_1(i-1, j-1), \delta(i, j) + \gamma_1(i, j-1)\}, \\ \gamma_2(i, j) &= \min\{\delta(i, j) + \gamma_2(i-1, j), 2 \times \delta(i, j) \\ &\quad + \gamma_2(i-1, j-1), \delta(i, j) + \gamma_2(i, j-1)\}. \end{aligned} \quad (22)$$

Once the cumulative distance matrix  $\Gamma$  has been defined, we seek a warping curve that aligns the time indices for each time series:



$$\begin{aligned}\phi(k) &= (\phi_s(k), \phi_{s'}(k)), \quad k \in \{1, \dots, K\}, \\ \phi(k) &\in \{1, \dots, m\} \times \{1, \dots, n\}.\end{aligned}\tag{23}$$

This warping curve was chosen such that once  $\mathbf{y}_1$  and  $\mathbf{y}_2$  are aligned, the cumulative distance between the series is minimized. To find such a curve, we find the lowest scoring path through the cumulative distance matrix  $\mathbf{\Gamma}$  subject to the following constraints:

$$\begin{aligned}(1) \quad & \phi(1) = (1,1) \\ (2) \quad & \phi(T) = (m,n) \\ (3) \quad & (\phi(k) - \phi(k-1)) \in \{(1,1), (1,0), (0,1)\} \forall k > 1.\end{aligned}\tag{24}$$

Constraint (1) and (2) ensure that the beginning and the end of the signals  $y_1$  and  $y_2$  are aligned. Constraint (3) ensures uniform length of step sizes and that the warping curve is monotonic increasing. An illustration of the alignment process for a pair of qualitatively similar and qualitatively different signals are presented in Figure 61 and Figure 62 respectively. Once a warping path has been defined, the Dynamic Time Warping distance between two signals (not a formal distance metric) is given by:

$$d_{DTW}(\mathbf{y}_1, \mathbf{y}_2) = \sum_{k=1}^T \Delta(\phi(k)).\tag{25}$$

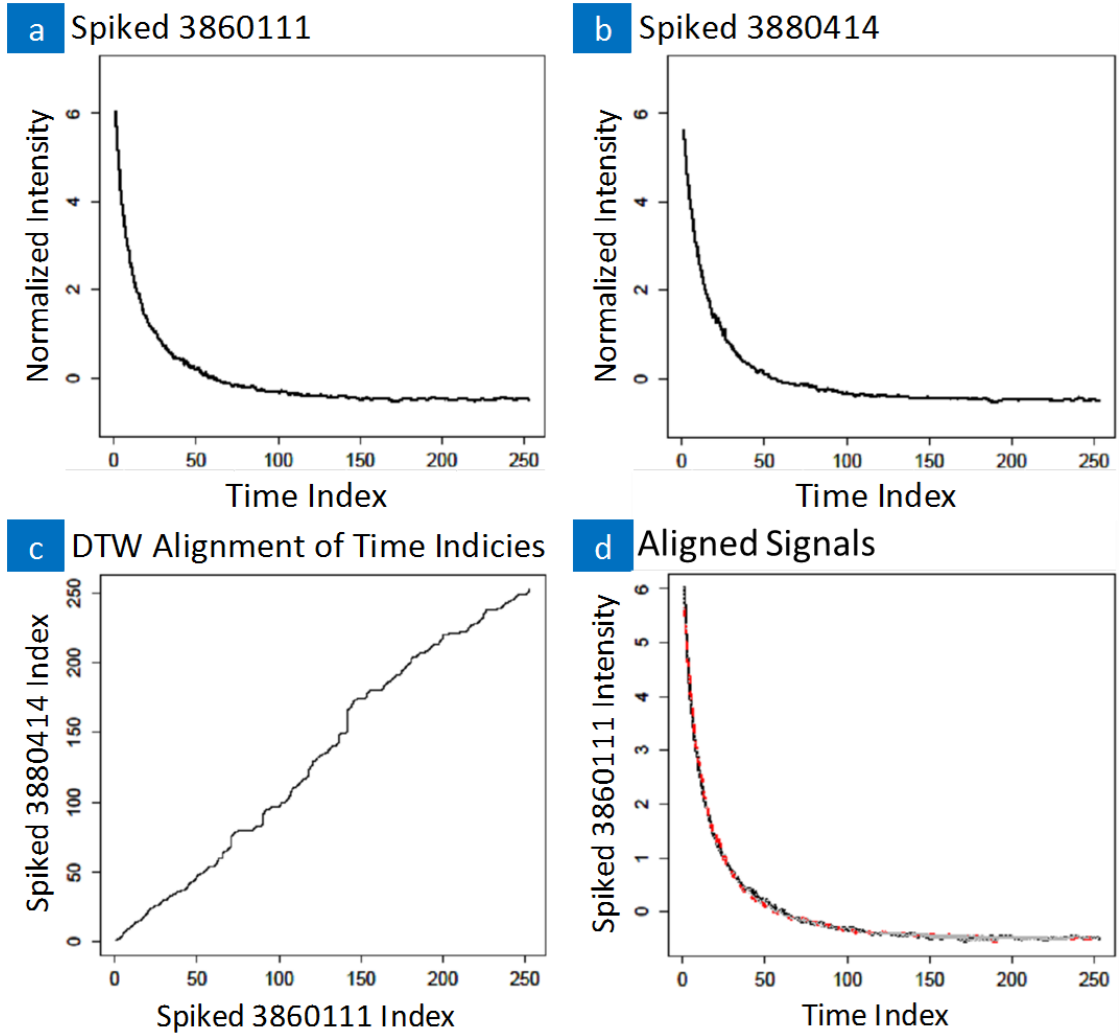


**Figure 61.** Two qualitatively similar spiked signals. The bottom left figure shows the alignment of their time indices. The bottom right figure demonstrates the small DTW distance (in gray) between the two DTW aligned signals.

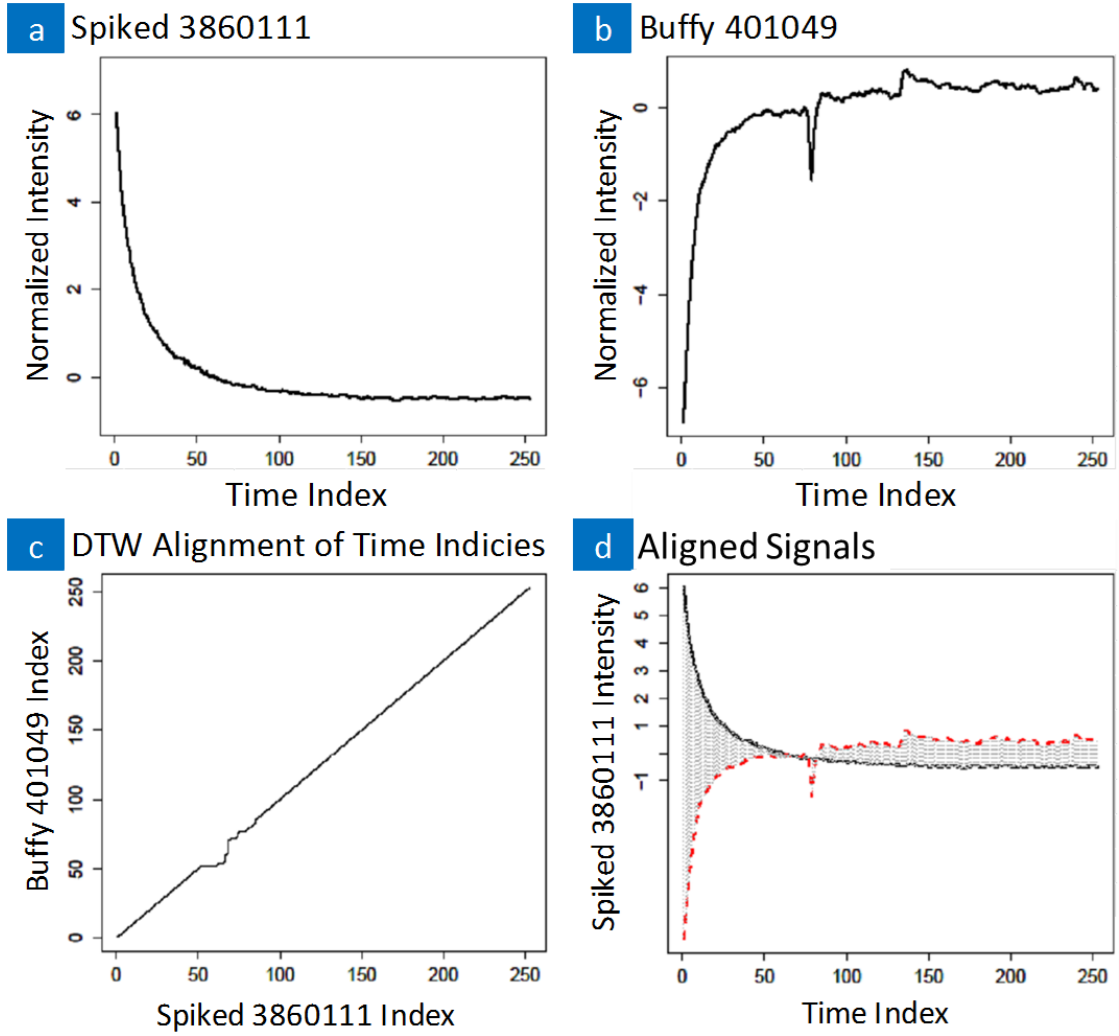


**Figure 62.** Two qualitatively different signals from different groups. The bottom left figure shows the alignment of their time indices. The bottom right figure demonstrates the large DTW distance (in gray) between the two DTW aligned signals.

For each step pattern, a dissimilarity matrix using DTW distance as the dissimilarity measure was constructed for the signals using the DTW package in R [453].

A training-test approach was used to develop a  $k$  nearest neighbor ( $k$ -nn) classifier [450] from the DTW distance dissimilarity matrices. The training set consisted of 10 Buffy signals and 28 Spiked Buffy signals. 10-fold cross-validation [450] was employed using 10,000 bootstrapped samples from the training set to determine which step pattern (symmetric 1 vs symmetric 2) and a number of nearest neighbors yielded the lowest misclassification rate Figure 63. The misclassification rate is defined as:

$$Err = \sum_{i=1}^N I(Y_i \neq \hat{Y}_i) \quad (26)$$

where  $Y_i$  denotes the true class of the signal  $y_i$  and  $\hat{Y}_i$  denotes the  $k$ -nn classifier predicted class for  $y_i$ .

Once the optimal step pattern and classifier design had been selected, the classifier was evaluated on the 22 signals of the test set. The study personnel who conducted the classification on this test set were blinded to the true class (Buffy vs Spiked Buffy) of the signals.

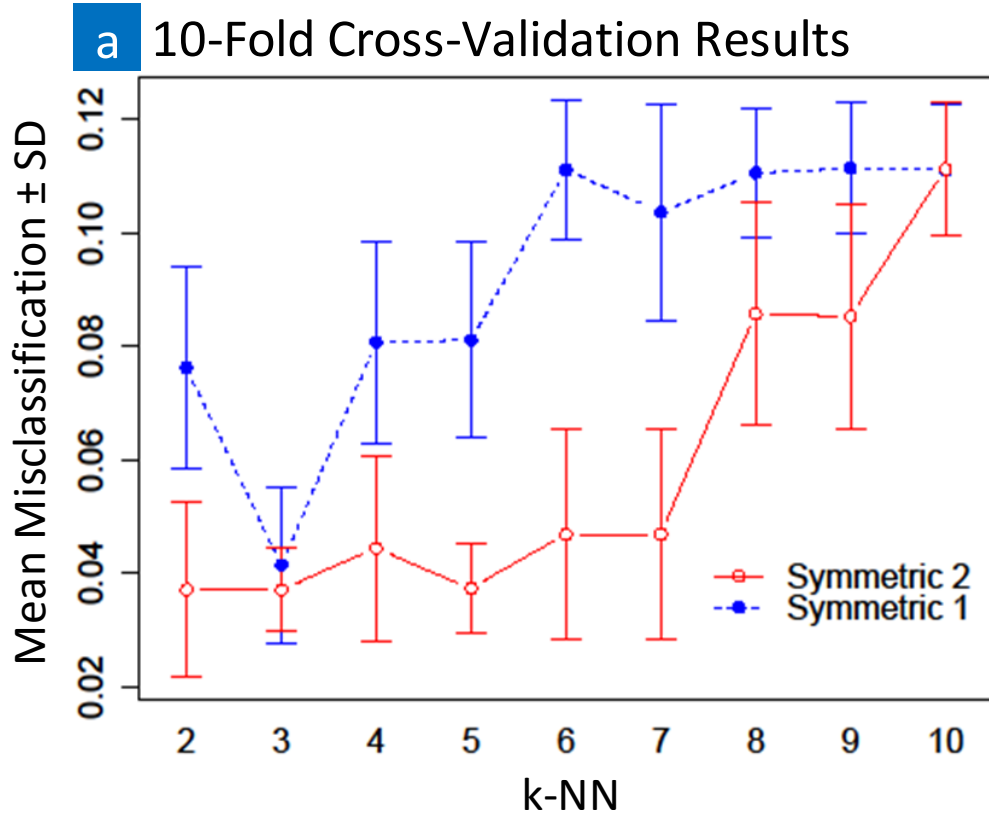


**Figure 63.** Cross-Validation Results. For each choice of  $k$ , 10,000 bootstrapped datasets were used to measure the misclassification rate.

#### 8.2.5. TRAINING SET CLASSIFICATION

A training validation test set approach was used to construct DTW distance based probabilistic modeling of surrounding observations (such as  $\kappa^{\text{th}}$ - nearest neighbors) [446]. The training data consisted of plain PBS (not shown), 10 buffy coat samples, Figure 59 (a), and 17 spiked buffy coat samples as presented in Figure 59 (b). A  $\kappa$ -fold cross-validation parameter selection was conducted using 10-fold cross validation on 10,000 bootstrapped samples from the training set of 27 signals for which

the class (buffy vs. spiked buffy) was known. The tuning parameters selected were those that minimized the mean and variance of the misclassification rate. The test set misclassification rate, classifier sensitivity, and classifier specificity were then used as criteria to measure the success of the devices in discriminating between positive and negative samples. The statistical table for training set is presented in Table 7. A positive predictor value (PPV) = 94% and negative predictor value (NPV) = 100% with accuracy = 96.3% was obtained for training set. One data was misclassified and was false positive or type I error. No false negatives were observed in training set.

#### 8.2.6. BLINDED TEST CLASSIFICATION

Figure 60 (a) and (b) presents the electrical signals for the blind test. Based on the training set, the tuning parameters were selected, 22 test signals presented in Figure 60 (a) and (b) (of class unknown to the personnel constructing the classifier) were classified using the training signals as reference signals. Table 8 presents the corresponding classification table for the blind test. A PPV=83%, NPV=90% and accuracy =86% was observed. A misclassification rate of ~14% was observed in these blind testing. 3 samples over 22 samples were misclassified. Two samples that were misclassified were false positive or type I error and one sample that was misclassified was false negative or type II error. This suggests the classifier is capable of differentiating electrical signals between samples that were plain buffy coat or buffy coat with cancer cells which is the first accomplishment for any nanotube biosensor device.

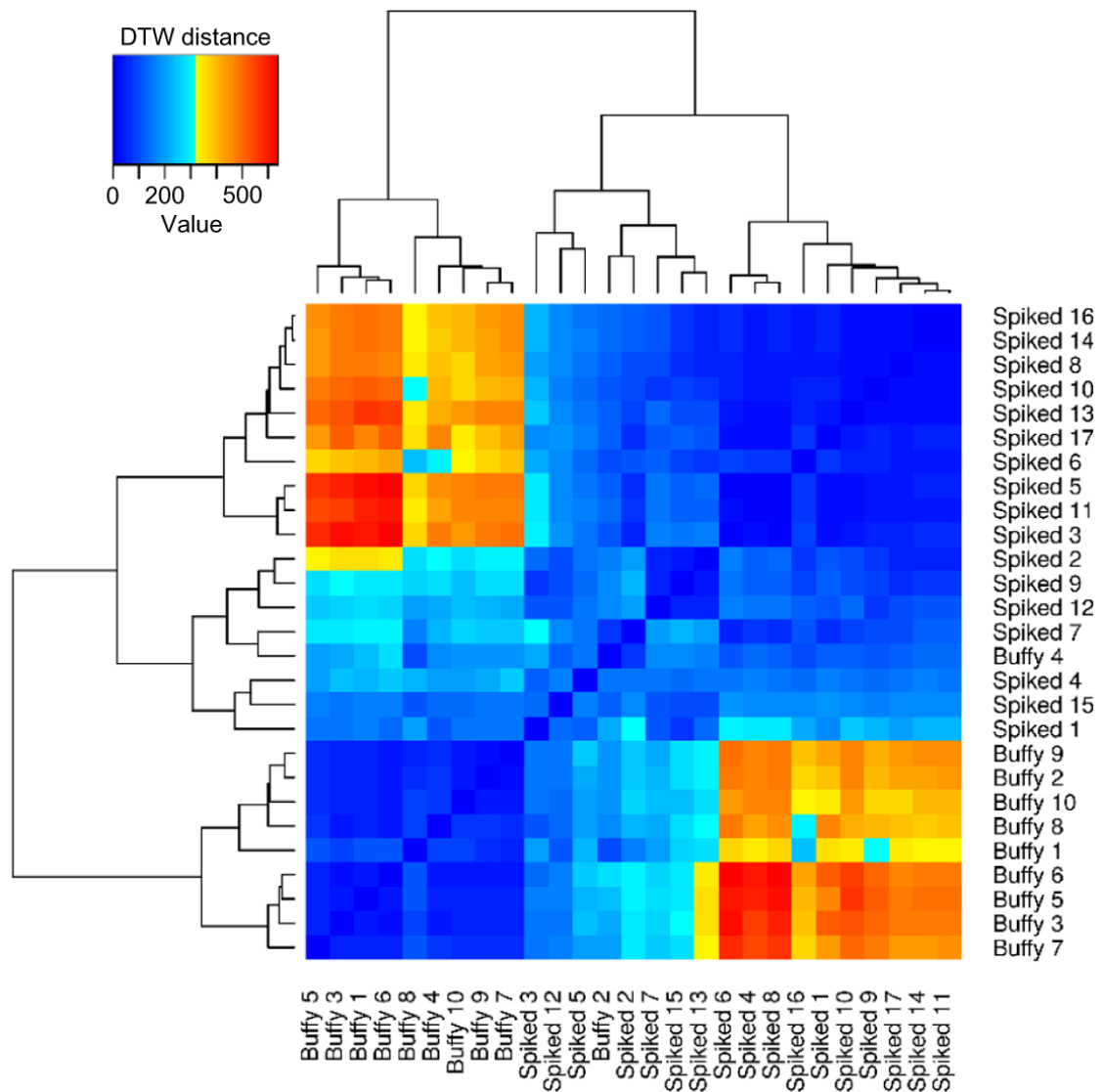


**Figure 64.** Heat map. Summary of the relationship between electrical signatures and the cellular-proteomic features namely overexpression of EpCAM in spiked buffy coats versus buffy coats. The statistical classifier naturally partitions the buffy versus spiked buffy coats suggests specific interactions are quite unique in their electrical signatures compared to non-specific interactions and establishes a relationship between electrical conductance data with proteomic features.

**Table 7.** Training classification of biosensor signals based on dynamic time warping.

		Condition training		
		Condition Positive	Condition Negative	
Test outcome	Test outcome positive	<b>True positive = 17</b>	<b>False positive = 1 (Type I error)</b>	PPV = 94%
	Test outcome negative	<b>False negative = 0 (Type II error)</b>	<b>True Negative = 9</b>	NPV = 100%
		Sensitivity = 100%	Specificity = 90%	Accuracy = 96.3%

**Table 8.** Blinded set classification of biosensor signals based on dynamic time warping.

		Blinded Test		
		Condition Positive	Condition Negative	
Test outcome	Test outcome positive	<b>True positive = 10</b>	<b>False positive = 2 (Type I error)</b>	PPV = 83%
	Test outcome negative	<b>False negative = 1 (Type II error)</b>	<b>True negative = 9</b>	NPV = 90%
		Sensitivity = 91%	Specificity = 90%	Accuracy = 86%

### 8.2.7. HEAT MAP

Figure 64 is the heat map of the between signal DTW distances for the signals used in the k-fold cross-validation tuning parameter selection and as reference signals for the classifier. 10-fold cross-validation on the bootstrap samples resulted in a final DTW distance based on  $\kappa$ -nn classifier utilizing a symmetric 2 step pattern and 3 nearest neighbors. In the margins of this figure a dendrogram of the complete-linkage agglomerative hierarchical clustering of the same is shown [450]. This demonstrates that on the training data, DTW distance as a dissimilarity measure, naturally partitions the sample data into two distinct clusters (with one misclassification) according to sample class. The statistical classifier partitions the buffy versus spiked buffy coats suggesting specific interactions are quite unique in their electrical signatures compared to non-specific interactions and establishes a relationship between electrical conductance data with biological and possibly proteomic features (presence or absence of cancer cells in buffy coats versus presence or absence of mesenchymal marker



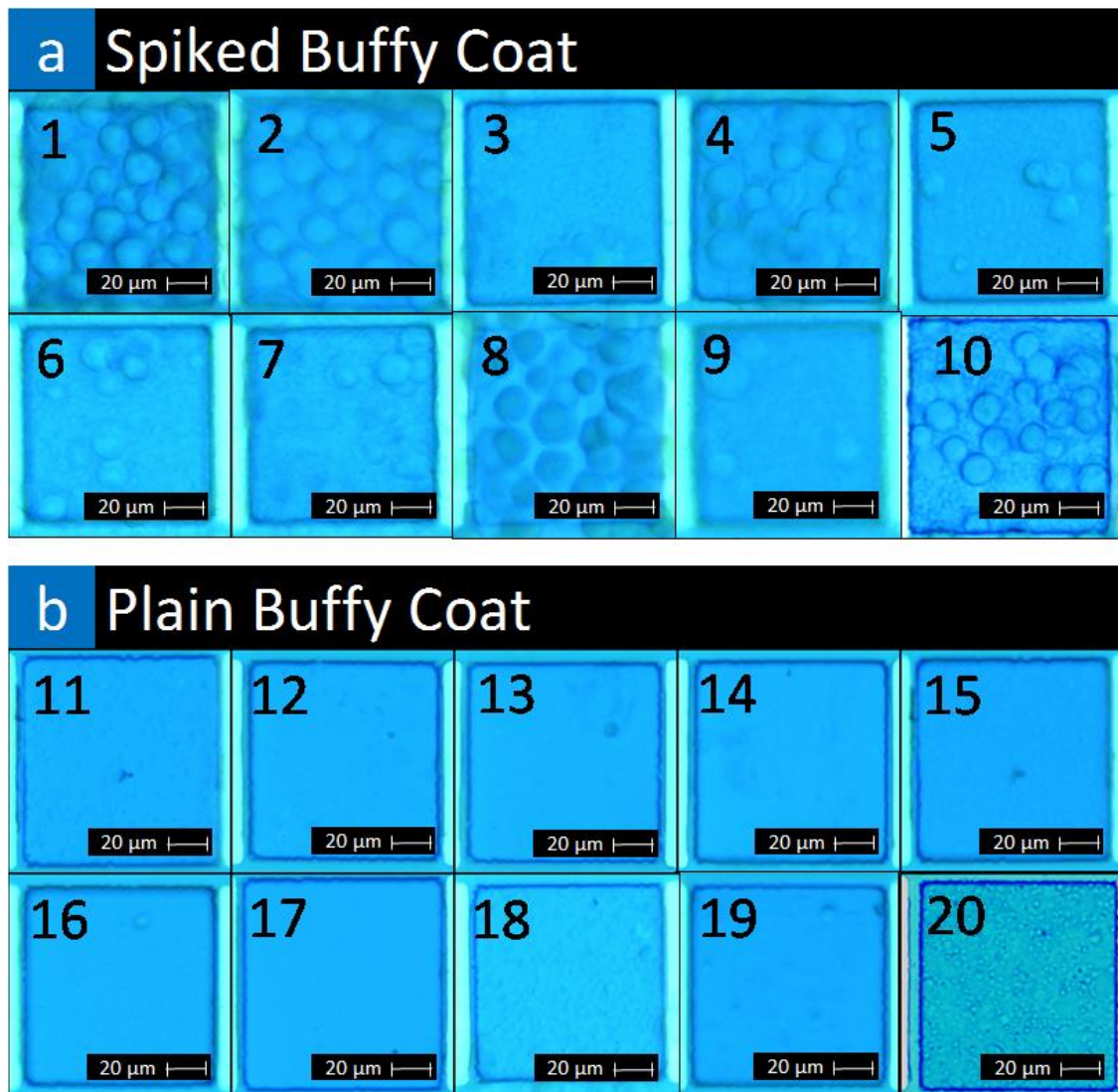


**Figure 65.** Cell Capture using EpCAM functionalized Nanotube Devices based on Optical Microscopy: (a) Optical microscopy of spiked cells in buffy coats using nanotube devices; (b) Optical microscopy of plain buffy coats.

EpCAM).

#### 8.2.8. CELL CAPTURE WITH SINGLE CELL SENSITIVITY AND CONFOCAL MICROSCOPY

The devices that gave positive signatures were then further processed to assess the ability to capture spiked MCF-7 cells from buffy coats. Figure 65 are the images from 22 processed samples from the blind test with both buffy and spiked buffy coats. Each image was taken of the device immediately after taking the electrical signature measurement. For easier presentation, the spiked buffy coats are presented in Figure 65 (a), the plain buffy coats are presented in Figure 65 (b) and Table 9 consisting of number of cells captured on the device in Figure 65 (a) and (b). The cells could be counted after imaging in a Nikon Eclipse optical microscope in the buffy coat using imaging software. The images show the ability to capture 1 to 20 cells per device and their positive/negative electrical signatures assessed from the classifier. Our buffy coat was mainly proteins and denatured hematologic cells, we were able to identify the MCF-7 cells which were quite distinct as these were spiked cells. The single cells captured in the plain buffy coat are believed to be one or two hematologic or white blood cells that were bound to the device.

Six devices were removed and also imaged using confocal microscopy as presented in Figure 66 (only 4 shown). The samples were washed three times to assess binding and stained for DAPI and EpCAM. A cover slip was placed on the device and imaged using confocal microscope. The images from devices as presented suggest single cell sensitivity as well as positive for EpCAM overexpression. The results

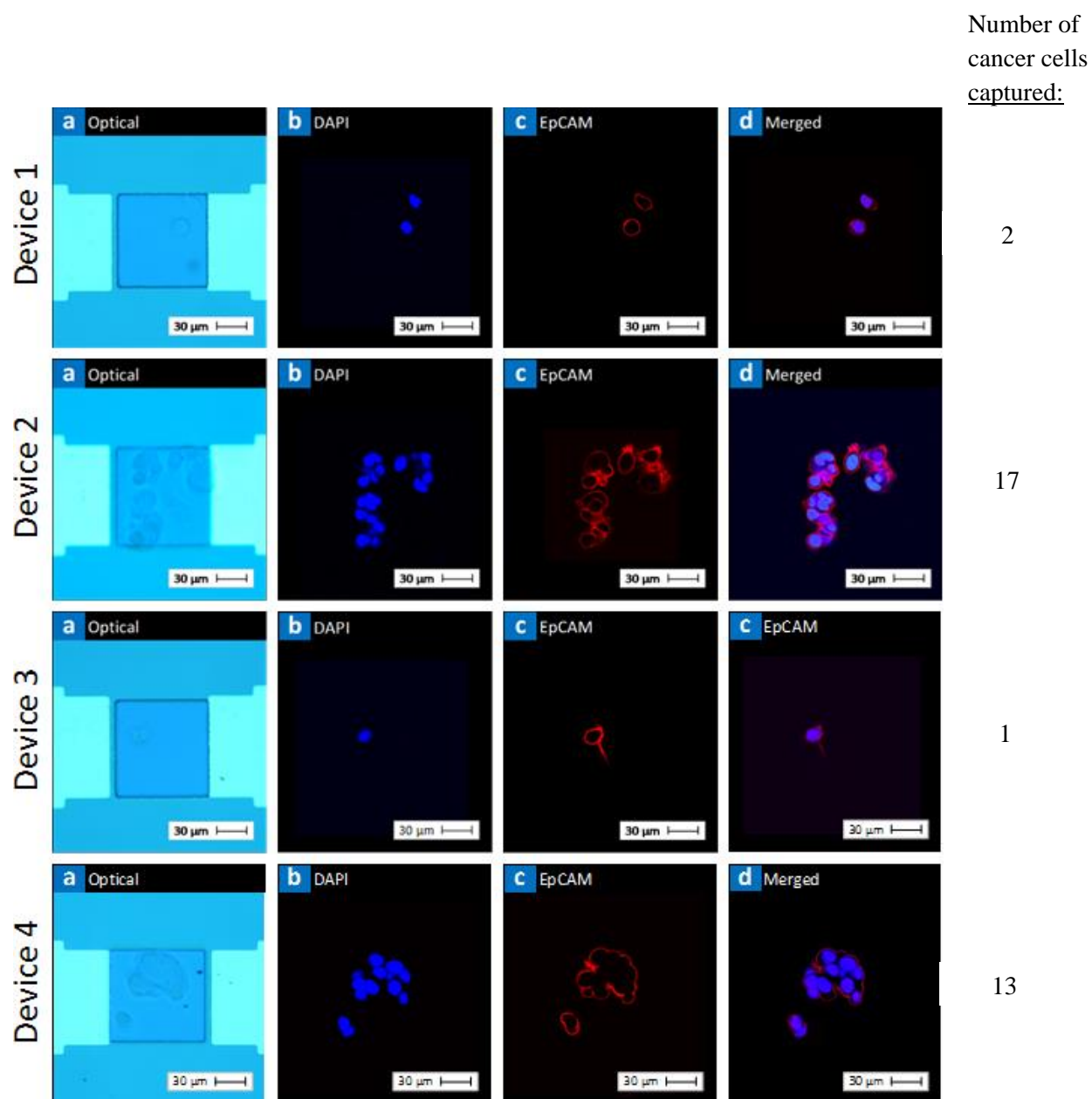


**Figure 66.** Cell Capture using Nanotube Devices using Confocal Microscope:  
Representative confocal images from 6 devices imaged (4 shown) of captured cells in  
spiked buffy coats ranging from 1-17 cells per 5  $\mu$ l sample.

**Table 9.** Captured cells on each device for both case and controls using optical microscope.

Device No	Spiked		Number of cells
	(+)	(-)	
1	✓		25
2	✓		22
3	✓		3
4	✓		14
5	✓		6
6	✓		9
7	✓		6
8	✓		19
9	✓		4
10	✓		19
11		x	0
12		x	0
13		x	1
14		x	0
15		x	0
16		x	1
17		x	0
18		x	0
19		x	2
20		x	2

suggest that the samples were bound to the nanotube device through cooperative binding of the receptors to the antibodies. Again, anywhere from ~1-17 cells were observed in confocal analysis, in line with optical microscopy observations.

### 8.3. DISCUSSION AND OUTLOOK

The ability of to distinguish samples that have cancer cells from samples that have no cancer cells in a medium such as blood/buffy coats in rapid manner for both large and small volumes can have significant implications in the clinic. The semiconducting nanotube arrays presented here is a promising technology with potential advantages in a clinical setting due to its simplicity. The technology requires minimal sample preparation, can perform assays in turbid/obscure media, can be adapted to profile different targets namely proteins, and cells, and has the capability for high-throughput operation (60-240 sensor arrays). For the first time, we have merged the nanotube sensor data with predictive statistical classifiers for liquid biopsy, an important step towards clinical translation with high sensitivity and specificity for a digital device. Our past work has also shown the detection of *f*-EpCAM up to ~1 ng/ml based on similar devices that were functionalized with anti-EPCAM antibodies using the same PASE functionalization protocol [359]. Our results on cell cultures and buffy coats thus suggest similarity in patterns that could potentially arise only from specific antibodies interacting with their corresponding EpCAM receptors. The ~91% sensitivity, ~82% specificity and ~86% accuracy in the blind classification test give us great confidence in development of this technology further for future clinical applications. One advantage is that our work shows the feasibility of classifying samples based on the device electrical signatures in short time frames (within few minutes), an important advantage in the clinic and considering that cells removed from their native microenvironment rapidly change their phenotype. Once classified, devices

that gave positive electrical signals can then be sent to a laboratory for further validation such as qPCR. With its capability for fast and sensitive cell capture, the nanotube arrays has the potential to become a useful tool for early screening of cancer cells from a drop of blood and also studies related to multiplexed drug screening and intracellular signaling. Although our study was focused on being able to classify signals from buffy coats that had cancer cells from the buffy coats that had no cancer cells based on nanotube micro-arrays functionalized with anti-EpCAM antibodies, the nanotube-assay can be expanded to integrate other complex cancer signatures and receptors namely HER-2 and EGFR, two important markers involved in metastases. Anti-HER-2 and anti-EGFR antibodies functionalized to the nanotube devices could potentially be useful in isolation of cells based on those markers. The system itself can be further improved through larger arrays, automated sample handling and development of statistical classifier for blood samples and the use of custom-aptamer technology for high specificity which are the focus of our future work. Therefore, the potential for these devices are high both for fine needle aspirates and circulating tumor cell capture and analysis and worth pursuing given the simplicity of the system.

## 8.4. METHODS

### 8.4.1. CNT-NETWORK FORMATION

IsoNanotubes-semiconducting single wall carbon nanotubes were used to fabricate a 4  $\mu\text{g}$  CNT film network on a dry oxidized (300 nm thickness) 4" silicon wafer and taken for microfabrication process. For details of this process please see Chapter 3.

#### 8.4.2. CLEAN ROOM PROCESSING

Generation 1 devices were used for the studies presented here. Details of the device fabrication process and characterization are presented in Chapter 3.

#### 8.4.3. RAMAN SPECTROSCOPY

Raman analysis was done at an excitation wavelength of ~532 nm using a XploRA Raman spectrometer (Horiba Scientific). The laser beam is focused onto the surface of the CNT film on top of a Si wafer substrate through a 50X objective lens. This measurement was repeated six times at different locations of the sample. The RBM ( $172\text{ cm}^{-1}$ ), Si ( $518\text{ cm}^{-1}$ ), D ( $1340\text{ cm}^{-1}$ ), G ( $1590\text{ cm}^{-1}$ ), and 2D ( $2673\text{ cm}^{-1}$ ) peaks were identified throughout the sample.

#### 8.4.4. DEVICE FUNCTIONALIZATION

Finished carbon nanotube sensors were functionalized with anti-EpCAM by a pyrene linker molecule. PASE (AnaSpec, Cat. No. 81238) were dissolved in methanol at 1 mM. Devices were incubated in the PASE solution for 2 hours at room temperature, and then rinsed with methanol. Devices were then incubated in Anti-EpCAM (EMD Bioscience, Cat. No. OP187) or anti-IgG (EMD Millipore, Cat. No. 411550), 20  $\mu\text{g/mL}$  in 1X Phosphate-buffered saline (PBS), for 2 hours at room temperature. After incubation, devices were rinsed in 1X PBS 3X. . Tween20 was used to block unfunctionalized nanotube sidewalls to minimize non-specific interactions. Devices were incubated with 0.5% Tween20 for 2 hours at room temperature. After incubation, devices were washed with water, and then incubated in 5  $\mu\text{l}$  droplets of 1X

PBS in a humid chamber at 4 °C before testing. For more detail of functionalization process please see Chapter 4.

#### 8.4.5. CELL CULTURE AND PREPARATION

The breast adenocarcinoma cell line, MCF-7, MCF-10A and SKBR-3 (ATCC, Cat. No. HTB-22; CRL-10317; HTB-30), was cultured under conditions as recommended by the supplier. MCF10 A is non-tumorigenic cells that are EpCAM negative and MCF-7 and SKBR-3 are EpCAM positive cell lines. Cells were grown for 3-4 days to reach ~80% confluence. The cells were then detached using Accutase solution (Sigma, Cat. No. A6964) centrifuged and re-suspended in 1X PBS at 20,000 cells/ $\mu$ L. This solution was used to spike the healthy buffy coat sample (James Graham Brown Cancer Center, Study No. C020-01) at 1:1 ratio for a final MCF-7 concentration of 10,000 cells/ $\mu$ L.

#### 8.4.6. CONFOCAL MICROSCOPY

After experimental data had been collected, the devices were saved for staining and confocal imaging. The devices were first rinsed with PBS to remove excess cells and buffy coat fragments and then incubated with 4% paraformaldehyde (Santa Cruz Biotechnology Inc., Cat. No. sc-281692). After initial preparation device were stained with anti-EpCAM (EMD Bioscience, Cat. No. OP187) primary antibody, anti-mouse IgG-TR (Santa Cruz Biotechnology Inc., Cat. No. sc-2781) Texas Red conjugated secondary antibody, and DAPI (Molecular Probes, Cat. No. D1306) according to the standard confocal staining protocol. A coverslip was placed on top of each device and



sealed before imaging. Confocal laser scanning microscopy images were obtained on a Nikon Eclipse T. with coverslip corrected objective focused at 600X.

#### 8.4.7. DEVICE TESTING

The testing platform is explained in great detail in Section 3.3. The testing protocol started with a hydrated device, and a 5  $\mu\text{L}$  droplet of 1X PBS, which was placed immediately after functionalization and left overnight. The bias was applied, and the sensor was monitored for the initial 3 minutes, then 5  $\mu\text{L}$  droplets of the sample solution, 1X PBS or buffy coat suspension, was pipetted directly into the standing 5  $\mu\text{L}$  droplets. Devices were monitored for 360 seconds after each addition of a new sample solution. The total duration of one test varied from 540 to 1980 seconds. To compare results among devices,  $I_{SD}$  data were normalized to obtain the  $G/G_0$  values for conductance. The sensor element was also imaged on an optical microscope to confirm the presence of cancer cells. The spiked buffy coat samples consisted of  $\sim 10,000$  MCF-7 cells/ $\mu\text{L}$  for these demonstrations. Such concentration was chosen to cover consistently the active sensor element surface with 0-30 cells at the sensor window for assessing cell capture per device.

#### 8.4.8. STATISTICAL CLASSIFIER

Statistical classification was done using DTW package in R. The sensitivity, specificity, and misclassification rate were then computed, considering Spiked Buffy to be a positive test and Buffy to be a negative test. Sensitivity is defined as  $TP/P$ , where  $TP$  denotes the number of positive test outcomes, and  $P$  denotes the number of true

positives. Specificity is defined as  $TN/N$ , where  $TN$  denotes the number of negative test outcomes, and  $N$  denotes the number of true negatives.

#### 8.4.9. DYNAMIC TIME WARPING (DTW)

The first step to developing the classifier for biosensor data is the identification of a suitable dissimilarity measure. Time series data from CNT biosensors are marked by the occurrence of prototypical features that herald the class of the series. Often the time domain of such series is irrelevant and complicates automatic feature detection. As an example, two time series with similar features are shown in Figure 67 (A). The red series is a phase shift of the blue series with a slight vertical lift. In this situation, a traditional distance metric such as Euclidean distance would conclude that the series are very dissimilar. Yet with respect to the prototypical feature, these series are quite similar. As a result, “warping” of the time domains of one or both of the series (through the insertions of gaps) is necessary for aligning the series for proper quantification of dissimilarity.

DTW is a class of dynamic programming algorithms that have been developed in order to align time series in such a manner so that a traditional distance metric can be used to quantify dissimilarity. The resulting alignment of the two series by DTW is shown in Figure 67 (B).

To calculate the DTW distance between two time series, Rai and Trainor *et al.* [446] utilized the methods presented by Sakoe and Chiba whose original introduction

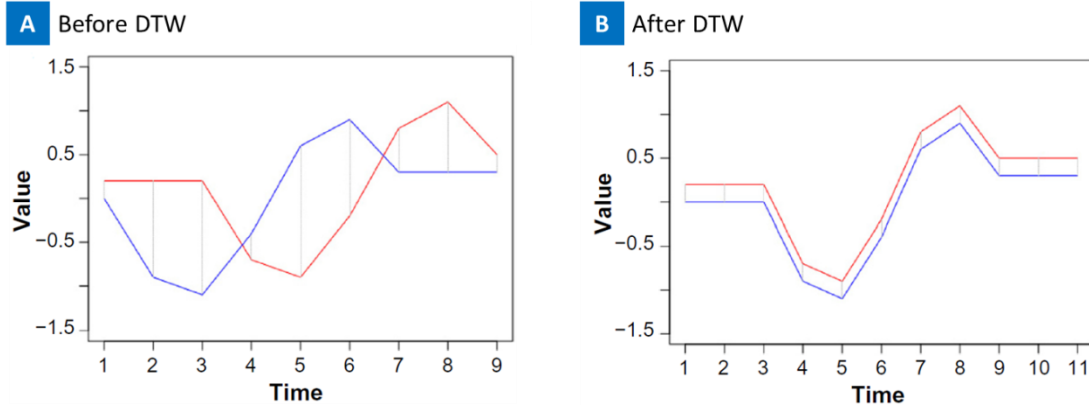


**Figure 67.** Dynamic time warping (DTW) for time series alignment. (A) Two qualitatively similar series. Red is a phase shift of blue with a slight vertical lift. Gray dashed line shows the vertical difference [446]. (The same series after dynamic time warping alignment.)

of DTW methodology provides a nice resource for researchers interested in DTW [454].

#### 8.4.10. K-NEAREST NEIGHBORS CLASSIFIER

$\kappa$ -nearest neighbor ( $\kappa$ -nn) classifier is a straightforward choice of classifier for measuring the dissimilarity of two series using the definition of a pseudo-distance metric (DTW distance) [455]. To build a  $\kappa$ -nearest neighbor classifier, where  $\kappa \in \mathbb{N}$ , we denote series data as:  $\{(\mathbf{y}_i, c_i) : i \in 1, 2, \dots, N\}$  where  $\mathbf{y}_i$  is a time series and  $c_i = g$  where  $g \in \mathcal{C}$  denotes the known class of the series. For each observation  $(\mathbf{y}_i, c_i)$  we find the neighborhood  $N_{\kappa}(\mathbf{y}_i)$  of the  $\kappa$  series  $\mathbf{y}_j$  with  $i \neq j$  such that those series have minimal  $\text{DTW}(\mathbf{y}_i, \mathbf{y}_j)$ . We then have empirical estimates of the probability of class membership for  $(\mathbf{y}_i, c_i)$ :

$$\hat{P}_g(\mathbf{y}_i) = \frac{1}{\kappa} \sum_{\mathbf{y}_j \in N_\kappa(\mathbf{y}_i)} 1_{c_j=g}(\mathbf{y}_j) \quad (27)$$

From this set of empirical probability estimates we chose:

$$\hat{c}_i = \operatorname{argmax}_{g \in \mathcal{C}} \hat{P}_g(\mathbf{y}_i) \quad (28)$$

In the case that there is a tie between two or more classes, the ties are broken at random.  $\hat{c}_i$  then represents the DTW distance based k-nn classification of the observation  $(\mathbf{y}_i, c_i)$ . Of course, predicting the class of  $(\mathbf{y}_i, c_i)$  given that  $c_i = g$  is already known is rarely of any interest. Instead we wish to build a library of series of known class and use this library to predict the class of series for which the class is unknown.

## CHAPTER 9

### LABEL-FREE CAPTURE OF BREAST CANCER CELLS SPIKED IN BLOOD USING CARBON NANOTUBE ANTIBODY MICRO-ARRAYS

#### 9.1. INTRODUCTION

Primary tumors release cancer cells into the bloodstream, resulting in the occurrence of so-called circulating tumor cells (CTCs). Number of recent studies has shown that detection of CTCs in peripheral blood can be useful for determining the spread of metastatic disease to distant sites, early diagnosis of cancer, predicting disease progression and suggesting therapeutic interventions [33, 48, 57, 64]. However, capturing and detecting CTCs in blood is very difficult because of their small population relative to preexisting blood cells [56, 173].

Several methods have already been proposed for isolating CTCs from peripheral blood, including density gradient [456, 457], filtration based on size and deformability, [84, 85, 88, 458-461], immunomagnetic beads [123, 176, 462], microfluidic mixing structures [78], microposts [73, 463, 464], spiral microchannels [465], and dielectric properties [466, 467], laminar vortices [468]. Immunomagnetic cell sorting using magnetic micro beads has become the most common method for isolating CTCs because of its relative high accuracy and the ability to be carried out using simple systems. However this method requires multi-processing steps involving multi-labeling protocols and fluorescence post image analyses to discriminate and identify CTCs. CellSearch (Janssen Diagnostics, LLC) is a commercially available product that is FDA approved and also uses immunomagnetic technology to enrich and capture CTCs. However, it has a limited performance for low-purity enriched sample containing CTCs

and residual blood cells; the enrichment process using fluorescence imaging requires a prolonged time and also has high risk of error. Therefore a CTC capturing method that is label-free, rapid, and simple is of great interest. While the technologies explained above are impressive, they are not necessarily optimal for rapid identification in clinic. A digital device by which small drops of blood could be rapidly analyzed by microarrays for the detection of CTCs in the clinic would thus have great utility [133]. We hypothesized that a CNT micro-array device functionalized with an antibody would allow for the rapid detection of CTCs. These devices rely on the principle that each cancer cell possesses thousands of overexpressed particular target receptors, so that cooperative binding to cognate antibodies would yield characteristic spikes in the electrical signal due to free energy change. The reduction in free energy for specific interactions is much higher than nonspecific interactions, and one can use CNT arrays to transduce the change in free energy into electrical signal [133].

Based on our success with using CNT micro-array device for capture of CTCs in buffy coat, here we have optimized the process with a new device design, generation 2, to attempt the capture and discriminate of CTCs directly in whole blood with no preprocessing.

In this chapter, we introduce a CNT micro-array device for capturing CTCs spiked in blood sample based on the interaction between functionalized CNT surface and cellular membrane receptor, similar to Chapter 7 and 8 studies, on the device. Additionally, we attempt to classify the electrical signal of each device based on the interaction type and captured CTCs on the device. To improve the capture efficiency

with blood samples, generation 2 device consisting of 3X3 mm sensing window, Figure 68 (A), were utilized to accommodate for high sample cell concentration in blood. A droplet of CTC spiked blood sample was injected on top of each CNT device, Figure 68 (B). Current passing through the device was monitored and recorded during this time. Devices were then analyzed under the optical microscope, Figure 68 (C and D), and further taken for immunofluorescent staining and confocal microscopic analysis of the captured cells. The interaction of cancer cells with antibody functionalized CNT surface generated a unique change in current vs. time signal. This can be explained by interaction of membrane receptors on the cell and the antibody functionalized to the surface of the nanotube resulting in change in free energy of the system [133]. This change in free energy can be caused by one or combination of factors, effect of membrane receptor proteins charge [469], cell membrane lipid bilayer interacting with surface of the nanotube [470] as a result of antibody-receptor binding, and surface stress implemented to the CNT surface and cell membrane as a result of the two anchoring by antibody-receptor binding which could additionally activate ion channels on the cell membrane introducing additional ionic charge to the environment surrounding the nanotube [471, 472]. These factors can eventually affect the carrier mobility or the carrier density of nanotubes resulting in change in conductance of CNT network [307]. To better understand the magnitude of these effects, statistical classifier method based on dynamic time warping (DTW) was developed, similar to Chapter 8, to identify and distinguish the electrical signature generated from each interaction leading to discrimination of devices with CTC spiked blood sample types.

## 9.2. MATERIAL AND METHODS

Detailed fabrication process and experimental setup are explained in chapter 3. Functionalization methods are discussed in detail in Chapter 4. Cell culture and preparations are explained in detail in section 7.2.

### 9.2.1. DEVICE DESIGN AND PRINCIPLE

Generation 2 of CNT micro-array devices, as described in section 3.1.3, were specifically designed for the objective of this chapter. Considering the need to process high volume and number of cells with blood samples, larger CNT film area was elected to accommodate for this objective.

Similar to the first generation of CNT devices, the second generation devices are consist of a simple two-terminal design at their core with CNT ultra-thin film network connecting the source and drain electrodes. In this design, the sensing channel consist of CNT network connecting the two electrodes, 3000  $\mu\text{m}$  in length and 3000  $\mu\text{m}$  in width, as seen in Figure 68 (A). As a result the sensing area of each device is  $9 \times 10^9 \mu\text{m}^2$ , allowing for  $\sim 22,500$  cells, assuming average 20  $\mu\text{m}$  diameter, to interact with the CNT device at one time.

The sensing area becomes very critical when we are considering processing blood samples as there are about 5 billion cells in 1 mL of blood. More than 99% of cells in blood are consist of red blood cells (RBCs), erythrocytes 93.8%, and platelets, thrombocytes 6.08%, which are much smaller, 2-8  $\mu\text{m}$  in diameter, than the remaining white blood cells (WBCs), leukocytes 10-30  $\mu\text{m}$ , which populate the remaining 0.13%



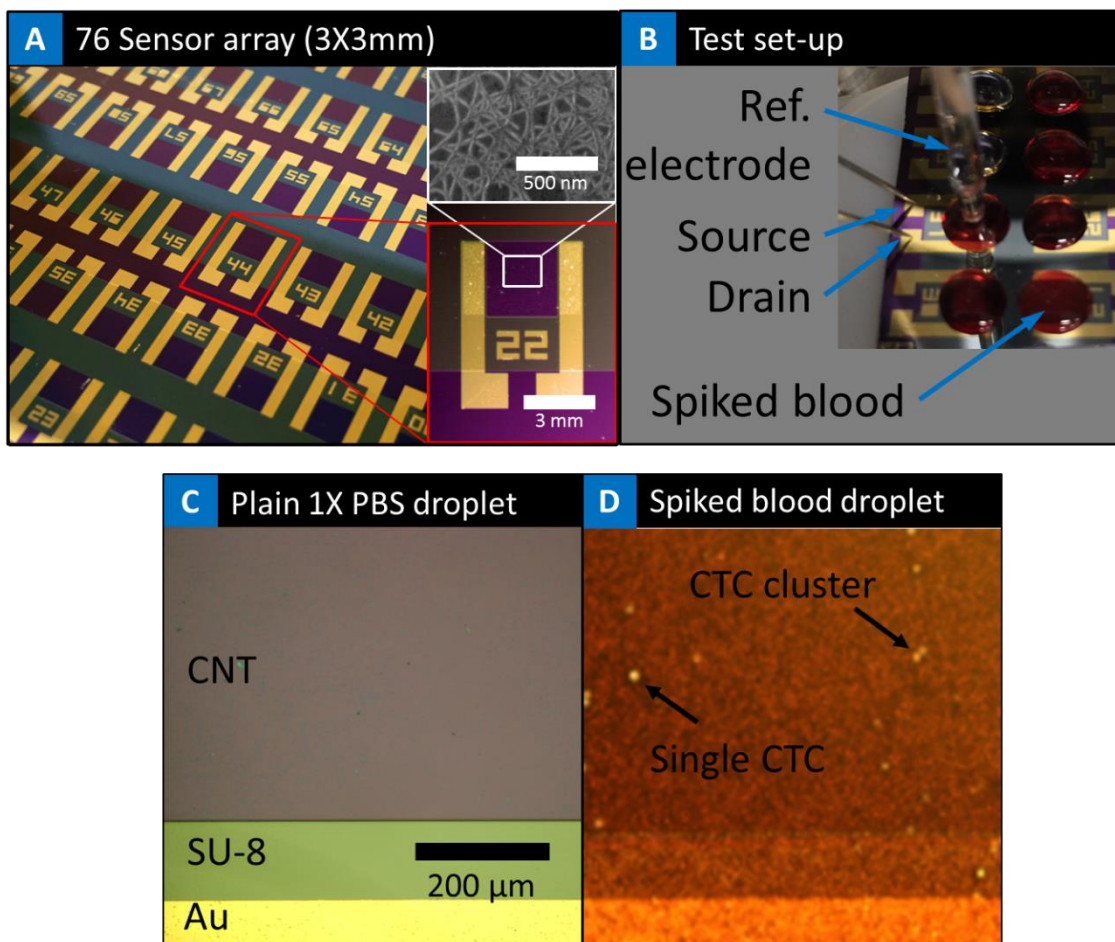


**Figure 68.** (A) Optical image of the wafer with 76 devices manufactured using photolithography, metal deposition and etching; bottom right panel shows an optical image of a single CNT device and top right panel shows a SEM image of the CNT network bridging the source-drain electrodes. (B) Test set up showing 6 devices on a chip. The source, drain and reference electrodes are observed with a spiked blood and 1X PBS sample droplets on the devices. (C) Optical microscope image of a device with a 1X PBS sample droplet on top. Here one can see, from bottom to top, the gold electrode, SU-8 photoresist polymer layer covering the electrode and the edge of the CNT film, and the CNT ultra-thin film. Similarly (D) shows an optical microscope image of similar device after cancer cell spiked blood droplet injection.

of cells in the blood and have great similarities to CTCs in their size and shape relative to RBCs and platelets. In a static blood sample/droplet the cells inside the blood start to settle immediately due to the forces of gravity, resulting in cells coming in contact and interacting with the base substrate surface. The initial observations on the optical microscope of cancer cell spiked blood sample droplets on top of the devices showed that the spiked cancer cells as part of their settling process get buried under RBCs and on top of the CNT network established on silicon substrate, getting sandwiched in between, as illustrated in Figure 69. This phenomenon opened the avenue to further attempts achieving better efficiently capturing CTCs in blood by functionalizing the nanotubes, as we will discuss in this chapter.

CNT devices used for the objectives of this chapter were fabricated using a 6  $\mu\text{g}$  CNT film. Higher relative film concentration was elected with respect to the device size, 3X3 mm, to maintain a uniform, continuous, and conductive CNT network. The fabrication process and the characterization of devices with these CNT films are discussed in detail in Chapter 3. To summarize, devices have an average resistance of 0.2 M $\Omega$  after annealing, and average mobility of 4.95 cm<sup>2</sup>/V-s. On-off ratio was determined for these devices once with back-gating, ,  $I_{\text{on}}/I_{\text{off}} = 11.2$ , and once with electrolyte liquid-gating, ,  $I_{\text{on}}/I_{\text{off}} = 134$ .

### 9.2.2. DEVICE FUNCTIONALIZATION

CNT devices were functionalized with anti-EpCAM, anti-HER-2, or anti-IgG antibodies using a pyrene linker molecule, Figure 72 (A). Devices were incubated in the PASE solution for 2 hours at room temperature, and then rinsed with methanol.

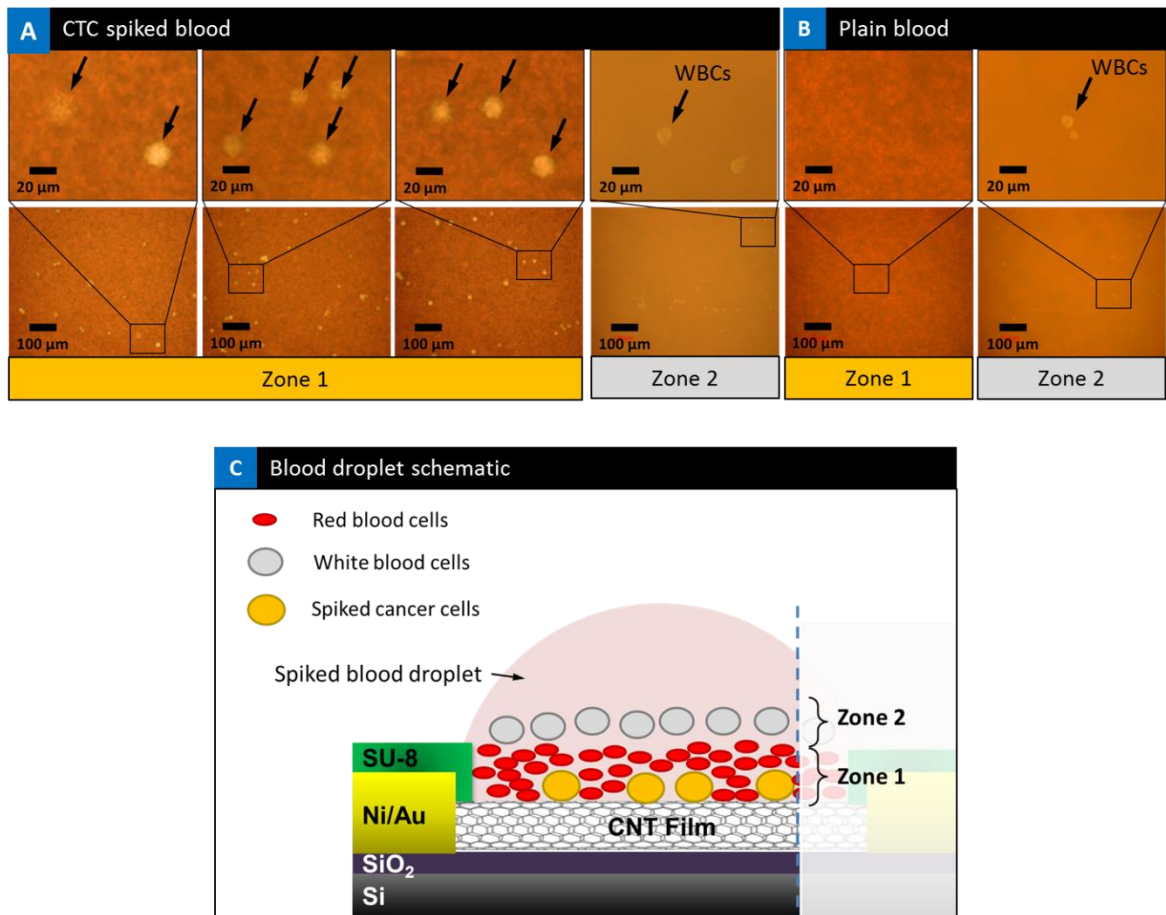


**Figure 69.** (A and B) Optical microscopic images of blood sample droplets on top of the device. (A) Three examples of spiked cancer cell blood samples. Spiked cancer cells are observed in the blood and marked with an arrow, one can clearly observe the cancer cells buried under the RBCs and on top of the substrate, CNT film. High concentration of RBCs is apparent on top of the marked cancer cells in “Zone 1”. (B) Plain blood sample. There are no cancer cells or WBCs observed in plain blood samples when the microscope is focused in “Zone 1” plane. On the other hand when image is focused in the plane of “Zone 2” WBCs are apparent in the image (right panel), floating above the RBCs. (C) Illustration of blood sample observations under the microscope, showing the arrangement of RBCs, WBCs, and spiked cancer cells and the classification of “Zone 1” and “Zone 2” accordingly.

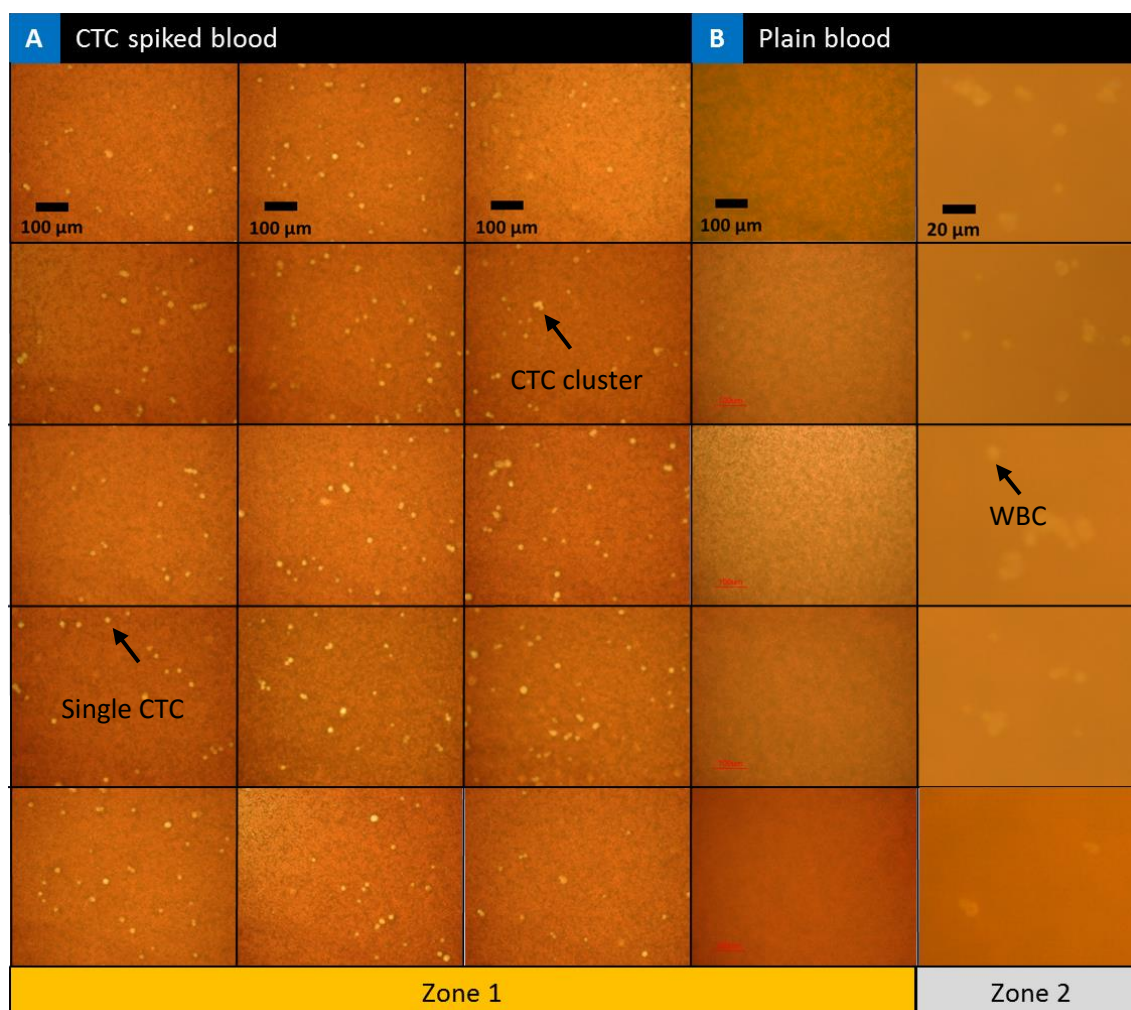


**Figure 70.** (A and B) Additional optical microscopic images of blood sample droplets on top of the device. (A) SKBR-3 spiked blood sample. SKBR-3 spiked cancer cells are observed in the blood at 20X magnification focused in “Zone 1”. 15 out of the 20 images analyzed to generate the data presented in Table 13 are shown here. (B) Plain blood sample. There are no cancer cells or WBCs observed in plain blood samples when the microscope is focused in “Zone 1” plane. On the other hand when image is focused in the plane of “Zone 2” WBCs are apparent in the image (right panel), floating above the RBCs. Scale bars on the first row correlate to all images in each column.

Devices were then incubated in anti-EpCAM (EMD Bioscience, Cat. No. OP187), anti-HER-2 (Cell Singnaling tech., Cat. No 2242S), or anti-IgG (EMD Millipore, Cat. No. 411550), 20 $\mu$ g/mL in 1X Phosphate-buffered saline (PBS) at 20  $\mu$ g/mL, for 2 hours at room temperature. After incubation, devices were rinsed in 1X PBS 3X. At last, devices were incubated with 0.5% Tween20 for 2 hours at room temperature. After incubation, devices were rinsed with 1X PBS, then stored inside a humid chamber at 4 °C with 20  $\mu$ L droplets of 1X PBS on top. For more detailed functionalization protocol please see Section 4.1.

### 9.2.3. BLOOD SAMPLE PREPARATION

Farhad Khosravi, Author of this thesis was the subject of all blood draws. Blood samples used and discussed in this chapter are all traced back to him as the only source and sole blood donor. This allowed for a control and identified blood source with the least degree of variation in each batch of blood samples.

Upon receiving approval from Worcester Polytechnic Institute's (WPI) Institutional Review Board (IRB), IRB#00007374, and completing biosafety, blood-borne pathogen, and standard microbiological practices trainings, the following protocol was developed under the guidance of Environmental Health and Safety department at WPI to collect and handle blood samples for the purposes of the experiments in this chapter.

As the blood sample volume defined for each set of testing in this chapter are set at 5  $\mu$ L, the total blood volume needed for each day of testing did not exceed 100



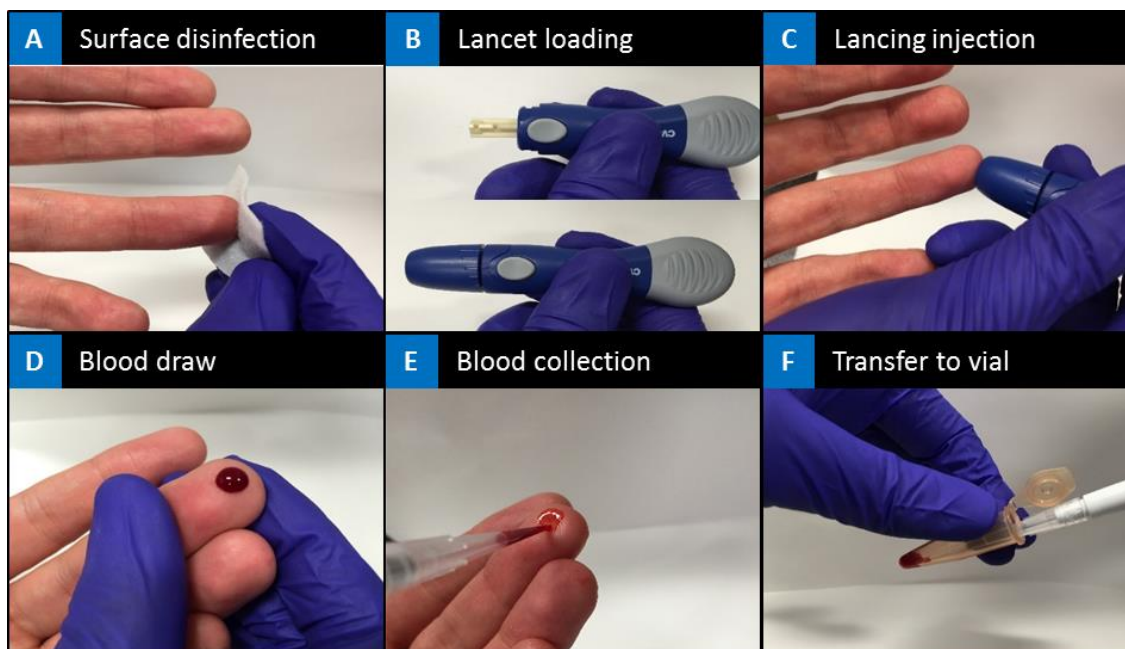


**Figure 71.** Capillary blood sampling using a lancing device. (A) Prepare the skin by applying sterile alcohol prep pads to the entry site and allow to air dry. (B) Load the lancing device with an ultra-thin lancet and prepare for puncture. (C) Puncture the skin with one quick, continuous and deliberate stroke. (D) Achieve a good flow of blood and wait for a ~100  $\mu$ L blood droplet to collect. (E) Collected exactly 50  $\mu$ L of the blood droplet using a micropipette, and then apply firm pressure to the site to stop bleeding. (F) Transfer the collected blood using a micropipette to a storage vial for further preparation. Prep pads, lancets, and lancing device were purchased from CVS pharmacy.

μL. Therefore, the blood draw protocol was generated around the volumes needed to minimize biohazardous waste generation and to maintain the health of the blood donor as the blood draws had to be executed frequently throughout the 21 days of testing. As a result, capillary sampling protocol provided by World Health Organization (WHO), “WHO guidelines on drawing blood: best practices in phlebotomy”, was adopted to generate a protocol to collect blood samples from a finger tip of the subject as presented in Figure 71. The collected blood was diluted 1:4 with blank or CTC spiked 1X PBS. This dilution protocol prevented the blood from clotting without the addition of any additional chemicals and allowed for determining an exact concentration of spiked CTCs levels in each sample.

#### 9.2.4. CELL CULTURE AND PREPARATION

SKBR-3 and MCF-7 carcinoma cell lines, and MCF-10A, normal epithelial cell line, were cultured and prepared for the objectives of the studies in this chapter. The cell culture method and preparations are explained in detail in Section 7.2. All cell lines were cultured and prepared individually according to ATCC’s guidelines, next they were detached from the culture flask using Accutase enzyme solution and suspended in 1X PBS buffer solution and taken for counting using a hemocytometer. Finally cells for each cell line were prepared at fixed concentrations of 800,000 cells/mL and 80,000 cells/mL in 1X PBS solution. Next the cell samples were diluted in blood 3:4 for a final spiked cell concentration of 1000 and 100 cells/5 μL. At this stage spiked blood samples were stored at 4 °C for same day testing. As test samples were injected onto the device at fixed volumes of 5 μL, the total number of the spiked cells injected to

each device was fixed at 1000 or 100 accordingly.

#### 9.2.5. EXPERIMENTAL DESIGN AND TESTING

There are two main variables within the design of experiment, sample type (plain, spiked MCF-7, MCF-10A, or SKBR-3 blood) and device type (IgG, HER-2, or EpCAM antibody functionalized). In addition, two cell concentrations were defined for each cell spiked sample type, 100 or 1000 cells. Table 10 presents the design of experiments and the number of replicates. Over all there were 10 replicate for each combination, 20 replicates indicates 10 for 100 cell concentration and 10 for 1000 cell concentration for that spiked sample type.

As discussed previously, Three cell lines of SKBR-3, positive control (over expressing HER-2), MCF-7, positive control (overexpressing EpCAM), and MCF-10A, negative control normal epithelial cell line (not overexpressing HER-2 or EpCAM), were cultured and prepared for these experiments. In addition to these three spiked sample types, plain non-spiked blood was also tested as the forth sample type, negative control, with each device type.

**Table 10.** Design of experiments.

		Sample type			
		Plain blood	SKBR-3 spiked blood	MCF-7 spiked blood	MCF-10A spiked blood
CNT device functionalization	IgG	10	20	20	20
	HER-2	10	20		20
	EpCAM	10		20	20



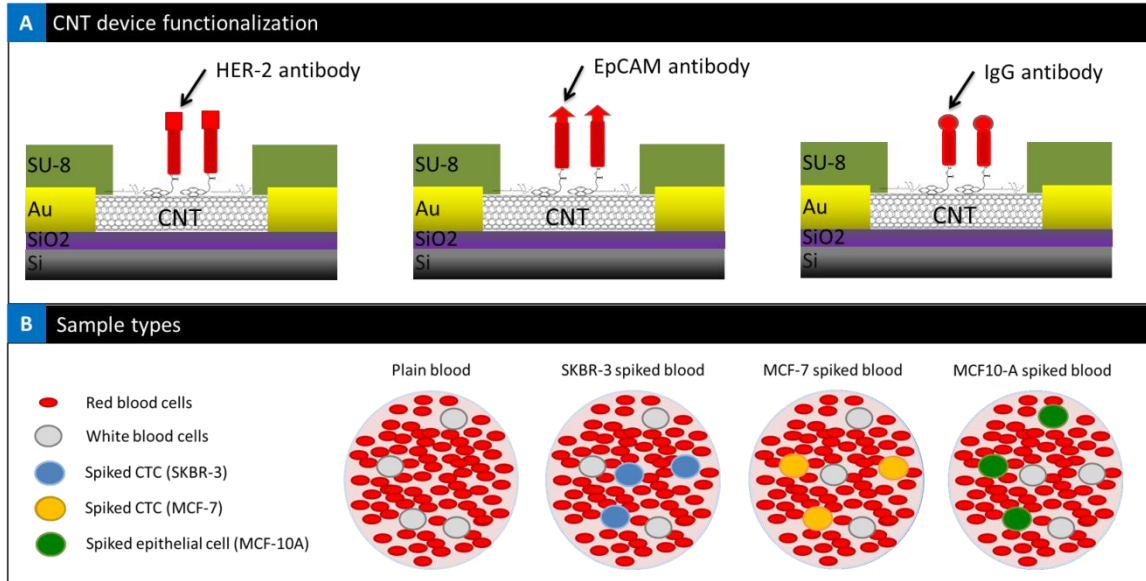


**Figure 72.** Schematic illustrating the (A) three CNT device functionalization variations, IgG, HER-2, and EpCAM antibody, functionalized to the surface of the CNT via PASE linker molecule, with tween-20 molecule covering the unfunctionalized CNT surface and (B) showing four sample types, plain blood, spiked SKBR-3 , MCF-7, and MCF-10A blood samples.

CNT devices were divided into three groups; first batch was functionalized with HER-2 antibody, second batch was functionalized with EpCAM antibody, and third batch was functionalized with non-specific IgG antibody via PASE linker molecule, tween-20 molecule was used to cover the non-functionalized CNT surface. Figure 72 illustrates the variations of CNT device functionalization and sample types. Table 10 summarizes the design of experiment. There are 17 unique combinations within sample types, device functionalization, and cell concentration, with 170 technical replicates. Four combinations were designed as positive controls (SKBR-3 spiked blood vs. anti-HER-2 functionalized CNT device and MCF-7 spiked blood vs. anti-EpCAM

functionalized CNT device, both at 100 and 1000 cell concentrations), with 40 overall replicates, shown in blue in Table 10. Thirteen other combinations shown in red were designed as negative controls, non-specific interaction.

The testing platform was set up on Signatone probe station. Agilent 4156C Semiconductor Parameter Analyzer equipped with a custom LabVIEW interface for monitoring the sensors and data collection. 100 mV  $V_{DS}$  was applied to source electrodes and 0 V  $V_G$  was applied using a Ag/AgCl reference electrode via the sample droplet, source-drain current,  $I_{SD}$ , was recorded for the duration of the test. The testing setup is demonstrated in Figure 68 (B). Throughout the testing, devices were kept inside a humidified chamber to prevent evaporation of the sample droplet. For the detail explanation of testing setup please see Section 3.3.

The testing protocol started with a hydrated device, 20  $\mu$ L droplet of 1X PBS on top of the device, which was placed immediately after functionalization which covers the whole 3x3 mm device window, Figure 68 (B and C). The bias was applied, and the sensor was monitored for the initial 4 minutes, then 5  $\mu$ L droplets of the sample solution, plain or spiked blood, was pipetted directly into the standing 20  $\mu$ L 1X PBS droplets, Figure 68 (B). Devices were monitored for 360 seconds after addition of the sample solution. The total duration of one test was 10 minutes long. To compare results among devices,  $I_{SD}$  data were normalized to obtain the  $\Delta G/G_0$  values for conductance. After end of the test, each CNT device was taken to be imaged on an optical microscope to confirm the presence of cancer cells and their orientation, Figure 68 (D) is an example of one of these images. Additionally, numbers of devices were taken for

immune staining and confocal analysis. The spiked blood samples consisted of ~1,000 or ~100 cells/5 $\mu$ L. This concentration of cells was chosen to be relevant to upper limit of clinical samples, as discussed in Chapter 1, and for proof of concept of this approach. Surface of the CNT device is capable of interacting with over 20,000 cells at one time, therefore fully capable of capturing 1,000 or 100 spiked cells.

### 9.3. RESULTS

In this section we will review the electrical, optical, and confocal data collected during the duration of the experiments proposed earlier. Additionally we will review the statistical analyses generated by processing the electrical conductance data.

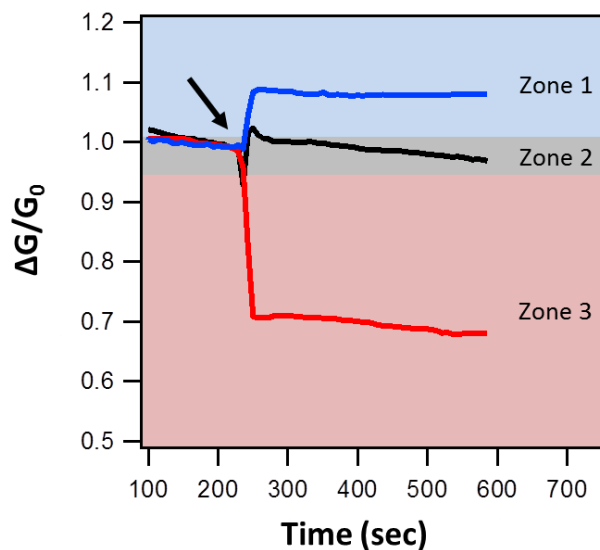


**Figure 73.** Signal type classification. Zone 1 represents devices that generated an increase in their signal after addition of sample droplet (>2%), blue line. Zone 2 represents devices that generated no significant change in their signal after addition of sample droplet (2%), black line. Zone 3 represents devices that generated decrease in their signal after addition of sample droplet (>2%), red line.

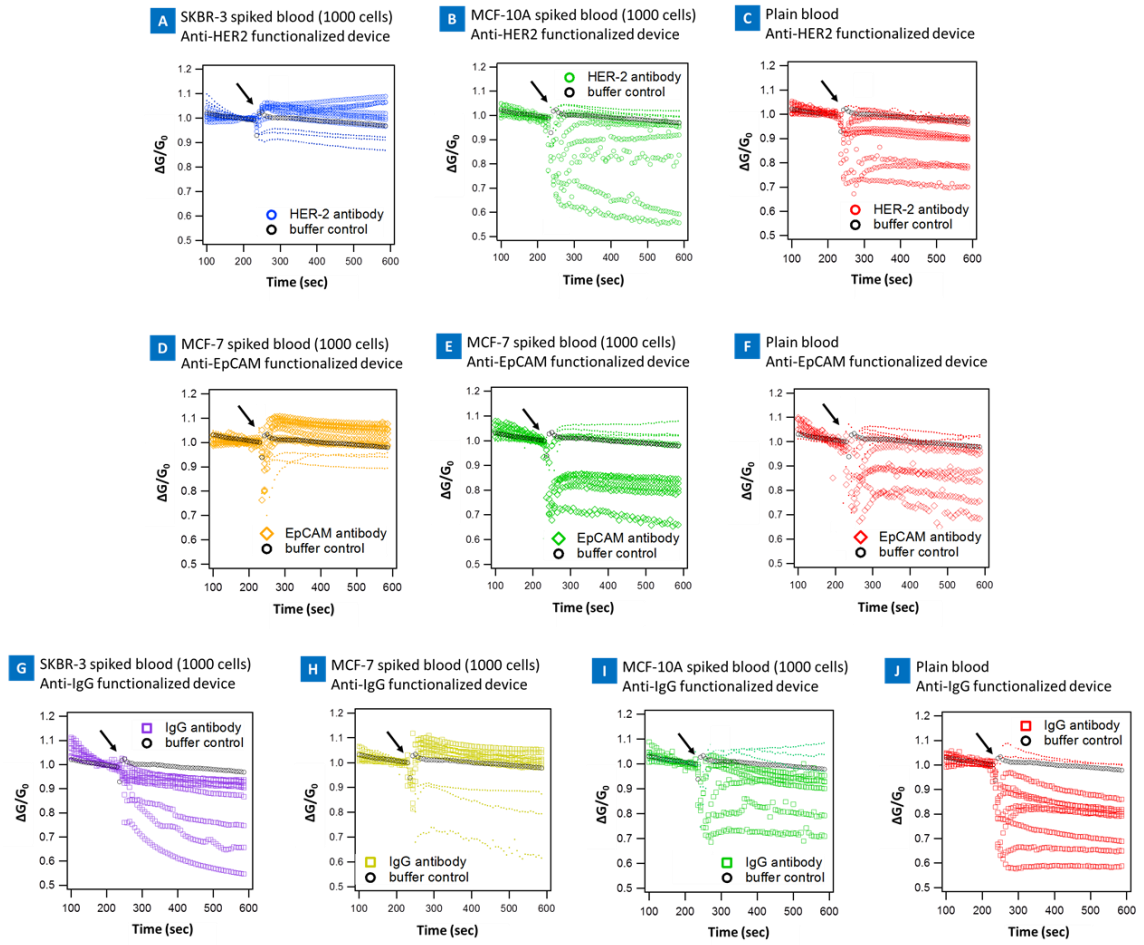


**Figure 74.** Merger of device array data for 1000 cells/5  $\mu$ L variation. Each panel correlates with one combination of sample type and device type with respect to design of experiment presented in Table 10, 10 replicates each. Each row correlates to one type of device functionalization, HER-2, EpCAM, and IgG. Plain blood samples are shown in red, MCF-10A in green, MCF-7 in orange and yellow, and SKBR-3 in blue and purple. The control buffer signal is shown in black marks in each panel as point of reference. If majority of signals in one panel were above or below the reference buffer control signal, they were plotted in marks, the rest of the data points that are not showing the same trend are plotted as dots. Arrow indicated the time of sample injection.

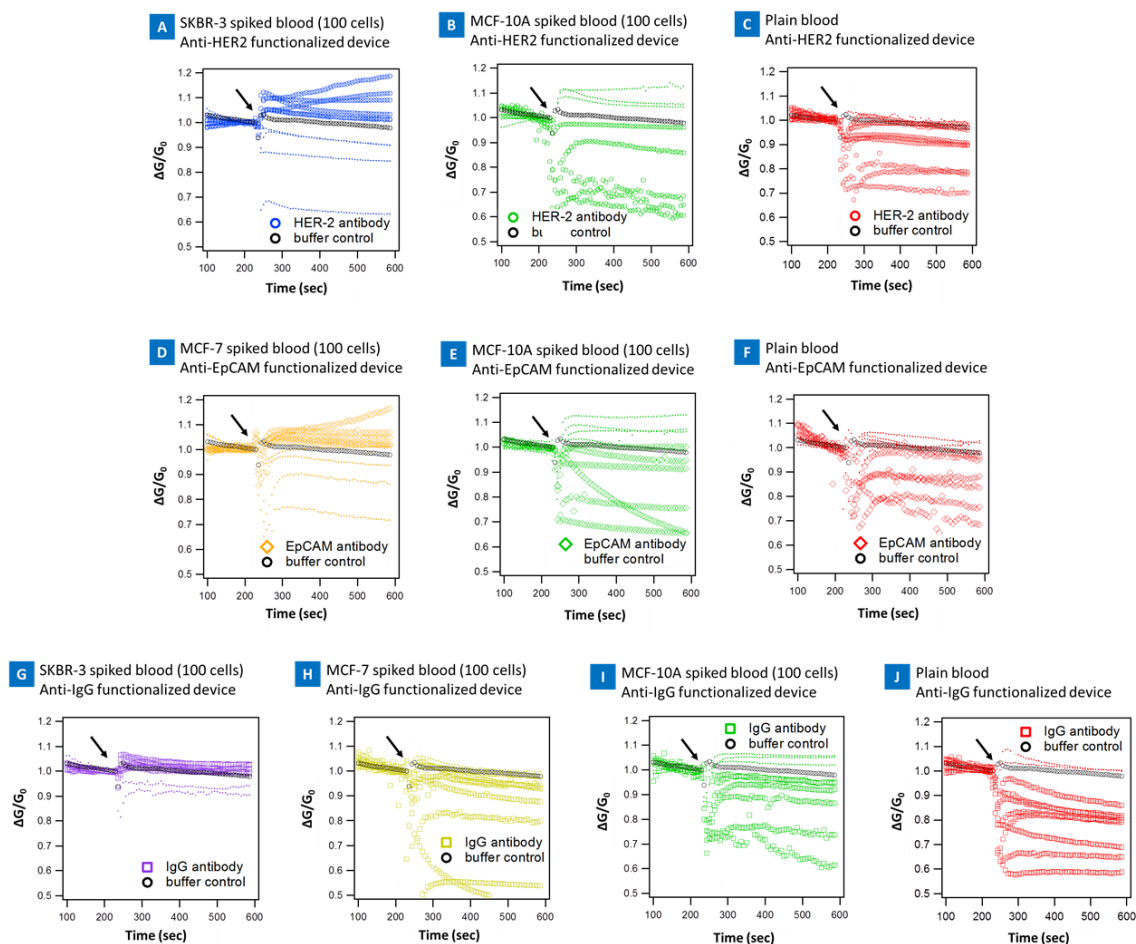


**Figure 75.** Merger of device array data for 100 cells/5  $\mu\text{L}$  variation. Each panel correlates with one combination of sample and device type with respect to design of experiment presented in Table 10, 10 replicates each. Each row correlates to one type of device functionalization, HER-2, EpCAM, and IgG. Plain blood samples are shown in red, MCF-10A in green, MCF-7 in orange and yellow, and SKBR-3 in blue and purple. The control buffer signal is shown in black marks in each panel for point of reference. If majority of signals in one panel were above or below the reference buffer control signal, they were plotted in marks, the rest of the data points that are not showing the same trend are plotted as dots. Arrow indicated the time of sample injection. Plain blood panels are replicates from Figure 74, as there are no spiked cell concentration variations within these samples.

Figure 74, 1000 cells/ 5 $\mu$ L cell concentration variation, and Figure 75, 100 cells/ 5 $\mu$ L cell concentration variation, present the electrical current signals collected during spiked blood experiments. Three types of signals were observed with respect to the buffer control, signal that increased, decreased, or did not significantly changed with respect to the buffer control. These three types of signals were classified as zone 1, 2, and 3 as presented in Figure 73. Each panel of the data presented in Figure 74 and Figure 75 were analyzed separately and the signals were plotted as marks or dots within each panel depending on if they were part of the majority or minority of the total signals for that panel, respectively. Overall 17 combinations, 4 positive controls and 13 negative controls, were defined in these experiments as they are presented in Figure 74 and Figure 75. It was observed that majority of signals in all 4 positive controls, Figure 74 (A and D) and Figure 75 (A and D), were located in “zone1” showing an increase in device conductance after the addition of the spiked samples, with respect to the buffer control. On the other hand majority of the signals, 11 out of the 13, in negative controls landed in “zone 3”, showing a decrease in their signal, device conductance, after addition of the sample droplet with respect to the buffer control. Table 11 summarizes the zone classification results for all the data presented here. Overall, we observed that specific interaction indicates an increase in the device conductance where non-specific interaction results in a decrease or no change in device conductance. These results show a great promise to discriminate spiked cancer cells in blood based on their effect on nanotubes electrical properties. In the next section we will use DTW statistical analysis classifier, as part of our collaboration with Patrick Trainor and Shesh Rai at University

**Table 11.** Signal classification results.

Experiment #	cell concentration	Device type	Smample type	Zone 1	Zone 2	Zone 3	total
1	1000	HER-2	SKBR-3	6	1	3	10
2	1000	HER-2	MCF-10A	3	2	5	10
3	-	HER-2	Plain	1	3	6	10
4	1000	EpCAM	MCF-7	5	2	3	10
5	1000	EpCAM	MCF-10A	3	1	6	10
6	1000	EpCAM	Plain	3	2	5	10
7	1000	IgG	SKBR-3	0	0	10	10
8	1000	IgG	MCF-7	5	2	3	10
9	1000	IgG	MCF-10A	3	1	6	10
10	-	IgG	Plain	2	0	8	10
11	100	HER-2	SKBR-3	6	0	4	10
12	100	HER-2	MCF-10A	3	0	7	10
13	100	EpCAM	MCF-7	6	1	3	10
14	100	EpCAM	MCF-10A	3	2	5	10
15	100	IgG	SKBR-3	3	5	2	10
16	100	IgG	MCF-7	1	2	7	10
17	100	IgG	MCF-10A	3	0	7	10

of Louisville, to investigate if there is a significant difference between specific and non-specific interaction with respect to the positive and negative controls presented here.

### 9.3.1. STATISTICAL ANALYSIS

After initial evaluations, we observed that SKBR-3 spiked blood data generated the most vivid statistical data. To better understand these findings, we will focus on presenting the plain, spiked SKBR-3, and MCF-10A blood samples in interaction with anti-HER-2 and anti-IgG functionalized devices, in this section.

In order to test whether the HER-2 functionalized devices could discriminate between SKBR-3 spiked blood samples and controls (plain blood and MCF-10A spiked blood), a classifier was constructed and the area under the receiver operator curve (AUC) was estimated by 10-fold cross-validation [473]. Both high (1,000 /5  $\mu$ L) and

low (100 / 5  $\mu$ L) concentrations of spiked cells were evaluated, separately. The primary endpoint was AUC in the high concentration condition, the low concentration tests were conducted as an exploratory analysis. A total of 30 replicates (10 replicates with 1,000 SKBR-3 cells / 5  $\mu$ L spiked, 10 replicates with no cells added, and 10 replicates with 1,000 MCF-10A cells / 5  $\mu$ L spiked) were used in training the high concentration condition classifier. To ensure balance between the SKBR-3 positive condition and negative condition, a random sample of 5 replicates with no cells and 5 replicates with 1,000 MCF-10A cells / 5  $\mu$ L spiked was combined as SKBR-3 negative. Whether the series observed with HER-2 antibody functionalized devices and SKBR-3 spiked blood could be discriminated from IgG functionalized devices was evaluated to determine if the HER-2 antibody and SKBR-3 spiked blood resulted in a specific as opposed to non-specific antibody-antigen interaction.

The discrimination tests were conducted utilizing a k-nearest neighbor classifier; please see Section 8.4.10 for more information on k-nearest neighbor classifier. A kernel-based learning method such as k-nearest neighbors was employed given a parametric model for device response has not been developed. The kernel was based on a pseudo-distance metric known as Dynamic Time Warping (DTW) distance [446, 474, 475]. Dynamic Time Warping (DTW) is a dynamic programming algorithm that seeks to find an optimal global or local alignment of two series in the time domain to minimize the total distance between the series with respect to a traditional distance metric such as Euclidean distance, see Section 8.4.9. The DTW-distance can then be used as dissimilarity metric for training kernel-based classifiers. Further details on the



DTW algorithm for use in classification can be found in Rai and Trainor (2016) [446]. The DTW algorithm alignments used a “Symmetric 2” step pattern and enforced a main-diagonal windowing constraint [475]. k-nearest neighbor classifiers predicted the class probabilities as:

$$\hat{P}_g(\mathbf{y}_i) = \frac{1}{k} \sum_{\mathbf{y}_j \in N_k(\mathbf{y}_i)} 1_{c_j=g}(\mathbf{y}_j) \quad (29)$$

where  $c_i$  denotes the sample type of the  $i$ th replicate  $\mathbf{y}_i$  represents the  $i$ th replicate series. 10-fold cross-validation was used to estimate the area under the receiver operator curve (AUC) and to select the optimal series normalization method and value of k. The series normalization methods evaluated were: mean-variance normalization of the entire series, slope correction followed by normalization, and slope correction followed by scaling by the value at a fixed time-point. Mean-variance normalization was defined as  $\mathbf{y}_i = \frac{\mathbf{y}_i - \bar{\mathbf{y}}_i}{s_{\mathbf{y}_i}}$  where  $\bar{\mathbf{y}}_i$  represents the mean of the  $i$ th replicate series and  $s_{\mathbf{y}_i}$  represents the standard deviation. Slope correction was conducted by fitting a linear model to the first 75 series sampling points to estimate the machine drift of the devices. In addition to evaluating slope correction followed by mean-variance normalization, slope correction followed by scaling the series by dividing by series value at a standardized time-point (50) was evaluated. Prior to normalization or scaling, the series were truncated to have length 150, with the length symmetric about the time-point of droplet deposition.

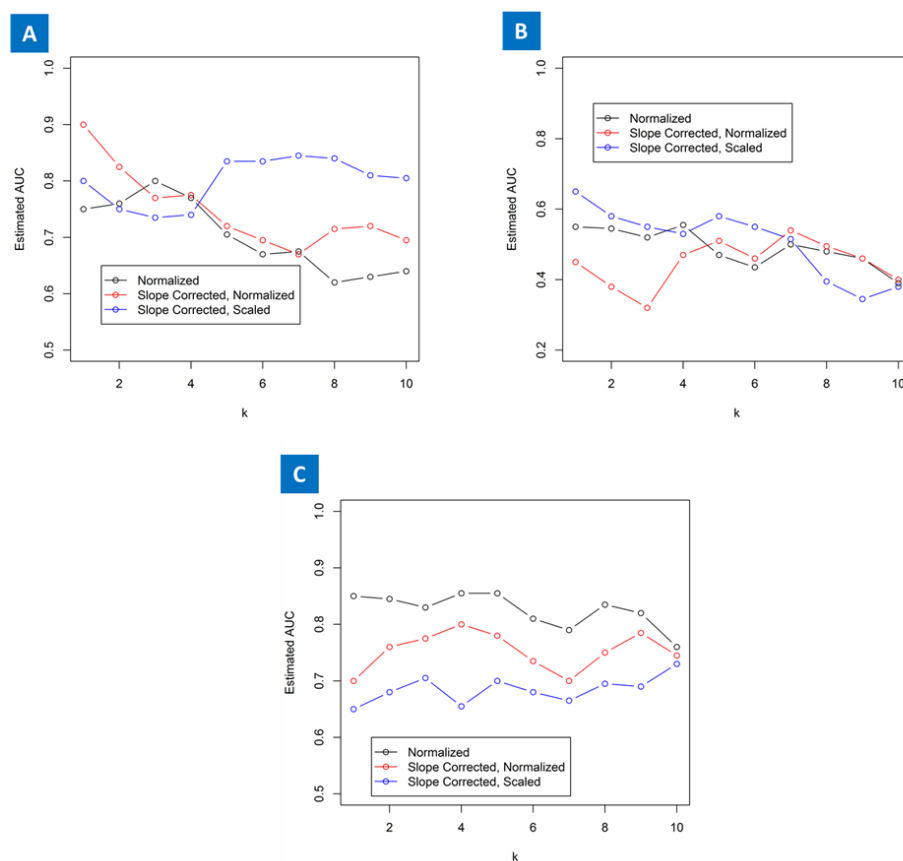


**Figure 76.** (A) Cross-validation estimated AUC for discriminating a high concentration of SKBR-3 cells given HER-2 antibody. (B) Cross-validation estimated AUC for discriminating a low concentration of SKBR-3 cells given HER-2 antibody. (C) Cross-validation estimated AUC for discriminating antibodies, anti-HER-2 and anti-IgG functionalized devices, given a high concentration SKBR-3 cells.

**Table 12.** CV-estimated confusion matrix for high concentration SKBR-3 cells.

True Class	Predicted Class	
	Negatives (Not spiked / MCF-10A)	Positives (SKBR-3 spiked)
Negatives (Not spiked / MCF-10A)	9	1
Positive (SKBR-3 spiked)	1	9

Cross validation (CV)-estimated AUC for the DTW distance based  $k$ -nn classifiers for the high concentration of SKBR-3 cells with HER-2 functionalized devices are shown in Figure 76 (A). The highest AUC for this condition was observed for the 1-nearest neighbor classifier with slope corrected normalized series. Class prediction using CV-estimation confusion matrix for high concentration SKBR-3 cells is presented in Table 12. AUC for discriminating a low concentration condition is shown in Figure 76 (B). AUC for the discrimination tests between antibodies (HER-2 versus IgG) with SKBR-3 cells spiked in blood is shown in Figure 76 (C).

Devices functionalized with HER-2 antibody were able to discriminate between blood spiked with a high concentration of SKBR-3 cells (1,000 / 5  $\mu$ L) and control blood (spiked with MCF-10A cells or not spiked, plain blood). 10-fold cross-validation estimated AUC for the 1-nearest neighbor DTW-distance based classifier was 0.90 after slope correction and normalization. One false negative and one false positive out of 10 positives and 10 negatives were observed in the cross-validation procedure, showing 90% sensitivity and 90% specificity. Sensitivity is defined as  $TP/P$ , where TP represents the number of correctly classified positive (SKBR-3 spiked) samples and P represents the total number of positive samples. Similarly, specificity is defined as  $TN/N$ , where TN represents the number of correctly classified negative samples (plain or MCF-10A spiked blood) and N represents the total number of negative samples. Of the replicates identified as true positives, 6/9 series finished higher, “zone 1”, after the rebound that followed droplet injection than the initial period, indicating a positive  $\Delta G$ ; of the replicates identified as true negatives, 7/9 series finished lower, “zone 3” after

the rebound that followed droplet injection than the initial period. This indicates that DTW classifier can more significantly discriminate the CTC spiked samples than a simple observation of change in device conductance, opening the way for a deeper analysis of the electrical data.

Devices functionalized with HER-2 antibody were unable to significantly discriminate between blood spiked with a low concentration of SKBR-3 cells (100 / 5  $\mu$ L) and control blood. 10-fold cross-validation estimated AUC for the 1-nearest neighbor DTW-distance based classifier was 0.45 after slope correction and normalization.

Fixing sample phenotype (blood spiked with a high concentration of SKBR-3 cells) allowed for discrimination of antibody functionalization, anti-HER-2 vs. anti-IgG functionalized device. 10-fold cross-validation estimated AUC for the 1-nearest neighbor DTW-distance based classifier was 0.70 after slope correction and normalization. Based on the results from fixing the sample phenotype and separately device phenotype, we can suggest that the significant difference seen in electrical signal with our positive controls must be as a result of HER-2 receptor, on the cell membrane, interaction with the HER-2 antibody on the surface of the CNT.

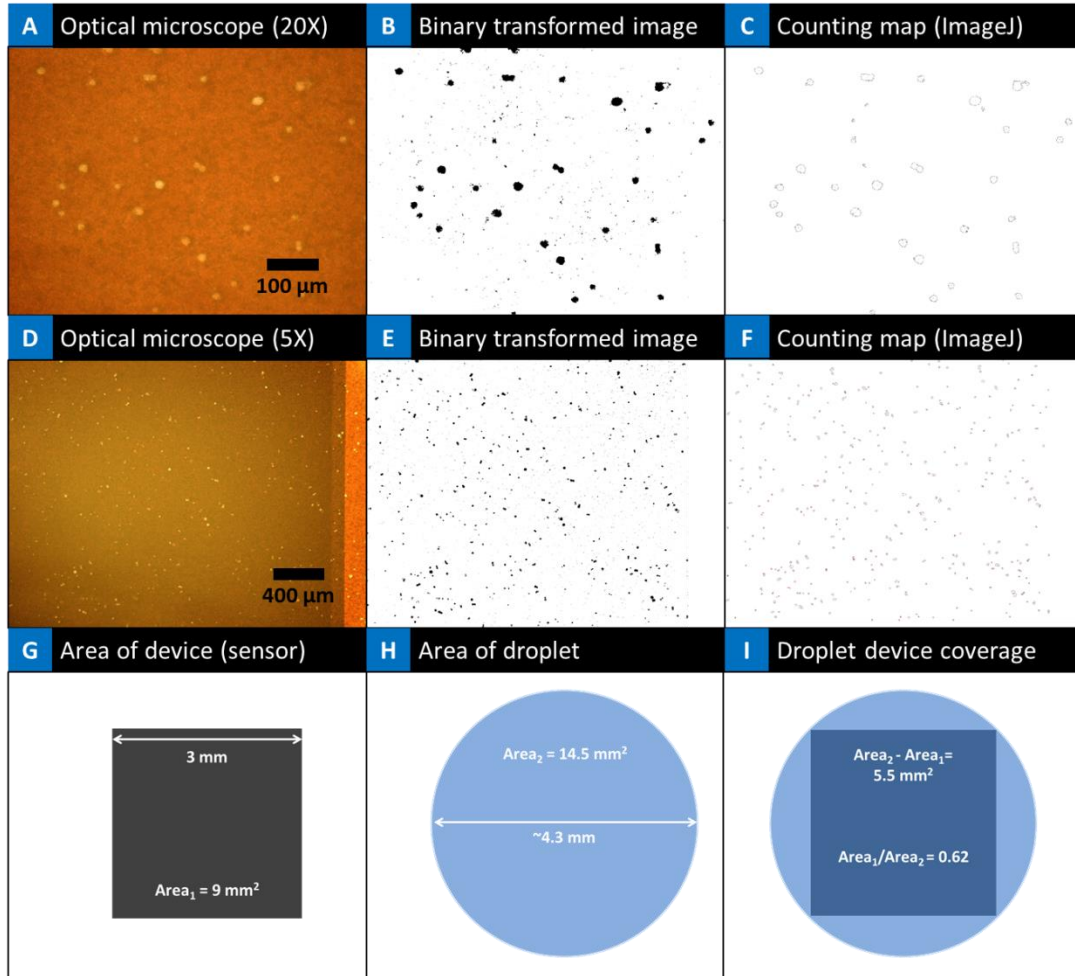
In this section we showed that using DTW classifier, we are able to discriminate CTCs spiked in blood with respect to sample and device type controls defined in the previous section. These analyses are an indicator that specific interaction between the cancer cell receptor and the antibody functionalized on the surface of the nanotube can

potentially result in significant change in nanotubes electrical property. This is a very promising indicator to discriminate presents of CTCs in blood.

### 9.3.2. OPTICAL MICROSCOPE IMAGE ANALYSIS

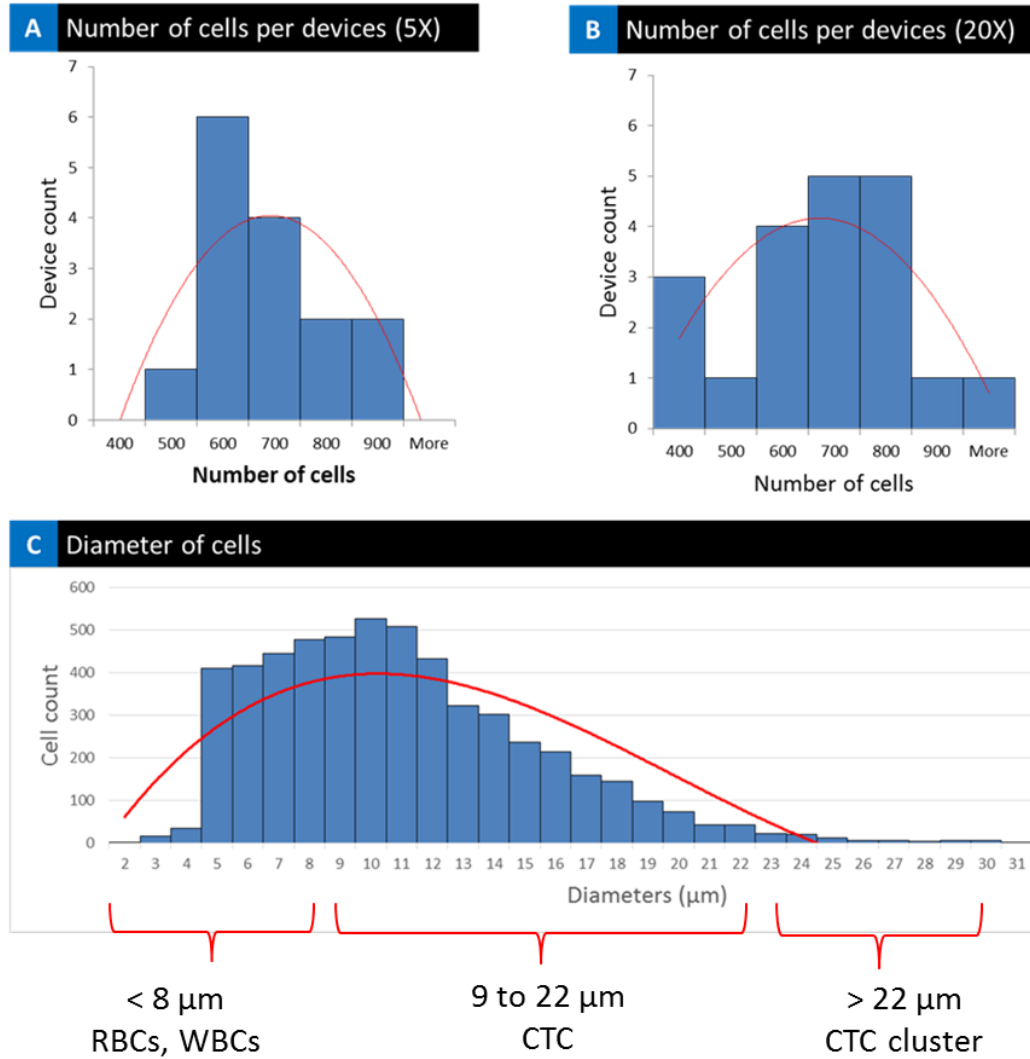
As a result of our observation in Section 9.2.1, with regards to blood droplets sample settling as illustrated in Figure 69 (C), we were able to image zone1 and further analyze the captured spiked CTCs using optical microscopy technique. All the devices were imaged under the optical microscope after the end of each test. Number of devices with 1000 spiked CTC samples were selected and their respective optical microscope images were taken for spiked cell analysis. 20, imaged at 20X magnification, and 15 devices, imaged at 5X magnification, were selected for further processing and analysis.

Figure 77 (A and D) present an example set of 20X and 5X optical images taken for image analysis. ImageJ software was used to process each image. Original optical images were converted to binary image and processed using ImageJ software to distinguish spiked cells, shown in black circles, from the red blood cell in the background by using color threshold function, Figure 77 (B and E). Next, ImageJ software's particle analysis function was used to count the number of cells and cell diameter for each set of images, Figure 77 (C and F), knowing the scale bar for each image. All the data from these analyses, including number of cells per image, cells per unit of area ( $\text{mm}^2$ ), diameter of cells, and number of cell per device calculated based on partial cell count and total device area,  $9 \text{ mm}^2$ , are presented in Table 13 and Table 14.



**Figure 77.** (A and D) Show optical microscope image of devices with spiked sample droplet on top. (B and E) Show binary conversion of the optical microscope images, highlighting the spiky cells in black and separating them from the background. (F and I) ImageJ analyses of binary images, based on diameter and shape, showing cell count map of each original optical image. (G-I) demonstrate surface area comparison of the square shaped device vs. circular droplet covering the device. CNT device is only covered by ~62% of the total droplet area.

Figure 77(G-I) shows the illustration of CNT device area vs. sample droplet covering the device. As shown, the sample droplet's diameter exceeds the device window to assure full coverage of the device. The nature of the square shape of the device and circular surface area of the droplets, results in the device only covering ~62% of the sample droplets base area. If we assume uniform and even coverage of spiked cells throughout the whole sample droplet's base area, we can only expect ~62% of the spiked cells to land on the device surface. In the case for 1000 cells/ 5 $\mu$ L, we expect for about 620 of the cells to land on the device surface on average. As presented in Table 13 and Table 14, on average 624 (20X images) and 623 (5X images) cells were captured and counted on each device which correlates with our calculations and expectations with regards to device geometry and droplet shape. Figure 78 presents histograms of cell count per device and cell diameter. On average, cell diameter was measured at 13  $\mu$ m for 20X images and 12  $\mu$ m for 5X images. 5X images have lower resolution of cells and therefore one can expect information loss and smaller cell diameter calculations. Overall, over 90% of cell diameter measured using imageJ software fall within the range of 6 to 22  $\mu$ m which is within our expectation for CTCs as discussed in Chapter 1. The measurements in the upper end, >20  $\mu$ m, can be a result of a cluster of two or three cells as seen in optical image on Figure 77 (A) and confocal image in Figure 79 (second row C), resulting in a larger diameter estimates. Lower end of the diameter measurements, < 8  $\mu$ m, have the potential to be misclassifications of either RBCs or WBCs miss classified as CTCs. On the other hand, these smaller cells can also be smaller CTC with smaller diameter due their size; loss of resolution after



**Figure 78.** Histogram of number of cells counted per device based on 5X (A) and 20 X (B) magnifications optical microscope images. (C) Presents the histogram of diameter of all cells counted.



**Table 13.** Cell count data per device based on 20X images.

Device number	Number of cells	Cells/mm <sup>2</sup>	Average diameter (μm)	Number of cells per device
1	33	78	10	706
2	31	74	11	663
3	24	57	10	514
4	24	57	15	514
5	15	36	14	321
6	33	78	14	706
7	32	76	11	685
8	22	52	13	471
9	16	38	13	342
10	32	76	13	685
11	36	86	12	771
12	24	57	14	514
13	39	93	15	835
14	30	71	16	642
15	30	71	14	642
16	25	59	15	535
17	35	83	15	749
18	49	117	14	1049
19	37	88	14	792
20	16	38	14	342
average	29	69	13	<b>624</b>
std. dev.	8	20	2	178

**Table 14.** Cell count data per device based on 5X images.

Device number	Number of cells	Cells/mm <sup>2</sup>	Average diameter (μm)	Number of cells per device
1	339	61	10	552
2	441	80	12	719
3	308	56	18	501
4	340	62	10	554
5	550	100	10	896
6	376	68	13	613
7	344	62	12	561
8	496	90	12	808
9	435	79	12	708
10	300	54	15	489
11	371	67	12	604
12	335	61	11	546
13	327	59	10	533
14	392	71	11	639
15	378	69	10	617
average	382	69	12	<b>623</b>
std. dev.	68	12	2	111

image processing can also reduce the diameter size calculated. Nevertheless, Optical image analysis presented here demonstrates a great confidence in the ability to capture CTCs and analyze their physical appearance using optical microscopy without disturbing the platform. To further understand the nature/type of cells captured, immunofluorescence techniques were used.

### 9.3.3. CONFOCAL IMAGE ANALYSIS

Four HER-2 functionalized devices injected with SKBR-3 spiked blood were taken for immunofluorescent staining and confocal microscopy without any further manipulation. The staining and imaging process is similar to what has been described in Section 7.2.1. Figure 79 demonstrates captured SKBR-3 cells on the device stained for cytokeratin (positive for epithelial cells and negative for WBCs) and CD45 (negative for epithelial cells and positive for WBCs). It is very impressive to be able to capture and maintain captured CTCs on the device for confocal microscopy. The staining protocol involves multi-level labeling/staining protocol with vigorous rinsing steps. The fact that the captured CTCs are still present and attached on top of the device shows the strong interaction of the cells to the functionalized CNT surface. In addition we were able to distinguish rare presence of WBCs from CTCs attached to the device using confocal microscopy, CD45 positive. In any setting, negative interactions, in this case sticking of WBCs to the device surface, are expected. The ability to cross out any non-specific interaction using confocal microscopy is of great advantage with our platform.

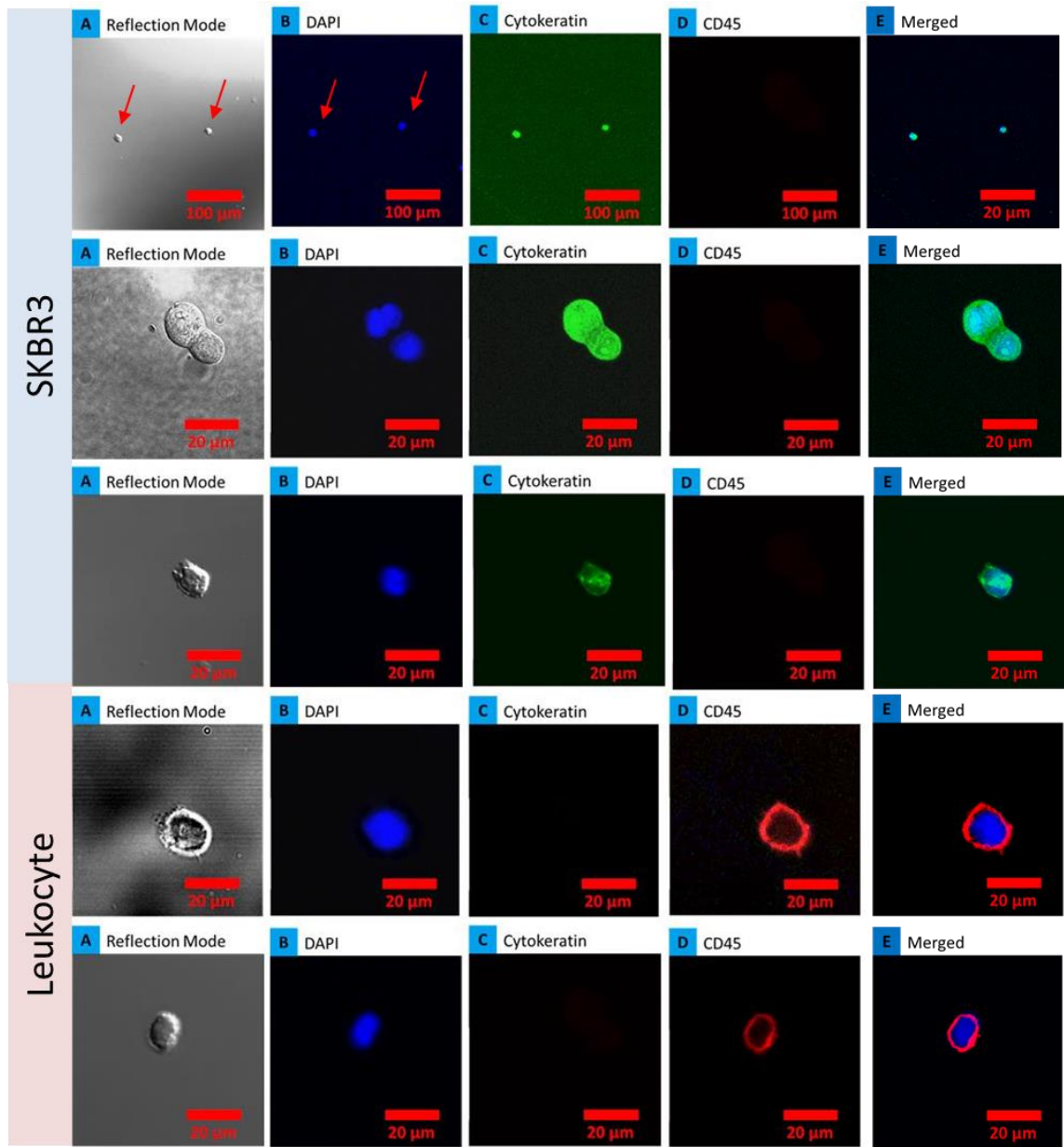


**Figure 79.** Cell differentiation using confocal microscopy: SKBR3 cells captured on chips from 3 devices showing positive staining for DAPI, cytokeratin (CK-19) and negative for CD45 and two images of leukocytes captured showing positive for DAPI and CD45 while negative for cytokeratin. (A) series of optical images; (B) DAPI nuclear stain; (C) CK19 stain for cancer cell and (D) CD45 for leukocytes and (E) merged image of nuclear and cytoplasmic stains.

#### 9.4. CONCLUSION AND FUTURE WORK

In this chapter we demonstrated the ability to capture spiked cancer cells in blood using our CNT micro-array platform. Additionally, we were able to distinguish cancer cells, SKBR-3, from non-cancerous cells, MCF-10A, and plain blood with statistical confidence using DTW classification resulting in 90% specificity and sensitivity with 1000 cells/ 5 $\mu$ L concentration samples. Using optical image analysis we confirmed capture and landing of all spiked cells on the CNT device with respect to device geometry. Finally we confirmed capture cells as CTCs using confocal microscopy and were able to distinguish false positives in an event of WBC attachment to device which are cytokeratin negative and CD45 positive unlike CTCs that are positive for cytokeratin and negative for CD45.

It would be interesting to further investigate the device response with biological replicates, different blood donors, to gain a higher confidence for the specific interactions we observed here. In addition, testing other cancer cell lines that over express HER-2, such as BT474, and functionalizing devices with other antibodies, such as IGF1R, that target other overexpressed receptors on CTCs can help better understand and further validate our observations here.

Here, we observed nonspecific interaction of cells with the CNT surface resulting in decrease in device conductance. Similar findings were also reported by McEuen's group with live cells [476] and lipid bilayer interaction with nanotubes [470]. In addition, we reported an increase in nanotube device conductance as a result of specific interaction of antibody functionalized CNT and cell membrane receptors in

blood samples. As also reported by other researchers, it is very difficult to single out the origin of the change in device conductance in a very complex system such as cell/nanotube hybrids. Identify the exact mechanism behind the changes observed in CNT electrical property, carrier mobility and density, as a result of these interactions requires sophisticated equipment in very controlled environment. Even though our broad range of controls, as part of the design of experiment, demonstrated high confidence in confirming the relation of the electrical signal to receptor and antibody interaction on the CNT surface, it still would be very interesting to further investigate the mechanism of this effect on CNT's electrical property.

A piezo-controlled manipulator pipetting system would be an effective tool to directly control the position and number of cells on the device and could enable studying the interaction mechanism and cell's effect on the electrical property of CNT device. Additionally, an electrode inside the micropipette to measure or control the potential inside the cell using "whole-cell" patch clamp configuration in which the pipette breaks into the cell center, with the membrane sealed around its edges, can enable us to study the effect of cell charge and its correlation with device electrical response. In this setting capacitive gating effect on the nanotube carrier density based on the known charge of the cell can be studied. The fragile nature of this seal would complicate the cell manipulation, but this configuration would allow us to perform more interesting experiments, such as measuring the change in nanotube conductance in response to an AC signal on the wire.

Although, confocal microscopy gives us an understanding on the type of cells captured on the device, based on presence of the over expressed receptors, It would also probably be fruitful to freeze a cell on a nanotube after an experiment, and coat the system with metal, to examine it with an SEM to get a high resolution image of the interaction of cell and CNT. Scanning photocurrent microscopy should also provide useful information about the nanotube behavior.

In its current form, our platform can be better integrated with an automated liquid handling system to fractionate 1 mL of blood to 5  $\mu$ L droplets per device to enable for high volume clinical studies. Finally, in future design improvements, microfluidic technology can be utilized to control the sample and volume of blood per device and create an integrated lab on a chip system.

Furthermore, a unique advantage to our platform is that each CNT micro-array is a separate device, after testing positive, the device can be removed and taken for further analysis, such as reverse transcription polymerase chain reaction (RT-PCR) and confocal microscopy (as presented in this chapter), to gain a deeper understanding of the genetic structure of the captured cells.

The CTC capture and electrical response that we have observed from semiconducting carbon nanotubes interacting with cells is an important step in the nanoscale electrical probing of biological systems utilizing them as multipurpose platform for capture and discrimination of diseased cells. Through some of the experiments suggested in this section, we hope that the nature of this response will be

elucidated, allowing nanotubes to be used for more advanced studies of cellular behavior.

## CHAPTER 10

### CONCLUSIONS AND FUTURE DIRECTIONS

#### 10.1. CONCLUSIONS

In this thesis we presented a carbon nanotube micro-array platform for detection of ions, free proteins and capture of breast cancer cells spiked in buffy coats and blood, Table 15. The contributions of the thesis for the broader nanobiotechnology community are as follows:

- Design and fabrication of 60-240 element nanotube micro-arrays for biomedical applications using semiconducting carbon nanotube, PASE functionalization protocol and clean room batch fabrication techniques.
- An in-depth understanding into sensing ions namely mercury and ammonium using semiconducting nanotube devices. 30 pM sensitivity for  $\text{Hg}^{2+}$  could be used in screening drinking water ( $\text{Hg}^{2+}$  ions limit set by most governmental EPA is ~10 nM).

**Table 15.** CNT micro-arrays for detection and capture of proteins and cells.

	Ions		Free proteins			<u>Spiked breast cancer cells</u>				
	Ammonium	Mercury	Biotin	EpCAM	IL-6	PBS	Buffy coat	Buffy coat	Blood	Blood
						SKBR-3	MCF-7	MCF-7	SKBR-3	MCF-7
<b>Device generation</b>	1	1	3	3	3	1	1	1	2	2
<b>Principle of detection/capture</b>	adhesion	adhesion	antibody	antibody	aptamer	antibody	antibody	antibody	antibody	antibody
<b>Detection limit</b>	300 nM	30 pM	1 ng/mL	1 ng/mL	1 pg/mL	1-25 cells/device	1-25 cells/device	1-25 cells/device	100-1000 cells/device	100-1000 cells/device



- Detection of cancer biomarkers such as IL-6/free proteins such as f-EpCAM using nanotube antibody or aptamer arrays. Detection of IL-6 at 1 pg/mL presents the applicability of nanotube arrays for cancer biomarker testing, IL-6 levels in serum >12 pg/mL have been correlated with large tumor size.
- Ability to detect and capture spiked breast cancer cells in buffy coats using nanotube micro-arrays with single cell sensitivity. The ability to distinguish samples that have cancer cells from samples that have no cancer cells in a medium such as blood/buffy coats in rapid manner for both large and small volumes can have significant implications in the clinic.
- Capture and isolation of spiked breast cancer cells overexpressing HER-2 receptors in blood using nanotube micro-arrays. These devices thus could be useful for capture and analysis of circulating tumor cells. Fractionation of blood sample over array of devices can enable rapid and simultaneous “liquid biopsy” analysis for circulating tumor cells.

As a result of these studies, we identified three key factors (film morphology, functionalization approach, and device geometry) which directly impact the device efficiency in detection and capture.

It was concluded that ultra-thin, < 100 nm, single layer SWNT array network is more sensitive to environmental changes and results in lower under layer channel

current fellow and higher on-off ration in comparison with thicker array networks, >100 nm.

PASE linker molecule was presented as an effective method to non-covalently anchor molecules and proteins to the surface of nanotube arrays. In addition, it was demonstrated that specific interaction of biomolecules to the surface of the nanotube can be further improved by using aptamer molecules instead of antibodies, thus increasing the binding sites and closing the gap in-between the anchored protein and SWNT surface due to the smaller size of the aptamer molecule. This approach enhanced and amplified the effect on the nanotube electrical property as result of analyte interaction with SWNT surface, increasing free protein detection limit from 1 ng/mL with antibodies to 1pg/mL using aptamers.

Finally, we understood that there is a fundamental tradeoff between decreasing target settling time and increasing sensitivity with respect to device geometry, active area. As active area on the device increases the sensitivity decreases and also does the settling time, which in return increases the capture yield of cells and diffusion efficiency of proteins on the nanotubes. This is evident especially with cell capture experiments in which the capture yield and number of cells needed to generate an electrical signature increases from 1-25 to 1000 from generation 1 to generation 2 devices which have ~1000X larger active area.

## 10.2. SUMMARY

Carbon nanotubes, with their nanoscale dimensions, high electrical sensitivity, ability for surface functionalization, and efficient operation in an electrolyte environment, can be excellent tools for probing biomolecular and cellular world. As we saw in Section 2.3, CNTs and transistor structures based on them have already been used to detect chemicals (i.e. gases), biomolecules (i.e. proteins, DNA, and enzymes), and even cells. In all these interactions, change in CNT conductance and/or shift in the CNT transistor threshold voltage was reported, but the mechanisms behind these responses are not always understood, especially with regards to cell interactions. Nevertheless, an integrated platform that utilizes CNTs in clinically relevant fashion for biomolecular detection, cell capture and classification is yet to be introduced. In this thesis, for the first time we demonstrated using thin film carbon nanotube networks for capturing circulating tumor cells and utilizing CNT's electrical properties to classify cell type, opening a whole new avenue for understanding and studying cellular interactions in clinically relevant setting.

To establish this platform, we fabricated an ultra-thin CNT film network using only  $\sim 1 \text{ mg/m}^2$  semiconducting CNT, 4  $\mu\text{g}$  film, utilizing vacuum filtration method, as described in Chapter 3. Ultra-thin CNT films described here are continuous, uniform, conductive, and almost single layer, at  $\ll 100 \text{ nm}$  thickness, exposing almost all nanotubes to surrounding environment. The vacuum filtration method allowed for a great degree of control on the mass concentration of CNT per film area and created a self-assembled network in a very simple and cost-effective way. Nano-micro material

preparation can be very expensive, CNTs are among the most expensive nanomaterials, using the vacuum filtration platform we were able to undercut the need for expensive and sophisticated facilities and equipment, such as chemical vapor evaporation (CVD), and fabricated thin films only using ~\$3 worth of material per 4 inch silicon wafer, \$800/1mg of CNT. We used these ultrathin cost effective CNT films to microfabricate CNT micro-array devices on Si/SiO<sub>2</sub> wafers, as discussed in Chapter 3. Three generations of devices were fabricated with CNT film windows of 20X20, 100X80, and 3000X3000  $\mu\text{m}$  for biomolecular, cell culture, and blood sample studies respectively. We characterized and functionalized these micro-array CNT devices and understood their electrical response and interaction with ions and other molecules, as described in Chapter 4. Next, we developed and optimized a viable functionalization protocol using PASE linker molecule, which pie stacks non-covalently on one end on CNT surface and covalently binds to antibodies on the other end. Here we demonstrated capturing gold nano particles on the surface of the functionalized CNT by specific interaction. Utilizing percolation theory we modeled conductivity of the CNT devices as a function of CNT film mass. We integrated these devices into our humid chamber system to control sample droplet evaporation rate and used our probe station platform to measure the conductance response of the nanotubes to complex molecular interactions using an electrolyte gate. We characterized analyte interaction with our CNT device using the Langmuir isotherm model and demonstrated that the magnitude and direction of the shift were directly related to the ionic charge concentration and interaction on the CNT surface.

We first presented our results with EpCAM biomarker interaction with functionalized CNT device complex in Chapter 5. These interactions caused a large threshold voltage shift and change in the conductivity of our CNT devices. We demonstrated that this response is directly related to the interaction of antibody, functionalized to the surface of the CNT, and its antigen, as non-specific antibody and antigen controls showed no significant change in electrical properties of the device. These findings went hand in hand with our earlier functionalization studies in Chapter 4, which visualized this same interaction using gold nanoparticles (NPs). These results together, showcased biosensing ability of our micro-array CNT devices and their capability to interact and capture biomarkers, such as EpCAM, and opened the door to further study the cell membrane receptor interaction with CNT surface. As cells and cell membranes are great complex systems, capturing them on the CNT surface using the antibody-receptor interaction and monitoring their effect on the electrical property of CNT in close proximity to its surface is of great interest.

In Chapter 6, we proposed using aptamers instead of antibodies for capture and detection of biomarkers. This allowed for a closer interaction of antigen to the CNT surface with respect to Debye length, as was presented with our AFM studies. As a result, we were able to demonstrate a very sensitive device response to very small concentrations of antigen, IL-6 target protein (1pg/mL). Even though using aptamers greatly improved sensitivity of our devices and showed great promise for higher interaction affinity with target protein, at the end we elected the antibody platform for our cell capture studies, as aptamers are much less available commercially and very

expensive to develop. However, this opens a new avenue for future studies on CNT micro-array devices utilizing aptamers for cell capture and discrimination.

We then described the results of our experiments with living cells spiked in phosphate buffer solution (PBS), Chapter 7, and in buffy coat, Chapter 8. Here for the first time, we demonstrated capturing cancer cells on a CNT thin film network and observed a unique electrical signal differentiating specific and non-specific interaction of the cancer cells on the device. We were able to differentiate the two types of interaction, specific and non-specific, with statistical confidence. Additionally, we attempted to correlate device signal intensity to the number of cells on the device using a model based on Kohlrausch-Williams-Watts (KWW) function. However, this relationship did not line up with our collected optical and electrical data. Nevertheless, further studies are needed before we can completely scratch out this relation between device signal intensity and number of cells on the device. To investigate this relationship further, we proposed live device imaging at the time of electrical signal collection to monitor the exact number of cells present on the device at the time of electrical signal generation. Additionally, manipulating number of cells on the device using a piezo-controlled manipulator pipette to control number of cells interacting with the device can shed more light on the mechanism of this interaction. Dynamic Time Warping (DTW) technique was used to build a classifier based on spiked buffy coat interactions with the CNT device and discriminate samples with cancer cells. This level of success was presented here for the first time utilizing CNT devices and DTW classifier. These results encouraged us to further investigate the clinical utility of this

platform. Even though ability to capture and discriminate CTCs is of great value in the clinic, preparing buffy coat samples still requires level of preparation and processing in the laboratory setting. The ability to process whole blood samples is of greater interest and opens the door for off-site and portable convenient analysis of blood samples for CTCs.

In Chapter 9 we explored the response of CNT micro-array devices with whole blood samples. Here we broadened the spectrum of our experimental design by adding more CTC cell lines and biomarkers of interest. We observed very promising results with regards to capturing CTCs on our devices, as presented in optical and confocal microscopy results. In addition, we saw distinguished difference with device signal signature for specific vs. non-specific interactions. When we placed CTC spiked blood sample on the device, however, we often saw a large increase in the CNT device conductance that occurred after the introduction of cancer cells on the functionalized device surface. The results suggest that the change in signal is due to the cell receptor membrane interacting with functionalized antibodies on CNT surface. Such interaction can result in cell membrane coming in contact with CNT surface. Charge associated with cell membrane bilayer can influence the CNT electrical properties. In addition, stress implemented to CNT and or cell membrane as a result of this interaction could additionally affect/activate ion channels on cell membrane causing releasing of ions and affecting the CNT surface charge field. However, we were unable to draw definitive conclusion for the origin of the change in signal, further studies to understand CNT-cell interaction and configuration is needed. We discussed attempts to image this

configuration using confocal microscopy, and explained how an SEM or photocurrent microscopy might provide more information. In addition, we were able to statistically discriminate SKBR-3 cancer cell lines spiked in blood from control MCF-10A non-cancerous cell line and plane blood with 90% sensitivity and specificity using DTW platform. These results are of great interest in the clinical setting. However, before being able to fully implement this technique in the clinic further work in regards to improving device sensitivity to number of cells captured from the samples is needed.

We also discussed a number of other directions for this study, including controlling the potential inside the cell through a whole-cell patch clamp configuration, using a piezo-controlled manipulator pipetting system to manipulate the exact number of cells and their orientation as they are interacting on the device, which can help gain a higher understanding of this interaction and the mechanism of device response.

### 10.3. FUTURE DIRECTIONS

Our experiments have demonstrated the great feasibility of utilizing carbon nanotubes for biosensing, cell capture and classification. We have developed a single platform based on CNT thin films to capture and discriminate living circulating tumor cells in spectrum of solutions, from phosphate buffer solution to whole blood, with great level of success. We have shown that CNT micro-arrays can be used effectively as nanoscale probes of biomolecular and cellular samples. Here we explore the exciting possibilities for these devices in many future research and applications. In number of directions this work can be complimented in the future: device design and integration,



functionalization technique, sample type, statistical analysis, post capture analysis of CTC.

To increase the device output, sensitivity, and efficiency, current microfluidic technologies can be utilized to develop an integrated lab-on-a chip platform to process and separate RBCs and WBCs, [477], introducing more purified sample for capture and discrimination of CTCs to possibly increase sensitivity. Additionally, microfluidics can enable controlled sample flow, type and volume per each device. At current design, integrating our devices with an automated liquid handling system to fractionate 1 mL of blood to 5  $\mu$ L droplets per device can enable our platform for high volume clinical studies.

Even though antibodies are the golden standard for specific antigen binding, exploring more effective functionalization method can be of interest to potentially increase the yield of the device. Studying capture and interaction yield of aptamers, affibodies, and antibody fragments in place of antibodies on our platform can introduce an opportunity for higher affinity interaction. Also smaller size of these molecules can introduce for higher number of binding sites thereby increasing CTC capture yield. Finally, targeting multiple biomarkers simultaneously, i.e. HER-2, EpCAM and IGF1R, can also increase the yield and sensitivity of the platform.

To better understand and validate the dynamic of the CTC capture and discrimination, variety of samples types can be tested. These samples types can vary by introducing new cancer cell type (i.e. BT474) or medium, multiple blood donors. In

addition to targeting cancer cells in blood, cancer cells collected by biopsy techniques such as fine needle aspiration can be tested and studied on our platform. Success with biopsy samples can be of great interest in the field of pathology opening the possibility of rapid on site sample analysis in the operating room.

More sophisticated statistical analysis can give us deeper understanding of the results. ANOVA model can be used further for a more robust design of experiment to shed more light on the origin of the interactions by closing in on the negative and positive controls. Dynamic time warping can be further improved to analyze biological replicates and to correlate gender, genetics, and family history to test results. In addition, work on DTW to recognize number of CTC captured from device signal would be of great interest.

The advantage of our platform is that each micro-array device is a separate unit, after testing positive, the device can be removed and taken for further analysis, such as reverse transcription polymerase chain reaction (RT-PCR) and confocal microscopy, to gain a deeper understanding of the genetic structure of the captured cells. These studies can further validate and improve upon our understanding of the specific interactions. As discussed Chapter 9, we also suggested directions for future research to further investigate the mechanism behind the change in the electrical signal as a result of the cell interaction with nanotubes.

## REFERENCES

- [1] L. A. Torre, F. Bray, R. L. Siegel, J. Ferlay, J. Lortet-Tieulent, and A. Jemal, "Global cancer statistics, 2012," *CA: a cancer journal for clinicians*, vol. 65, pp. 87-108, 2015.
- [2] A. Jemal, F. Bray, M. M. Center, J. Ferlay, E. Ward, and D. Forman, "Global cancer statistics," *CA: A Cancer Journal for Clinicians*, vol. 61, pp. 69-90, 2011.
- [3] R. L. Siegel, K. D. Miller, and A. Jemal, "Cancer statistics, 2016," *CA: A cancer journal for clinicians*, 2015.
- [4] H. Esmaeilsabzali, T. V. Beischlag, M. E. Cox, A. M. Parameswaran, and E. J. Park, "Detection and isolation of circulating tumor cells: principles and methods," *Biotechnology advances*, vol. 31, pp. 1063-1084, 2013.
- [5] D. Hanahan and R. A. Weinberg, "The hallmarks of cancer," *cell*, vol. 100, pp. 57-70, 2000.
- [6] G. P. Gupta and J. Massagué, "Cancer metastasis: building a framework," *Cell*, vol. 127, pp. 679-695, 2006.
- [7] C. L. Chaffer and R. A. Weinberg, "A perspective on cancer cell metastasis," *Science*, vol. 331, pp. 1559-1564, 2011.
- [8] D. Hanahan and R. A. Weinberg, "Hallmarks of cancer: the next generation," *cell*, vol. 144, pp. 646-674, 2011.
- [9] S. Paget, "The distribution of secondary growths in cancer of the breast " *The Lancet*, vol. 133, pp. 571-573, 3/23/ 1889.
- [10] T. R. Ashworth, "A case of cancer in which cells similar to those in tumors were seen in the blood after death.," *Medical Journal of Australia*, vol. 14, pp. 146-149, 1869.
- [11] S. A. Joosse, T. M. Gorges, and K. Pantel, "Biology, detection, and clinical implications of circulating tumor cells," *EMBO molecular medicine*, vol. 7, pp. 1-11, 2015.
- [12] V. Plaks, C. D. Koopman, and Z. Werb, "Circulating tumor cells," *Science (New York, NY)*, vol. 341, 2013.
- [13] N. Gerges, J. Rak, and N. Jabado, "New technologies for the detection of circulating tumour cells," *British medical bulletin*, vol. 94, pp. 49-64, 2010.
- [14] P. Paterlini-Brechot and N. L. Benali, "Circulating tumor cells (CTC) detection: clinical impact and future directions," *Cancer letters*, vol. 253, pp. 180-204, 2007.
- [15] S. Mocellin, U. Keilholz, C. R. Rossi, and D. Nitti, "Circulating tumor cells: the 'leukemic phase' of solid cancers," *Trends in molecular medicine*, vol. 12, pp. 130-139, 2006.
- [16] K. Jacob, C. Sollier, and N. Jabado, "Circulating tumor cells: detection, molecular profiling and future prospects," *Expert review of proteomics*, vol. 4, pp. 741-756, 2007.

- [17] J. W. Uhr and K. Pantel, "Controversies in clinical cancer dormancy," *Proceedings of the National Academy of Sciences*, vol. 108, pp. 12396-12400, 2011.
- [18] C. Alix-Panabières and K. Pantel, "Circulating tumor cells: liquid biopsy of cancer," *Clinical chemistry*, vol. 59, pp. 110-118, 2013.
- [19] Z. Candar, A. Ritchie, J. Hopkirk, and R. Long, "The prognostic value of circulating tumor cells in patients with breast cancer," *Surgery, gynecology & obstetrics*, vol. 115, p. 291, 1962.
- [20] C. Colombo, F. Rolfo, and G. Maggi, "Further research on the isolation of tumor cells from circulating blood," *Minerva medica*, vol. 50, pp. 2217-2223, 1959.
- [21] F. Graeber, "The methodology of cytological cancer diagnosis, especially the demonstration of tumor cells in the circulating blood in man," *Verhandlungen der Deutschen Gesellschaft für Pathologie*, vol. 45, pp. 264-266, 1960.
- [22] M. Romsdahl, J. Potter, R. Malmgren, E. Chu, C. Brindley, and R. Smith, "A clinical study of circulating tumor cells in malignant melanoma," *Surgery, gynecology & obstetrics*, vol. 111, p. 675, 1960.
- [23] M. D. Romsdahl, E. W. Chu, R. Hume, and R. R. Smith, "The time of metastasis and release of circulating tumor cells as determined in an experimental system," *Cancer*, vol. 14, pp. 883-888, 1961.
- [24] H. Saito, "Studies on cancer cells in the circulating blood. II. Experimental study on the fate of intraportally injected tumor cells and metastasis formation," *Acta medica et biologica*, vol. 9, p. 151, 1961.
- [25] H. Soost, "On the incidence of tumor cells in the circulating blood," *Deutsche medizinische Wochenschrift (1946)*, vol. 85, p. 893, 1960.
- [26] J. Wilson, "The detection of tumor cells in circulating blood," *The Bulletin of the Tulane Medical Faculty*, vol. 18, p. 171, 1959.
- [27] G. Wuest and G. Birk, "Demonstration and incidence of tumor cells in circulating human blood," *Die Medizinische Welt*, vol. 17, p. 922, 1962.
- [28] W. Qian, Y. Zhang, and W. Chen, "Capturing cancer: emerging microfluidic technologies for the capture and characterization of circulating tumor cells," *Small*, vol. 11, pp. 3850-3872, 2015.
- [29] E. J. Shpall and R. Jones, "Release of tumor cells from bone marrow [editorial; comment]," *Blood*, vol. 83, pp. 623-625, 1994.
- [30] E. J. Shpall, S. M. Stemmer, S. I. Bearman, S. Myers, M. Purdy, and R. B. Jones, "New strategies in marrow purging for breast cancer patients receiving high-dose chemotherapy with autologous bone marrow transplantation," *Breast cancer research and treatment*, vol. 26, pp. S19-S23, 1993.
- [31] W. Brugger, K. J. Bross, M. Glatt, F. Weber, R. Mertelsmann, and L. Kanz, "Mobilization of tumor cells and hematopoietic progenitor cells into peripheral blood of patients with solid tumors," *Blood*, vol. 83, pp. 636-640, 1994.
- [32] L. Weiss and U. Gerdig, "Barrier cells: stromal regulation of hematopoiesis and blood cell release in normal and stressed murine bone marrow," *Blood*, vol. 78, pp. 975-990, 1991.

- [33] M. Cristofanilli, G. T. Budd, M. J. Ellis, A. Stopeck, J. Matera, M. C. Miller, *et al.*, "Circulating tumor cells, disease progression, and survival in metastatic breast cancer," *New England Journal of Medicine*, vol. 351, pp. 781-791, 2004.
- [34] S. J. Cohen, C. J. Punt, N. Iannotti, B. H. Saidman, K. D. Sabbath, N. Y. Gabrail, *et al.*, "Relationship of circulating tumor cells to tumor response, progression-free survival, and overall survival in patients with metastatic colorectal cancer," *Journal of clinical oncology*, vol. 26, pp. 3213-3221, 2008.
- [35] J. S. de Bono, H. I. Scher, R. B. Montgomery, C. Parker, M. C. Miller, H. Tissing, *et al.*, "Circulating tumor cells predict survival benefit from treatment in metastatic castration-resistant prostate cancer," *Clinical Cancer Research*, vol. 14, pp. 6302-6309, 2008.
- [36] A. D. Rhim, E. T. Mirek, N. M. Aiello, A. Maitra, J. M. Bailey, F. McAllister, *et al.*, "EMT and dissemination precede pancreatic tumor formation," *Cell*, vol. 148, pp. 349-361, 2012.
- [37] K. Pantel, C. Alix-Panabières, and S. Riethdorf, "Cancer micrometastases," *Nature reviews Clinical oncology*, vol. 6, pp. 339-351, 2009.
- [38] B. Kubuschok, B. Passlick, J. Izbicki, O. Thetter, and K. Pantel, "Disseminated tumor cells in lymph nodes as a determinant for survival in surgically resected non-small-cell lung cancer," *Journal of Clinical Oncology*, vol. 17, pp. 19-19, 1999.
- [39] K. Pantel and R. H. Brakenhoff, "Dissecting the metastatic cascade," *Nature Reviews Cancer*, vol. 4, pp. 448-456, 2004.
- [40] J.-Y. Pierga, C. Bonneton, A. Vincent-Salomon, P. de Cremoux, C. Nos, N. Blin, *et al.*, "Clinical significance of immunocytochemical detection of tumor cells using digital microscopy in peripheral blood and bone marrow of breast cancer patients," *Clinical Cancer Research*, vol. 10, pp. 1392-1400, 2004.
- [41] S. Watmough and M. Flynn, "A review of pain management interventions in bone marrow biopsy," *Journal of clinical nursing*, vol. 20, pp. 615-623, 2011.
- [42] K. G. Trewhitt, "Bone marrow aspiration and biopsy: collection and interpretation," in *Oncology nursing forum*, 2001, pp. 1409-1424.
- [43] P. Vanhelleputte, K. Nijs, M. Delforge, G. Evers, and S. Vanderschueren, "Pain during bone marrow aspiration: prevalence and prevention," *Journal of pain and symptom management*, vol. 26, pp. 860-866, 2003.
- [44] H. Johnson, D. Burke, C. Plews, R. Newell, and L. Parapia, "Improving the patient's experience of a bone marrow biopsy—an RCT," *Journal of clinical nursing*, vol. 17, pp. 717-725, 2008.
- [45] B. Panchapakesan, R. Caprara, V. Velasco, J. Loomis, B. King, P. Xu, *et al.*, "Micro-and nanotechnology approaches for capturing circulating tumor cells," *Cancer nanotechnology*, vol. 1, pp. 3-11, 2010.
- [46] I. Surgeon, "Cancer's circulation problem," *Science*, vol. 327, pp. 1072-1074, 2010.
- [47] A. Gradilone, G. Naso, C. Raimondi, E. Cortesi, O. Gandini, B. Vincenzi, *et al.*, "Circulating tumor cells (CTCs) in metastatic breast cancer (MBC): prognosis,

- drug resistance and phenotypic characterization," *Annals of Oncology*, vol. 22, pp. 86-92, 2011.
- [48] K. Pantel, R. H. Brakenhoff, and B. Brandt, "Detection, clinical relevance and specific biological properties of disseminating tumour cells," *Nature Reviews Cancer*, vol. 8, pp. 329-340, 2008.
  - [49] T. L. Whiteside, "Immune suppression in cancer: effects on immune cells, mechanisms and future therapeutic intervention," in *Seminars in cancer biology*, 2006, pp. 3-15.
  - [50] P. T. Went, A. Lugli, S. Meier, M. Bundi, M. Mirlacher, G. Sauter, *et al.*, "Frequent EpCam protein expression in human carcinomas," *Human pathology*, vol. 35, pp. 122-128, 2004.
  - [51] J. S. Ross, J. A. Fletcher, G. P. Linette, J. Stec, E. Clark, M. Ayers, *et al.*, "The Her-2/neu gene and protein in breast cancer 2003: biomarker and target of therapy," *The oncologist*, vol. 8, pp. 307-325, 2003.
  - [52] S. M. Dhanasekaran, T. R. Barrette, D. Ghosh, R. Shah, S. Varambally, K. Kurachi, *et al.*, "Delineation of prognostic biomarkers in prostate cancer," *Nature*, vol. 412, pp. 822-826, 2001.
  - [53] D. Herlyn, M. Herlyn, Z. Stepkowski, and H. Koprowski, "Monoclonal antibodies in cell-mediated cytotoxicity against human melanoma and colorectal carcinoma," *European journal of immunology*, vol. 9, pp. 657-659, 1979.
  - [54] P. Baeuerle and O. Gires, "EpCAM (CD326) finding its role in cancer," *British journal of cancer*, vol. 96, pp. 417-423, 2007.
  - [55] K. Pachmann, O. Camara, A. Kavallaris, U. Schneider, S. Schunemann, and K. Hoffken, "Quantification of the response of circulating epithelial cells to neoadjuvant treatment for breast cancer: a new tool for therapy monitoring," *Breast Cancer Res*, vol. 7, pp. R975-979, 2005.
  - [56] W. J. Allard, J. Matera, M. C. Miller, M. Repollet, M. C. Connelly, C. Rao, *et al.*, "Tumor cells circulate in the peripheral blood of all major carcinomas but not in healthy subjects or patients with nonmalignant diseases," *Clinical Cancer Research*, vol. 10, pp. 6897-6904, 2004.
  - [57] M. C. Miller, G. V. Doyle, and L. W. Terstappen, "Significance of circulating tumor cells detected by the CellSearch system in patients with metastatic breast colorectal and prostate cancer," *Journal of oncology*, vol. 2010, 2009.
  - [58] V. Müller, N. Stahmann, S. Riethdorf, T. Rau, T. Zabel, A. Goetz, *et al.*, "Circulating tumor cells in breast cancer: correlation to bone marrow micrometastases, heterogeneous response to systemic therapy and low proliferative activity," *Clinical Cancer Research*, vol. 11, pp. 3678-3685, 2005.
  - [59] D. F. Hayes and J. Smerage, "Is there a role for circulating tumor cells in the management of breast cancer?," *Clinical Cancer Research*, vol. 14, pp. 3646-3650, 2008.
  - [60] Z. Panteleakou, P. Lembessis, A. Sourla, N. Pissimissis, A. Polyzos, C. Deliveliotis, *et al.*, "Detection of circulating tumor cells in prostate cancer patients: methodological pitfalls and clinical relevance," *Mol Med*, vol. 15, pp. 101-114, 2009.

- [61] S. Meng, D. Tripathy, S. Shete, R. Ashfaq, B. Haley, S. Perkins, *et al.*, "HER-2 gene amplification can be acquired as breast cancer progresses," *Proceedings of the National Academy of Sciences of the United States of America*, vol. 101, pp. 9393-9398, 2004.
- [62] R. Ghossein and S. Bhattacharya, "Molecular detection and characterisation of circulating tumour cells and micrometastases in solid tumours," *European Journal of Cancer*, vol. 36, pp. 1681-1694, 2000.
- [63] G. T. Budd, M. Cristofanilli, M. J. Ellis, A. Stopeck, E. Borden, M. C. Miller, *et al.*, "Circulating tumor cells versus imaging—predicting overall survival in metastatic breast cancer," *Clinical Cancer Research*, vol. 12, pp. 6403-6409, 2006.
- [64] S. Riethdorf, H. Fritsche, V. Müller, T. Rau, C. Schindlbeck, B. Rack, *et al.*, "Detection of circulating tumor cells in peripheral blood of patients with metastatic breast cancer: a validation study of the CellSearch system," *Clinical Cancer Research*, vol. 13, pp. 920-928, 2007.
- [65] C. Sun, R. Zhang, M. Gao, and X. Zhang, "A rapid and simple method for efficient capture and accurate discrimination of circulating tumor cells using aptamer conjugated magnetic beads and surface-enhanced Raman scattering imaging," *Analytical and Bioanalytical Chemistry*, vol. 407, pp. 8883-8892, Nov 2015.
- [66] A. H. Fischer, "Circulating tumor cells: seeing is believing," *Archives of pathology & laboratory medicine*, vol. 133, pp. 1367-1369, 2009.
- [67] R. Beveridge, "Circulating tumor cells in the management of metastatic breast cancer patients," *Community oncology*, vol. 4, pp. 79-82, 2007.
- [68] U. De Giorgi, V. Valero, E. Rohren, S. Dawood, N. T. Ueno, M. C. Miller, *et al.*, "Circulating tumor cells and [18F] fluorodeoxyglucose positron emission tomography/computed tomography for outcome prediction in metastatic breast cancer," *Journal of Clinical Oncology*, vol. 27, pp. 3303-3311, 2009.
- [69] R. L. Eifler, J. Lind, D. Falkenhagen, V. Weber, M. B. Fischer, and R. Zeillinger, "Enrichment of circulating tumor cells from a large blood volume using leukapheresis and elutriation: proof of concept," *Cytometry Part B: Clinical Cytometry*, vol. 80, pp. 100-111, 2011.
- [70] A. A. Powell, A. H. Talasaz, H. Zhang, M. A. Coram, A. Reddy, G. Deng, *et al.*, "Single cell profiling of circulating tumor cells: transcriptional heterogeneity and diversity from breast cancer cell lines," *PloS one*, vol. 7, p. e33788, 2012.
- [71] A. H. Talasaz, A. A. Powell, D. E. Huber, J. G. Berbee, K.-H. Roh, W. Yu, *et al.*, "Isolating highly enriched populations of circulating epithelial cells and other rare cells from blood using a magnetic sweeper device," *Proceedings of the National Academy of Sciences*, vol. 106, pp. 3970-3975, 2009.
- [72] C.-Y. Wen, L.-L. Wu, Z.-L. Zhang, Y.-L. Liu, S.-Z. Wei, J. Hu, *et al.*, "Quick-response magnetic nanospheres for rapid, efficient capture and sensitive detection of circulating tumor cells," *ACS nano*, vol. 8, pp. 941-949, 2013.

- [73] S. Nagrath, L. V. Sequist, S. Maheswaran, D. W. Bell, D. Irimia, L. Ulkus, *et al.*, "Isolation of rare circulating tumour cells in cancer patients by microchip technology," *Nature*, vol. 450, pp. 1235-1239, 2007.
- [74] A. A. Adams, P. I. Okagbare, J. Feng, M. L. Hupert, D. Patterson, J. Göttert, *et al.*, "Highly efficient circulating tumor cell isolation from whole blood and label-free enumeration using polymer-based microfluidics with an integrated conductivity sensor," *Journal of the American Chemical Society*, vol. 130, pp. 8633-8641, 2008.
- [75] K. T. Helzer, H. E. Barnes, L. Day, J. Harvey, P. R. Billings, and A. Forsyth, "Circulating tumor cells are transcriptionally similar to the primary tumor in a murine prostate model," *Cancer research*, vol. 69, pp. 7860-7866, 2009.
- [76] B. J. Kirby, M. Jodari, M. S. Loftus, G. Gakhar, E. D. Pratt, C. Chanel-Vos, *et al.*, "Functional characterization of circulating tumor cells with a prostate-cancer-specific microfluidic device," *PloS one*, vol. 7, p. e35976, 2012.
- [77] J. P. Gleghorn, E. D. Pratt, D. Denning, H. Liu, N. H. Bander, S. T. Tagawa, *et al.*, "Capture of circulating tumor cells from whole blood of prostate cancer patients using geometrically enhanced differential immunocapture (GEDI) and a prostate-specific antibody," *Lab on a chip*, vol. 10, pp. 27-29, 2010.
- [78] S. L. Stott, C.-H. Hsu, D. I. Tsukrov, M. Yu, D. T. Miyamoto, B. A. Waltman, *et al.*, "Isolation of circulating tumor cells using a microvortex-generating herringbone-chip," *Proceedings of the National Academy of Sciences*, vol. 107, pp. 18392-18397, 2010.
- [79] W. Sheng, O. O. Ogunwobi, T. Chen, J. Zhang, T. J. George, C. Liu, *et al.*, "Capture, release and culture of circulating tumor cells from pancreatic cancer patients using an enhanced mixing chip," *Lab on a Chip*, vol. 14, pp. 89-98, 2014.
- [80] J.-Y. Chen, W.-S. Tsai, H.-J. Shao, J.-C. Wu, J.-M. Lai, S.-H. Lu, *et al.*, "Sensitive and Specific Biomimetic Lipid Coated Microfluidics to Isolate Viable Circulating Tumor Cells and Microemboli for Cancer Detection," *PloS one*, vol. 11, p. e0149633, 2016.
- [81] A. F. Sarioglu, N. Aceto, N. Kojic, M. C. Donaldson, M. Zeinali, B. Hamza, *et al.*, "A microfluidic device for label-free, physical capture of circulating tumor cell clusters," *Nature methods*, vol. 12, pp. 685-691, 2015.
- [82] L. S. Lim, M. Hu, M. C. Huang, W. C. Cheong, A. T. L. Gan, X. L. Looi, *et al.*, "Microsieve lab-chip device for rapid enumeration and fluorescence in situ hybridization of circulating tumor cells," *Lab on a Chip*, vol. 12, pp. 4388-4396, 2012.
- [83] S. Zheng, H. Lin, J.-Q. Liu, M. Balic, R. Datar, R. J. Cote, *et al.*, "Membrane microfilter device for selective capture, electrolysis and genomic analysis of human circulating tumor cells," *Journal of Chromatography A*, vol. 1162, pp. 154-161, 2007.
- [84] S. Zheng, H. K. Lin, B. Lu, A. Williams, R. Datar, R. J. Cote, *et al.*, "3D microfilter device for viable circulating tumor cell (CTC) enrichment from blood," *Biomedical microdevices*, vol. 13, pp. 203-213, 2011.



- [85] H. K. Lin, S. Zheng, A. J. Williams, M. Balic, S. Groshen, H. I. Scher, *et al.*, "Portable filter-based microdevice for detection and characterization of circulating tumor cells," *Clinical Cancer Research*, vol. 16, pp. 5011-5018, 2010.
- [86] R. Riahi, P. Gogoi, S. Sepehri, Y. Zhou, K. Handique, J. Godsey, *et al.*, "A novel microchannel-based device to capture and analyze circulating tumor cells (CTCs) of breast cancer," *International journal of oncology*, vol. 44, pp. 1870-1878, 2014.
- [87] P. Gogoi, S. Sepehri, Y. Zhou, M. A. Gorin, C. Paolillo, E. Capoluongo, *et al.*, "Development of an Automated and Sensitive Microfluidic Device for Capturing and Characterizing Circulating Tumor Cells (CTCs) from Clinical Blood Samples," *PloS one*, vol. 11, p. e0147400, 2016.
- [88] S. J. Tan, R. L. Lakshmi, P. Chen, W.-T. Lim, L. Yobas, and C. T. Lim, "Versatile label free biochip for the detection of circulating tumor cells from peripheral blood in cancer patients," *Biosensors and Bioelectronics*, vol. 26, pp. 1701-1705, 2010.
- [89] S. J. Tan, L. Yobas, G. Y. H. Lee, C. N. Ong, and C. T. Lim, "Microdevice for the isolation and enumeration of cancer cells from blood," *Biomedical microdevices*, vol. 11, pp. 883-892, 2009.
- [90] K. Loutharback, J. D'Silva, L. Liu, A. Wu, R. H. Austin, and J. C. Sturm, "Deterministic separation of cancer cells from blood at 10 mL/min," *AIP advances*, vol. 2, p. 042107, 2012.
- [91] H. Mohamed, M. Murray, J. N. Turner, and M. Caggana, "Isolation of tumor cells using size and deformation," *Journal of Chromatography A*, vol. 1216, pp. 8289-8295, 2009.
- [92] A. A. S. Bhagat, H. W. Hou, L. D. Li, C. T. Lim, and J. Han, "Pinched flow coupled shear-modulated inertial microfluidics for high-throughput rare blood cell separation," *Lab on a Chip*, vol. 11, pp. 1870-1878, 2011.
- [93] J. Sun, M. Li, C. Liu, Y. Zhang, D. Liu, W. Liu, *et al.*, "Double spiral microchannel for label-free tumor cell separation and enrichment," *Lab on a chip*, vol. 12, pp. 3952-3960, 2012.
- [94] S. S. Kuntaegowdanahalli, A. A. S. Bhagat, G. Kumar, and I. Papautsky, "Inertial microfluidics for continuous particle separation in spiral microchannels," *Lab on a Chip*, vol. 9, pp. 2973-2980, 2009.
- [95] K.-A. Hyun, K. Kwon, H. Han, S.-I. Kim, and H.-I. Jung, "Microfluidic flow fractionation device for label-free isolation of circulating tumor cells (CTCs) from breast cancer patients," *Biosensors and Bioelectronics*, vol. 40, pp. 206-212, 2013.
- [96] E. Sollier, D. E. Go, J. Che, D. R. Gossett, S. O'Byrne, W. M. Weaver, *et al.*, "Size-selective collection of circulating tumor cells using Vortex technology," *Lab on a Chip*, vol. 14, pp. 63-77, 2014.
- [97] Y. Tang, J. Shi, S. Li, L. Wang, Y. E. Cayre, and Y. Chen, "Microfluidic device with integrated microfilter of conical-shaped holes for high efficiency and high purity capture of circulating tumor cells," *Scientific reports*, vol. 4, 2014.

- [98] J. Wang, W. Lu, C. Tang, Y. Liu, J. Sun, X. Mu, *et al.*, "Label-free Isolation and mRNA Detection of Circulating Tumor Cells from Patients with metastatic lung cancer for disease diagnosis and monitoring therapeutic efficacy," *Analytical chemistry*, vol. 87, pp. 11893-11900, 2015.
- [99] X. Fan, C. Jia, J. Yang, G. Li, H. Mao, Q. Jin, *et al.*, "A microfluidic chip integrated with a high-density PDMS-based microfiltration membrane for rapid isolation and detection of circulating tumor cells," *Biosensors and Bioelectronics*, vol. 71, pp. 380-386, 2015.
- [100] S. Yamamoto, J. Fei, M. Okochi, K. Shimizu, A. Yusa, N. Kondo, *et al.*, "Efficient capturing of circulating tumor cells using a magnetic capture column and a size-selective filter," *Bioprocess and biosystems engineering*, vol. 38, pp. 1693-1704, 2015.
- [101] S. Hou, L. Zhao, Q. Shen, J. Yu, C. Ng, X. Kong, *et al.*, "Polymer Nanofiber-Embedded Microchips for Detection, Isolation, and Molecular Analysis of Single Circulating Melanoma Cells," *Angewandte Chemie International Edition*, vol. 52, pp. 3379-3383, 2013.
- [102] Q. Shen, L. Xu, L. Zhao, D. Wu, Y. Fan, Y. Zhou, *et al.*, "Specific Capture and Release of Circulating Tumor Cells Using Aptamer-Modified Nanosubstrates," *Advanced Materials*, vol. 25, pp. 2368-2373, 2013.
- [103] S. Wang, K. Liu, J. Liu, Z. T. F. Yu, X. Xu, L. Zhao, *et al.*, "Highly efficient capture of circulating tumor cells by using nanostructured silicon substrates with integrated chaotic micromixers," *Angewandte Chemie International Edition*, vol. 50, pp. 3084-3088, 2011.
- [104] E. Reátegui, N. Aceto, E. J. Lim, J. P. Sullivan, A. E. Jensen, M. Zeinali, *et al.*, "Tunable nanostructured coating for the capture and selective release of viable circulating tumor cells," *Advanced Materials*, vol. 27, pp. 1593-1599, 2015.
- [105] W. Chen, S. Weng, F. Zhang, S. Allen, X. Li, L. Bao, *et al.*, "Nanoroughened surfaces for efficient capture of circulating tumor cells without using capture antibodies," *ACS nano*, vol. 7, pp. 566-575, 2012.
- [106] L. Chen, X. Liu, B. Su, J. Li, L. Jiang, D. Han, *et al.*, "Aptamer-Mediated Efficient Capture and Release of T Lymphocytes on Nanostructured Surfaces," *Advanced Materials*, vol. 23, pp. 4376-4380, 2011.
- [107] S.-K. Lee, G.-S. Kim, Y. Wu, D.-J. Kim, Y. Lu, M. Kwak, *et al.*, "Nanowire substrate-based laser scanning cytometry for quantitation of circulating tumor cells," *Nano letters*, vol. 12, pp. 2697-2704, 2012.
- [108] N. Zhang, Y. Deng, Q. Tai, B. Cheng, L. Zhao, Q. Shen, *et al.*, "Electrospun TiO<sub>2</sub> Nanofiber-Based Cell Capture Assay for Detecting Circulating Tumor Cells from Colorectal and Gastric Cancer Patients," *Advanced Materials*, vol. 24, pp. 2756-2760, 2012.
- [109] J. A. Phillips, Y. Xu, Z. Xia, Z. H. Fan, and W. Tan, "Enrichment of cancer cells using aptamers immobilized on a microfluidic channel," *Analytical chemistry*, vol. 81, pp. 1033-1039, 2008.
- [110] J. Sekine, S. C. Luo, S. Wang, B. Zhu, H. R. Tseng, and H. h. Yu, "Functionalized conducting polymer nanodots for enhanced cell capturing: the

- synergistic effect of capture agents and nanostructures," *Advanced Materials*, vol. 23, pp. 4788-4792, 2011.
- [111] J. Ouyang, M. Chen, W. J. Bao, Q. W. Zhang, K. Wang, and X. H. Xia, "Morphology Controlled Poly (aminophenylboronic acid) Nanostructures as Smart Substrates for Enhanced Capture and Release of Circulating Tumor Cells," *Advanced Functional Materials*, vol. 25, pp. 6122-6130, 2015.
  - [112] C. Wang, M. Ye, L. Cheng, R. Li, W. Zhu, Z. Shi, *et al.*, "Simultaneous isolation and detection of circulating tumor cells with a microfluidic silicon-nanowire-array integrated with magnetic upconversion nanoprobe," *Biomaterials*, vol. 54, pp. 55-62, 2015.
  - [113] W. Li, E. Reátegui, M.-H. Park, S. Castleberry, J. Z. Deng, B. Hsu, *et al.*, "Biodegradable nano-films for capture and non-invasive release of circulating tumor cells," *Biomaterials*, vol. 65, pp. 93-102, 2015.
  - [114] B. P. Viraka Nellore, R. Kanchanapally, A. Pramanik, S. S. Sinha, S. R. Chavva, A. Hamme, *et al.*, "Aptamer-conjugated graphene oxide membranes for highly efficient capture and accurate identification of multiple types of circulating tumor cells," *Bioconjugate chemistry*, vol. 26, pp. 235-242, 2015.
  - [115] H.-S. Moon, K. Kwon, S.-I. Kim, H. Han, J. Sohn, S. Lee, *et al.*, "Continuous separation of breast cancer cells from blood samples using multi-orifice flow fractionation (MOFF) and dielectrophoresis (DEP)," *Lab on a Chip*, vol. 11, pp. 1118-1125, 2011.
  - [116] P. R. Gascoyne, J. Noshari, T. J. Anderson, and F. F. Becker, "Isolation of rare cells from cell mixtures by dielectrophoresis," *Electrophoresis*, vol. 30, pp. 1388-1398, 2009.
  - [117] R. M. Mohamadi, I. Ivanov, J. Stojcic, R. K. Nam, E. H. Sargent, and S. O. Kelley, "Sample-to-Answer Isolation and mRNA Profiling of Circulating Tumor Cells," *Analytical chemistry*, vol. 87, pp. 6258-6264, 2015.
  - [118] D. Issadore, J. Chung, H. Shao, M. Liong, A. A. Ghazani, C. M. Castro, *et al.*, "Ultrasensitive clinical enumeration of rare cells ex vivo using a micro-hall detector," *Science translational medicine*, vol. 4, pp. 141ra92-141ra92, 2012.
  - [119] C. M. Castro, A. A. Ghazani, J. Chung, H. Shao, D. Issadore, T.-J. Yoon, *et al.*, "Miniaturized nuclear magnetic resonance platform for detection and profiling of circulating tumor cells," *Lab on a Chip*, vol. 14, pp. 14-23, 2014.
  - [120] R. M. Mohamadi, J. D. Besant, A. Mephram, B. Green, L. Mahmoudian, T. Gibbs, *et al.*, "Nanoparticle-Mediated Binning and Profiling of Heterogeneous Circulating Tumor Cell Subpopulations," *Angewandte Chemie International Edition*, vol. 54, pp. 139-143, 2015.
  - [121] E. Ozkumur, A. M. Shah, J. C. Ciciliano, B. L. Emmink, D. T. Miyamoto, E. Brachtel, *et al.*, "Inertial focusing for tumor antigen-dependent and-independent sorting of rare circulating tumor cells," *Science translational medicine*, vol. 5, pp. 179ra47-179ra47, 2013.
  - [122] N. M. Karabacak, P. S. Spuhler, F. Fachin, E. J. Lim, V. Pai, E. Ozkumur, *et al.*, "Microfluidic, marker-free isolation of circulating tumor cells from blood samples," *Nature protocols*, vol. 9, pp. 694-710, 2014.

- [123] K. Hoshino, Y.-Y. Huang, N. Lane, M. Huebschman, J. W. Uhr, E. P. Frenkel, *et al.*, "Microchip-based immunomagnetic detection of circulating tumor cells," *Lab on a Chip*, vol. 11, pp. 3449-3457, 2011.
- [124] A.-E. Saliba, L. Saias, E. Psychari, N. Minc, D. Simon, F.-C. Bidard, *et al.*, "Microfluidic sorting and multimodal typing of cancer cells in self-assembled magnetic arrays," *Proceedings of the National Academy of Sciences*, vol. 107, pp. 14524-14529, 2010.
- [125] X. Yu, R. He, S. Li, B. Cai, L. Zhao, L. Liao, *et al.*, "Magneto-Controllable Capture and Release of Cancer Cells by Using a Micropillar Device Decorated with Graphite Oxide-Coated Magnetic Nanoparticles," *Small*, vol. 9, pp. 3895-3901, 2013.
- [126] L. Yang, J. C. Lang, P. Balasubramanian, K. R. Jatana, D. Schuller, A. Agrawal, *et al.*, "Optimization of an enrichment process for circulating tumor cells from the blood of head and neck cancer patients through depletion of normal cells," *Biotechnology and bioengineering*, vol. 102, pp. 521-534, 2009.
- [127] S.-I. Han and K.-H. Han, "Electrical Detection Method for Circulating Tumor Cells Using Graphene Nanoplates," *Analytical Chemistry*, vol. 87, pp. 10585-10592, 2015.
- [128] G. Vona, A. Sabile, M. Louha, V. Sitruk, S. Romana, K. Schütze, *et al.*, "Isolation by size of epithelial tumor cells: a new method for the immunomorphological and molecular characterization of circulating tumor cells," *The American journal of pathology*, vol. 156, pp. 57-63, 2000.
- [129] W. Asghar, Y. Wan, A. Ilyas, R. Bachoo, Y.-t. Kim, and S. M. Iqbal, "Electrical fingerprinting, 3D profiling and detection of tumor cells with solid-state micropores," *Lab on a Chip*, vol. 12, pp. 2345-2352, 2012.
- [130] F. Zheng, Y. Cheng, J. Wang, J. Lu, B. Zhang, Y. Zhao, *et al.*, "Aptamer-Functionalized Barcode Particles for the Capture and Detection of Multiple Types of Circulating Tumor Cells," *Advanced Materials*, vol. 26, pp. 7333-7338, 2014.
- [131] Y. Gu, C. Ju, Y. Li, Z. Shang, Y. Wu, Y. Jia, *et al.*, "Detection of circulating tumor cells in prostate cancer based on carboxylated graphene oxide modified light addressable potentiometric sensor," *Biosensors and Bioelectronics*, vol. 66, pp. 24-31, 2015.
- [132] Y. S. Hsiao, S. C. Luo, S. Hou, B. Zhu, J. Sekine, C. W. Kuo, *et al.*, "3D Bioelectronic Interface: Capturing Circulating Tumor Cells onto Conducting Polymer-Based Micro/Nanorod Arrays with Chemical and Topographical Control," *Small*, vol. 10, pp. 3012-3017, 2014.
- [133] F. Khosravi, P. Trainor, S. N. Rai, G. Kloecker, E. Wickstrom, and B. Panchapakesan, "Label-free capture of breast cancer cells spiked in buffy coats using carbon nanotube antibody micro-arrays," *Nanotechnology*, vol. 27, p. 13LT02, 2016.
- [134] H. J. Yoon, T. H. Kim, Z. Zhang, E. Azizi, T. M. Pham, C. Paoletti, *et al.*, "Sensitive capture of circulating tumour cells by functionalized graphene oxide nanosheets," *Nature nanotechnology*, vol. 8, pp. 735-741, 2013.

- [135] N. Saucedo-Zeni, S. Mewes, R. Niestroj, L. Gasiorowski, D. Murawa, P. Nowaczyk, *et al.*, "A novel method for the in vivo isolation of circulating tumor cells from peripheral blood of cancer patients using a functionalized and structured medical wire," *International journal of oncology*, vol. 41, pp. 1241-1250, 2012.
- [136] H. Wang, G. Yue, C. Dong, F. Wu, J. Wei, Y. Yang, *et al.*, "Carboxybetaine methacrylate-modified nylon surface for circulating tumor cell capture," *ACS applied materials & interfaces*, vol. 6, pp. 4550-4559, 2014.
- [137] H. Zhang, Z. Jia, C. Wu, L. Zang, G. Yang, Z. Chen, *et al.*, "In Vivo Capture of Circulating Tumor Cells Based on Transfusion with a Vein Indwelling Needle," *ACS applied materials & interfaces*, vol. 7, pp. 20477-20484, 2015.
- [138] T. L. Halo, K. M. McMahon, N. L. Angeloni, Y. Xu, W. Wang, A. B. Chinen, *et al.*, "NanoFlares for the detection, isolation, and culture of live tumor cells from human blood," *Proceedings of the National Academy of Sciences*, vol. 111, pp. 17104-17109, 2014.
- [139] P. G. Schiro, M. Zhao, J. S. Kuo, K. M. Koehler, D. E. Sabath, and D. T. Chiu, "Sensitive and High-Throughput Isolation of Rare Cells from Peripheral Blood with Ensemble-Decision Aliquot Ranking," *Angewandte Chemie International Edition*, vol. 51, pp. 4618-4622, 2012.
- [140] H. Etayash, K. Jiang, S. Azmi, T. Thundat, and K. Kaur, "Real-time Detection of Breast Cancer Cells Using Peptide-functionalized Microcantilever Arrays," *Scientific reports*, vol. 5, 2015.
- [141] H. J. Lee, J. H. Oh, J. M. Oh, J. M. Park, J. G. Lee, M. S. Kim, *et al.*, "Efficient Isolation and Accurate In Situ Analysis of Circulating Tumor Cells Using Detachable Beads and a High-Pore-Density Filter," *Angewandte Chemie International Edition*, vol. 52, pp. 8337-8340, 2013.
- [142] B. J. Green, T. Saberi Safaei, A. Mephram, M. Labib, R. M. Mohamadi, and S. O. Kelley, "Beyond the Capture of Circulating Tumor Cells: Next-Generation Devices and Materials," *Angewandte Chemie International Edition*, 2015.
- [143] S. Seal, "A sieve for the isolation of cancer cells and other large cells from the blood," *Cancer*, vol. 17, pp. 637-642, 1964.
- [144] P. D. Rye, H. Høifødt, G. Overli, and O. Fodstad, "Immunobead filtration: a novel approach for the isolation and propagation of tumor cells," *The American journal of pathology*, vol. 150, p. 99, 1997.
- [145] P. Rostagno, J. Moll, J. Bisconte, and C. Caldani, "Detection of rare circulating breast cancer cells by filtration cytometry and identification by DNA content: sensitivity in an experimental model," *Anticancer research*, vol. 17, pp. 2481-2485, 1996.
- [146] S. C. Hur, N. K. Henderson-MacLennan, E. R. McCabe, and D. Di Carlo, "Deformability-based cell classification and enrichment using inertial microfluidics," *Lab on a Chip*, vol. 11, pp. 912-920, 2011.
- [147] M. Herlyn, Z. Steplewski, D. Herlyn, and H. Koprowski, "Colorectal carcinoma-specific antigen: detection by means of monoclonal antibodies,"

- Proceedings of the National Academy of Sciences*, vol. 76, pp. 1438-1442, 1979.
- [148] D. P. Edwards, K. T. Grzyb, L. G. Dressler, R. E. Mansel, D. T. Zava, G. W. Sledge, *et al.*, "Monoclonal antibody identification and characterization of a Mr 43,000 membrane glycoprotein associated with human breast cancer," *Cancer research*, vol. 46, pp. 1306-1317, 1986.
  - [149] S. Szala, M. Froehlich, M. Scollon, Y. Kasai, Z. Steplewski, H. Koprowski, *et al.*, "Molecular cloning of cDNA for the carcinoma-associated antigen GA733-2," *Proceedings of the National Academy of Sciences*, vol. 87, pp. 3542-3546, 1990.
  - [150] D. Sansonno and F. Dammacco, "Expression and distribution of a human colon-carcinoma-associated antigen in normal and diseased liver tissue," *Pathobiology*, vol. 61, pp. 193-196, 1993.
  - [151] R. P. Takes, R. J. B. de Jong, E. Schuurin, J. Hermans, A. A. Vis, S. V. Litvinov, *et al.*, "Markers for assessment of nodal metastasis in laryngeal carcinoma," *Archives of Otolaryngology-Head & Neck Surgery*, vol. 123, pp. 412-419, 1997.
  - [152] S. Zhang, H. S. Zhang, V. E. Reuter, S. F. Slovin, H. I. Scher, and P. O. Livingston, "Expression of potential target antigens for immunotherapy on primary and metastatic prostate cancers," *Clinical Cancer Research*, vol. 4, pp. 295-302, 1998.
  - [153] C. J. de Boer, J. H. van Krieken, C. M. Janssen-van Rhijn, and S. V. Litvinov, "Expression of Ep-CAM in normal, regenerating, metaplastic, and neoplastic liver," *The Journal of pathology*, vol. 188, pp. 201-206, 1999.
  - [154] I. G. Martin, S. G. Cutts, K. Birbeck, S. Gray, and P. Quirke, "Expression of the 17-1A antigen in gastric and gastro-oesophageal junction adenocarcinomas: a potential immunotherapeutic target?," *Journal of clinical pathology*, vol. 52, pp. 701-704, 1999.
  - [155] R. B. Poczatek, R. B. MYERS, U. MANNE, D. K. OELSCHLAGER, H. L. WEISS, D. G. BOSTWICK, *et al.*, "Ep-Cam levels in prostatic adenocarcinoma and prostatic intraepithelial neoplasia," *The Journal of urology*, vol. 162, pp. 1462-1466, 1999.
  - [156] P. Ruck, G. Wichert, R. Handgretinger, and E. Kaiserling, "Ep-CAM in malignant liver tumours," *The Journal of pathology*, vol. 191, pp. 102-103, 2000.
  - [157] K. Chang, Y.-Y. Kong, B. Dai, D.-W. Ye, Y.-Y. Qu, Y. Wang, *et al.*, "Combination of circulating tumor cell enumeration and tumor marker detection in predicting prognosis and treatment effect in metastatic castration-resistant prostate cancer," *Oncotarget*, vol. 6, pp. 41825-41836, 2015.
  - [158] S. M. Santana, H. Liu, N. H. Bander, J. P. Gleghorn, and B. J. Kirby, "Immunocapture of prostate cancer cells by use of anti-PSMA antibodies in microdevices," *Biomedical microdevices*, vol. 14, pp. 401-407, 2012.
  - [159] D. Harari and Y. Yarden, "Molecular mechanisms underlying ErbB2/HER2 action in breast cancer," *Oncogene*, vol. 19, 2000.

- [160] C. V. Pecot, F. Z. Bischoff, J. A. Mayer, K. L. Wong, T. Pham, J. Bottsford-Miller, *et al.*, "A novel platform for detection of CK+ and CK- CTCs," *Cancer discovery*, vol. 1, pp. 580-586, 2011.
- [161] O. C. Farokhzad, S. Jon, A. Khademhosseini, T.-N. T. Tran, D. A. LaVan, and R. Langer, "Nanoparticle-aptamer bioconjugates a new approach for targeting prostate cancer cells," *Cancer research*, vol. 64, pp. 7668-7672, 2004.
- [162] K.-M. Song, S. Lee, and C. Ban, "Aptamers and their biological applications," *Sensors*, vol. 12, pp. 612-631, 2012.
- [163] A. D. Ellington and J. W. Szostak, "In vitro selection of RNA molecules that bind specific ligands," *nature*, vol. 346, pp. 818-822, 1990.
- [164] C. Tuerk and L. Gold, "Systematic evolution of ligands by exponential enrichment: RNA ligands to bacteriophage T4 DNA polymerase," *Science*, vol. 249, pp. 505-510, 1990.
- [165] U. Dharmasiri, S. Balamurugan, A. A. Adams, P. I. Okagbare, A. Obubuafo, and S. A. Soper, "Highly efficient capture and enumeration of low abundance prostate cancer cells using prostate-specific membrane antigen aptamers immobilized to a polymeric microfluidic device," *Electrophoresis*, vol. 30, pp. 3289-3300, 2009.
- [166] Y. Wan, Y.-t. Kim, N. Li, S. K. Cho, R. Bachoo, A. D. Ellington, *et al.*, "Surface-immobilized aptamers for cancer cell isolation and microscopic cytology," *Cancer research*, vol. 70, pp. 9371-9380, 2010.
- [167] Y. Wan, M. Mahmood, N. Li, P. B. Allen, Y. t. Kim, R. Bachoo, *et al.*, "Nanotextured substrates with immobilized aptamers for cancer cell isolation and cytology," *Cancer*, vol. 118, pp. 1145-1154, 2012.
- [168] Y. Song, Z. Zhu, Y. An, W. Zhang, H. Zhang, D. Liu, *et al.*, "Selection of DNA aptamers against epithelial cell adhesion molecule for cancer cell imaging and circulating tumor cell capture," *Analytical chemistry*, vol. 85, pp. 4141-4149, 2013.
- [169] P. Wülfing, J. Borchard, H. Buerger, S. Heidl, K. S. Zänker, L. Kiesel, *et al.*, "HER2-positive circulating tumor cells indicate poor clinical outcome in stage I to III breast cancer patients," *Clinical Cancer Research*, vol. 12, pp. 1715-1720, 2006.
- [170] S. Miltenyi, W. Müller, W. Weichel, and A. Radbruch, "High gradient magnetic cell separation with MACS," *Cytometry*, vol. 11, pp. 231-238, 1990.
- [171] C. Griwatz, B. Brandt, G. Assmann, and K. Zänker, "An immunological enrichment method for epithelial cells from peripheral blood," *Journal of immunological methods*, vol. 183, pp. 251-265, 1995.
- [172] B. Brandt, R. Junker, C. Griwatz, S. Heidl, O. Brinkmann, A. Semjonow, *et al.*, "Isolation of prostate-derived single cells and cell clusters from human peripheral blood," *Cancer research*, vol. 56, pp. 4556-4561, 1996.
- [173] E. Racila, D. Euhus, A. J. Weiss, C. Rao, J. McConnell, L. W. Terstappen, *et al.*, "Detection and characterization of carcinoma cells in the blood," *Proceedings of the National Academy of Sciences*, vol. 95, pp. 4589-4594, 1998.

- [174] T. M. Morgan, P. H. Lange, and R. L. Vessella, "Detection and characterization of circulating and disseminated prostate cancer cells," *Front Biosci*, vol. 12, pp. 3000-3009, 2007.
- [175] G. Deng, M. Herrler, D. Burgess, E. Manna, D. Krag, and J. F. Burke, "Enrichment with anti-cytokeratin alone or combined with anti-EpCAM antibodies significantly increases the sensitivity for circulating tumor cell detection in metastatic breast cancer patients," *Breast Cancer Research*, vol. 10, pp. 1-11, 2008.
- [176] S. Kim, S.-I. Han, M.-J. Park, C.-W. Jeon, Y.-D. Joo, I.-H. Choi, *et al.*, "Circulating tumor cell microseparator based on lateral magnetophoresis and immunomagnetic nanobeads," *Analytical chemistry*, vol. 85, pp. 2779-2786, 2013.
- [177] U. A. Gurkan, T. Anand, H. Tas, D. Elkan, A. Akay, H. O. Keles, *et al.*, "Controlled viable release of selectively captured label-free cells in microchannels," *Lab on a chip*, vol. 11, pp. 3979-3989, 2011.
- [178] K. T. Kotz, W. Xiao, C. Miller-Graziano, W.-J. Qian, A. Russom, E. A. Warner, *et al.*, "Clinical microfluidics for neutrophil genomics and proteomics," *Nature medicine*, vol. 16, pp. 1042-1047, 2010.
- [179] D. A. Vickers, E. J. Chory, and S. K. Murthy, "Separation of two phenotypically similar cell types via a single common marker in microfluidic channels," *Lab on a chip*, vol. 12, pp. 3399-3407, 2012.
- [180] U. Hassan and R. Bashir, "Electrical cell counting process characterization in a microfluidic impedance cytometer," *Biomedical microdevices*, vol. 16, pp. 697-704, 2014.
- [181] N. N. Watkins, U. Hassan, G. Damhorst, H. Ni, A. Vaid, W. Rodriguez, *et al.*, "Microfluidic CD4+ and CD8+ T lymphocyte counters for point-of-care HIV diagnostics using whole blood," *Science translational medicine*, vol. 5, pp. 214ra170-214ra170, 2013.
- [182] S. K. Murthy, A. Sin, R. G. Tompkins, and M. Toner, "Effect of flow and surface conditions on human lymphocyte isolation using microfluidic chambers," *Langmuir*, vol. 20, pp. 11649-11655, 2004.
- [183] R. Kalluri and R. A. Weinberg, "The basics of epithelial-mesenchymal transition," *The Journal of clinical investigation*, vol. 119, pp. 1420-1428, 2009.
- [184] M. Yu, S. Stott, M. Toner, S. Maheswaran, and D. A. Haber, "Circulating tumor cells: approaches to isolation and characterization," *The Journal of cell biology*, vol. 192, pp. 373-382, 2011.
- [185] F. A. Coumans, G. van Dalum, M. Beck, and L. W. Terstappen, "Filter characteristics influencing circulating tumor cell enrichment from whole blood," *PloS one*, vol. 8, p. e61770, 2013.
- [186] M. Hosokawa, H. Kenmotsu, Y. Koh, T. Yoshino, T. Yoshikawa, T. Naito, *et al.*, "Size-based isolation of circulating tumor cells in lung cancer patients using a microcavity array system," *PloS one*, vol. 8, p. e67466, 2013.



- [187] S. D. Puckett, P. P. Lee, D. M. Ciombor, R. K. Aaron, and T. J. Webster, "Nanotextured titanium surfaces for enhancing skin growth on transcutaneous osseointegrated devices," *Acta Biomaterialia*, vol. 6, pp. 2352-2362, 2010.
- [188] J. H. Park, B. G. Chung, W. G. Lee, J. Kim, M. D. Brigham, J. Shim, *et al.*, "Microporous cell-laden hydrogels for engineered tissue constructs," *Biotechnology and bioengineering*, vol. 106, pp. 138-148, 2010.
- [189] W. G. Lee, U. Demirci, and A. Khademhosseini, "Microscale electroporation: challenges and perspectives for clinical applications," *Integrative Biology*, vol. 1, pp. 242-251, 2009.
- [190] Y. S. Song, R. L. Lin, G. Montesano, N. G. Durmus, G. Lee, S.-S. Yoo, *et al.*, "Engineered 3D tissue models for cell-laden microfluidic channels," *Analytical and bioanalytical chemistry*, vol. 395, pp. 185-193, 2009.
- [191] J. Lu, M. P. Rao, N. C. MacDonald, D. Khang, and T. J. Webster, "Improved endothelial cell adhesion and proliferation on patterned titanium surfaces with rationally designed, micrometer to nanometer features," *Acta biomaterialia*, vol. 4, pp. 192-201, 2008.
- [192] D. Khang, S. Y. Kim, P. Liu-Snyder, G. T. R. Palmore, S. M. Durbin, and T. J. Webster, "Enhanced fibronectin adsorption on carbon nanotube/poly (carbonate) urethane: independent role of surface nano-roughness and associated surface energy," *Biomaterials*, vol. 28, pp. 4756-4768, 2007.
- [193] M. J. Biggs, R. G. Richards, N. Gadegaard, C. D. Wilkinson, R. O. Oreffo, and M. J. Dalby, "The use of nanoscale topography to modulate the dynamics of adhesion formation in primary osteoblasts and ERK/MAPK signalling in STRO-1+ enriched skeletal stem cells," *Biomaterials*, vol. 30, pp. 5094-5103, 2009.
- [194] K. Anselme, P. Davidson, A. Popa, M. Giazzone, M. Liley, and L. Ploux, "The interaction of cells and bacteria with surfaces structured at the nanometre scale," *Acta biomaterialia*, vol. 6, pp. 3824-3846, 2010.
- [195] R. Flemming, C. Murphy, G. Abrams, S. Goodman, and P. Nealey, "Effects of synthetic micro-and nano-structured surfaces on cell behavior," *Biomaterials*, vol. 20, pp. 573-588, 1999.
- [196] E. Lamers, R. v. Horssen, J. t. Riet, F. v. Delft, R. Luttge, X. Walboomers, *et al.*, "The influence of nanoscale topographical cues on initial osteoblast morphology and migration," 2010.
- [197] P. Zorlutuna, Z. Rong, P. Vadgama, and V. Hasirci, "Influence of nanopatterns on endothelial cell adhesion: Enhanced cell retention under shear stress," *Acta biomaterialia*, vol. 5, pp. 2451-2459, 2009.
- [198] M. A. Wozniak, K. Modzelewska, L. Kwong, and P. J. Keely, "Focal adhesion regulation of cell behavior," *Biochimica et Biophysica Acta (BBA)-Molecular Cell Research*, vol. 1692, pp. 103-119, 2004.
- [199] L. Wang, W. Asghar, U. Demirci, and Y. Wan, "Nanostructured substrates for isolation of circulating tumor cells," *Nano Today*, vol. 8, pp. 374-387, 2013.

- [200] S. Wang, H. Wang, J. Jiao, K. J. Chen, G. E. Owens, K. i. Kamei, *et al.*, "Three-Dimensional Nanostructured Substrates toward Efficient Capture of Circulating Tumor Cells," *Angewandte Chemie*, vol. 121, pp. 9132-9135, 2009.
- [201] M. Lin, J.-F. Chen, Y.-T. Lu, Y. Zhang, J. Song, S. Hou, *et al.*, "Nanostructure embedded microchips for detection, isolation, and characterization of circulating tumor cells," *Accounts of chemical research*, vol. 47, pp. 2941-2950, 2014.
- [202] W. He, H. Wang, L. C. Hartmann, J.-X. Cheng, and P. S. Low, "In vivo quantitation of rare circulating tumor cells by multiphoton intravital flow cytometry," *Proceedings of the National Academy of Sciences*, vol. 104, pp. 11760-11765, 2007.
- [203] J. Fritz, M. Baller, H. Lang, H. Rothuizen, P. Vettiger, E. Meyer, *et al.*, "Translating biomolecular recognition into nanomechanics," *Science*, vol. 288, pp. 316-318, 2000.
- [204] A. Gupta, D. Akin, and R. Bashir, "Detection of bacterial cells and antibodies using surface micromachined thin silicon cantilever resonators," *Journal of Vacuum Science & Technology B*, vol. 22, pp. 2785-2791, 2004.
- [205] B. Ilic, D. Czaplewski, H. G. Craighead, P. Neuzil, C. Campagnolo, and C. Batt, "Mechanical resonant immunospecific biological detector," *Applied Physics Letters*, vol. 77, pp. 450-452, 2000.
- [206] L. Johnson, A. K. Gupta, A. Ghafoor, D. Akin, and R. Bashir, "Characterization of vaccinia virus particles using microscale silicon cantilever resonators and atomic force microscopy," *Sensors and Actuators B: Chemical*, vol. 115, pp. 189-197, 2006.
- [207] H. Sone, A. Ikeuchi, T. Izumi, H. Okano, and S. Hosaka, "Femtogram mass biosensor using self-sensing cantilever for allergy check," *Japanese journal of applied physics*, vol. 45, p. 2301, 2006.
- [208] G. Wu, R. H. Datar, K. M. Hansen, T. Thundat, R. J. Cote, and A. Majumdar, "Bioassay of prostate-specific antigen (PSA) using microcantilevers," *Nature biotechnology*, vol. 19, pp. 856-860, 2001.
- [209] S. Li, L. Orona, Z. Li, and Z.-Y. Cheng, "Biosensor based on magnetostrictive microcantilever," *Applied Physics Letters*, vol. 88, p. 3507, 2006.
- [210] Y. Alapan, K. Icoz, and U. A. Gurkan, "Micro-and nanodevices integrated with biomolecular probes," *Biotechnology advances*, vol. 33, pp. 1727-1743, 2015.
- [211] Y. Arntz, J. D. Seelig, H. Lang, J. Zhang, P. Hunziker, J. Ramseyer, *et al.*, "Label-free protein assay based on a nanomechanical cantilever array," *Nanotechnology*, vol. 14, p. 86, 2002.
- [212] J. Pei, F. Tian, and T. Thundat, "Glucose biosensor based on the microcantilever," *Analytical Chemistry*, vol. 76, pp. 292-297, 2004.
- [213] B. Dhayal, W. A. Henne, D. D. Doorneweerd, R. G. Reifengerger, and P. S. Low, "Detection of bacillus subtilis spores using peptide-functionalized cantilever arrays," *Journal of the American Chemical Society*, vol. 128, pp. 3716-3721, 2006.

- [214] Y. Zhang and Y.-p. Zhao, "An effective method of determining the residual stress gradients in a micro-cantilever," *Microsystem technologies*, vol. 12, pp. 357-364, 2006.
- [215] D. L. Haus, H. X. Nguyen, E. M. Gold, N. Kamei, H. Perez, H. D. Moore, *et al.*, "CD133-enriched Xeno-free human embryonic-derived neural stem cells expand rapidly in culture and do not form teratomas in immunodeficient mice," *Stem cell research*, vol. 13, pp. 214-226, 2014.
- [216] W. Harb, A. Fan, T. Tran, D. C. Danila, D. Keys, M. Schwartz, *et al.*, "Mutational analysis of circulating tumor cells using a novel microfluidic collection device and qPCR assay," *Translational oncology*, vol. 6, pp. 528-IN1, 2013.
- [217] E. Pailler, N. Auger, C. Lindsay, P. Vielh, A. Islas-Morris-Hernandez, I. Borget, *et al.*, "High level of chromosomal instability in circulating tumor cells of ROS1-rearranged non-small-cell lung cancer," *Annals of Oncology*, p. mdv165, 2015.
- [218] K.-A. Hyun, J. Kim, H. Gwak, and H.-i. Jung, "Isolation and enrichment of circulating biomarkers for cancer screening, detection, and diagnostics," *Analyst*, vol. 141, pp. 382-392, 2016.
- [219] R. Payne, F. Wang, N. Su, J. Krell, A. Zebrowski, E. Yagüe, *et al.*, "Viable circulating tumour cell detection using multiplex RNA in situ hybridisation predicts progression-free survival in metastatic breast cancer patients," *British journal of cancer*, vol. 106, pp. 1790-1797, 2012.
- [220] T. Hillig, A. B. Nygaard, L. Nekiunaite, J. Klingelhöfer, and G. Sölétormos, "In vitro validation of an ultra-sensitive scanning fluorescence microscope for analysis of Circulating Tumor Cells," *Apmis*, vol. 122, pp. 545-551, 2014.
- [221] D. S. Hong, I. Garrido-Laguna, S. Ekmekcioglu, G. S. Falchook, A. Naing, J. J. Wheler, *et al.*, "Dual inhibition of the vascular endothelial growth factor pathway: a phase 1 trial evaluating bevacizumab and AZD2171 (cediranib) in patients with advanced solid tumors," *Cancer*, vol. 120, pp. 2164-2173, 2014.
- [222] Q. Lv, L. Gong, T. Zhang, J. Ye, L. Chai, C. Ni, *et al.*, "Prognostic value of circulating tumor cells in metastatic breast cancer: a systemic review and meta-analysis," *Clinical and Translational Oncology*, pp. 1-9, 2015.
- [223] G. Corkill and R. Rapley, "The Manipulation of Nucleic Acids: Basic Tools and Techniques," *Molecular Biomethods Handbook Second Edition*. Ed: Walker, JM, Rapley, R. Humana Press, NJ, USA, 2008.
- [224] H. J. Yoon, M. Kozminsky, and S. Negrath, "Emerging role of nanomaterials in circulating tumor cell isolation and analysis," *ACS nano*, vol. 8, pp. 1995-2017, 2014.
- [225] S. Iijima, "Helical microtubules of graphitic carbon," *nature*, vol. 354, pp. 56-58, 1991.
- [226] S. Iijima and T. Ichihashi, "Single-Shell Carbon Nanotubes of 1-Nm Diameter," *Nature*, vol. 363, pp. 603-605, Jun 17 1993.

- [227] H. Zhu, C. Xu, D. Wu, B. Wei, R. Vajtai, and P. Ajayan, "Direct synthesis of long single-walled carbon nanotube strands," *Science*, vol. 296, pp. 884-886, 2002.
- [228] A. Kis and A. Zettl, "Nanomechanics of carbon nanotubes," *Philosophical Transactions of the Royal Society of London A: Mathematical, Physical and Engineering Sciences*, vol. 366, pp. 1591-1611, 2008.
- [229] H. Dai, "Carbon nanotubes: opportunities and challenges," *Surface Science*, vol. 500, pp. 218-241, 2002.
- [230] W. A. De Heer, A. Chatelain, and D. Ugarte, "A carbon nanotube field-emission electron source," *Science*, vol. 270, pp. 1179-1180, 1995.
- [231] E. T. Thostenson, Z. Ren, and T.-W. Chou, "Advances in the science and technology of carbon nanotubes and their composites: a review," *Composites science and technology*, vol. 61, pp. 1899-1912, 2001.
- [232] H. Dai, J. H. Hafner, A. G. Rinzler, D. T. Colbert, and R. E. Smalley, "Nanotubes as nanoprobe in scanning probe microscopy," *Nature*, vol. 384, pp. 147-150, 1996.
- [233] P. Avouris, "Molecular electronics with carbon nanotubes," *Accounts of Chemical Research*, vol. 35, pp. 1026-1034, 2002.
- [234] P. G. Collins, K. Bradley, M. Ishigami, and A. Zettl, "Extreme oxygen sensitivity of electronic properties of carbon nanotubes," *science*, vol. 287, pp. 1801-1804, 2000.
- [235] J. Wang, "Carbon-nanotube based electrochemical biosensors: A review," *Electroanalysis*, vol. 17, pp. 7-14, 2005.
- [236] A. Thess, R. Lee, P. Nikolaev, and H. Dai, "Crystalline ropes of metallic carbon nanotubes," *Science*, vol. 273, p. 483, 1996.
- [237] J. G. Kiang and G. C. Tsokos, "Heat shock protein 70 kDa: molecular biology, biochemistry, and physiology," *Pharmacology & therapeutics*, vol. 80, pp. 183-201, 1998.
- [238] T. L. Brown, H. E. LeMay, and R. Wilson, *Chemistry: The central science*: Prentice Hall Englewood Cliffs, NJ, 1988.
- [239] R. S. Ruoff, D. Qian, and W. K. Liu, "Mechanical properties of carbon nanotubes: theoretical predictions and experimental measurements," *Comptes Rendus Physique*, vol. 4, pp. 993-1008, 2003.
- [240] P. L. McEuen, M. S. Fuhrer, and H. K. Park, "Single-walled carbon nanotube electronics," *Ieee Transactions on Nanotechnology*, vol. 1, pp. 78-85, Mar 2002.
- [241] W. Li, S. Xie, L. Qian, and B. Chang, "Large-scale synthesis of aligned carbon nanotubes," *Science*, vol. 274, p. 1701, 1996.
- [242] J. Kong, H. T. Soh, A. M. Cassell, C. F. Quate, and H. Dai, "Synthesis of individual single-walled carbon nanotubes on patterned silicon wafers," *Nature*, vol. 395, pp. 878-881, 1998.
- [243] J.-F. Colomer, C. Stephan, S. Lefrant, G. Van Tendeloo, I. Willems, Z. Konya, *et al.*, "Large-scale synthesis of single-wall carbon nanotubes by catalytic chemical vapor deposition (CCVD) method," *Chemical Physics Letters*, vol. 317, pp. 83-89, 2000.

- [244] J.-P. Salvetat, A. J. Kulik, J.-M. Bonard, G. A. D. Briggs, T. Stöckli, K. Méténier, *et al.*, "Elastic modulus of ordered and disordered multiwalled carbon nanotubes," *Advanced Materials*, vol. 11, pp. 161-165, 1999.
- [245] A. H. Barber, R. Andrews, L. S. Schadler, and H. D. Wagner, "On the tensile strength distribution of multiwalled carbon nanotubes," *Applied Physics Letters*, vol. 87, p. 203106, 2005.
- [246] I. Kaplan-Ashiri, S. R. Cohen, K. Gartsman, V. Ivanovskaya, T. Heine, G. Seifert, *et al.*, "On the mechanical behavior of WS<sub>2</sub> nanotubes under axial tension and compression," *Proceedings of the National Academy of Sciences of the United States of America*, vol. 103, pp. 523-528, 2006.
- [247] R. Saito, G. Dresselhaus, and M. S. Dresselhaus, *Physical properties of carbon nanotubes* vol. 35: World Scientific, 1998.
- [248] A. K. Geim and K. S. Novoselov, "The rise of graphene," *Nature materials*, vol. 6, pp. 183-191, 2007.
- [249] M. S. Dresselhaus, G. Dresselhaus, and P. C. Eklund, *Science of fullerenes and carbon nanotubes: their properties and applications*: Academic press, 1996.
- [250] P. L. McEuen and J.-Y. Park, "Electron transport in single-walled carbon nanotubes," *Mrs Bulletin*, vol. 29, pp. 272-275, 2004.
- [251] M. Dragoman, "Electronic devices based on carbon nanotubes and graphene," *Proceedings of the Romanian Academy Series A-Mathematics Physics Technical Sciences Information Science*, vol. 10, pp. 91-98, 2009.
- [252] S. Rosenblatt, H. Lin, V. Sazonova, S. Tiwari, and P. L. McEuen, "Mixing at 50GHz using a single-walled carbon nanotube transistor," *Applied Physics Letters*, vol. 87, p. 153111, 2005.
- [253] D. Stewart and F. Léonard, "Photocurrents in nanotube junctions," *Physical review letters*, vol. 93, p. 107401, 2004.
- [254] J. U. Lee, "Band-gap renormalization in carbon nanotubes: Origin of the ideal diode behavior in carbon nanotube p-n structures," *Physical Review B*, vol. 75, p. 075409, 2007.
- [255] J. Misewich, R. Martel, P. Avouris, J. Tsang, S. Heinze, and J. Tersoff, "Electrically induced optical emission from a carbon nanotube FET," *Science*, vol. 300, pp. 783-786, 2003.
- [256] P. R. Wallace, "The band theory of graphite," *Physical Review*, vol. 71, p. 622, 1947.
- [257] N. Hamada, S.-i. Sawada, and A. Oshiyama, "New one-dimensional conductors: graphitic microtubules," *Physical Review Letters*, vol. 68, p. 1579, 1992.
- [258] S. Reich, J. Maultzsch, C. Thomsen, and P. Ordejon, "Tight-binding description of graphene," *Physical Review B*, vol. 66, p. 035412, 2002.
- [259] J. W. Wilder, L. C. Venema, A. G. Rinzler, R. E. Smalley, and C. Dekker, "Electronic structure of atomically resolved carbon nanotubes," *Nature*, vol. 391, pp. 59-62, 1998.
- [260] T. W. Odom, J.-L. Huang, P. Kim, and C. M. Lieber, "Atomic structure and electronic properties of single-walled carbon nanotubes," *Nature*, vol. 391, pp. 62-64, 1998.

- [261] L. Yang and J. Han, "Electronic structure of deformed carbon nanotubes," *Physical Review Letters*, vol. 85, p. 154, 2000.
- [262] E. Minot, Y. Yaish, V. Sazonova, J.-Y. Park, M. Brink, and P. L. McEuen, "Tuning carbon nanotube band gaps with strain," *Physical review letters*, vol. 90, p. 156401, 2003.
- [263] M. J. Treacy, T. Ebbesen, and J. Gibson, "Exceptionally high Young's modulus observed for individual carbon nanotubes," 1996.
- [264] B. Yakobson, "Mechanical relaxation and "intramolecular plasticity" in carbon nanotubes," *Applied Physics Letters*, vol. 72, pp. 918-920, 1998.
- [265] M.-F. Yu, O. Lourie, M. J. Dyer, K. Moloni, T. F. Kelly, and R. S. Ruoff, "Strength and breaking mechanism of multiwalled carbon nanotubes under tensile load," *Science*, vol. 287, pp. 637-640, 2000.
- [266] B. C. Edwards, "Design and deployment of a space elevator," *Acta Astronautica*, vol. 47, pp. 735-744, 2000.
- [267] V. Sazonova, Y. Yaish, H. Üstünel, D. Roundy, T. A. Arias, and P. L. McEuen, "A tunable carbon nanotube electromechanical oscillator," *Nature*, vol. 431, pp. 284-287, 2004.
- [268] M. Krüger, M. Buitelaar, T. Nussbaumer, C. Schönenberger, and L. Forro, "The electrochemical carbon nanotube field-effect transistor," *arXiv preprint cond-mat/0009171*, 2000.
- [269] S. Rosenblatt, Y. Yaish, J. Park, J. Gore, V. Sazonova, and P. L. McEuen, "High performance electrolyte gated carbon nanotube transistors," *Nano Letters*, vol. 2, pp. 869-872, 2002.
- [270] K. Besteman, J.-O. Lee, F. G. Wiertz, H. A. Heering, and C. Dekker, "Enzyme-coated carbon nanotubes as single-molecule biosensors," *Nano letters*, vol. 3, pp. 727-730, 2003.
- [271] K. Bradley, A. Davis, J.-C. P. Gabriel, and G. Grüner, "Integration of cell membranes and nanotube transistors," *Nano letters*, vol. 5, pp. 841-845, 2005.
- [272] I. Heller, J. Kong, K. A. Williams, C. Dekker, and S. G. Lemay, "Electrochemistry at single-walled carbon nanotubes: the role of band structure and quantum capacitance," *Journal of the American Chemical Society*, vol. 128, pp. 7353-7359, 2006.
- [273] B. M. Quinn, C. Dekker, and S. G. Lemay, "Electrodeposition of noble metal nanoparticles on carbon nanotubes," *Journal of the American Chemical Society*, vol. 127, pp. 6146-6147, 2005.
- [274] A. D. K. Jones and T. Bekkedahl, "Storage of hydrogen in single-walled carbon nanotubes," *Nature*, vol. 386, p. 377, 1997.
- [275] Z. Liu, W. Cai, L. He, N. Nakayama, K. Chen, X. Sun, *et al.*, "In vivo biodistribution and highly efficient tumour targeting of carbon nanotubes in mice," *Nature nanotechnology*, vol. 2, pp. 47-52, 2007.
- [276] S. S. Wong, J. D. Harper, P. T. Lansbury, and C. M. Lieber, "Carbon nanotube tips: high-resolution probes for imaging biological systems," *Journal of the American Chemical Society*, vol. 120, pp. 603-604, 1998.

- [277] S. S. Wong, E. Joselevich, A. T. Woolley, C. L. Cheung, and C. M. Lieber, "Covalently functionalized nanotubes as nanometre-sized probes in chemistry and biology," *Nature*, vol. 394, pp. 52-55, 1998.
- [278] Z. Liu, G. Yang, Y. Z. Lee, D. Bordelon, J. Lu, and O. Zhou, "Carbon nanotube based microfocus field emission x-ray source for microcomputed tomography," *Applied Physics Letters*, vol. 89, p. 103111, 2006.
- [279] Y. Nosh, Y. Ohno, S. Kishimoto, and T. Mizutani, "n-type carbon nanotube field-effect transistors fabricated by using Ca contact electrodes," *Applied Physics Letters*, vol. 86, p. 073105, 2005.
- [280] R. Martel, V. Derycke, C. Lavoie, J. Appenzeller, K. Chan, J. Tersoff, *et al.*, "Ambipolar electrical transport in semiconducting single-wall carbon nanotubes," *Physical Review Letters*, vol. 87, p. 256805, 2001.
- [281] S. Rosenblatt, "Pushing the limits of carbon nanotube transistors," Cornell University, 2006.
- [282] A. J. Bard and L. R. Faulkner, "Electrochemical methods: principles and applications," *Electrochemical Methods: Principles and Applications*, pp. 386-428, 2001.
- [283] H. Harned and B. Owen, "The Physical Chemistry of Electrolytic Solutions Reinhold Pub," *Corp., New York*, vol. 354, 1958.
- [284] R. Dulbecco and M. Vogt, "PLAQUE FORMATION AND ISOLATION OF PURE LINES WITH POLIOMYELITIS VIRUSES," *The Journal of Experimental Medicine*, vol. 99, pp. 167-182, 06/01/received 1954.
- [285] J. Heinze. (1981, 01). Allen J. Bard and Larry F. Faulkner *Electrochemical Methods ? Fundamentals and Applications*. Wiley, New York 1980, 718 + XVIII S., Preis: £ 14.70., *Berichte der Bunsengesellschaft für physikalische Chemie* Volume 85, Issue 11. *Berichte der Bunsengesellschaft für physikalische Chemie* 85(11), 1085-1086. Available: <http://onlinelibrary.wiley.com/doi/10.1002/bbpc.19810851142/abstract>
- [286] D. Lide, "2004 Handbook of Chemistry and Physics," ed: London: CRC Press, 2003.
- [287] I. Heller, S. Chatoor, J. Männik, M. A. Zevenbergen, C. Dekker, and S. G. Lemay, "Influence of electrolyte composition on liquid-gated carbon nanotube and graphene transistors," *Journal of the American Chemical Society*, vol. 132, pp. 17149-17156, 2010.
- [288] L. Larrimore, S. Nad, X. Zhou, H. Abruña, and P. L. McEuen, "Probing Electrostatic Potentials in Solution with Carbon Nanotube Transistors," *Nano Letters*, vol. 6, pp. 1329-1333, 2006/07/01 2006.
- [289] Q. Cao and J. A. Rogers, "Ultrathin films of single-walled carbon nanotubes for electronics and sensors: a review of fundamental and applied aspects," *Advanced Materials*, vol. 21, pp. 29-53, 2009.
- [290] J. Kong, N. R. Franklin, C. Zhou, M. G. Chapline, S. Peng, K. Cho, *et al.*, "Nanotube molecular wires as chemical sensors," *Science*, vol. 287, pp. 622-625, 2000.

- [291] P. Qi, O. Vermesh, M. Grecu, A. Javey, Q. Wang, H. Dai, *et al.*, "Toward large arrays of multiplex functionalized carbon nanotube sensors for highly sensitive and selective molecular detection," *Nano Letters*, vol. 3, pp. 347-351, 2003.
- [292] B. Mahar, C. Laslau, R. Yip, and Y. Sun, "Development of carbon nanotube-based sensors—a review," *Sensors Journal, IEEE*, vol. 7, pp. 266-284, 2007.
- [293] C. B. Jacobs, M. J. Peairs, and B. J. Venton, "Review: Carbon nanotube based electrochemical sensors for biomolecules," *Analytica Chimica Acta*, vol. 662, pp. 105-127, 2010.
- [294] N. Shao, S. Lu, E. Wickstrom, and B. Panchapakesan, "Integrated molecular targeting of IGF1R and HER2 surface receptors and destruction of breast cancer cells using single wall carbon nanotubes," *Nanotechnology*, vol. 18, p. 315101, 2007.
- [295] N. Shao, E. Wickstrom, and B. Panchapakesan, "Nanotube–antibody biosensor arrays for the detection of circulating breast cancer cells," *Nanotechnology*, vol. 19, p. 465101, 2008.
- [296] J. Kong and H. Dai, "Full and modulated chemical gating of individual carbon nanotubes by organic amine compounds," *The Journal of Physical Chemistry B*, vol. 105, pp. 2890-2893, 2001.
- [297] K. Bradley, J.-C. P. Gabriel, A. Star, and G. Grüner, "Short-channel effects in contact-passivated nanotube chemical sensors," *Applied Physics Letters*, vol. 83, pp. 3821-3823, 2003.
- [298] X. Liu, Z. Luo, S. Han, T. Tang, D. Zhang, and C. Zhou, "Band engineering of carbon nanotube field-effect transistors via selected area chemical gating," *Applied Physics Letters*, vol. 86, p. 243501, 2005.
- [299] J. Novak, E. Snow, E. Houser, D. Park, J. Stepnowski, and R. McGill, "Nerve agent detection using networks of single-walled carbon nanotubes," *Applied physics letters*, vol. 83, pp. 4026-4028, 2003.
- [300] X. Cui, M. Freitag, R. Martel, L. Brus, and P. Avouris, "Controlling energy-level alignments at carbon nanotube/Au contacts," *Nano Letters*, vol. 3, pp. 783-787, 2003.
- [301] T. Someya, J. Small, P. Kim, C. Nuckolls, and J. T. Yardley, "Alcohol vapor sensors based on single-walled carbon nanotube field effect transistors," *Nano letters*, vol. 3, pp. 877-881, 2003.
- [302] E. S. Snow and F. K. Perkins, "Capacitance and conductance of single-walled carbon nanotubes in the presence of chemical vapors," *Nano Letters*, vol. 5, pp. 2414-2417, 2005.
- [303] E. Snow, F. Perkins, E. Houser, S. Badescu, and T. Reinecke, "Chemical detection with a single-walled carbon nanotube capacitor," *Science*, vol. 307, pp. 1942-1945, 2005.
- [304] J. A. Robinson, E. S. Snow, S. C. Badescu, T. L. Reinecke, and F. K. Perkins, "Role of defects in single-walled carbon nanotube chemical sensors," *Nano letters*, vol. 6, pp. 1747-1751, 2006.



- [305] S. N. Kim, J. F. Rusling, and F. Papadimitrakopoulos, "Carbon nanotubes for electronic and electrochemical detection of biomolecules," *Advanced materials*, vol. 19, pp. 3214-3228, 2007.
- [306] B. L. Allen, P. D. Kichambare, and A. Star, "Carbon nanotube field-effect-transistor-based biosensors," *Advanced Materials*, vol. 19, pp. 1439-1451, 2007.
- [307] G. Gruner, "Carbon nanotube transistors for biosensing applications," *Analytical and bioanalytical chemistry*, vol. 384, pp. 322-335, 2006.
- [308] K. Bradley, M. Briman, A. Star, and G. Gruner, "Charge transfer from adsorbed proteins," *Nano Letters*, vol. 4, pp. 253-256, 2004.
- [309] A. Star, E. Tu, J. Niemann, J. C. P. Gabriel, C. S. Joiner, and C. Valcke, "Label-free detection of DNA hybridization using carbon nanotube network field-effect transistors," *Proceedings of the National Academy of Sciences of the United States of America*, vol. 103, pp. 921-926, Jan 24 2006.
- [310] E.-L. Gui, L.-J. Li, P. S. Lee, A. Lohani, S. Mhaisalkar, Q. Cao, *et al.*, "Electrical detection of hybridization and threading intercalation of deoxyribonucleic acid using carbon nanotube network field-effect transistors," *Applied Physics Letters*, vol. 89, p. 232104, 2006.
- [311] R. J. Chen, S. Bangsaruntip, K. A. Drouvalakis, N. W. S. Kam, M. Shim, Y. Li, *et al.*, "Noncovalent functionalization of carbon nanotubes for highly specific electronic biosensors," *Proceedings of the National Academy of Sciences*, vol. 100, pp. 4984-4989, 2003.
- [312] H. Cai, X. Cao, Y. Jiang, P. He, and Y. Fang, "Carbon nanotube-enhanced electrochemical DNA biosensor for DNA hybridization detection," *Analytical and bioanalytical chemistry*, vol. 375, pp. 287-293, 2003.
- [313] J. Koehne, J. Li, A. M. Cassell, H. Chen, Q. Ye, H. T. Ng, *et al.*, "The fabrication and electrochemical characterization of carbon nanotube nanoelectrode arrays," *Journal of Materials Chemistry*, vol. 14, pp. 676-684, 2004.
- [314] X. Tang, S. Bansaruntip, N. Nakayama, E. Yenilmez, Y.-I. Chang, and Q. Wang, "Carbon nanotube DNA sensor and sensing mechanism," *Nano Letters*, vol. 6, pp. 1632-1636, 2006.
- [315] X. Yu, B. Munge, V. Patel, G. Jensen, A. Bhirde, J. D. Gong, *et al.*, "Carbon nanotube amplification strategies for highly sensitive immunodetection of cancer biomarkers," *Journal of the American Chemical Society*, vol. 128, pp. 11199-11205, 2006.
- [316] J. P. Kim, B. Y. Lee, J. Lee, S. Hong, and S. J. Sim, "Enhancement of sensitivity and specificity by surface modification of carbon nanotubes in diagnosis of prostate cancer based on carbon nanotube field effect transistors," *Biosensors and Bioelectronics*, vol. 24, pp. 3372-3378, 2009.
- [317] J. Yang, R. Zhang, Y. Xu, P. He, and Y. Fang, "Direct electrochemistry study of glucose oxidase on Pt nanoparticle-modified aligned carbon nanotubes electrode by the assistance of chitosan-CdS and its biosensing for glucose," *Electrochemistry Communications*, vol. 10, pp. 1889-1892, 2008.

- [318] F. N. Ishikawa, B. Stauffer, D. A. Caron, and C. Zhou, "Rapid and label-free cell detection by metal-cluster-decorated carbon nanotube biosensors," *Biosensors and Bioelectronics*, vol. 24, pp. 2967-2972, 2009.
- [319] Q. Shen, S. K. You, S. G. Park, H. Jiang, D. Guo, B. Chen, *et al.*, "Electrochemical biosensing for cancer cells based on TiO<sub>2</sub>/CNT nanocomposites modified electrodes," *Electroanalysis*, vol. 20, pp. 2526-2530, 2008.
- [320] Z. Liu, X. Sun, N. Nakayama-Ratchford, and H. Dai, "Supramolecular chemistry on water-soluble carbon nanotubes for drug loading and delivery," *ACS nano*, vol. 1, pp. 50-56, 2007.
- [321] Y. Xiao, X. Gao, O. Taratula, S. Treado, A. Urbas, R. D. Holbrook, *et al.*, "Anti-HER2 IgY antibody-functionalized single-walled carbon nanotubes for detection and selective destruction of breast cancer cells," *BMC cancer*, vol. 9, p. 351, 2009.
- [322] N. W. S. Kam, M. O'Connell, J. A. Wisdom, and H. Dai, "Carbon nanotubes as multifunctional biological transporters and near-infrared agents for selective cancer cell destruction," *Proceedings of the National Academy of Sciences of the United States of America*, vol. 102, pp. 11600-11605, 2005.
- [323] G. Gruner, "Carbon nanotube transistors for biosensing applications," *Anal Bioanal Chem*, vol. 384, pp. 322-35, Jan 2006.
- [324] A. B. Artyukhin, M. Stadermann, R. W. Friddle, P. Stroeve, O. Bakajin, and A. Noy, "Controlled electrostatic gating of carbon nanotube FET devices," *Nano letters*, vol. 6, pp. 2080-2085, 2006.
- [325] Z. Wu, Z. Chen, X. Du, J. M. Logan, J. Sippel, M. Nikolou, *et al.*, "Transparent, conductive carbon nanotube films," *Science*, vol. 305, pp. 1273-1276, 2004.
- [326] B. King and B. Panchapakesan, "Vacuum filtration based formation of liquid crystal films of semiconducting carbon nanotubes and high performance transistor devices," *Nanotechnology*, vol. 25, p. 175201, 2014.
- [327] M. S. Shaffer, X. Fan, and A. Windle, "Dispersion and packing of carbon nanotubes," *Carbon*, vol. 36, pp. 1603-1612, 1998.
- [328] B. Dan, A. W. Ma, E. H. H  roz, J. Kono, and M. Pasquali, "Nematic-like alignment in SWNT thin films from aqueous colloidal suspensions," *Industrial & Engineering Chemistry Research*, vol. 51, pp. 10232-10237, 2012.
- [329] X. Fan, B. C. King, J. Loomis, E. M. Campo, J. Hegseth, R. W. Cohn, *et al.*, "Nanotube liquid crystal elastomers: photomechanical response and flexible energy conversion of layered polymer composites," *Nanotechnology*, vol. 25, p. 355501, 2014.
- [330] B. King and B. Panchapakesan, "Vacuum filtration based formation of liquid crystal films of semiconducting carbon nanotubes and high performance transistor devices," *Nanotechnology*, vol. 25, May 2 2014.
- [331] M. S. Arnold, A. A. Green, J. F. Hulvat, S. I. Stupp, and M. C. Hersam, "Sorting carbon nanotubes by electronic structure using density differentiation," *Nature nanotechnology*, vol. 1, pp. 60-65, 2006.

- [332] J. Cambedouzou, J. L. Sauvajol, A. Rahmani, E. Flahaut, A. Peigney, and C. Laurent, "Raman spectroscopy of iodine-doped double-walled carbon nanotubes," *Physical Review B*, vol. 69, Jun 2004.
- [333] A. M. Rao, P. Eklund, S. Bandow, A. Thess, and R. E. Smalley, "Evidence for charge transfer in doped carbon nanotube bundles from Raman scattering," *Nature*, vol. 388, pp. 257-259, 1997.
- [334] L. Hu, D. Hecht, and G. Grüner, "Percolation in transparent and conducting carbon nanotube networks," *Nano Letters*, vol. 4, pp. 2513-2517, 2004.
- [335] G. Pike and C. Seager, "Percolation and conductivity: A computer study. I," *Physical review B*, vol. 10, p. 1421, 1974.
- [336] D. Stauffer and A. Aharony, *Introduction to percolation theory*: CRC press, 1994.
- [337] M. Stadermann, S. Papadakis, M. Falvo, J. Novak, E. Snow, Q. Fu, *et al.*, "Nanoscale study of conduction through carbon nanotube networks," *Physical Review B*, vol. 69, p. 201402, 2004.
- [338] J. Sandler, J. Kirk, I. Kinloch, M. Shaffer, and A. Windle, "Ultra-low electrical percolation threshold in carbon-nanotube-epoxy composites," *Polymer*, vol. 44, pp. 5893-5899, 2003.
- [339] B. Kim, J. Lee, and I. Yu, "Electrical properties of single-wall carbon nanotube and epoxy composites," *Journal of Applied Physics*, vol. 94, pp. 6724-6728, 2003.
- [340] C. Laurent, E. Flahaut, and A. Peigney, "The weight and density of carbon nanotubes versus the number of walls and diameter," *Carbon*, vol. 48, pp. 2994-2996, 2010.
- [341] K. Maehashi, T. Katsura, K. Kerman, Y. Takamura, K. Matsumoto, and E. Tamiya, "Label-free protein biosensor based on aptamer-modified carbon nanotube field-effect transistors," *Analytical Chemistry*, vol. 79, pp. 782-787, Jan 2007.
- [342] J. P. Kim, B. Y. Lee, S. Hong, and S. J. Sim, "Ultrasensitive carbon nanotube-based biosensors using antibody-binding fragments," *Analytical Biochemistry*, vol. 381, pp. 193-198, Oct 15 2008.
- [343] T. Dürkop, S. Getty, E. Cobas, and M. Fuhrer, "Extraordinary mobility in semiconducting carbon nanotubes," *Nano letters*, vol. 4, pp. 35-39, 2004.
- [344] R. J. Chen, Y. Zhang, D. Wang, and H. Dai, "Noncovalent sidewall functionalization of single-walled carbon nanotubes for protein immobilization," *Journal of the American Chemical Society*, vol. 123, pp. 3838-3839, 2001.
- [345] H. Kuzmany, A. Kukovecz, F. Simon, M. Holzweber, C. Kramberger, and T. Pichler, "Functionalization of carbon nanotubes," *Synthetic Metals*, vol. 141, pp. 113-122, 2004.
- [346] K. Balasubramanian and M. Burghard, "Chemically functionalized carbon nanotubes," *Small*, vol. 1, pp. 180-192, 2005.
- [347] L. Chen, H. Xie, and W. Yu, *Functionalization methods of carbon nanotubes and its applications*: INTECH Open Access Publisher, 2011.

- [348] A. Hirsch, "Functionalization of single-walled carbon nanotubes," *Angewandte Chemie International Edition*, vol. 41, pp. 1853-1859, 2002.
- [349] E. Katz, "Application of bifunctional reagents for immobilization of proteins on a carbon electrode surface: oriented immobilization of photosynthetic reaction centers," *Journal of Electroanalytical Chemistry*, vol. 365, pp. 157-164, 1994.
- [350] H. Jaegfeldt, T. Kuwana, and G. Johansson, "Electrochemical stability of catechols with a pyrene side chain strongly adsorbed on graphite electrodes for catalytic oxidation of dihydronicotinamide adenine dinucleotide," *Journal of the American Chemical Society*, vol. 105, pp. 1805-1814, 1983.
- [351] V. A. Karachevtsev, S. G. Stepanian, A. Y. Glamazda, M. V. Karachevtsev, V. V. Eremenko, O. S. Lytvyn, *et al.*, "Noncovalent interaction of single-walled carbon nanotubes with 1-pyrenebutanoic acid succinimide ester and glucoseoxidase," *The Journal of Physical Chemistry C*, vol. 115, pp. 21072-21082, 2011.
- [352] P. C. Weber, D. Ohlendorf, J. Wendoloski, and F. Salemme, "Structural origins of high-affinity biotin binding to streptavidin," *Science*, vol. 243, pp. 85-88, 1989.
- [353] B. Y. Lee, M. G. Sung, J. Lee, K. Y. Baik, Y.-K. Kwon, M.-S. Lee, *et al.*, "Universal parameters for carbon nanotube network-based sensors: can nanotube sensors be reproducible?," *ACS nano*, vol. 5, pp. 4373-4379, 2011.
- [354] K. Bradley, J.-C. P. Gabriel, M. Briman, A. Star, and G. Grüner, "Charge transfer from ammonia physisorbed on nanotubes," *Physical review letters*, vol. 91, p. 218301, 2003.
- [355] T. H. Kim, J. Lee, and S. Hong, "Highly selective environmental nanosensors based on anomalous response of carbon nanotube conductance to mercury ions," *The Journal of Physical Chemistry C*, vol. 113, pp. 19393-19396, 2009.
- [356] M. Lee, J. Lee, T. H. Kim, H. Lee, B. Y. Lee, J. Park, *et al.*, "100 nm scale low-noise sensors based on aligned carbon nanotube networks: overcoming the fundamental limitation of network-based sensors," *Nanotechnology*, vol. 21, p. 055504, 2009.
- [357] B. Y. Lee, S. M. Seo, D. J. Lee, M. Lee, J. Lee, J.-H. Cheon, *et al.*, "Biosensor system-on-a-chip including CMOS-based signal processing circuits and 64 carbon nanotube-based sensors for the detection of a neurotransmitter," *Lab on a Chip*, vol. 10, pp. 894-898, 2010.
- [358] A. Star, J. C. P. Gabriel, K. Bradley, and G. Gruner, "Electronic detection of specific protein binding using nanotube FET devices," *Nano Letters*, vol. 3, pp. 459-463, Apr 2003.
- [359] F. Khosravi, B. King, B. Panchapakesan, S. Rai, G. Kloecker, and E. Wickstrom, "Nanotube Devices for Digital Profiling of Cancer Biomarkers and Circulating Tumor Cells," *2013 Ieee 7th International Conference on Nano/Molecular Medicine and Engineering (Nanomed)*, pp. 107-112, 2013.
- [360] J. Wang, G. D. Liu, and M. R. Jan, "Ultrasensitive electrical biosensing of proteins and DNA: Carbon-nanotube derived amplification of the recognition

- and transduction events," *Journal of the American Chemical Society*, vol. 126, pp. 3010-3011, Mar 17 2004.
- [361] M. T. Martinez, Y. C. Tseng, N. Ormategui, I. Loinaz, R. Eritja, and J. Bokor, "Label-Free DNA Biosensors Based on Functionalized Carbon Nanotube Field Effect Transistors," *Nano Letters*, vol. 9, pp. 530-536, Feb 2009.
  - [362] X. C. Dong, C. M. Lau, A. Lohani, S. G. Mhaisalkar, J. Kasim, Z. X. Shen, *et al.*, "Electrical detection of femtomolar DNA via gold-nanoparticle enhancement in carbon-nanotube-network field-effect transistors," *Advanced Materials*, vol. 20, pp. 2389-+, Jun 18 2008.
  - [363] T. Dastagir, E. S. Forzani, R. Zhang, I. Amlani, L. A. Nagahara, R. Tsui, *et al.*, "Electrical detection of hepatitis C virus RNA on single wall carbon nanotube-field effect transistors," *Analyst*, vol. 132, pp. 738-740, 2007.
  - [364] S. Y. Ly and N. S. Cho, "Diagnosis of human hepatitis B virus in non-treated blood by the bovine IgG DNA-linked carbon nanotube biosensor," *Journal of Clinical Virology*, vol. 44, pp. 43-47, Jan 2009.
  - [365] N. Shao, E. Wickstrom, and B. Panchapakesan, "Nanotube-antibody biosensor arrays for the detection of circulating breast cancer cells," *Nanotechnology*, vol. 19, Nov 19 2008.
  - [366] B. C. King, M. Clark, T. Burkhead, P. Sethu, S. Rai, G. Kloecker, *et al.*, "Electrical detection of specific versus non-specific binding events in breast cancer cells," *Biosensing and Nanomedicine V*, vol. 8460, 2012.
  - [367] E. D. Minot, A. M. Janssens, I. Heller, H. A. Heering, C. Dekker, and S. G. Lemay, "Carbon nanotube biosensors: The critical role of the reference electrode," *Applied Physics Letters*, vol. 91, Aug 27 2007.
  - [368] I. Heller, A. M. Janssens, J. Mannik, E. D. Minot, S. G. Lemay, and C. Dekker, "Identifying the mechanism of biosensing with carbon nanotube transistors," *Nano Letters*, vol. 8, pp. 591-595, Feb 2008.
  - [369] S. Khezrian, A. Salimi, H. Teymourian, and R. Hallaj, "Label-free electrochemical IgE aptasensor based on covalent attachment of aptamer onto multiwalled carbon nanotubes/ionic liquid/chitosan nanocomposite modified electrode," *Biosensors & Bioelectronics*, vol. 43, pp. 218-225, May 2013.
  - [370] H.-M. So, K. Won, Y. H. Kim, B.-K. Kim, B. H. Ryu, P. S. Na, *et al.*, "Single-walled carbon nanotube biosensors using aptamers as molecular recognition elements," *Journal of the American Chemical Society*, vol. 127, pp. 11906-11907, 2005.
  - [371] O. S. Kwon, S. J. Park, and J. Jang, "A high-performance VEGF aptamer functionalized polypyrrole nanotube biosensor," *Biomaterials*, vol. 31, pp. 4740-4747, 2010.
  - [372] B. S. Munge, C. E. Krause, R. Malhotra, V. Patel, J. S. Gutkind, and J. F. Rusling, "Electrochemical immunosensors for interleukin-6. Comparison of carbon nanotube forest and gold nanoparticle platforms," *Electrochemistry communications*, vol. 11, pp. 1009-1012, 2009.
  - [373] R. Malhotra, V. Patel, J. P. Vaqu  , J. S. Gutkind, and J. F. Rusling, "Ultrasensitive electrochemical immunosensor for oral cancer biomarker IL-6

- using carbon nanotube forest electrodes and multilabel amplification," *Analytical chemistry*, vol. 82, pp. 3118-3123, 2010.
- [374] T. Li and M. Yang, "Electrochemical sensor utilizing ferrocene loaded porous polyelectrolyte nanoparticles as label for the detection of protein biomarker IL-6," *Sensors and Actuators B: Chemical*, vol. 158, pp. 361-365, 2011.
- [375] R. Stoltenburg, C. Reinemann, and B. Strehlitz, "SELEX--a (r)evolutionary method to generate high-affinity nucleic acid ligands," *Biomol Eng*, vol. 24, pp. 381-403, Oct 2007.
- [376] S. D. Jayasena, "Aptamers: an emerging class of molecules that rival antibodies in diagnostics," *Clin Chem*, vol. 45, pp. 1628-50, Sep 1999.
- [377] C. S. Ferreira, K. Papamichael, G. Guilbault, T. Schwarzacher, J. Garipey, and S. Missailidis, "DNA aptamers against the MUC1 tumour marker: design of aptamer-antibody sandwich ELISA for the early diagnosis of epithelial tumours," *Anal Bioanal Chem*, vol. 390, pp. 1039-50, Feb 2008.
- [378] I. Burbulis, K. Yamaguchi, R. Yu, O. Resnekov, and R. Brent, "Quantifying small numbers of antibodies with a 'near-universal' protein-DNA chimera," *Nat Methods*, vol. 4, pp. 1011-3, Dec 2007.
- [379] T. G. McCauley, N. Hamaguchi, and M. Stanton, "Aptamer-based biosensor arrays for detection and quantification of biological macromolecules," *Anal Biochem*, vol. 319, pp. 244-50, Aug 15 2003.
- [380] Z. Cao, R. Tong, A. Mishra, W. Xu, G. C. Wong, J. Cheng, *et al.*, "Reversible cell-specific drug delivery with aptamer-functionalized liposomes," *Angew Chem Int Ed Engl*, vol. 48, pp. 6494-8, 2009.
- [381] G. De Rosa and M. I. La Rotonda, "Nano and Microtechnologies for the Delivery of Oligonucleotides with Gene Silencing Properties," *Molecules*, vol. 14, p. 2801, 2009.
- [382] C. S. Ferreira, M. C. Cheung, S. Missailidis, S. Bisland, and J. Garipey, "Phototoxic aptamers selectively enter and kill epithelial cancer cells," *Nucleic Acids Res*, vol. 37, pp. 866-76, Feb 2009.
- [383] J. Zhou and J. J. Rossi, "Cell-Specific Aptamer-Mediated Targeted Drug Delivery," *Oligonucleotides*, vol. 21, pp. 1-10, 10/30/received 11/16/accepted 2011.
- [384] T. Kishimoto, "Interleukin-6: from basic science to medicine-40 years in immunology," *Annu. Rev. Immunol.*, vol. 23, pp. 1-21, 2005.
- [385] D. R. Hodge, E. M. Hurt, and W. L. Farrar, "The role of IL-6 and STAT3 in inflammation and cancer," *European journal of cancer*, vol. 41, pp. 2502-2512, 2005.
- [386] G. Bellone, C. Smirne, F. A. Mauri, E. Tonel, A. Carbone, A. Buffolino, *et al.*, "Cytokine expression profile in human pancreatic carcinoma cells and in surgical specimens: implications for survival," *Cancer Immunology, Immunotherapy*, vol. 55, pp. 684-698, 2006.
- [387] J. Li, H.-Y. Mo, G. Xiong, L. Zhang, J. He, Z.-F. Huang, *et al.*, "Tumor microenvironment macrophage inhibitory factor directs the accumulation of interleukin-17-producing tumor-infiltrating lymphocytes and predicts favorable

- survival in nasopharyngeal carcinoma patients," *Journal of Biological Chemistry*, vol. 287, pp. 35484-35495, 2012.
- [388] D. Anestakis, S. Petanidis, S. Kalyvas, C. M. Nday, O. Tsave, E. Kioseoglou, *et al.*, "Mechanisms and Applications of Interleukins in Cancer Immunotherapy," *International journal of molecular sciences*, vol. 16, pp. 1691-1710, 2015.
  - [389] G. Xie, Q. Yao, Y. Liu, S. Du, A. Liu, Z. Guo, *et al.*, "IL-6-induced epithelial-mesenchymal transition promotes the generation of breast cancer stem-like cells analogous to mammosphere cultures," *International journal of oncology*, vol. 40, pp. 1171-1179, 2012.
  - [390] J. A. Gasche, J. Hoffmann, C. R. Boland, and A. Goel, "Interleukin-6 promotes tumorigenesis by altering DNA methylation in oral cancer cells," *International Journal of Cancer*, vol. 129, pp. 1053-1063, 2011.
  - [391] W. Lou, Z. Ni, K. Dyer, D. J. Tweardy, and A. C. Gao, "Interleukin-6 induces prostate cancer cell growth accompanied by activation of Stat3 signaling pathway," *The prostate*, vol. 42, pp. 239-242, 2000.
  - [392] T. D. Chung, J. J. Yu, M. T. Spiotto, M. Bartkowski, and J. W. Simons, "Characterization of the role of IL-6 in the progression of prostate cancer," *The Prostate*, vol. 38, pp. 199-207, 1999.
  - [393] G. Zhang and I. Adachi, "Serum interleukin-6 levels correlate to tumor progression and prognosis in metastatic breast carcinoma," *Anticancer research*, vol. 19, pp. 1427-1432, 1999.
  - [394] J.-Y. Blay, S. Negrier, V. Combaret, S. Attali, E. Goillot, Y. Merrouche, *et al.*, "Serum level of interleukin 6 as a prognosis factor in metastatic renal cell carcinoma," *Cancer Research*, vol. 52, pp. 3317-3322, 1992.
  - [395] Y. C. Chung and Y. F. Chang, "Serum interleukin-6 levels reflect the disease status of colorectal cancer," *Journal of surgical oncology*, vol. 83, pp. 222-226, 2003.
  - [396] J.-W. Miao, L.-J. Liu, and J. Huang, "Interleukin-6-induced epithelial-mesenchymal transition through signal transducer and activator of transcription 3 in human cervical carcinoma," *International journal of oncology*, vol. 45, pp. 165-176, 2014.
  - [397] N. Nishimoto, Y. Kanakura, K. Aozasa, T. Johkoh, M. Nakamura, S. Nakano, *et al.*, "Humanized anti-interleukin-6 receptor antibody treatment of multicentric Castleman disease," *Blood*, vol. 106, pp. 2627-2632, 2005.
  - [398] P. Emery, E. Keystone, H. Tony, A. Cantagrel, R. Van Vollenhoven, A. Sanchez, *et al.*, "IL-6 receptor inhibition with tocilizumab improves treatment outcomes in patients with rheumatoid arthritis refractory to anti-tumour necrosis factor biologicals: results from a 24-week multicentre randomised placebo-controlled trial," *Annals of the rheumatic diseases*, vol. 67, pp. 1516-1523, 2008.
  - [399] J. S. Smolen and R. N. Maini, "Interleukin-6: a new therapeutic target," *Arthritis Research and Therapy*, vol. 8, p. S5, 2006.
  - [400] B. E. Barton, "Interleukin-6 and new strategies for the treatment of cancer, hyperproliferative diseases and paraneoplastic syndromes," 2005.

- [401] M. H. Zaki, J. A. Nemeth, and M. Trikha, "CNTO 328, a monoclonal antibody to IL-6, inhibits human tumor-induced cachexia in nude mice," *International journal of cancer*, vol. 111, pp. 592-595, 2004.
- [402] A. Sun, J. S. Chia, Y. F. Chang, and C. P. Chiang, "Serum interleukin-6 level is a useful marker in evaluating therapeutic effects of levamisole and Chinese medicinal herbs on patients with oral lichen planus," *Journal of oral pathology & medicine*, vol. 31, pp. 196-203, 2002.
- [403] R. Madhok, A. Crilly, J. Watson, and H. A. Capell, "Serum interleukin 6 levels in rheumatoid arthritis: correlations with clinical and laboratory indices of disease activity," *Annals of the Rheumatic Diseases*, vol. 52, pp. 232-234, 1993.
- [404] N. Nishimoto, K. Terao, T. Mima, H. Nakahara, N. Takagi, and T. Kakehi, "Mechanisms and pathologic significances in increase in serum interleukin-6 (IL-6) and soluble IL-6 receptor after administration of an anti-IL-6 receptor antibody, tocilizumab, in patients with rheumatoid arthritis and Castleman disease," *Blood*, vol. 112, pp. 3959-3964, 2008.
- [405] L. Fayad, M. J. Keating, J. M. Reuben, S. O'Brien, B.-N. Lee, S. Lerner, *et al.*, "Interleukin-6 and interleukin-10 levels in chronic lymphocytic leukemia: correlation with phenotypic characteristics and outcome," *Blood*, vol. 97, pp. 256-263, 2001.
- [406] P. Debye, "Dielectric Properties of Pure Liquids," *Chem. Rev.*, vol. 19, pp. 171-182, october 17, 1936 1936.
- [407] Y. C. Chung and Y. F. Chang, "Serum interleukin-6 levels reflect the disease status of colorectal cancer," *Journal of Surgical Oncology*, vol. 83, pp. 222-226, Aug 2003.
- [408] J. Y. Blay, S. Negrier, V. Combaret, S. Attali, E. Goillot, Y. Merrouche, *et al.*, "Serum Level of Interleukin-6 as a Prognosis Factor in Metastatic Renal-Cell Carcinoma," *Cancer Research*, vol. 52, pp. 3317-3322, Jun 15 1992.
- [409] F. M. Brichory, D. E. Misek, A. M. Yim, M. C. Krause, T. J. Giordano, D. G. Beer, *et al.*, "An immune response manifested by the common occurrence of annexins I and II autoantibodies and high circulating levels of IL-6 in lung cancer," *Proceedings of the National Academy of Sciences of the United States of America*, vol. 98, pp. 9824-9829, Aug 14 2001.
- [410] K. Pachmann, P. Heiß, U. Demel, and G. Tilz, "Detection and quantification of small numbers of circulating tumour cells in peripheral blood using laser scanning cytometer (LSC®)," *Clinical chemistry and laboratory medicine*, vol. 39, pp. 811-817, 2001.
- [411] K. Pachmann, J. H. Clement, C.-P. Schneider, B. Willen, O. Camara, U. Pachmann, *et al.*, "Standardized quantification of circulating peripheral tumor cells from lung and breast cancer," *Clinical Chemical Laboratory Medicine*, vol. 43, pp. 617-627, 2005.
- [412] M. Tewes, B. Aktas, A. Welt, S. Mueller, S. Hauch, R. Kimmig, *et al.*, "Molecular profiling and predictive value of circulating tumor cells in patients with metastatic breast cancer: an option for monitoring response to breast



- cancer related therapies," *Breast cancer research and treatment*, vol. 115, pp. 581-590, 2009.
- [413] M. S. Bretscher, "The molecules of the cell membrane," *Sci Am*, vol. 253, pp. 100-8, Oct 1985.
- [414] W. A. Osta, Y. Chen, K. Mikhitarian, M. Mitas, M. Salem, Y. A. Hannun, *et al.*, "EpCAM is overexpressed in breast cancer and is a potential target for breast cancer gene therapy," *Cancer research*, vol. 64, pp. 5818-5824, 2004.
- [415] H. D. Soule, T. M. Maloney, S. R. Wolman, W. D. Peterson, R. Brenz, C. M. McGrath, *et al.*, "Isolation and characterization of a spontaneously immortalized human breast epithelial cell line, MCF-10," *Cancer research*, vol. 50, pp. 6075-6086, 1990.
- [416] C. C. Benz, G. K. Scott, J. C. Sarup, R. M. Johnson, D. Tripathy, E. Coronado, *et al.*, "Estrogen-dependent, tamoxifen-resistant tumorigenic growth of MCF-7 cells transfected with HER2/neu," *Breast Cancer Res Treat*, vol. 24, pp. 85-95, 1992.
- [417] K. Subik, J.-F. Lee, L. Baxter, T. Strzepak, D. Costello, P. Crowley, *et al.*, "The Expression Patterns of ER, PR, HER2, CK5/6, EGFR, Ki-67 and AR by Immunohistochemical Analysis in Breast Cancer Cell Lines," *Breast Cancer : Basic and Clinical Research*, vol. 4, pp. 35-41, 05/20 2010.
- [418] M. Balzar, M. Winter, C. De Boer, and S. Litvinov, "The biology of the 17–1A antigen (Ep-CAM)," *Journal of Molecular Medicine*, vol. 77, pp. 699-712, 1999.
- [419] G. Williams and D. C. Watts, "Non-symmetrical dielectric relaxation behaviour arising from a simple empirical decay function," *Transactions of the Faraday Society*, vol. 66, pp. 80-85, 1970.
- [420] R. Kohlrausch, "Theorie des elektrischen Rückstandes in der Leidener Flasche," *Annalen der Physik*, vol. 167, pp. 179-214, 1854.
- [421] B. Flora, "Mapping disease - Microarrays super-power genetic content analysis," *Econtent*, vol. 30, pp. 12-13, Mar 2007.
- [422] A. A. Dmitriev, V. I. Kashuba, K. Haraldson, V. N. Senchenko, T. V. Pavlova, A. V. Kudryavtseva, *et al.*, "Genetic and epigenetic analysis of non-small cell lung cancer with NotI-microarrays," *Epigenetics*, vol. 7, pp. 502-513, May 2012.
- [423] J. Flach, F. Dicker, S. Schnittger, S. Schindela, A. Kohlmann, T. Haferlach, *et al.*, "An accumulation of cytogenetic and molecular genetic events characterizes the progression from MDS to secondary AML: an analysis of 38 paired samples analyzed by cytogenetics, molecular mutation analysis and SNP microarray profiling," *Leukemia*, vol. 25, pp. 713-718, Apr 2011.
- [424] D. A. Lashkari, J. L. DeRisi, J. H. McCusker, A. F. Namath, C. Gentile, S. Y. Hwang, *et al.*, "Yeast microarrays for genome wide parallel genetic and gene expression analysis," *Proceedings of the National Academy of Sciences of the United States of America*, vol. 94, pp. 13057-13062, Nov 25 1997.

- [425] E. M. Weidenhammer, B. F. Kahl, L. Wang, L. Wang, M. Duhon, J. A. Jackson, *et al.*, "Multiplexed, targeted gene expression profiling and genetic analysis on electronic microarrays," *Clinical Chemistry*, vol. 48, pp. 1873-1882, Nov 2002.
- [426] L. Florens, M. P. Washburn, J. D. Raine, R. M. Anthony, M. Grainger, J. D. Haynes, *et al.*, "A proteomic view of the Plasmodium falciparum life cycle," *Nature*, vol. 419, pp. 520-526, Oct 3 2002.
- [427] M. Fulwyler, "Electronic separation of biological cells by volume," *Science*, vol. 150, pp. 910-911, 1965.
- [428] J. P. Whelan, A. W. Kusterbeck, G. A. Wemhoff, R. Bredehorst, and F. S. Ligler, "Continuous-Flow Immunosensor for Detection of Explosives," *Analytical Chemistry*, vol. 65, pp. 3561-3565, Dec 15 1993.
- [429] H. Davies, L. Lomas, and B. Austen, "Profiling of amyloid beta peptide variants using SELDI ProteinChip (R) arrays," *Biotechniques*, vol. 27, pp. 1258-1261, Dec 1999.
- [430] N. H. H. Heegaard and R. T. Kennedy, "Identification, quantitation, and characterization of biomolecules by capillary electrophoretic analysis of binding interactions," *Electrophoresis*, vol. 20, pp. 3122-3133, Oct 1999.
- [431] G. Zheng, F. Patolsky, Y. Cui, W. U. Wang, and C. M. Lieber, "Multiplexed electrical detection of cancer markers with nanowire sensor arrays," *Nature biotechnology*, vol. 23, pp. 1294-1301, 2005.
- [432] J. Okuno, K. Maehashi, K. Kerman, Y. Takamura, K. Matsumoto, and E. Tamiya, "Label-free immunosensor for prostate-specific antigen based on single-walled carbon nanotube array-modified microelectrodes," *Biosensors & Bioelectronics*, vol. 22, pp. 2377-2381, Apr 15 2007.
- [433] P. Lin, F. Yan, J. J. Yu, H. L. W. Chan, and M. Yang, "The Application of Organic Electrochemical Transistors in Cell-Based Biosensors," *Advanced Materials*, vol. 22, pp. 3655-+, Sep 1 2010.
- [434] S. Nagrath, L. V. Sequist, S. Maheswaran, D. W. Bell, D. Irimia, L. Ulkus, *et al.*, "Isolation of rare circulating tumour cells in cancer patients by microchip technology," *Nature*, vol. 450, pp. 1235-U10, Dec 20 2007.
- [435] S. L. Stott, C. H. Hsu, D. I. Tsukrov, M. Yu, D. T. Miyamoto, B. A. Waltman, *et al.*, "Isolation of circulating tumor cells using a microvortex-generating herringbone-chip," *Proceedings of the National Academy of Sciences of the United States of America*, vol. 107, pp. 18392-18397, Oct 26 2010.
- [436] K. Pachmann, P. Heiss, U. Demel, and G. Tilz, "Detection and quantification of small numbers of circulating tumour cells in peripheral blood using laser scanning cytometer (LSC (R))," *Clinical Chemistry and Laboratory Medicine*, vol. 39, pp. 811-817, Sep 2001.
- [437] Y. T. Lu, L. B. Zhao, Q. L. Shen, M. A. Garcia, D. X. Wu, S. Hou, *et al.*, "NanoVelcro Chip for CTC enumeration in prostate cancer patients," *Methods*, vol. 64, pp. 144-152, Dec 1 2013.
- [438] H. Lee, T. J. Yoon, J. L. Figueiredo, F. K. Swirski, and R. Weissleder, "Rapid detection and profiling of cancer cells in fine-needle aspirates," *Proceedings of*

- the National Academy of Sciences of the United States of America*, vol. 106, pp. 12459-12464, Jul 28 2009.
- [439] M. Munz, P. A. Baeuerle, and O. Gires, "The emerging role of EpCAM in cancer and stem cell signaling," *Cancer research*, vol. 69, pp. 5627-5629, 2009.
  - [440] M. Balzar, M. J. Winter, C. J. de Boer, and S. V. Litvinov, "The biology of the 17-1A antigen (Ep-CAM)," *Journal of Molecular Medicine-Jmm*, vol. 77, pp. 699-712, Oct 1999.
  - [441] B. T. F. van der Gun, L. J. Melchers, M. H. J. Ruiters, L. F. M. H. de Leij, P. M. J. McLaughlin, and M. G. Rots, "EpCAM in carcinogenesis: the good, the bad or the ugly," *Carcinogenesis*, vol. 31, pp. 1913-1921, Nov 2010.
  - [442] A. Majumdar, "Bioassays based on molecular nanomechanics," *Disease Markers*, vol. 18, pp. 167-174, 2002.
  - [443] A.C. Cambon, K.B. Baumgartner, G.N. Brock, N.G. F.Cooper, D.Wu, and S. N. Rai, "Classification of Clinical Outcomes Using High-Throughput Informatics: Part 2- Non-Parametric Method Reviews. Journal of Model Assisted Statistics and Applications," *Model Assisted Statistics and Applications*, vol. 10, pp. 89-107, 2015.
  - [444] A.C.Cambon, K.B. Baumgartner, G.N. Brock, N.G.F Cooper, D. Wu, and S. N. Rai, "Classification of Clinical Outcomes Using High-Throughput Informatics: Part 1- Non-Parametric Method Reviews.," *Journal of Model Assisted Statistics and Applications*, vol. 10, pp. 3-23, 2015.
  - [445] S. N. Rai, J. Pan, A. Cambon, J. B. Chaires, and N. C. Garbett, "Group classification based on high-dimensional data: application to differential scanning calorimetry plasma thermogram analysis of cervical cancer and control samples," *Open Access Medical Statistics*, vol. 3, pp. 1-9, 2013.
  - [446] S. Rai, P. Trainor, F. Khosravi, G. Kloecker, and B. Panchapakesan, "Classification of biosensor time series using dynamic time warping: applications in screening cancer cells with characteristic biomarkers," *Open Access Medical Statistics*, vol. 6, p. 21, 2016.
  - [447] M. Müller, *Information retrieval for music and motion* vol. 2: Springer, 2007.
  - [448] L. R. Rabiner and B.-H. Juang, *Fundamentals of speech recognition* vol. 14: PTR Prentice Hall Englewood Cliffs, 1993.
  - [449] H. Sakoe and S. Chiba, "Dynamic programming algorithm optimization for spoken word recognition," *Acoustics, Speech and Signal Processing, IEEE Transactions on*, vol. 26, pp. 43-49, 1978.
  - [450] T. Hastie, R. Tibshirani, J. Friedman, T. Hastie, J. Friedman, and R. Tibshirani, *The elements of statistical learning* vol. 2: Springer, 2009.
  - [451] T.-c. Fu, "A review on time series data mining," *Engineering Applications of Artificial Intelligence*, vol. 24, pp. 164-181, 2011.
  - [452] D. Bernad, "Finding patterns in time series: a dynamic programming approach," *Advances in knowledge discovery and data mining*, 1996.
  - [453] T. Giorgino, "Computing and visualizing dynamic time warping alignments in R: the dtw package," *Journal of statistical Software*, vol. 31, pp. 1-24, 2009.

- [454] H. Sakoe and S. Chiba, "Dynamic programming algorithm optimization for spoken word recognition," *IEEE transactions on acoustics, speech, and signal processing*, vol. 26, pp. 43-49, 1978.
- [455] T. Hastie, J. H. Friedman, and R. Tibshirani, *The elements of statistical learning : data mining, inference, and prediction*, 2nd ed. New York: Springer, 2009.
- [456] J.-M. Park, J.-Y. Lee, J.-G. Lee, H. Jeong, J.-M. Oh, Y. J. Kim, *et al.*, "Highly efficient assay of circulating tumor cells by selective sedimentation with a density gradient medium and microfiltration from whole blood," *Analytical chemistry*, vol. 84, pp. 7400-7407, 2012.
- [457] R. Rosenberg, R. Gertler, J. Friederichs, K. Fuehrer, M. Dahm, R. Phelps, *et al.*, "Comparison of two density gradient centrifugation systems for the enrichment of disseminated tumor cells in blood," *Cytometry*, vol. 49, pp. 150-158, 2002.
- [458] T. Gerhardt, S. Woo, and H. Ma, "Chromatographic behaviour of single cells in a microchannel with dynamic geometry," *Lab on a Chip*, vol. 11, pp. 2731-2737, 2011.
- [459] S. M. McFaul, B. K. Lin, and H. Ma, "Cell separation based on size and deformability using microfluidic funnel ratchets," *Lab on a chip*, vol. 12, pp. 2369-2376, 2012.
- [460] M. S. Kim, T. S. Sim, Y. J. Kim, S. S. Kim, H. Jeong, J.-M. Park, *et al.*, "SSA-MOA: a novel CTC isolation platform using selective size amplification (SSA) and a multi-obstacle architecture (MOA) filter," *Lab on a Chip*, vol. 12, pp. 2874-2880, 2012.
- [461] W. Sun, C. Jia, T. Huang, W. Sheng, G. Li, H. Zhang, *et al.*, "High-performance size-based microdevice for the detection of circulating tumor cells from peripheral blood in rectal cancer patients," *PloS one*, vol. 8, p. e75865, 2013.
- [462] C.-L. Chen, K.-C. Chen, Y.-C. Pan, T.-P. Lee, L.-C. Hsiung, C.-M. Lin, *et al.*, "Separation and detection of rare cells in a microfluidic disk via negative selection," *Lab on a Chip*, vol. 11, pp. 474-483, 2011.
- [463] N. M. Karabacak, P. S. Spuhler, F. Fachin, E. J. Lim, V. Pai, E. Ozkumur, *et al.*, "Microfluidic, marker-free isolation of circulating tumor cells from blood samples," *Nat Protoc*, vol. 9, pp. 694-710, Mar 2014.
- [464] S. D. Mikolajczyk, L. S. Millar, P. Tsinberg, S. M. Coutts, M. Zomorodi, T. Pham, *et al.*, "Detection of EpCAM-negative and cytokeratin-negative circulating tumor cells in peripheral blood," *Journal of oncology*, vol. 2011, 2011.
- [465] H. W. Hou, M. E. Warkiani, B. L. Khoo, Z. R. Li, R. A. Soo, D. S.-W. Tan, *et al.*, "Isolation and retrieval of circulating tumor cells using centrifugal forces," *Scientific reports*, vol. 3, 2013.
- [466] V. Gupta, I. Jafferji, M. Garza, V. O. Melnikova, D. K. Hasegawa, R. Pethig, *et al.*, "ApoStream™, a new dielectrophoretic device for antibody independent isolation and recovery of viable cancer cells from blood," *Biomicrofluidics*, vol. 6, p. 024133, 2012.
- [467] F. Fabbri, S. Carloni, W. Zoli, P. Ulivi, G. Gallerani, P. Fici, *et al.*, "Detection and recovery of circulating colon cancer cells using a dielectrophoresis-based

- device: KRAS mutation status in pure CTCs," *Cancer letters*, vol. 335, pp. 225-231, 2013.
- [468] S. C. Hur, A. J. Mach, and D. Di Carlo, "High-throughput size-based rare cell enrichment using microscale vortices," *Biomicrofluidics*, vol. 5, p. 022206, 2011.
  - [469] I. Heller, A. M. Janssens, J. Männik, E. D. Minot, S. G. Lemay, and C. Dekker, "Identifying the mechanism of biosensing with carbon nanotube transistors," *Nano Letters*, vol. 8, pp. 591-595, 2008.
  - [470] X. Zhou, J. M. Moran-Mirabal, H. G. Craighead, and P. L. McEuen, "Supported lipid bilayer/carbon nanotube hybrids," *Nature nanotechnology*, vol. 2, pp. 185-190, 2007.
  - [471] C. E. Morris, "Mechanosensitive ion channels," *Journal of Membrane Biology*, vol. 113, pp. 93-107, 1990.
  - [472] S. Tripathi, "Mechanical stress mechanisms and the cell," *Circ Res*, vol. 72, pp. 239-245, 1993.
  - [473] T. Hastie, R. Tibshirani, and J. H. Friedman, *The elements of statistical learning : data mining, inference, and prediction*, 2nd ed. New York, NY: Springer, 2009.
  - [474] D. J. Berndt and J. Clifford, "Finding patterns in time series: a dynamic programming approach," in *Advances in knowledge discovery and data mining*, M. F. Usama, P.-S. Gregory, S. Padhraic, and U. Ramasamy, Eds., ed: American Association for Artificial Intelligence, 1996, pp. 229-248.
  - [475] H. Sakoe and S. Chiba, "Dynamic-Programming Algorithm Optimization for Spoken Word Recognition," *Ieee Transactions on Acoustics Speech and Signal Processing*, vol. 26, pp. 43-49, 1978.
  - [476] L. L. Ouellette, "Chemical and Biological Sensing with Carbon Nanotubes in Solution," Cornell University, 2008.
  - [477] D. R. Gossett, W. M. Weaver, A. J. Mach, S. C. Hur, H. T. K. Tse, W. Lee, *et al.*, "Label-free cell separation and sorting in microfluidic systems," *Analytical and bioanalytical chemistry*, vol. 397, pp. 3249-3267, 2010.